An experimental test for the existence of the Euler wake velocity, validating Eulerlet theory by using a bluff body in a low-speed wind tunnel

By

Kiran Chalasani

(B. Eng., M.Sc.)

Ph.D. Thesis   2020

An experimental test for the existence of the Euler wake velocity, validating Eulerlet theory by using a bluff body in a low-speed wind tunnel

Kiran Chalasani

School of Computing, Science, and Engineering

University of Salford, Manchester, UK

Submitted in Partial Fulfilment of the Requirements for the Degree of Doctor of Philosophy, July 2020

Abstract

The application of manoeuvrability problems in aerodynamics mainly works for Reynolds average Navier-Stokes equations particularly for a uniform, steady flow past a fixed body. Further, consider large Reynolds number such that the flow is not turbulent, and the boundary layer is negligibly small and the impermeability boundary condition holds. Instead of using standard techniques and theory for describing the problem, a new method is employed based upon the concept of matching two different Green's integral representations over a common boundary, one given by approximations valid in the near-field and the other by approximations in the far-field such that, a near-field Euler flow is matched to a far-field Oseen flow.

Far from the body, linearise the velocity to the uniform stream yielding Oseen flow to leading order and match the near-field Euler and far-field Oseen flow on a common matching boundary. In particular, match the Green's integral representations that use Green's functions which are point force solutions. This gives new Green's functions which we call Eulerlets and are obtained by collapsing the diffuse wake of the corresponding Oseenlets onto a wake line represented by Heaviside and delta functions. The matching equates terms on the common boundary yielding the Bernoulli equation.

One important consequence of the model is the presence of a new Euler wake velocity which is not captured in standard models. This has a constant unchanging downstream profile and arises from the matching to the far-field Oseen wake velocity. The drag calculation is shown to originate solely from a new wake inflow term comprising of layers of different velocities slipping past each other meaning that drag is possible in Euler flow from the momentum loss. So, the model includes a new drag Euler slip wake countering D'Alembert's paradox. The theory is tested against a wake inflow problem, as this is where it differs from standard Euler representations. In particular, we consider uniform flow past a circular cylinder which is the classic textbook problem demonstrating D'Alembert's paradox.

An experiment is devised to test Eulerlet theory for steady, incompressible, uniform Euler flow past a fixed, closed body. This theory predicts the existence of an Euler wake that has a constant unchanged profile at any downstream station. To experimentally test the theory, a circular cylinder with an axis perpendicular to the flow direction is placed in a closed low-speed wind tunnel. The velocity profile is obtained by a hot-wire anemometer

attached to a novel design purpose-built probe arm moved by an external traverse mechanism and determined at three downstream stations. The Euler wake velocity is then calculated by taking away the potential velocity from the experimentally evaluated fluid velocity. The potential velocity in the wake region itself is estimated by extrapolation from its value outside the wake. The same underlying Euler wake velocity profile is found at two of the three stations, as predicted by the theory. For the third downstream station furthest away, diffusive turbulent effects occur, increasing energy in the wake well and so contaminating the results.

Acknowledgement

<u>Declaration</u>

I, Kiran Chalasani, declare that this thesis is my original work, and has not been submitted elsewhere for any award. Any section, part or phrasing that has been used or copied from other literature or documents copied has been referenced at the point of use as well as in the reference section of the thesis work.

………………………   ………………………….

Signature   Date

Table of Contents

Notation

ρ	Density of fluid in kg/m^3
t	Time is seconds
p	Pressure of the fluid
δ_{ij}	Kronecker delta
μ	Coefficient of viscosity
U	Free stream velocity
ϕ	Velocity potential satisfying the Laplace equation
ω_i	Wake velocity
u_i	Perturbed velocity
u_i^{Oseen}	Perturbed Oseen velocity
η	The wake variable in two-dimensions
χ	Wake velocity potential
V	Volume of the fluid
r	Radius of the cylinder in two-dimension
$u_j^{\dagger}$	Total velocity
$p^{\dagger}$	Total pressure
Re	Dimension less Reynolds number
k	Dimensionless wake number
l	Length of the cylinder
δ	Dirac delta function of the variables of the space
ε_{ijk}	Three dimensional Levi-Civita symbol
D_i	Unit force in x_1 direction
$H(x_1)$	Heaviside function in x_1 direction
n_i	Outward point normal
n_i^v	Outward point normal to the given volume

a_1 & a_m	Fourier coefficients
Σ	A region of space
$d\Sigma$	Element of space
K_o	Modified Bessel function of zero order
C_D	Coefficient of drag
C_p	Coefficient of pressure
p_{dim}	Dimensional pressure
$R_1, R_2,$ & R_3	Resistance
I	Current
T	Temperature
K_1	Betz constant

a_1 & a_m	Fourier coefficients
Σ	A region of space

Table of figures

List of tables

1 Introduction

1.1 Manoeuvrability Bodies

The manoeuvrability of fish and marine mammals attained at swimming speeds is remarkably good even for unsteady flow and despite fluid turbulence. The desire to predict the motion and analysis of manoeuvring bodies such as airships, submarines, marine animal propulsion, aircraft and missile guidance is for faster and stable design to be able to understand the complete physical phenomena of the flow domain. The application of manoeuvrability problems is of interest to aerodynamicists. So far, different theories have been suggested to model the flow more accurately such as flow past a sphere by Stokes in (1851), the aerodynamic forces on airship hulls by Max Munk (1924), (Jones, R.T, 1979) slender body theory by Lighthill (Lighthill, 1960), thin aerofoil theory, thin wing theory, Oseenlets theory by Chadwick (Chadwick, 1998), vortex lattice methods, panel methods and so on for different Reynolds numbers.

It was Stokes (1851) that first obtained a solution for flow past a sphere by neglecting the inertia of the fluid for small Reynolds numbers. Whitehead (1889) gives a solution for non-negligible Reynolds number flows by considering the higher-order approximations, but the assumption is incompatible with the free stream condition. The expansion terms are not satisfying the boundary conditions except for the leading term. It is common for all finite length scale bodies with the uniform stream. This whole phenomenon is called the Whitehead paradox. In two-dimensional flow, even the first term is incompatible, and this is called the Stokes paradox. Neither the Stokes equation nor the equations for potential flow are uniformly valid throughout the fluid domain and instead breakdown far from the body. Later, the paradox has been resolved by Oseen (1910) (Proudman and Pearson, 1957).

Munk (1924) developed slender body theory to understand the aerodynamic loads exerted on an airship hull by considering the elongated rigid body moving in a fluid. Munk considers different sections of the body, so that flow generated by one section is determined independently from the other and at the same time making sure the body is adequately slender and not changing abruptly. Slender body theory works on the principle of potential flow theory and conservation of momentum along the body axis (Yu and Eloy, 2018).

The aerodynamic forces are calculated based on an irrotational perfect fluid, however, vortices in the fluid are present created by fluid viscosity even though this is very small. The

results will give a good understanding of the aerodynamic forces of an airship if the viscous effects are negligible compared to the inertia forces. The fluid velocity is given by a velocity potential and pressure is then given by the Bernoulli equation. The pressure is integrated over the surface, giving the resultant distribution of longitudinal and lateral forces along the ship. (Tuckerman, 1976).

Munk has, however, used the knowledge of the detailed pressure distribution based upon velocity potentials to show the effect of changing shape upon the flow. This is achieved by reducing the problem to that of solving two-dimensional flow problems at a series of sections along the body length. Potential flow theory is adequate for predicting surface pressure forces and moments at different angles concerning airship hull structural rigidity. However, moments calculated are overpredicted compared to the wind tunnel tests even at small angles. As mentioned earlier, we cannot neglect the viscous effects for the real fluids and that decreases the unstable moment and increases the local lift. Later, Upson and Klikoff have explained the discrepancy in the pitching moment (Tuckerman, 1976).

Lighthill (1960) worked on extending slender body theory for body aspect ratio asymptotically small and deforming swimming bodies by body force calculations using momentum conservation. This theory showed that the average total force only depends on the kinematics of the tail of the periodically deforming fish (Lighthill, 1960). Later, Lighthill proposed an elongated body theory to understand the kinematics, energetics of swimming and drag reduction mechanism for fish (Alexander, 1977: Webb, 1975, Videler, 1981: Ehrensteian and Eloy, 2013). However, some drawbacks in Lighthill slender body theory are noted as it can only be applied for asymptotically small aspect ratio and it doesn't obey the Kutta condition (Yu and Eloy, 2018).

Slender body theory allows for an approximate solution of the governing equation modelling a physical phenomenon that is affected by the presence of bodies, which are long and thin. Potential flow problems include animal locomotion (Lighthill, 1960)(Lighthill, 1971), the force on airship hulls (Munk, 1924)(Jones, R.T, 1979), the force on wings (Jones, 1946) and ship hydrodynamics (Newman, 1970) have been solved using slender body theory and it has wider applications in heat transfer and composite materials as well (Borker and Koch, 2018).

The basic idea in slender body theory is to obtain the strength of a line of singularities placed along centreline of the slender filament that approximates the field of interest around the filament. The singularity for a potential flow problem is a point source of mass, for a heat transfer problem a point source of heat and for a Stokes flow problem a point force. The

strength of the singularity is found by matching the near-field solution and far-field solution (Borker and Koch, 2018).

Following the Stokes approximation and Whitehead paradox, Lamb (1911) provided a solution for flow past a circular cylinder by additionally considering the inertia terms and gave the drag force on the circular cylinder for small Reynolds numbers. Later, Oseen provided a solution for the same problem by considering the far-field boundary conditions and including the momentum equations as a correction term. Oseen (1927) studied the problem extensively and gave the solution for the flow past various bodies at small Reynolds numbers. Lamb (Lamb, 1911), extended the work to elliptical cylinders and obtained an expansion formula using the Oseen approximation. Then, Filon (Filon, 1927) (Filon, 1926) used the Oseen approximation to give the formula for drag and lift of a cylinder in terms of the circulation and inflow along the wake. It is an extension of the Kutta-Joukowski theorem (Imai, 1951). By including the inertia terms, Oseen improved the flow picture far from the body.

Furthermore, there are drawbacks with slender body theory because it is not able to model the vortex wake and viscous separation and diffusion. Oseen theory models thus in the far-field, but the near-field is important for manoeuvring bodies at high Reynolds number. So, the idea is to model near-field and far-field with appropriate theories. Oseen equations are more accurate as flow goes far from the body, so that the approximation is very good over an infinitely extended region of the flow field and Stokes approximation is highly accurate near to the body (Imai, 1951). However, Stokes flow can be used for low Reynolds numbers and many manoeuvring problems are large Reynolds number. Instead of using Oseen's representation of Oseen flow, (Chadwick, 1998) used Oseen flow with Greens representation and Taylor expansion to give a more accurate flow model in the far-field called Oseenlet theory. Now the challenge is to match this to a more accurate near-field flow for high Reynolds number (Chadwick, Christian and Chalasani, 2019).

The Euler equations, obtained from Navier-Stokes equations by neglecting the small viscous term at high Reynolds number, has many important practical uses in aerodynamics and hydrodynamics, but also some theoretical difficulties. Euler Theory is a good approximation for high Reynolds numbers in the near field, but the standard potential flow representation fails to overcome D'Alembert's paradox. So, the challenge is to develop a model in the near and far-field by using Euler flow and Oseen flow respectively. Similarity can be drawn from near-field Stokes and far-field Oseen approximation for small Reynolds

number, see, for example, (Proudman and Pearson, 1957), and Kaplun and Lagerstrom (1967) (Chadwick and Kapoulas, 2014).

Eulerlets are introduced in the near-field model in a similar way to Oseenlets in the far-field model by a Green's representation. The model follows Green's representation such that the body moves in an infinite incompressible inviscid fluid in such a way that the flow is of irrotational, continuous Eulerian type everywhere and the velocity distribution in the downstream wake captured. A non-viscous boundary element method involving a convolution integral formulation is developed to determine directly the fluid actions and velocity flow field associated with a body manoeuvring in a fluid (Chadwick, Christian and Chalasani, 2019). Euler flow has many advantages in providing quick accurate solutions and insight into flow physics. However, it is unable to determine accurately the drag force due to D'Alembert's paradox for closed streamline flows; even if free streamline theory is considered, the physics and predictions resulting with this theory are unrealistic and poor (Kiya and Arie, 1977).

1.2 Review of State of the Art

Research studies in the manoeuvrability of an aerofoil, airships, submarine manoeuvring, and marine animal propulsion have been carried out for more than hundred years, with interest in finding the accurate mathematical model that enables us to determine manoeuvring characteristics. The major motivation of this research was to model the flow domain more accurately with Oseenlets and Eulerlets as experimentally validate this model. Oseen equations are more valuable for analytically tractable solutions. So far different types of Oseen solutions were produced in two and three-dimensional problems such as Oseen approximation for a circular cylinder and uniform motion of a sphere through a viscous fluid by Lamb (Lamb, 1911), Filon (1926) Faxen (1927), and Goldstein (1924,1931). Tomotika and Aoi (1950) solved the Oseen equations using in simple multipole expansions, similar solutions are provided (Dennis and Kochbiyik, 1990) for flow past an inclined elliptical body with respect to the flow (Gustafsson and Protas, 2013) (Dennis and Kochbiyik, 1990). Faxen was the first to obtain a rigorous analytical solution for the purely viscous drag of a sphere moving parallel with walls bounding a fluid space (Lindgren, 1999). The Oseen equations have been used to model the far-field Oseen flow at low Reynolds number and asymptotically matched to near-field Stokes flows (Happel & Bernner 1991; Kaplun & Lagerstrom 1957; Lagerstrom 1964; Proudman & Pearson 1957). They used the decomposition of the velocity into a potential velocity and a wake velocity used by Lamb (1932) and Goldstein (1929,1931)(Chadwick, 2002).

Recent work on Oseen flow, Chadwick presented the far-field Oseen velocity description for a fixed body in a uniform flow-field (Chadwick, 1998). It was shown how the far-field velocity is represented by an integral distribution of Oseenlets, as described by Oseen. This relies on certain far-field integral contributions tending to zero, as subsequently shown by (Fishwick, N and Chadwick, 2006). This far-field velocity representation can then be matched to a near-field flow, such as the low Reynolds number Stokes flow (Chadwick, 2013). For the high Reynolds number steady flow, it can also be continued into the near-field giving an Oseen flow for slender-bodies (Chadwick, 2002). For this case, a discrepancy in the description of the wake is found between the Oseen model and the standard inviscid potential flow model. This gives rise to a difference between the two models for the calculation of the forces on the slender body. Subsequently, experiment verified that the Oseen model, rather than the potential flow model, evaluated lift correctly for slender bodies of different elliptic cross-section (Chadwick *et al.*, 2010). Similarly, by comparing the lift Oseenlets and the inviscid potential horseshoe vortex, a new slender wing potential flow model is obtained (Chadwick, 2005). This is different from standard potential flow theory in that it also includes a singular vortex-wake-velocity part originating from the lift Oseenlets. This is the core of the Oseen vortex line (Chadwick, 2006). This difference also produces a lift discrepancy between existing Euler and Oseen flow models which leads to a proposal for an alternative model from the Oseen flow in the high Reynolds number limit (Chadwick and Hatam, 2007). This suggests developing a new Euler model by considering Eulerlets, which in (Chadwick and Kapoulas, 2014) are obtained from Oseenlets in the limit as the Reynolds number tends to infinity. In this case, the term that produces the difference and discrepancy within the Eulerlet is a nonpotential core originating from the limiting value of the singular vortex-wake-velocity part that lies along a semi-infinite wake half-line.

1.3 Challenges

Despite the amount of research in mathematical modelling of flow past a bluff body, there are many limitations and challenges to adapt the actual Navier-Stokes equations to the present-day requirement and define one model for all. Here, we are not proposing the one solution for all but, trying to develop an Euler model which have the potential to provide one overarching general solution. To start that, Eulerlet theory is going to verify against the bluff body in a low-speed wind tunnel to capture the Eulerslip wake. The challenges to verify the theory are the type of model, Reynolds number, type of anemometer and distances behind the bluff body required. All of the above parameters are further discussed in Chapter 5and 6.

1.4 Research Motivation

By neglecting viscous term in the near-field, we will obtain Euler flow from Navier-Stokes flow. Euler equations have many important applications in aerodynamics and hydrodynamics, but also some theoretical difficulties. The challenge is to define the drag for Euler slip wake and overcome the D'Alembert's paradox as we mentioned in the previous section. Chadwick in (2014) explained the lift discrepancy for the three-dimensional potential flow. The idea is to model a flow domain for high Reynolds number by using the matched asymptotic approach. Matching far-field Oseen flow and near-field Stokes flow for small Reynolds number was presented by Proudman and Pearson (1957), and Kaplun and Lagerstrom (1967). In this problem, consider uniform, steady flow past a fixed body such that in the far-field the Oseen flow approximation holds. Take Reynolds number as a limit and far-field go to infinity, and asymptotically match the resulting near-field Euler flow to the far-field Oseen flow. This result in an Euler wake previously not modelled that has a constant downstream profile. so, an experimental test is desired to investigate whether this Euler wake is present.

1.5 The Aims of the Research

The first aim of this present work is continuously developing the theoretical mathematical model for flow past a bluff body at high Reynolds number by using Euler equations. In other words, defining the new Euler flow description for the given velocity by a boundary integral distribution of Eulerlets over the boundary. In particular, the benchmark problem of a circular cylinder is investigated. The main aim is to then test this model by experiment in a low-speed wind tunnel by looking at the downstream wake profile using a hot- wire anemometer and moved by a novel-design traverse mechanism

1.6 The Objective of the Research

The primary focus for both theory and experiment will be the flow characteristics of the benchmark problem of an infinite length circular cylinder. Since a wealth of information exists from these previous studies, a new mathematical modelling was desired which could measure the velocities at high Reynolds numbers in the wake and provide us with some insight into the flow behaviour. So far, different measurement techniques used by different authors include flow visualization, surface pressure measurements, mean and RMS force measurement, oil film, and single component hot-wire velocity measurements. The focus of the research is on finding Euler slip wake for high Reynolds numbers for flow past a bluff body. There are many limitations and challenges in using Euler equations and emulating the

same inflow past a bluff body problem at high Reynolds numbers. To address these challenges, a theoretical, numerical and experimental investigation has been done with the following objectives:

- Review related works and background study.

- Define the theoretical equations for flow past a bluff body circular cylinder.

- Write a numerical modelling program in Fortran to check the results against the existing standard results.

- Generate and prepare the appropriate sets of data to carry out the experimental study of the proposed flow past a circular cylinder for a given Reynolds number using pitot tube, hot-wire anemometer and traverse mechanism.

- Find the velocity of flow just before a circular cylinder using hot-wire anemometer.

- Record the total velocity using hot-wire anemometer at different distances from the infinite length circular cylinder.

- Calculate the potential velocity of the flow domain using experimental data.

- Calculate the wake velocity across the flow domain at different distances from the back of the cylinder, using potential velocity and total velocity.

- Plot all the wake velocity profiles and compare against the theoretical and numerical results.

1.7 Research Methodology

The idea is to match near-field Euler equations and far-field Oseen equations for high Reynolds number. The work is done in three phases, which is theoretical, numerical and experimental. In Phase 1, Eulerlets and Oseenlets are defined by using Green's integral equations to match the near-field and far-field with respective approaches. In Phase 2, I have used the same equations to replicate the flow model with theoretical results by using Fortran programming. In Phase 3, wind tunnel experiments are conducted to observe the Euler slip wake by using the hot-wire anemometer.
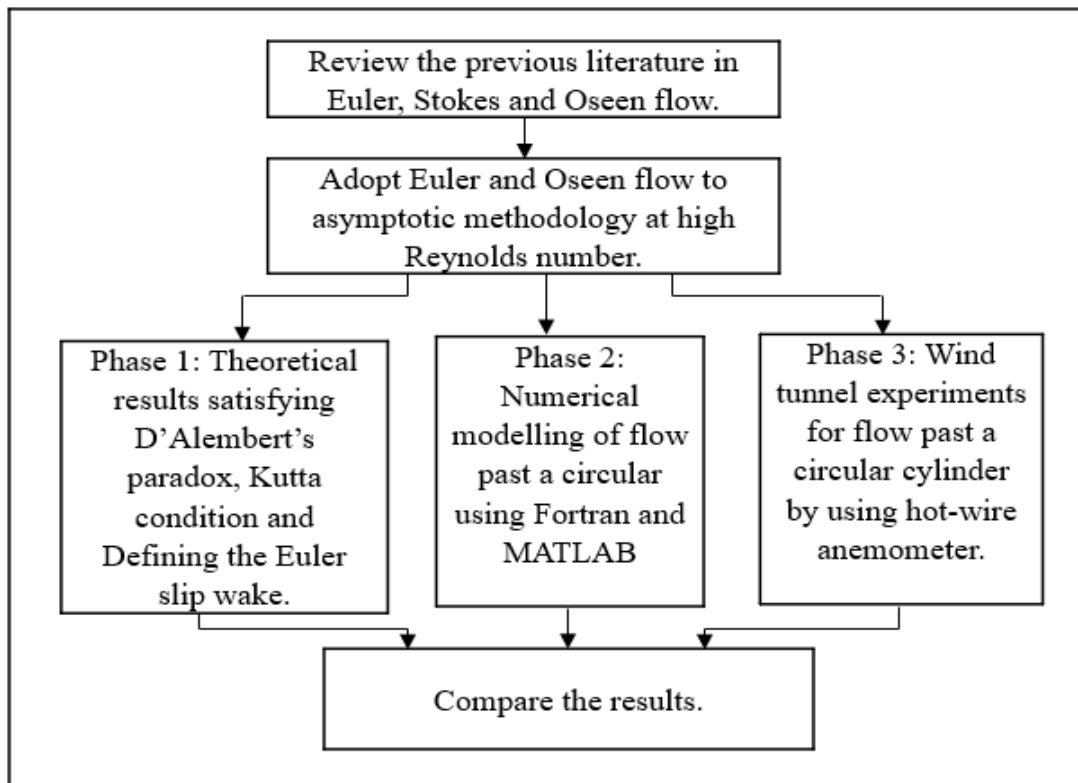
Figure 1.1 Research methodology

1.8 Contribution of the Study

The main contribution of this study is an asymptotic approach given by the Euler equation for high Reynolds numbers. Earlier methodologies accurately design the asymptotic approach for low Reynolds numbers. This outcome is a solution for D'Alembert's paradox and calculation of the wake drag by using Euler slip wake. This representation provides an overarching general framework not only encompassing existing methods but can also be extended to model the next generation time-dependent and time oscillatory manoeuvring problems. The experiments are in line with theory and able to record the Euler slip wake.

Chapter 2

2 Fundamental concepts

2.1 Chapter review

In this chapter, the technical terms used in this work are introduced. Also, some background is given for Oseen flow, Euler flow, flow past a circular cylinder, numerical modelling and wind tunnel experiments.

2.1.1.1 Viscosity

In all real fluids, a shearing deformation is accompanied by shearing stress. The shearing stress is proportional to the rate of shearing deformation. The constant of proportionality is called the coefficient of viscosity, μ. thus,

$$\text{Shear stress} = \mu * \text{transverse gradient of velocity}$$

2.1.1.2 Inviscid flow

By contrast, inviscid fluid assumes no friction, thermal conduction, or diffusion. By using the term inviscid flow instead of an inviscid fluid, we emphasize that the viscous shear stress is negligibly small because the combined product of viscosity and the shearing velocity gradient has a small effect on the flow field and not that the fluid viscosity is zero (Bertin and Smith, Michael, 2002).

2.1.1.3 Source and Sink

A source is defined as a point from which fluid issues and flows radially outward such that the continuity equation is satisfied everywhere, but at the singularity that exists at the source centre.

In source flow streamlines are directed away from the origin and the opposite case is that of a sink flow, where the streamlines are directed toward the origin.

The potential function for the two-dimensional source centred at the origin is

$$\emptyset = K/2\pi \ \ln \ r$$

Where r is the radial coordinate from the centre of the source and K is the source strength, see figure 2.1.
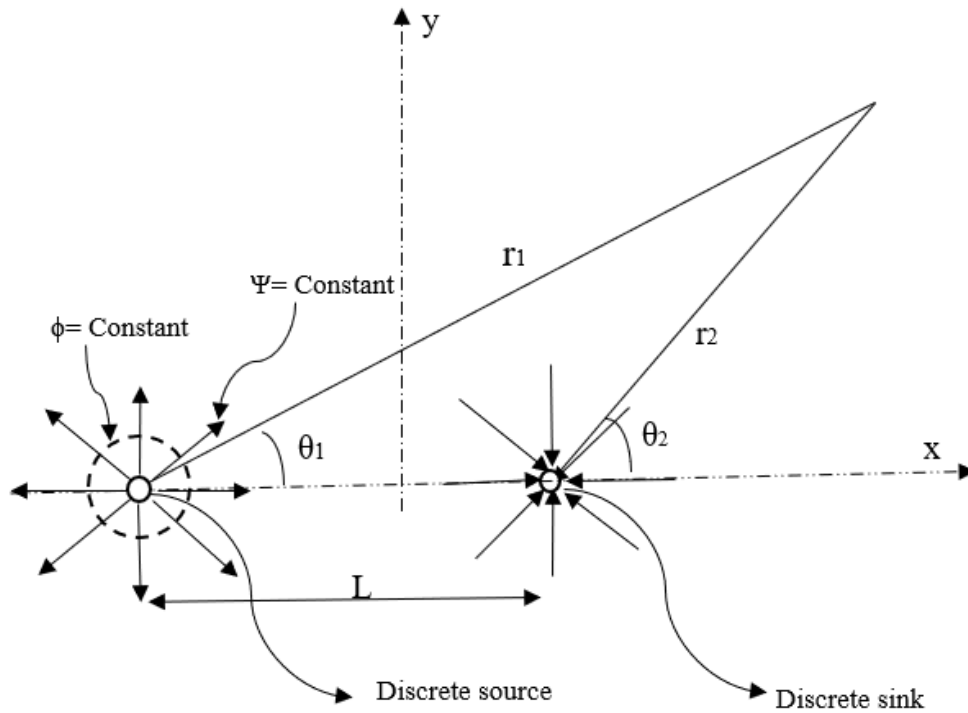
Figure 2.1 Source and Sink

2.1.1.4 Doublet

A doublet is defined to be the singularity resulting when a source and a sink of equal strength are made to approach each other, such that the product of their strengths and their distance apart remains constant at a preselected finite value in the limit as the distance between them approaches zero. The line along which the approach is made is called the axis of the doublet.
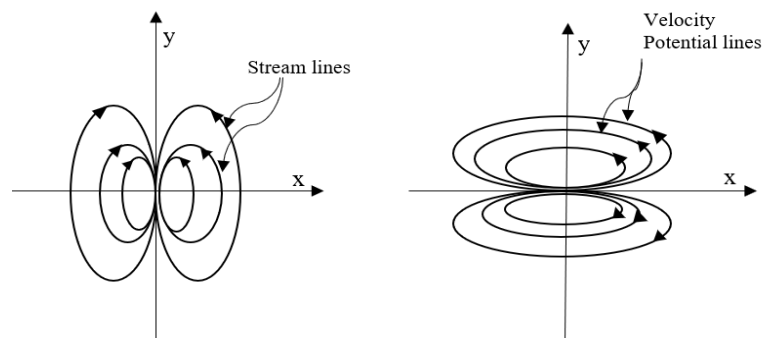
Figure 2.2 Doublet of streamlines and potential lines

10

2.1.2 Reynolds number

The Reynolds number represents a ratio of convective to diffusive influences, the limit of very high Reynolds number implies negligible diffusion. In high speeds external flows around streamlined bodies, for example, the flow well away from the body might be treated as inviscid. However, the approximation is not valid in the boundary layer or wake regions.

$$Re = \frac{\rho Vd}{\mu} = \frac{Vd}{\nu} = \frac{Inertia\ force}{Viscous\ force}$$

μ is the dynamic viscosity of the fluid

ν is the kinematic viscosity of the fluid

d is the diameter of the cylinder

V is the velocity of the fluid

ρ is the density of the fluid

Reynolds number is a dimensionless number and it predicts whether the flow is laminar, transition or turbulent referring to the flow properties as mentioned above.

2.2 Material derivative

First, let us discuss the different ways to describe the flow. Mainly we use either the Lagrangian description or Eulerian description.

In Eulerian description velocities of the flow are given at fixed points in space as time varies. So both measuring device and frame of reference are fixed. For example, the Eulerian form of expressing position vector is (Burr, 2003)

$$X_i = X_i(x_1, x_2, x_3, t)$$

Where X_i tracks the fluid point, x_i is the cartesian co-ordinate at t is time. In the Lagrangian description, the quantities of the flow are given for a particular moving particle at a varying time. For example, the Lagrangian form of expressing position vector is

$$x_i = x_i(X_1, X_2, X_3, t)$$

Fluid properties like pressure, velocity, density, temperature can be represented in both Lagrangian and Eulerian description. For example, the density of the fluid in material description in the Lagrangian form will be (Kartha, 2017)

$$\rho = \rho(X_1, X_2, X_3, t) = \rho(X_i, t)$$

In the above equation material position of the fluid particle is (X_1, X_2, X_3, t).

The same density of the fluid in Eulerian form will be

$$\rho = \rho(X_i(x_1, x_2, x_3, t), t) = \rho(X_i(x_j, t), t)$$

The time rate of change of any property of the continuum fluid with respect to the particles is called the **Material derivative** of the property. The properties of the particles can change with respect to time. The material derivative is a Lagrangian concept but works in an Eulerian reference frame. A fluid element is often called a material element. They are deformed as they move, but they are not broken up. Let's discuss an example. Consider a property 'γ' of properties of temperature, density, velocity components of the fluid element. In general, this will depend on the time, t, and on the position ($x=x_1$, $y=x_2$, $z=x_3$) of the fluid element at that time. So

$$\gamma = \gamma(x, y, z, t) = \gamma(r, t)$$

where γ (x, y, z) is the position vector. Now suppose we move with the fluid element which has coordinates (x (t), y(t), z(t)). In a small time δt, suppose that the element moves from (x, y, z) to (x+ δx, y+ δy, z+ δz). There will be a corresponding small change in γ, denoted by δγ. (Tobias, 2005)

$$\delta\gamma = \frac{\partial\gamma}{\partial t}\delta t + \frac{\partial\gamma}{\partial x}\delta x + \frac{\partial\gamma}{\partial z}\delta y + \frac{\partial\gamma}{\partial z}\delta z$$

The observed rate of change of γ for that fluid element will be

$$\frac{d\gamma}{dt} = \frac{\partial\gamma}{\partial t} + \frac{\partial\gamma}{\partial x}\frac{dx}{dt} + \frac{\partial\gamma}{\partial y}\frac{dy}{dt} + \frac{\partial\gamma}{\partial z}\frac{dz}{dt}$$

The velocity of the fluid element is its rate of change of position

$$\frac{dr}{dt} = U = (u, v, w) = (\frac{dx}{dt}, \frac{dy}{dt}, \frac{dz}{dt})$$

Hence

$$\frac{d\gamma}{dt} = \frac{\partial\gamma}{\partial t} + u\frac{\partial\gamma}{\partial x} + v\frac{\partial\gamma}{\partial y} + w\frac{\partial\gamma}{\partial z}$$

$$\frac{d\gamma}{dt} = \frac{\partial\gamma}{\partial t} + U.\nabla\gamma$$

Note:

(1) U. ∇ is defined by the Cartesian expansion

$$U.\nabla = u\frac{\partial}{\partial x} + v\frac{\partial}{\partial y} + w\frac{\partial}{\partial z}$$

(2) $\frac{d\gamma}{dt}$ is the rate of change of γ moving with the fluid element.

(3) $\frac{\partial\gamma}{\partial t}$ is the rate of change of γ at a fixed point in space.

In fluid dynamics, the time rate of change for a fluid element is usually denoted by $\frac{D}{Dt}$ thus

$$\frac{D\gamma}{Dt} \equiv \frac{\partial\gamma}{\partial t} + U.\nabla\gamma$$

The first term in the above equation which is $\frac{\partial\gamma}{\partial t}$ is a local property of the fluid element and $U.\nabla\gamma$ is a convective term.

When we assume flow is steady, this means it is observed to be the same at all time from a fixed position. so $\frac{\partial}{\partial t} = 0$.

Streamline: A line everywhere tangent to the fluid velocity v at a given time.

2.3 D'Alembert's paradox

D'Alembert's paradox formulated by the mathematician D'Alembert in 1752 compares observation of substantial drag (resistance to motion) in nearly incompressible and inviscid (small viscosity) fluids, such as water and air at subsonic speeds, with the theoretical prediction of zero drag potential flow, which is an inviscid, incompressible, irrotational and steady flow. The pressure and velocity with streamlines in a section of potential flow around a three-dimensional circular cylinder take the form (with the flow from left to right) given in figure 2.3.

D'Alembert's stated, "It seems to me that the theory (Potential flow), developed in all possible rigor, gives, at least in several cases, a strictly vanishing resistance, a singular paradox which I leave to future geometers to elucidate" (Johnson and Hoffman, 2010).

Frictionless Flow: Zero Drag   Real Flow: Finite Drag
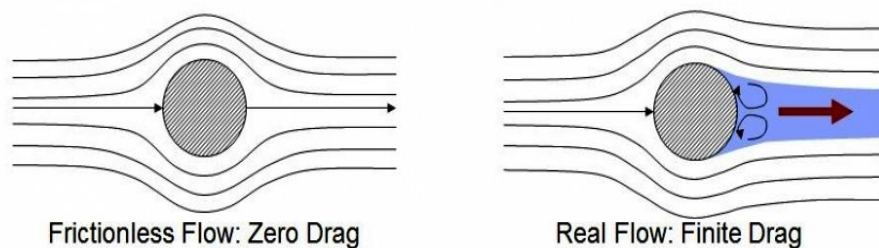
Figure 2.3 Difference between the theoretical and experimental drag (Fehrm, 2017)

2.4 Kutta condition

For uniform flow past an aerofoil, there is a stagnation point at the trailing edge. The flow over the topside conforms to the upper surface of the aerofoil. The flow over both the topside and the underside join up at the trailing edge and leave the aerofoil travelling parallel to one another. This is known as the Kutta condition.

2.5 No-slip boundary condition

A common type of idealized boundary found in the applications of fluid dynamics is the impermeable wall. The overall boundary condition for viscous fluids at such a wall is that there be no relative motion between the wall and the fluid immediately in contact with the wall. Conceptually, this condition can be analysed into two conditions and there is to be no perpendicular motion nor tangential motion of the fluid relative to the wall. The condition requiring no perpendicular motion is often called the impermeability condition. Fluid cannot penetrate the boundary so, fluid slips past the boundary, and

$$u. \, n = 0$$

For potential flow

$$\nabla \phi. \, n = 0$$

The condition requiring no tangential motion is called the no-slip condition (Day, 1990). The no-slip boundary condition says that at the interface between a moving fluid and a stationary wall, both the normal and tangential components of the fluid velocity field are equal to zero.

On the other hand, the free-slip boundary condition says that at the interface between a moving fluid and a stationary wall, the normal component of the fluid velocity field is equal to zero, but the tangential component is unrestricted. This condition is also sometimes called the no-penetration condition, for obvious reasons (Prabhakara and Deshpande, 2004).

2.6 Review of Oseen equations

As already mentioned, Stokes approximation provided a solution for flow past a sphere for small Reynolds number and the solution provides logarithmic divergence as distance goes far from the body. This whole phenomenon is called Stokes paradox. Later, this difficulty is overcome by using Oseen approximation. Oseen (1910) provided a uniformly

valid first approximation to the velocity and all its derivatives are itself a linear problem which may be solved analytically. Inertia terms are considered where the flow is almost attained uniform-stream and that permits a linear approximation to be made which yields the Oseen equations (Proudman and Pearson, 1957). The advantage of Oseen approximation lies essentially in that it becomes more and more accurate as the distance from the cylinder increases (Imai, 1951). An approximate solution of Oseen's equations was given by Lamb (1911) for low Reynolds number and subsequently extended by both Bairstow and Lang (1923) and Tomotika and Aoi (1950). Later, the Oseen approximation is used to model the far-field and asymptotically matched to the near-field with Stokes approximation by Happel & Brenner 1991; Kaplun & Lagerstrom 1957; Lagerstrom 1964; Proudman & Pearson 1957. They use the decomposition of the velocity into a potential velocity and a wake velocity used by Lamb (1932) and Goldstein (1929,1931). Wake velocity and potential velocity cannot be considered to be independent from each other. Chadwick (1998) pointed out the setbacks of the Lamb-Goldstein approach, how Goldstein assumption fails to hold, because the wake and potential velocity are regular everywhere except along the positive axis and leads to an incorrect calculation of lift. Instead, Chadwick (1998) used Green's surface integral distribution to find Oseen velocity by Green's functions and they are called Oseenlets. The far-field pressure and velocity are defined by using the Taylor series expansion of Oseenlets. Chadwick (2002), this paper used a distribution of Oseenlets in slender body theory with laminar and Oseen flow and concludes that the Oseen equations are approximately valid everywhere and the slip boundary condition can be applied on the surface of the slender body. So far, the potential models determine the lift from potential velocity, only and vortex wake velocity has been neglected in the calculation, which is half of the total lift inadvertently omitted, which is considered in slender bodies in Oseen flow. Chadwick (Chadwick, 2005) used potential theory to represent the lifting elements of a slender wing with applications in slender bodies and large aspect wings. A slender wing is represented by a vortex sheet which is defined as the integral distribution of lifting elements and the lifting element is called a horseshoe vortex. A horseshoe vortex representation using Oseenlets is given by a constant distribution of spanwise lift Oseenlets. This contribution is evaluated by considering the lift Oseenlets in the limit of high Reynolds number but laminar flow. Chadwick also suggested evaluating the additional viscous lift force by using Oseen flow theory (Chadwick 2009).

2.7 Review of Euler equations

Euler equations are simplified form of the more general Navier-Stokes equations of fluid dynamics and can be considered as where viscous effects of the fluid are neglected,

these are known as inviscid flows. Such flows are arising where the Reynolds number is high (Craft, 2010). The Euler equations express conservation of mass, momentum and total energy of fluid at vanishingly small viscosity. One of the most obvious contrasts is that Navier-Stokes equations dissipate energy, whereas Euler equations conserve energy. The application of Euler equations in a flow past a sphere to problems of resistance led to paradoxes like D'Alembert's zero-drag, although it has been used to find the lift force in aerodynamics with great effect. The discovery of viscous stress in the 19th century led to an erosion of interest in Euler's equations (Darrigol and Frisch, 2007). Recently we can see a strong renewal of interest in Euler equations like weak solutions by John Hoffman (2008), Young measure solutions (László and Wiedemann, 2012) & Chadwick (2013) Eulerlets are some of the examples(Chadwick and Kapoulas, 2014). Chadwick (1998) paper gives the accuracy of Oseen equations in the far-field and role of Stokes approximation in the relatively narrow near-field region for small Reynolds numbers. Later, Chadwick (2013) provided a top-down approach by first giving a boundary integral description to the Euler equation in terms of Green's functions which we called Eulerlets.

2.8 Review of flow past a bluff body using asymptotic flow models

In the last century, fluid dynamics developed many perturbation theories and still, we can see so many challenging perturbation problems. The problem of defining the steady flow past fixed bodies in a uniform stream of an inviscid incompressible fluid is an old one. A considerable amount of physical and mathematical models has been created for different Reynolds numbers ranging from zero to infinity. It was first considered by Stokes (1851) and discussed subsequently by many authors.

For practical purposes, the first approximation to these second-order effects would doubtless be adequate, but the purely mathematical difficulties encountered in their calculation raise fundamental questions concerning the general nature of expansions for flow fields at small Reynolds numbers (Proudman and Pearson, 1957).

Previous results for steady motion of a viscous fluid past a circular cylinder may be roughly divided into two categories. Firstly, there are solutions of Oseen's linearized equations valid at low Reynolds numbers. Secondly, there are the approximate numerical solutions of the full equation of motion. After different approximations are made for the Oseen equations, Proudman and Pearson made a general observation in agreement with Lamb's formula. That is, the order of accuracy involved in the matched asymptotic to the

exact governing equations by Oseen theory is the best it can be and there is no virtue in improving it. Kaplun (Kaplun, 1957), therefore gives the second approximation to Lamb's solution to the Navier-Stokes equation. This is obtained by matching a solution of Oseen's equations far enough from the cylinder with an inner solution based on Stokes's theory (Dennis, S C R and Shimshoni, 1965). The matching principle discussed is of great generality, applied initially for low Reynolds numbers and later applied to expansions for high Reynolds numbers and it yields the classical matching rules of a boundary layer theory. Chadwick (Chadwick and Kapoulas, 2014), presented the two-dimensional case by matching the Euler flow to a far-field Oseen flow to determine the appropriate description for the Green's function Eulerlets. In the present work, Eulerlets and Oseenlets are used to match in the near and far-field to find out Euler drag and Euler lift for the flow past a circular cylinder.

2.9 Review on numerical modelling and the wind tunnel tests

Numerical methods and wind tunnel tests are two different methods for flow visualization, calculating moments and forces, surface pressure measurements and boundary layer distribution. However, numerical methods are based on approximated fluid flow theories, whereas wind tunnel tests are used to validate the results with numerical methods. Both numerical modelling and wind tunnel experiments are helpful in the study of flow past a circular cylinder to understand the complete flow properties of the flow domain. Let's review each one separately and start with the numerical modelling

For two-dimensional flow past a circular cylinder numerical solution are classified into two types. In the first method, the solution will be obtained by integrating the equations of steady motion. Thom (1928) gave the first solution at Reynolds number of 10 and 20, it explains about a maximum separation of streamlines, Pressure at any point in the flow, surface pressure, drag and pressure distribution. Kawaguti (1953) published a solution for Reynolds number 40, it explains the laminar wake which agrees with experiments. Apelt (1961) published solution at Reynolds number 40, provided a steady-state solution for higher Reynolds numbers and the length of the stationary vortex pair attached to the cylinder. Later, Allen and Southwell (1955) gives solutions at different Reynolds numbers from 0 to 10^3 and Dennis and Shimsoni (1965) for the Reynolds number range from 0.01 to 10^6, though they are numerically inaccurate at high Reynolds numbers. Takami & Keller (1969), provided one reliable solution for a steady motion for Reynolds number 60 (Dennis and Gau-Zu, 1970).

Integrating time-dependent equations are the second type. In the present work, we are mainly interested in steady motion problems, steady said to be when the mean steady flow settled down to steady-state in the wind tunnel test section with time. Fortran is used to write a numerical solution for flow past a circular cylinder to capture the wake distribution for different Reynolds numbers, far-field decay for laminar flow, pressure distribution over a circular cylinder for different Reynolds numbers, streamlines for subcritical laminar flow and turbulent flow.

Wind tunnels played an important role in aerodynamics to understand and analyse the flow domain for particular airfoil profiles. A scaled object is placed in the wind tunnel and air or water will be used as a fluid to simulate the movement of an object through the fluid. A force balance is used to mount the profile to calculate the forces such as drag and lift as the fluid interacts with the profile. A scaled model used in the wind tunnel can only mimic the actual- size model moving in still air. Reynolds number is set to be the same for a scaled and actual model to ensure same flow characteristics. The wall of the test section influences the results as these are called blockage effects. Blockage effects should not be more than 5% of the overall duct cross-section. Wind tunnel wall correction factors are often cited to make the results equivalent to wall-free results (Smith, 2008). Wind tunnels are used in combination with new efficient measurement methods such as, for instance, non-intrusive Laser-Doppler Anemometer (LDA), Particle Image Velocimetry (PIV) and Hot-wire Anemometer (HWA). Such experiments have then played a major role in a better understanding of flow physics and allowed the development of new numerical approaches (Favier, 2010). In the present work, hot-wire anemometer is used to understand the flow physics of high Reynolds numbers.

2.10 Divergence theorem

Divergence theorem relates volume integrals to the surface integrals of vector fields. Let V be the volume in xyz space with surface S. Let n denote unit normal vector to S pointing in the outward direction. Let $\mathbf{F}$ be a vector field whose components have continuous partial derivatives. The divergence theorem states

$$\iint_S (\mathrm{F}.\mathrm{n})\mathrm{dS} = \iiint_V (\mathrm{divF})\mathrm{dV}$$

The theorem holds for any vector $\mathbf{u}$, not just velocity vector. The integral qualities measure flux out for vector $\mathbf{u}$.
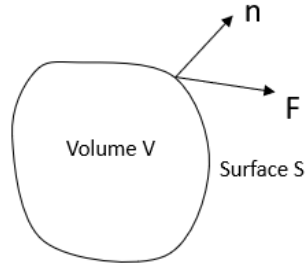
Figure 2.4 Representation of Divergence theorem.

2.11 Green's functions

Green's theorem gives a relationship between the line integral of a vector field around a plane curve to a double integral of the derivative of the vector field in the interior of the curve. These are particular fundamental solutions that satisfy a suitable homogeneous boundary condition on the boundary of a particular domain and the use of Green's functions eliminates the unknown boundary quantity, giving an integral representation involving the prescribed data only (Martin and Rizzo, 1995). Let 'A' be a region in the plane with boundary curve C and F= (M, N) a vector field defined on 'A', such that

$$\iint_A Div\ (F)dxdy = \int_C F.n\ dl$$

where dl is an element of the curve C. In the present work, Green's theorem is used in combination with the divergence theorem. They have computed from solutions of boundary integral equations for the source distribution over the boundary surfaces. The analysis shown in this work is for the problem with one spatial dimension only. However, it can be extended easily to two and three spatial dimensions using Fourier transform methods. Let us consider a linear homogeneous equation of the form

$$\mathcal{L}u(x) = f(x) \tag{a}$$

where $u(x)$, $f(x)$ are functions whose domain is C. $\mathcal{L}$ is a linear differential operator acts on x. we can write a solution in the form

$$u(x) = \int_C G(x,x_0)\ f(x_0)dx_0.$$

In the above equation $G(x,x_0)$ is called the Green's function. $u(x)$ is the response at x to the influence given by a source function f(x). The integral can be thought of as the sum over influence created by sources at each value of x_0. Let us consider an example as shown in figure 2.5, G is the Green's function, coordinate **x** represent a point in the fluid and coordinate **y** parameterize the Green's integration. Applying Green's function to find out the velocity of the point in the fluid gives

19

$$\int G(x, x_0)\, u_i(y) - \int G(y, x_0)\, u_i^{(k)}(x) = 0.$$
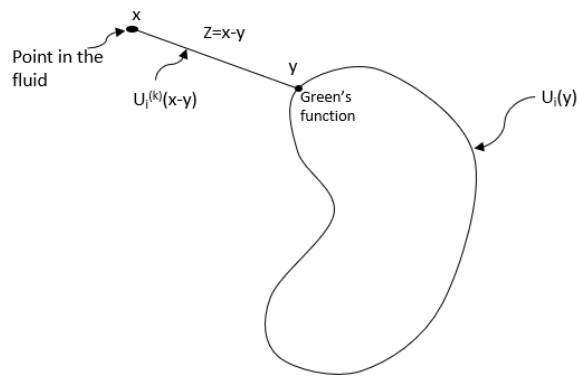
Figure 2.5 Green's integral representation

2.12 Dirac delta function:

The Dirac delta function is a mathematical abstraction which is often used to describe a physical phenomenon. Instead, it is said to be a distribution. It is a generalised idea of functions but can be used only inside integrals. Dirac's delta function is defined by the following property

$$\delta(x) = \begin{cases} 0 & x \neq 0 \\ \infty & x = 0 \end{cases}$$

$$\int_{-\infty}^{\infty} \delta(x)dx = 1.$$

If $0 \in [-\infty, \infty]$ and zero otherwise. It is infinitely peaked at x=0 with a total area of unity.
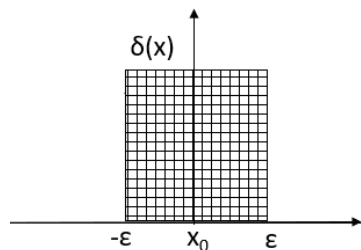
Figure 2.6 Geometrical representation of Dirac delta function.

The function of $\delta(x)$ can get progressively thinner and higher in such a way that the area under the curve is always equal to one. From figure 2.6

$$\delta(x) = 0 \qquad \text{for } x > \epsilon, x < -\epsilon$$

$$\delta(x) = \frac{1}{2\epsilon} \qquad \text{for } \epsilon \leq x \leq \epsilon.$$

20

The derivative of a Delta function:

The fundamental equation that defines derivatives if the delta function $\delta(x)$ is

$$x\delta'(x) = -\delta(x).$$

Relationship to the Heaviside step function and Dirac delta function

Let us consider H (x) is a Heaviside step function and it is defined as

$$H(x) = \begin{cases} 0 & x < 0 \\ 1 & x \geq 1. \end{cases}$$
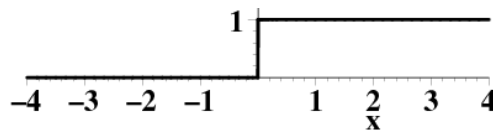
Figure 2.7 Geometrical representation of Heaviside function.

The step function is related to the Dirac delta function by

$$\delta(x) = \frac{d}{dx}H(x) \text{ and } H(x) = \int_{-\infty}^{\infty} \delta(x)dx.$$

Chapter 3

3 Matching far-field Oseen flow on to the near-field Euler flow

3.1 Chapter review

The present chapter is structured as follows. In the first section, a statement of the problem is given where the Navier-Stokes equation is approximated in the far-field to produce the Oseen equation and in the near-field to produce the Euler equation. The relative size of the terms in the Navier-Stokes equation is carefully documented together with the size of the near-and far fields in terms of the Reynolds number. In the next section, the far-field Oseen integral representation in terms of Oseenlets is given, and the high Reynolds number limit is taken. This is obtained by considering momentum losses in the wake that must be conserved and results in a constant distribution of Dirac delta functions along an infinite half-line in the wake. Then, the near-field representation is given in terms of the Eulerlets, and these are described and shown to be Green's functions of the Euler equations as well as matching to the far-field collapsed Oseenlets. In the next section, the near and far-field integral representations are matched which results in the Euler flow representation of the velocity as an integral distribution of Eulerlets over the body surface with the strength given by the force distribution. In the last section, separated flow past a circular cylinder is considered for the high Reynolds number, subcritical laminar flow at a Reynolds number of 8.4 $*10^5$. It is shown that all the essential flow physics is captured. The streamlines compare well with flow visualization, and the pressure distribution around the circular cylinder is a reasonable match given the approximation made.

3.2 Navier-Stokes equation

Consider a steady, incompressible fluid of density ρ and viscosity μ such that the Navier-Stokes equation

$$\rho u_j \frac{Du_i}{Dt} = -\frac{dp}{dx_i} + \mu \frac{d^2 u_i}{dx_j dx_j} - f_i \, , \quad \frac{du_i}{dx_i} = 0$$

where,

$$\frac{D}{Dt} = \frac{d}{dt} + u_j \frac{d}{dx_j}$$

The time-independent Navier-Stokes equation

$$\rho u_j \frac{du_i}{dx_j} = -\frac{dp}{dx_i} + \mu \frac{d^2 u_i}{dx_j dx_j} - f_i \; ; \quad \frac{du_i}{dx_i} = 0 \qquad (1)$$

holds throughout the fluid. So, u and p are the fluid velocity and pressure, respectively. The Cartesian coordinates are given by x_i, $1 \le i \le 2$ for two-dimensional flow. The Einstein convention of repeated suffix implying a summation is used such that $a_i b_i = a_1 b_1 + a_2 b_2 + a_3 b_3$ in three-dimensions, for example. f_i is the body force.

3.3 Oseen equations

Here, we concentrate on

1) Derivation and conditions
2) Green's integral representation
3) Singular force solutions.

3.3.1 Derivations and Conditions

Consider an exterior problem such that the far-field boundary condition is that the fluid velocity tends toward a uniform stream aligned to the x_1 axis of magnitude U, and so in the far-field, the Navier-Stokes equation is approximated by the Oseen equation. The velocity u_i and pressure p then approximate to the Oseen velocity u_i^{oseen} and Oseen pressure p^{oseen},

$$\text{Substituting,} \; u_i = U\delta_{i1} + u_i^{Oseen}: \text{Where,} \; \left| \frac{u_i^{oseen}}{U} \right| << O(1)$$

and δ_{ij} is the Kronecker delta. The perturbed velocity is u_i^{oseen} from equation 2, with $f_i = 0$,

$$\rho u_j \frac{du_i}{dx_j} = -\frac{dp}{dx_i} + \mu \frac{d^2 u_i}{dx_j dx_j}$$

Let us take the left-hand side of the above equation and substitute the Oseen velocity and seek for the perturbed solution to the uniform flow. The flow is incompressible and steady so, the density is assumed to be constant.

$$(U\delta_{j1} + u_j^{oseen}) \frac{d}{dx_j} (U\delta_{i1} + u_i^{oseen}) = -\frac{dp^{oseen}}{dx_i} + \mu \frac{d^2}{dx_j dx_j} (U\delta_{i1} + u_i^{oseen})$$

The term $\frac{d}{dx_j} U\delta_{i1} = 0$ and substitute in the above equation gives

$$(U\delta_{j1} + u_j^{oseen}) \frac{d}{dx_j} u_i^{oseen} = -\frac{dp^{oseen}}{dx_i} + \mu \frac{d^2}{dx_j dx_j} u_i^{oseen}$$

$$U\delta_{j1}\frac{d}{dx_j}u_i^{oseen} + u_j^{oseen}\frac{d}{dx_j}u_i^{oseen} = -\frac{dp^{oseen}}{dx_i} + \mu\frac{d^2}{dx_jdx_j}u_i^{oseen}$$

$u_j^{oseen}\dfrac{d}{dx_j}u_i^{oseen}$ is neglected because of the order of smallness.

$$U\delta_{j1}\frac{d}{dx_j}u_i^{oseen} = -\frac{dp^{oseen}}{dx_i} + \mu\frac{d^2}{dx_jdx_j}u_i^{oseen}$$

From $\delta_{j1}\dfrac{d}{dx_j} = \delta_{11}\dfrac{d}{dx_1} + \delta_{21}\dfrac{d}{dx_2} = \dfrac{d}{dx_1}$

$$U\frac{d}{dx_1}u_i^{oseen} = -\frac{dp^{oseen}}{dx_i} + \mu\frac{d^2}{dx_jdx_j}u_i^{oseen} \qquad (2)$$

Equation (2) represents the perturbed Oseen equation, which is same as equation (1) except pressure and velocity terms and they are replaced with Oseen pressure and Oseen velocity and body forces are neglected.

3.3.2 Green's integral representation

In this section, Oseen is dropped from the Oseen velocity and pressure, and are given by u_i and p throughout. The velocity can be represented by a surface integral and it can be equated to a surface integral in the near-field obtained from solving the near-field flow.

Consider a volume of fluid v_y in Oseen flow, then from the Oseen equation

$$\int_{v_y}\left(\rho U\frac{du_i}{dx_1} + \frac{dp}{dx_i} - \mu\frac{d^2u_i}{dx_jdx_j} + f_i\right)dv = 0$$

We want a term that gives the result $u_j(x)$ so, consider the variable. $z = x-y$, the volume integral $dv_y = dy_1 * dy_2 * dy_3$ and multiplying the above integral by $u_i(y)$, To obtain point force solutions, we must consider $f_i^{(j)} = \delta_{ij}\delta(z)$ where $\delta(z)$ is a Dirac delta function such that the spatial integration across it is unity, $\int_\Sigma\delta(z)d\Sigma = 1$. This gives

$$\int_{v_y}\left(\rho U\frac{du_i^{(j)}(z)}{dx_1} + \frac{dp^{(j)}(z)}{dx_i} - \mu\frac{d^2u_i^{(j)}(z)}{dx_jdx_j} + f_i^{(j)}(z)\right)u_i(y)dv_y = 0$$

Hence, the last term gives $\int_{v_y}\delta_{ij}\delta(z)u_i(y)dv_y = u_j(x)$ as per required. However, other terms give a volume integral whereas we require a surface integral. So, we are going to use the divergence theorem. Therefore, let us consider including further the volume integral terms such that

24

$$\int_{v_y} \left[\left(\rho U \frac{du_i^{(j)}(z)}{dx_1} + \frac{dp^{(j)}(z)}{dx_i} - \mu \frac{d^2 u_i^{(j)}(z)}{dx_k dx_k} + f_i^{(j)}(z) \right) u_i(y) \right.$$

$$\left. - \left(\rho U \frac{du_i(y)}{dy_1} + \frac{dp(y)}{dy_i} - \mu \frac{d^2 u_i(y)}{dy_k dy_k} + f_i(y) \right) u_i^{(j)}(z) \right] dv_y = 0$$

Now,

$$\frac{df(z)}{dx_i} = \frac{dz_j}{dx_i} * \frac{df(z)}{dz_j} = \delta_{ij} \frac{d}{dz_j} f(z) = \frac{d}{dz_j} f(z)$$

$$\frac{df(z)}{dy_i} = \frac{dz_j}{dy_i} * \frac{df(z)}{dz_j} = -\delta_{ij} \frac{d}{dz_j} f(z) = -\frac{d}{dz_j} f(z)$$

$$\therefore \frac{d}{dx_i} f(z) = -\frac{d}{dy_i} f(z)$$

$$\Rightarrow \int_{v_y} \left[\left(-\rho U \frac{du_i^{(j)}(z)}{dy_1} - \frac{dp^{(j)}(z)}{dy_i} - \mu \frac{d^2 u_i^{(j)}(z)}{dy_k dy_k} + f_i^{(j)}(z) \right) u_i(y) \right.$$

$$\left. + \left(-\rho U \frac{du_i(y)}{dy_1} - \frac{dp(y)}{dy_i} + \mu \frac{d^2 u_i(y)}{dy_k dy_k} - f_i(y) \right) u_i^{(j)}(z) \right] dv_y = 0$$

$$\Rightarrow \int_{v_y} \left[\left(-\rho U \frac{d\left(u_i^{(j)}(z)u_i(y)\right)}{dy_1} - \frac{d\left(p^{(j)}(z)u_i(y) + p(y)u_i^{(j)}(z)\right)}{dy_i} - \mu \frac{d}{dy_k}\left(\frac{du_i^{(j)}(z)}{dy_k} u_i(y) \right) \right. \right.$$

$$\left. \left. + \mu \frac{d}{dy_k}\left(\frac{du_i(y)}{dy_k} u_i^{(j)}(z) \right) \right) dv_y \right] = \int_{v_y} \left(-f_i^{(j)}(z)u_i(y) + f_i(y)u_i^{(j)}(z) \right) dv_y$$

Since, $\frac{du_i(y)}{dy_i} = 0, \frac{du_i^{(j)}(z)}{dy_i} = -\frac{du_i^{(j)}(y)}{dz_i} = 0$; from the continuity equation. The body force is zero

in the above equation. So, the right-hand side of the equation will be $\int_{v_y} \left(f_i(y)u_i^{(j)}(z) \right) dv_y =$

0 and $\int_{v_y} \left(-f_i^{(j)}(z)u_i(y) \right) dv_y$ becomes

$$\int_{v_y} \left(-f_i^{(j)}(z)u_i(y) \right) dv_y = -\int_{v_y} \left(\delta(z)u_j(y) \right) dv_y, \qquad f_i^{(j)} = \delta\delta_{ij}$$

As we already have z=x-y, however, z=0 will make the equation to x=y. so the above
equation will be

$$\int_{v_y} \left(-f_i^{(j)}(z)u_i(y) \right) dv_y = -u_j(x) \int_{v_y} \left(\delta(z) \right) dv_y = -u_j(x)$$

$$\Rightarrow \int_{v_y} \left[\left(-\rho U \frac{d\left(u_i^{(j)}(z)u_i(y)\right)}{dy_1} - \frac{d\left(p^{(j)}(z)u_i(y) + p(y)u_i^{(j)}(z)\right)}{dy_i} - \mu \frac{d}{dy_k}\left(\frac{du_i^{(j)}(z)}{dy_k}u_i(y)\right) \right. \right.$$

$$\left. \left. + \mu \frac{d}{dy_k}\left(\frac{du_i(y)}{dy_k}u_i^{(j)}(z)\right) \right) dv_y \right] = -u_i(x)$$

Consider v_y enclosed by S_m and S_∞ where S_m is an inner surface and S_∞ is an outer surface at infinity, see figure 3.1. Then applying divergence theorem to the above Oseen equation gives

$$-u_i(x) = \int_{S_m+S_\infty} \left[\left(-\rho U u_i^{(j)}(z)u_i(y)n_1^v \right) - \left(p^{(j)}(z)u_i(y) + p(y)u_i^{(j)}(z) \right) n_i^v \right.$$

$$\left. - \mu \left(\frac{du_i^{(j)}(z)}{dy_k}u_i(y) \right) n_k^v + \mu \left(\frac{du_i(y)}{dy_k}u_i^{(j)}(z) \right) n_k^v \right] ds$$
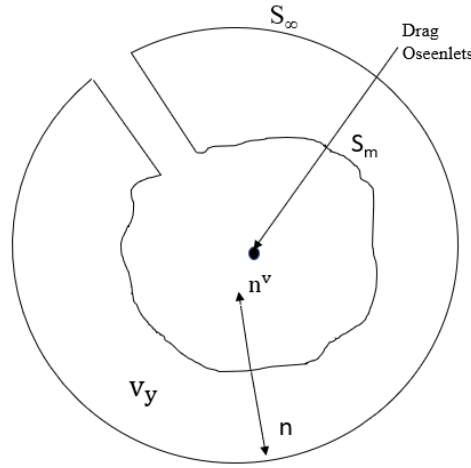
Figure 3.1 Representation of normals n and n^v

where n_i^v is the outward pointing normal to the volume v_y. The surface integral contribution S_∞ decays to zero and the outward pointing normal to S_m is $n_i = -n_i^v$, see figure 3.1. Apply Green's function to the above equation will give

$$u_i(x) = \int_{S_m} \left[\left(-\rho U u_i^{(j)}(z)u_i(y)n_1 \right) - \left(p^{(j)}(z)u_i(y) + p(y)u_i^{(j)}(z) \right) n_i \right.$$

$$\left. - \mu \left(\frac{du_i^{(j)}(z)}{dy_k}u_i(y) \right) n_k + \mu \left(\frac{du_i(y)}{dy_k}u_i^{(j)}(z) \right) n_k \right] ds$$

is the Green's integral representation of the velocity.

3.4 Unit force solutions

3.4.1 Potentials ϕ and χ

We now express this integral in terms of the velocity potential and the above green's integral representation of the velocity equation follows that the same Helmholtz-Hodge vector decomposition also holds for the Oseen velocity such that given in equation (4). This is called the Lamb-Goldstein velocity decomposition such as

$$u = \nabla\phi + \omega \qquad (3)$$

$$u_i = \frac{d\phi}{dx_i} + \omega_i$$

Substitute into the Oseen equations

$$\rho U \frac{du_i}{dx_1} = -\frac{dp}{dx_i} + \mu \frac{d^2 u_i}{dx_j dx_j}, \quad |x_j| > 0 \text{ gives}$$

$$\rho U \frac{d}{dx_1}\left(\frac{d\phi}{dx_i} + \omega_i\right) = -\frac{dp}{dx_i} + \mu \frac{d^2}{dx_j dx_j}\left(\frac{d\phi}{dx_i} + \omega_i\right)$$

$$\rho U \frac{d}{dx_1}\left(\frac{d\phi}{dx_i}\right) + \rho U \frac{d}{dx_1}\omega_i = -\frac{dp}{dx_i} + \mu \frac{d^2}{dx_j dx_j}\left(\frac{d\phi}{dx_i}\right) + \mu \frac{d^2}{dx_j dx_j}\omega_i$$

$$\rho U \frac{d}{dx_i}\left(\frac{d\phi}{dx_1}\right) + \rho U \frac{d}{dx_1}\omega_i + \frac{dp}{dx_i} = \mu \frac{d^2}{dx_j dx_j}\left(\frac{d\phi}{dx_i}\right) + \mu \frac{d^2}{dx_j dx_j}\omega_i$$

$$\rho U \frac{d}{dx_i}\left(\frac{d\phi}{dx_1}\right) + \rho U \frac{d}{dx_1}\omega_i + \frac{dp}{dx_i} = \mu \frac{d}{dx_i}\left(\frac{d^2\phi}{dx_j dx_j}\right) + \mu \frac{d^2}{dx_j dx_j}\omega_i$$

$$\frac{d}{dx_i}\left(\rho U \frac{d\phi}{dx_1} + p\right) + \rho U \frac{d}{dx_1}\omega_i = \mu \frac{d}{dx_i}\left(\frac{d^2\phi}{dx_j dx_j}\right) + \mu \frac{d^2}{dx_j dx_j}\omega_i$$

Let $\rho U \frac{d}{dx_i}\left(\frac{d\phi}{dx_1}\right) = -\frac{dp}{dx_i}$ Such that $p = -\rho U \frac{d\phi}{dx_1}$

This gives $\frac{d}{dx_i}\left(\frac{d\phi}{dx_i}\right) = 0$

$$\frac{d}{dx_i}\left(\rho U \frac{d\phi}{dx_1} + p\right) + \rho U \frac{d}{dx_1}\omega_i = \mu \frac{d^2}{dx_j dx_j}\omega_i$$

We can now write down the equation for the wake velocity and the velocity potential

$$\rho U \frac{d\omega_i}{dx_1} = \mu \frac{d^2\omega_i}{dx_j dx_j}, \frac{d}{dx_i}\left(\frac{d\phi}{dx_i}\right) = 0 \qquad (4)$$

The above equation is the linearized equation for the far-field

27

$$\left(\frac{d^2}{dx_j dx_j} - 2k\frac{d}{dx_1}\right)\omega_i = 0 \quad \text{where } k = \frac{\rho U}{2\mu}$$

is the equation for wakefield governed by the diffusion equation and below equation is the vector form

$$(\nabla^2 - 2k\frac{d}{dx_1})\,\omega = 0 \tag{5}$$

3.4.2 Representation of ω by potential χ

Now consider the diffusion equation for an arbitrary function χ. Look for a typical solution of the form

$$\left(\frac{d^2}{dx_j dx_j} - 2K\frac{d}{dx_1}\right)\chi = 0$$

$$\text{Let. } \chi e^{-kx_1} = \chi^*,$$

which gives $\chi = \chi^* e^{kx_1}$, calculate derivatives

$$\frac{d\chi}{dx_1} = \frac{d}{dx_1}\left(e^{kx_1}\chi^*\right) = e^{kx_1}\left(\frac{d\chi^*}{dx_1} + k\chi^*\right)$$

$$\frac{d\chi}{dx_j} = \frac{d}{dx_j}\left(e^{kx_1}\chi^*\right) = e^{kx_1}\left(\frac{d\chi^*}{dx_j} + k\chi^*\delta_{j1}\right), \qquad \therefore \text{Since } \frac{dx_1}{dx_j} = \delta_{j1}$$

$$\frac{d}{dx_j}\frac{d\chi}{dx_j} = \frac{d}{dx_j}\left(\frac{d\chi^*}{dx_j} + k\chi^*\delta_{j1}\right)e^{kx_1}$$

$$\frac{d}{dx_j}\frac{d\chi}{dx_j} = \left(\frac{d^2\chi^*}{dx_j dx_j} + k\frac{d\chi^*}{dx_j}\delta_{j1}\right)e^{kx_1} + k\frac{dx_1}{dx_j}\left(\frac{d\chi^*}{dx_j} + k\chi^*\delta_{j1}\right)e^{kx_1}$$

$$\frac{d}{dx_j}\frac{d\chi}{dx_j} = \left(\frac{d^2\chi^*}{dx_j dx_j} + 2k\frac{d\chi^*}{dx_j}\delta_{j1}\right)e^{kx_1} + k^2\delta_{j1}\delta_{j1}\chi^* e^{kx_1}$$

$$\therefore \delta_{j1}\delta_{j1} = \delta_{11}\delta_{11} + \delta_{21}\delta_{21} = 1$$

$$\frac{d}{dx_j}\frac{d\chi}{dx_j} = \left(\frac{d^2\chi^*}{dx_j dx_j} + 2k\frac{d\chi^*}{dx_j} + k^2\chi^*\right)e^{kx_1}$$

Substitute the above equation into the diffusion equation

$$\left(\frac{d^2\chi^*}{dx_j dx_j} + 2k\frac{d\chi^*}{dx_j} + k^2\chi^*\right)e^{kx_1} - 2k\left(\frac{d\chi^*}{dx_1} + k\chi^*\right)e^{kx_1} = 0$$

28

$$\left(\frac{d^2\chi^*}{dx_j dx_j} + 2k\frac{d\chi^*}{dx_j} - 2k\frac{d\chi^*}{dx_j} + (k^2 - 2k^2)\chi^*\right)e^{kx_1} = 0$$

$$\left(\frac{d^2\chi^*}{dx_j dx_j} + (k^2 - 2k^2)\chi^*\right)e^{kx_1} = 0$$

$$(\nabla^2 - k^2)\chi^* = 0 \tag{6}$$

3.4.3 2-D Oseenlets representation

In 2-D, $(\nabla^2 - k^2)\chi^* = 0$ is the modified Bessel equation of order zero and we will seek for the separable solution to the modified Bessel equation.

$$\nabla^2 \equiv \frac{1}{r}\frac{d}{dr}(r\frac{d}{dr}) + \frac{1}{r^2}\frac{d^2}{d\theta^2}$$

$$\chi^*(r, \theta) = R^*(r)H^*(\theta)$$

In cylindrical polar, r is the two-dimensional radial length and the solution which is a function of the radial variable is called Ko(kr).

$$r = \sqrt{x_1^2 + x_2^2} \text{ and } \theta = \cos^{-1}(\frac{x_1}{r}), \qquad x_i x_i = r^2$$

$$\frac{1}{r}\frac{d}{dr}(r\frac{d\chi^*}{dr}) + \frac{1}{r^2}\frac{d^2\chi^*}{d\theta^2} - k^2\chi^*$$

Substitute the separated variable solution $R^*(r)H^*(\theta)$ for χ^* to give

$$H^*\frac{1}{r}\frac{d}{dr}(r\frac{dR^*}{dr}) + \frac{R^*}{r^2}\frac{d^2H^*}{d\theta^2} - k^2R^*H^* = 0$$

Choose the solutions $H^*(\theta) = \begin{cases} \sin(m\theta) \\ \cos(m\theta) \end{cases}$

$$\frac{d^2H^*}{d\theta^2} = -m^2H^* \text{ equation of simple harmonic motion.}$$

$$H^*\frac{1}{r}\frac{d}{dr}(r\frac{dR^*}{dr}) - \frac{R^*}{r^2}m^2H^* - k^2R^*H^* = 0$$

$$\frac{1}{r}\frac{d}{dr}(r\frac{dR^*}{dr}) - \frac{R^*}{r^2}m^2 - k^2R^* = 0$$

Multiply the above equation with r^2

$$r\frac{d}{dr}(r\frac{dR^*}{dr}) - R^*m^2 - k^2R^*r^2 = 0$$

29

$$r\frac{d}{dr}(r\frac{dR^*}{dr}) - R^*(m^2 + k^2r^2) = 0$$

$$r\left(r\frac{d^2R^*}{dr^2} + \frac{dR^*}{dr}\right) - R^*(m^2 + k^2r^2) = 0$$

$r^2\frac{d^2R^*}{dr^2} + r\frac{dR^*}{dr} - R^*(m^2 + k^2r^2) = 0$ is a modified Bessel equation of order m

The solution to the modified Bessel equation is

$$R^*(r) = \alpha I_m(kr) + \beta K_m(kr)$$

$I_m(kr)$ is a first kind and $K_m(kr)$ is a second kind.
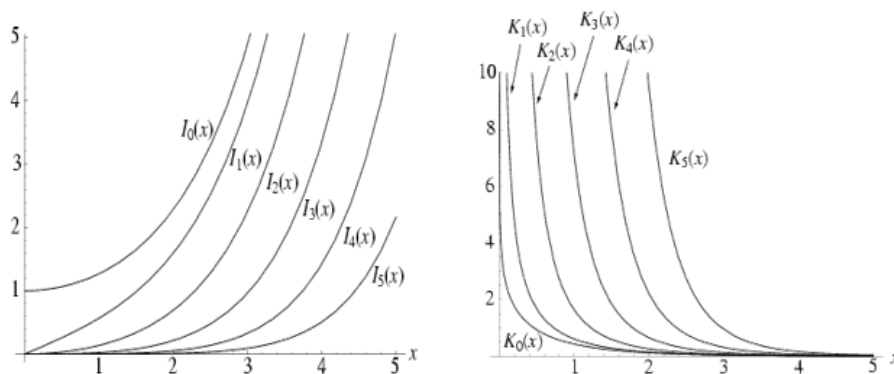
Figure 3.2 Modified Bessel function of the first and second type

Modified Bessel function first kind is not considered as these solutions are unphysical as kr $\rightarrow$ ∞

$$R^*(r) \equiv R_m{}^*(r) = K_m(kr)$$

For a fundamental solution, we consider $m = 0, H^*(\theta) = $ constant

Properties of Ko(kr):

As kr $\rightarrow$ 0, $(\nabla^2 - k^2) \rightarrow \nabla^2$, and so we approach $\nabla^2\chi^* = 0$ which has a solution a function of the radial variable given by **lnr.**
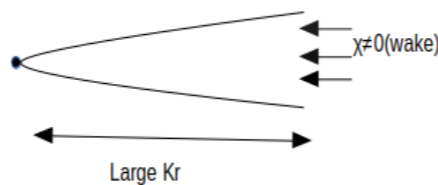
Figure 3.3 Properties of a radial variable in the wake and non-wake region

$K_0(kr)$ is a fundamental solution as kr $\rightarrow \infty$

$$\lim_{kr \to \infty} K_0(kr) \sim \left(\frac{\Pi}{2kr}\right)^{\frac{1}{2}} e^{-kr}$$

So, as $kr \to 0$, $\lim_{kr \to 0} K_0(kr) \sim -\ln(kr)$. $K_0(kr)$ behaves like a point source as $kr \to 0$

For Drag Oseenlets, consider potential $\phi^{(1)}$ must satisfy

$$\frac{d^2\phi^{(1)}}{dx_i dx_i} = 0, \qquad (\nabla^2\phi^{(1)} = 0)$$

$$\phi^{(1)} = \frac{1}{2\pi\rho U}\ln r$$

Wake velocity is

$$\omega_i^{(1)} = \frac{d\chi^{(1)}}{dx_i} - 2k\chi^{(1)}\delta_{i1}$$

This ensures that

$$\frac{d\omega_i^{(1)}}{dx_i} = \frac{d^2\chi^{(1)}}{dx_i dx_i} - 2k\frac{d\chi^{(1)}}{dx_1}\delta_{i1}$$

$$\frac{d\omega_i^{(1)}}{dx_i} = \frac{d^2\chi^{(1)}}{dx_i dx_i} - 2k\left(\delta_{11}\frac{d}{dx_1} + \delta_{21}\frac{d}{dx_1}\right)\chi^{(1)}$$

$$\frac{d\omega_i^{(1)}}{dx_i} = 0, \text{vanishing divergence}$$

$$\frac{d^2\chi^{(1)}}{dx_i dx_i} - 2k\frac{d\chi^{(1)}}{dx_1} = 0$$

$$\text{As } (\nabla^2 - 2k\frac{d}{dx_1})\chi = 0$$

The drag Oseenlets potentials are then taken to be

$$\phi^{(1)} = \frac{1}{2\pi\rho U}\ln r, \qquad \chi^{(1)} = \frac{e^{kx_1}}{2\pi\rho U}K_0(kr)$$

This gives velocity and pressure now obtained from

$$u_i^{(1)} = \frac{d\phi^{(1)}}{dx_1} + \omega_i^{(1)}$$

$$u_i^{(1)} = \frac{d\phi^{(1)}}{dx_1} + \frac{d\chi^{(1)}}{dx_j} - 2k\chi^{(1)}\delta_{i1}$$

31

$$u_i^{(1)} = \frac{d}{dx_1}\left(\phi^{(1)} + \chi^{(1)}\right) - 2k\chi^{(1)}\delta_{i1}$$

$$p^{(1)} = -\rho U \frac{d\phi^{(1)}}{dx_1}$$

$u_i^{(1)} = \frac{1}{2\pi\rho U}\left(\frac{d}{dx_i}\left(\ln r + e^{kx_1}K_0(kr)\right) - 2ke^{kx_1}K_0(kr)\delta_{i1}\right)$; k=Re/2, Re= Reynolds number, k is dimensionless wake number. The properties of the dimensionless number are the same as the Reynolds number.	(7)
$p^{(1)} = -\frac{1}{2\pi}\frac{d}{dx_1}(\ln r)$	(8)

3.5 Outflow

Consider the outflow from the drag Oseenlets.

Outflow $= \oint_{\partial\Sigma} u_i n_i \, dl$ where $\partial\Sigma$ in the boundary of a fluid domain Σ

$$= \oint_{d\Sigma}\left[\frac{\partial}{\partial x_i}\left(\phi^{(1)} + \chi^{(1)}\right) - 2k\chi^{(1)}\delta_{i1}\right]n_i dl$$

$\dfrac{\partial\phi^{(1)}}{\partial x_i}$ represents the potential velocity

$\dfrac{\partial}{\partial x_i}\left(\chi^{(1)}\right) - 2k\chi^{(1)}\delta_{i1}$ represents the wake velocity
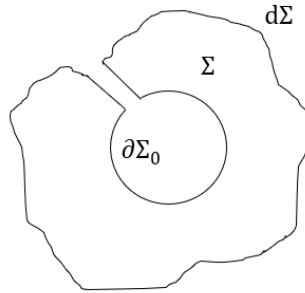
Figure 3.4 Domain Σ

$\iint_\Sigma \frac{du_i}{dx_i} ds = \oint_\Sigma u_i \, n_i dl = 0$ is true since the continuity equation holds in the region of Σ. Integral around the outer boundary is equal to the integral around the inner boundary. Let us consider the inner boundary a circle of radius called $\partial\Sigma_0$. Now we will calculate the potential contribution and wake contribution separately. It is illustrated in figure 3.4.

3.6 Potential contribution

$$\text{Outflow} = \oint_{\partial \Sigma_0} u_i n_i \, dl$$

$$= \oint_{\partial \Sigma_0} \frac{d}{dx_i} \phi^{(1)} n_i \, dl$$

$$= \oint_{\partial \Sigma_0} \left(n_1 \frac{d}{dx_1} + n_2 \frac{d}{dx_2} \right) \phi^{(1)} \, dl$$

But, $\left(n_1 \frac{d\phi^{(1)}}{dx_1} + n_2 \frac{d\phi^{(1)}}{dx_2} \right) = n \cdot \nabla \phi^{(1)} = \frac{d}{dr} \phi^{(1)}$, when n is normal to the circle.

$$\text{Outflow} = \oint_{\partial \Sigma_0} \frac{d}{dr} \phi^{(1)} \, dl = \int_0^{2\pi} \frac{1}{2\pi\rho U} \left(\frac{1}{r} \right) r \, d\theta$$
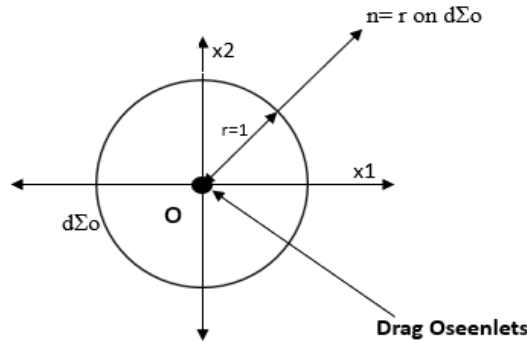
Figure 3.4 Representation of drag Oseenlets

$$\text{Outflow} = \int_0^{2\pi} \frac{1}{2\pi\rho U} \, d\theta, \because \phi^{(1)} = \frac{1}{2\pi\rho U} \ln r$$

$$\boxed{\text{Potential contribution for outflow} = \oint_{\partial \Sigma_0} \frac{d}{dr} \phi^{(1)} \, dl = \frac{1}{\rho U}} \qquad (9)$$

3.7 Wake contribution

$$\text{Outflow} = \oint_{\partial \Sigma_0} u_i n_i \, dl$$

$$= \oint_{\partial \Sigma_0} \left(\frac{\partial}{\partial x_i} \left(\chi^{(1)} \right) - 2k\chi^{(1)} \delta_{i1} \right) n_i \, dl$$

$$= \oint_{\partial \Sigma_0} \left(n_i \frac{\partial}{\partial x_i} \left(\chi^{(1)} \right) - 2k\chi^{(1)} \delta_{i1} n_i \right) dl$$

33

$$= \oint_{\partial\Sigma_0} \left[\left(n_1 \frac{\partial}{\partial x_1} + n_2 \frac{\partial}{\partial x_2} \right) \chi^{(1)} - 2k\chi^{(1)}n_1 \right] dl$$

$$\text{Outflow} = \oint_{\partial\Sigma_0} \left[n_1 \left(\frac{\partial\chi^{(1)}}{\partial x_1} - 2k\chi^{(1)} \right) + n_2 \frac{\partial\chi^{(1)}}{\partial x_2} \right] dl$$

$$\text{We know,} \ \chi^{(1)} = \frac{e^{kx_1}}{2\pi\rho U} K_o(kr)$$

$$\frac{\partial}{\partial x_1}\left(\chi^{(1)}\right) = \frac{1}{2\pi\rho U} \frac{\partial}{\partial x_1}\left(e^{kx_1}K_o(kr)\right)$$

$$= \frac{1}{2\pi\rho U}\left[e^{kx_1}\frac{\partial}{\partial x_1}\left(K_o(kr)\right) + ke^{kx_1}K_o(kr)\right]$$

$$= \frac{1}{2\pi\rho U}e^{kx_1}\left[\frac{\partial}{\partial x_1}\left(K_o(kr)\right) + kK_o(kr)\right]$$

$$\frac{\partial}{\partial x_1}\left(\chi^{(1)}\right) - 2k\chi^{(1)} = \frac{1}{2\pi\rho U}e^{kx_1}\left[\frac{\partial}{\partial x_1}\left(K_o(kr)\right) + kK_o(kr)\right] - \frac{2k}{2\pi\rho U}e^{kx_1}K_o(kr)$$

$$= \frac{1}{2\pi\rho U}e^{kx_1}\left[\frac{\partial}{\partial x_1}\left(K_o(kr)\right) - kK_o(kr)\right]$$

$$\text{Outflow} = \oint_{\partial\Sigma_0}\left[\frac{n_1}{2\pi\rho U}e^{kx_1}\left[\frac{\partial}{\partial x_1}\left(K_o(kr)\right) - kK_o(kr)\right] + \frac{n_2}{2\pi\rho U}\frac{\partial}{\partial x_2}e^{kx_1}K_o(kr)\right]dl$$

$$= \frac{1}{2\pi\rho U}\oint_{\partial\Sigma_0}e^{kx_1}\left[\left(n_1\frac{\partial}{\partial x_1} + n_2\frac{\partial}{\partial x_2}\right)K_o(kr) - kn_1K_o(kr)\right]dl$$

$$= \frac{1}{2\pi\rho U}\oint_{\partial\Sigma_0}e^{kx_1}\left[\frac{\partial}{\partial r}K_o(kr) - kn_1K_o(kr)\right]dl$$

$$\because \left(n_1\frac{\partial}{\partial x_1} + n_2\frac{\partial}{\partial x_2}\right)K_o(kr) = n.\nabla K_o(kr)$$

$$\text{Outflow} = \frac{1}{2\pi\rho U}\oint_{\partial\Sigma_0}e^{kr\cos\theta}\left[\frac{\partial}{\partial r}K_o(kr) - k\cos\theta K_o(kr)\right]r\,d\theta$$

We have two different solutions for the given modified Bessel function, and they are depending on kr. The first case is as kr→0 and second case is kr→∞. From figure 3.4, Integral over path Σ is same as integral over path $\mathbf{d\Sigma}$. Let contour $\mathbf{\Sigma}$ path around point tending to zero. As $kr \to 0, K_o(kr) \sim \ln(kr)$

$$\frac{\partial}{\partial r}K_o(kr) \sim \frac{\partial}{\partial r}\ln(kr) = -\frac{1}{r}$$

$$\therefore \lim_{kr \to 0} \frac{\partial}{\partial r} K_o(kr) \sim \frac{1}{r}$$

$$\text{Outflow} = \frac{1}{2\pi\rho U} \int_0^{2\pi} [1 + O(kr)] \left[-\frac{1}{r} - k\cos\theta[-\ln(kr)] \right] r d\theta$$

$$= \frac{1}{2\pi\rho U} \int_0^{2\pi} [1 + O(kr)][-1 + kr\cos\theta[-\ln(kr)]] d\theta$$

$$= \frac{-1}{2\pi\rho U} \int_0^{2\pi} d\theta + \frac{1}{2\pi\rho U} kr\ln(kr) \int_0^{2\pi} \cos\theta d\theta$$

$$\text{Outflow} = \frac{-1}{\rho U} \qquad\qquad \therefore \int_0^{2\pi} \cos\theta = 0$$

$$\therefore \lim_{kr \to 0} \text{Outflow} \sim \frac{-1}{\rho U} \qquad\qquad (10a)$$

In the Second case as $kr \to \infty$, $K_o(kr) \sim \left(\frac{\Pi}{2kr}\right)^{\frac{1}{2}} e^{-kr}$, From   Abramowitz   and   Strgun (Abramowitz and Stegun, 1972)

$$K_o(kr) \sim \left(\frac{\Pi}{2kr}\right)^{\frac{1}{2}} e^{-kr}, \qquad \therefore \frac{\partial}{\partial r} K_o(kr) \sim -k\left(\frac{\Pi}{2kr}\right)^{\frac{1}{2}} e^{-kr}$$

$$\text{Outflow} = \frac{1}{2\pi\rho U} \oint_{\partial \Sigma_0} e^{kr\cos\theta} \left[\frac{\partial}{\partial r} K_o(kr) - k\cos\theta K_o(kr) \right] r d\theta$$

$$\text{Outflow} = \frac{1}{2\pi\rho U} \int_0^{2\pi} e^{kr\cos\theta} \left[-k\left(\frac{\Pi}{2kr}\right)^{\frac{1}{2}} e^{-kr} - k\cos\theta \left(\frac{\Pi}{2kr}\right)^{\frac{1}{2}} e^{-kr} \right] r d\theta$$

$$= \frac{-1}{2\pi\rho U} (kr) \left(\frac{\Pi}{2kr}\right)^{\frac{1}{2}} \int_0^{2\pi} e^{-kr(1-\cos\theta)} [1 + \cos\theta] d\theta$$

$$= \frac{-1}{2\pi\rho U} \left(\frac{\Pi}{2}\right)^{\frac{1}{2}} (kr)^{\frac{1}{2}} \int_0^{2\pi} e^{-kr(1-\cos\theta)} [1 + \cos\theta] d\theta$$

$$= \frac{-1}{2\pi\rho U} \left(\frac{\Pi}{2}\right)^{\frac{1}{2}} (kr)^{\frac{1}{2}} \int_{-\Pi}^{\Pi} e^{-kr(1-\cos\theta)} [1 + \cos\theta] d\theta$$

$$= \frac{-1}{2\pi\rho U}\left(\frac{\Pi}{2}\right)^{\frac{1}{2}}(kr)^{\frac{1}{2}}\int_{-\Pi}^{\Pi}e^{-kr\left(\frac{\theta^2}{2}\right)}2d\theta$$

$$= \frac{-1}{2\pi\rho U}\left(\frac{\Pi}{2}\right)^{\frac{1}{2}}(kr)^{\frac{1}{2}}2*\int_{-\infty}^{\infty}e^{-kr\left(\frac{\theta^2}{2}\right)}d\theta$$

For $|\theta| \ll 1$ rad ; $\cos\theta \approx 1 - \frac{\theta^2}{2!}$

$$\Rightarrow 1 - \cos\theta \approx 1 - \left(1 - \frac{\theta^2}{2}\right) = \frac{\theta^2}{2}$$

$$1 + \cos\theta = 2$$
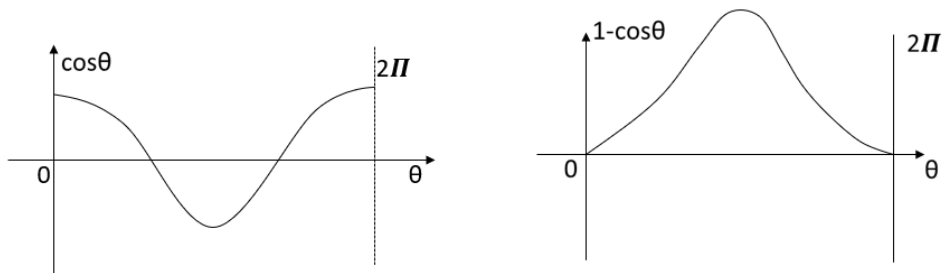
Figure 3.5 Cosine distribution

$$= \frac{-1}{2\pi\rho U}\left(\frac{\Pi}{2}\right)^{\frac{1}{2}}2*(kr)^{\frac{1}{2}}\left(\frac{2\Pi}{kr}\right)^{\frac{1}{2}}$$

$$\int_{-\infty}^{\infty}e^{-a\theta^2}d\theta = \left(\frac{\Pi}{a}\right)^{\frac{1}{2}};$$

$$\int_{-\infty}^{\infty}d\theta \Rightarrow \int_{-\Pi}^{\Pi}d\theta$$

$$\therefore \lim_{kr\to\infty}\text{Outflow} \sim \frac{-1}{\rho U}$$	(11b)

Outflow from $\chi^{(1)} = \oint_{\partial\Sigma_0}w_i n_i \, dl = \oint_{\partial\Sigma_0}\left(\frac{\partial}{\partial x_i}\left(\chi^{(1)}\right) - 2k\chi^{(1)}\delta_{i1}\right)n_i \, dl$

Outflow $= \frac{-1}{\rho U}$ for $kr \to 0$ and $kr \to \infty$

Outflow and inflow are balanced at the origin due to mass conservation and it is represented in figure 3.6.

36
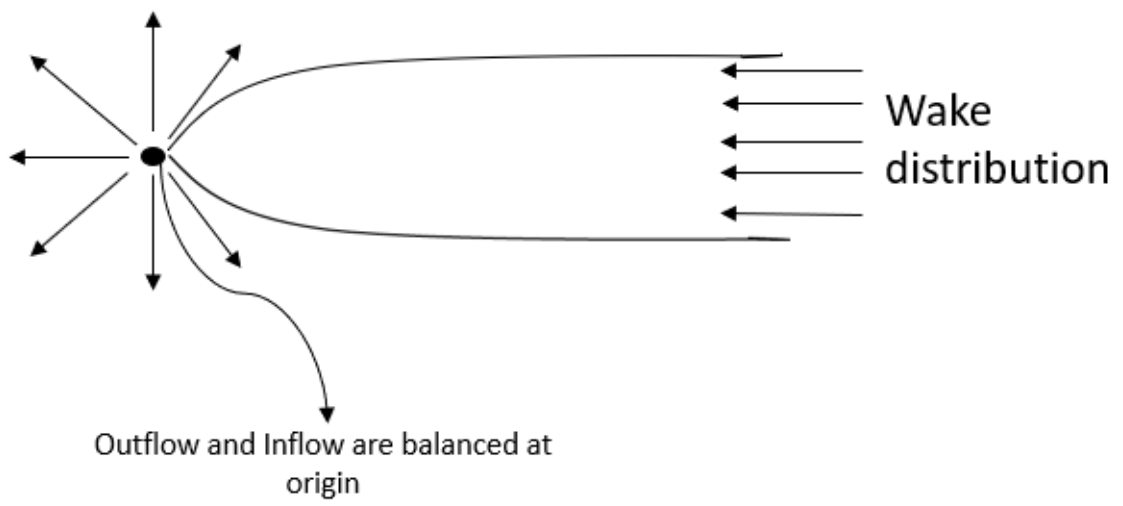
Figure 3.6 Wake Distribution

3.8 Eulerlets theory

Consider the steady-state 2-dimensional Euler equation in the tensor form

$$u_j \frac{\partial}{\partial x_j} u_i = -\frac{\partial p}{\partial x_i}.$$

In the near field, let us still assume negligible diffusion and s the viscosity is set to zero. However, now relax the small-velocity perturbation condition, and so include all the terms in the velocity representation $u_i^E = U\delta_{i1} + u_i$ to approximate the Navier-Stokes equations by the Euler equations given by

$$\left(U\frac{\partial u_i}{\partial x_1} + u_j\frac{\partial u_i}{\partial x_j}\right) = -\frac{\partial p}{\partial x_i}.$$

Normalise the above Euler equation by $u_i = Uu_i$; $p=\rho U^2 p$; $x_i = Lx_i$ which gives

$$\left(\frac{\partial u_i}{\partial x_1} + u_j\frac{\partial u_i}{\partial x_j}\right) = -\frac{\partial p}{\partial x_i}. \tag{12a}$$

The Eulerlets are defined as the unit force fundamental solution such that the normalised Eulerlet equation is

$$\left(\frac{\partial u_i^{(k)}}{\partial x_1} + u_j^{(k)}\frac{\partial u_i^{(k)}}{\partial x_j}\right) = -\frac{\partial p^{(k)}}{\partial x_i} - \delta\delta_{ik} \tag{12b}$$

where $u_j^{(k)}\frac{\partial u_i^{(k)}}{\partial x_j}$ is the kth Eulerlet expression for the term $u_j\frac{\partial u_i}{\partial x_j}$, and $\delta = \delta(x_1)\delta(x_2)$.

Differential properties of the Dirac Delta function δ'. Oseen gives the Oseenlets in two-dimensional flow as from equation (8) as

$$u_i^{(1)} = \frac{1}{2\pi}\left(\frac{d}{dx_i}\left(\ln r + e^{kx_1}K_0(kr)\right) - 2ke^{kx_1}K_0(kr)\delta_{i1}\right).$$

The Dirac delta function is obtained by taking the limiting value of the wake velocity part of the drag Oseenlets $w_1^{(1)}$ such that

$$w_1^{(1)} = \lim_{Re\to\infty}\left[\frac{1}{2\pi}\left(\frac{d}{dx_1}\left(e^{kx_1}K_0(kr)\right) - 2ke^{kx_1}K_0(kr)\right)\right]$$

 In the far-field, the x_1 scaling is of order O(Re), whereas the x_∞ scaling is of order O(1). So, for large Re=2k, we approximate for $x_1 \gg |x_\infty|$. This gives from the work of Abramowitz and Stegun (Abramowitz and Stegun, 1972)

$$e^{kx_1}K_0(kr) \sim \left(\frac{\Pi}{2kr}\right)^{\frac{1}{2}} e^{-k(r-x_1)} \sim \left(\frac{\Pi}{2kr}\right)^{\frac{1}{2}} e^{-kx_2^2/2x_1}; \ r = \sqrt{x_1^2 + x_1^2}$$

$$\left(\frac{\Pi}{2kr}\right)^{\frac{1}{2}} e^{-\eta^2}, \eta = \left(\frac{k}{2x_1}\right)^{\frac{1}{2}} x_2$$

where η is the same as the boundary layer variable, except in BLT $x_1^{BLT} = O(1), x_2^{BLT} = O\left(\frac{1}{\sqrt{Re}}\right)$, whereas in the far wake $x_1 = O(Re)$, $x_2 = O(1)$. However, both give the same parabolic wake/ boundary layer profile described by η due to stretching of the x_1 coordinate relative to the others. In the near-field, the scaling is $x_i = O(1)$, and so $\eta = O((Re)^{\frac{1}{2}})$. For large Re, η is large and so diffusion is suppressed, meaning that the wake does not diffuse. The two-dimensional drag is given as a far-field momentum deficit. For the two-dimensional Oseenlets unit drag comes from the wake velocity and so

$$-\int_{-\infty}^{\infty} w_1 dx_2 \sim \frac{1}{\sqrt{\pi}} \int_{-\infty}^{\infty} e^{-\eta^2} d\eta = 1 = \int_{-\infty}^{\infty} H(x_1)\delta(x_2)dx_2$$

where $H(x_1)$ is the Heaviside function $H(x_1) = 0$ for $x_1 < 0, and \ H(x_1) = 1$ for $x_1 \geq 0$, and where $\delta(x_2)$ is a Dirac delta function whose derivative satisfies the property and so the limiting value of the derivative is

$$\frac{\partial}{\partial x_2} w_1^{(1)} = \lim_{Re \to \infty} \left[\frac{1}{2\pi} \frac{\partial}{\partial x_2} \left(\frac{d}{dx_1}\left(e^{kx_1}K_0(kr)\right) - 2ke^{kx_1}K_0(kr)\right)\right] = 0$$

$$-\int_{-\infty}^{\infty} \frac{\partial w_1}{\partial x_2} dx_2 \sim 2\sqrt{\frac{k}{\pi x_1}} \int_{-\infty}^{\infty} \eta e^{-\eta^2} d\eta = 0 = \int_{-\infty}^{\infty} H(x_1)\delta'(x_2)dx_2$$

and so $\delta'(x_2) = 0$ for $x_2 \neq 0$ where the dash denotes a derivative and $\int \delta(x_2)dx_2 = 1$ for an integration passing across $x_2 = 0$. It is seen that the distribution represented here is not smooth and well-behaved in the usual sense because of the property that the Dirac delta function derivative is zero, and this has an important physical significance which we shall find later in Chapter 7 implies that the resulting wake flow consists of layers of fluid that slip past each other with vanishingly small tangential stress between layers. For fluid applications, Dirac delta function models drag Eulerlet wake and the solution is symmetric and derivative must be zero. However, this does not affect all standard properties of the Dirac delta function. We note that the integral contributions from the derivative of $e^{kx_1}K_0(kr)$ with respect to the co-ordinate, x_1 are of order $1/x_1 = O(1/Re) \to 0$ as $Re \to \infty$. So, the two-dimensional Oseenlet

collapses to the wake line to give drag Eulerlet as the Reynolds number goes to infinity which gives

$$u_i^{(1)} = \frac{1}{2\pi}\frac{\partial}{\partial x_i}(\ln r) - H(x_1)\delta(x_2)\delta_{i1}$$	(13)
$$u_i^{(2)} = \frac{1}{2\pi}\varepsilon_{ij3}\frac{\partial}{\partial x_i}(\ln r) = \frac{1}{2\pi}[-\theta]_{,i}$$	(14)

where $u_i^{(k)}$ is generated by a unit point force at the origin in the kth direction, for the Cartesian coordinates x_i in Einstein tensor notation such that a comma denotes a derivative. In two-dimensions, the radius and polar angle are given by r and θ respectively. The Heaviside function is denoted by $H(x_1)$ where $H(x_1)=0$ for $x_1 < 0$ and $H(x_1)=1$ for $x_1 > 0$. The Dirac delta function is given by δ with the additional property that its derivative is zero and this does not contradict the delta function property $x\frac{\partial\delta(x)}{\partial x} = -\delta(x)$, which still holds. Kronecker delta is given by $\delta_{ij} = 1$ for i=j and $\delta_{ij} = 0$ for i≠j, and the Levi-Civita symbol $\varepsilon_{ijk} = 1$ for (i,j,k)=(1,2,3), (2,3,1), (3,1,2), $\varepsilon_{ijk} = -1$ for (i,j,k)=(1,3,2), (2,1,3), (3,2,1), $\varepsilon_{ijk} = 0$ otherwise. We note that this Dirac delta function is obtained when taking the Oseenlets high Reynolds number limit, and consequently has different differential properties from the usual Dirac delta function obtained from Fourier analysis. The drag Eulerlet is pictorially represented in Figure 3.7 and k=Re/2 as k→∞ in equation (8), then the wake collapses onto the wake line but must have the same inflow. The inflow from equation (11a) for the normalised wake velocity is -1 (actual wake velocity from equation (11b) is $\frac{-1}{\rho U}$) and so the Euler wake term must give inflow of -1, and so is $w_i^{(1)} = -H(x_1)\delta(x_2)\delta_{i1}$.
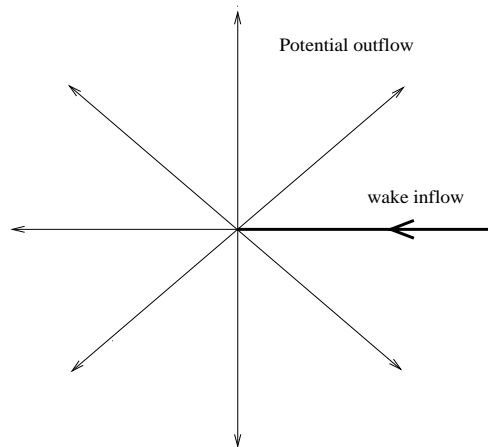
Figure 3.7 Streamlines for the drag Eulerlets

3.8.1 Euler slip wake

Here we discuss Euler slip wake. This is a wake flow where layers of fluid slip past each other, that arises as a consequence of the representation by an Eulerlet distribution. First reflect on the Euler flow boundary condition which is that the normal velocity is zero, and so the flow can slip along the boundary like figure 3.8 (a).
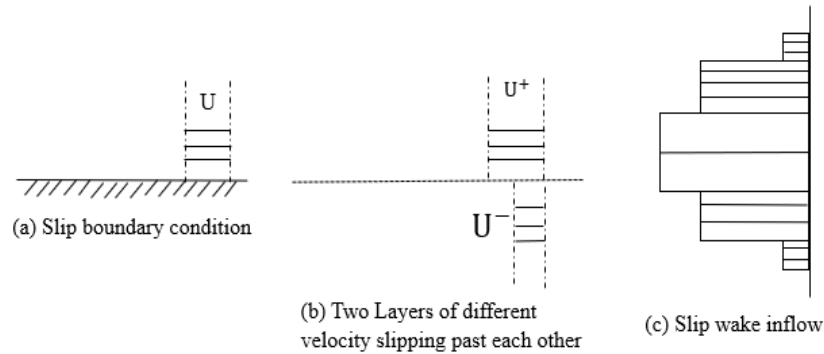
Figure 3.8 Different types of slip wakes

Using the same argument with regards to slip, another possible flow is a layer of fluid with a constant uniform flow velocity U^+ slipping over another layer of fluid with a different constant uniform flow velocity U^- like figure 3.8 (b).

Extending this argument further, it is seen that a possible wake inflow is a series of layers of fluid slipping past each other with different constant velocities such that in each layer the velocity is constant, and so the derivative and vorticity is zero, see figure 3.8 (c).

The Eulerlet distribution is not modelling the boundary layer but wake inflow distribution. Although the Eulerlet has a wake inflow, the solution does have a wake that flows downstream. The Eulerlet distribution is defined as a wake inflow distribution with terms including Heaviside function, Dirac delta function and Kronecker delta as is shown in equation (13). Each function has it's own properties, however, Dirac delta function is the one which captures the wake which is mathematically expressed in section 2.12 and showed in figure 2.6. For example, if we consider figure 3.8(c), each rectangle block represents one layer of fluid symmetric to the origin and it is captured using Dirac delta function. The numerical solution is given in the Fortran code.

In this limit, this flow is represented by a wake inflow distribution of drag Eulerlets which have the derivative of the wake velocity zero, and therefore also the vorticity is zero. Consider drag Eulerlets solution $u_j^{(1)}, p^{(1)}$ and we are seeking for a solution of the form

41

$$u_i^{(1)} = \frac{1}{2\pi}\frac{\partial}{\partial x_i}(\ln r) - H(x_1)\delta(x_2)\delta_{i1}, \qquad r = \sqrt{x_1^2 + x_1^2}$$

The above solution must satisfy the following

1) Zero vorticity $\dfrac{\partial u_j^{(1)}}{\partial x_i} = \dfrac{\partial u_i^{(1)}}{\partial x_j}$

2) Mass conservation $\dfrac{\partial u_1^{(1)}}{\partial x_1} + \dfrac{\partial u_2^{(1)}}{\partial x_2} = 0$

3) Unit force solution $D_i = \oiint \delta(x_1)\delta(x_2)\delta_{i1}ds = \delta_{i1}$

4) Pressure field to satisfy the Euler equations

Also, we use the following properties

$$\frac{\partial H(x_1)}{\partial x_1} = \delta(x_1); \quad \frac{\partial\delta(x_2)}{\partial x_2} = 0$$

3.8.2 Zero vorticity

The Eulerlet velocity from equation (13)

$$\frac{\partial u_j^{(1)}}{\partial x_i} = \frac{1}{2\pi}\frac{\partial}{\partial x_i}\frac{\partial}{\partial x_j}(\ln r) - \frac{\partial}{\partial x_i}H(x_1)\delta(x_2)\delta_{j1}$$

Consider wake term from the above equation

$$\frac{\partial}{\partial x_i}\big[H(x_1)\delta(x_2)\delta_{j1}\big] = \delta_{i1}\frac{\partial}{\partial x_1}\big[H(x_1)\delta(x_2)\delta_{j1}\big] + \delta_{i2}\frac{\partial}{\partial x_2}\big[H(x_1)\delta(x_2)\delta_{j1}\big]$$

$$\frac{\partial}{\partial x_i}\big[H(x_1)\delta(x_2)\delta_{j1}\big] = \delta_{i1}\delta_{j1}\delta(x_2)\frac{\partial H(x_1)}{\partial x_1} + \delta_{i2}\delta_{j1}H(x_1)\frac{\partial}{\partial x_2}\delta(x_2)$$

$$\frac{\partial}{\partial x_i}\big[H(x_1)\delta(x_2)\delta_{j1}\big] = \delta_{i1}\delta_{j1}\delta(x_2)\frac{\partial H(x_1)}{\partial x_1}$$

$$\frac{\partial}{\partial x_i}\big[H(x_1)\delta(x_2)\delta_{j1}\big] = \delta_{i1}\delta_{j1}\delta(x_2)\delta(x_1)$$

$$\frac{\partial u_j^{(1)}}{\partial x_i} = \frac{1}{2\pi}\frac{\partial}{\partial x_i}\frac{\partial}{\partial x_j}(\ln r) - \delta_{i1}\delta_{j1}\delta(x_2)\delta(x_1)$$

$$\frac{\partial u_i^{(1)}}{\partial x_j} = \frac{1}{2\pi}\frac{\partial}{\partial x_j}\frac{\partial}{\partial x_i}(\ln r) - \delta_{j1}\delta_{i1}\delta(x_2)\delta(x_1) = \frac{\partial u_j^{(1)}}{\partial x_i}$$

$$\therefore \frac{\partial u_i^{(1)}}{\partial x_j} = \frac{\partial u_j^{(1)}}{\partial x_i}$$

3.8.3 Pressure field

From the Euler equation

$$\left(\frac{\partial u_i}{\partial x_1} + u_j \frac{\partial u_i}{\partial x_j} \right) = -\frac{\partial p}{\partial x_i}$$

From the continuity equation, the second term in the above equation is

$$u_j^{(1)} \frac{\partial u_i^{(1)}}{\partial x_j} = u_j^{(1)} \frac{\partial u_j^{(1)}}{\partial x_i} = \frac{1}{2} \frac{\partial \left(u_j^{(1)} u_j^{(1)} \right)}{\partial x_i}$$

And the first term is

$$\frac{\partial u_i^{(1)}}{\partial x_1} = \frac{\partial^2 \phi^{(1)}}{\partial x_1 \, \partial x_i} + \delta(x_1)\delta(x_2)\delta_{i1}$$

So for r>0, Euler velocity decomposes and it leads to $\delta(x_1)\delta(x_2)\delta_{i1} = 0$ and the above equation will be

$$\frac{\partial u_i^{(1)}}{\partial x_1} = \frac{\partial^2 \phi^{(1)}}{\partial x_1 \, \partial x_i}$$

Now substitute the manipulated first and second term into the Euler equation will give

$$\frac{\partial^2 \phi^{(1)}}{\partial x_1 \, \partial x_i} + \frac{1}{2} \frac{\partial \left(u_j^{(1)} u_j^{(1)} \right)}{\partial x_i} = -\frac{\partial p}{\partial x_i}$$

Integrating the above equation gives

$$p^{(1)} = -\frac{\partial \phi^{(1)}}{\partial x_1} - \frac{1}{2} u_j^{(1)} u_j^{(1)} \tag{11}$$

$$\phi^{(1)} \equiv \frac{1}{2\pi} \ln r \tag{12}$$

$$u_j^{(1)} = \frac{\partial \phi^{(1)}}{\partial x_j} + w_j^{(1)} \tag{13}$$

$$w_j^{(1)} \equiv -H(x_1)\delta(x_2)\delta_{i1} \tag{14}$$

3.8.4 Unit drag force

$D_i = \iint_\Sigma \delta(x_1, x_2)\delta_{i1}\, d\Sigma = \delta_{i1}$ we need to check whether this statement is correct or not and from Eulerlet equation

$$\left(\delta_{j1} + u_j^{(1)}\right)\frac{\partial u_j^{(1)}}{\partial x_j} = -\frac{\partial p^{(1)}}{\partial x_i} - \delta(x_1)\delta(x_2)\delta_{i1}$$

$$\delta(x_1)\delta(x_2)\delta_{i1} = -\frac{\partial p^{(1)}}{\partial x_i} - \left(\delta_{j1} + u_j^{(1)}\right)\frac{\partial u_j^{(1)}}{\partial x_j}$$

$$\text{So, } D_i = \iint_\Sigma \left[-\frac{\partial p^{(1)}}{\partial x_i} - \left(\delta_{j1} + u_j^{(1)}\right)\frac{\partial u_j^{(1)}}{\partial x_j}\right] d\Sigma$$

We have $p^{(1)} = -\frac{\partial \phi^{(1)}}{\partial x_1} - \frac{1}{2}u_j^{(1)}u_j^{(1)}$, differentiate the pressure equation with respect to the x_i will give

$$\frac{\partial p^{(1)}}{\partial x_i} = -\frac{\partial}{\partial x_i}\frac{\partial \phi^{(1)}}{\partial x_1} - \frac{\partial}{\partial x_i}(\frac{1}{2}u_j^{(1)}u_j^{(1)})$$

Substitute the above equation in D_i

$$D_i = \iint_\Sigma \left[\frac{\partial}{\partial x_i}\frac{\partial \phi^{(1)}}{\partial x_1} + \frac{\partial}{\partial x_i}(\frac{1}{2}u_j^{(1)}u_j^{(1)}) - \left(\delta_{j1} + u_j^{(1)}\right)\frac{\partial u_j^{(1)}}{\partial x_j}\right] d\Sigma$$

$$D_i = \iint_\Sigma \left[\frac{\partial}{\partial x_i}\frac{\partial \phi^{(1)}}{\partial x_1} + \frac{\partial}{\partial x_i}(\frac{1}{2}u_j^{(1)}u_j^{(1)}) - \delta_{j1}\frac{\partial u_j^{(1)}}{\partial x_i} - \frac{\partial}{\partial x_i}(\frac{1}{2}u_j^{(1)}u_j^{(1)})\right] d\Sigma$$

$$D_i = \iint_\Sigma \left[\frac{\partial}{\partial x_i}\frac{\partial \phi^{(1)}}{\partial x_1} - \delta_{j1}\frac{\partial u_j^{(1)}}{\partial x_i}\right] d\Sigma$$

$$D_i = \iint_\Sigma \left[\frac{\partial}{\partial x_i}\frac{\partial \phi^{(1)}}{\partial x_1} - \frac{\partial u_1^{(1)}}{\partial x_1}\right] d\Sigma$$

$$D_i = \iint_\Sigma \left[-\frac{\partial}{\partial x_i}\left(\frac{-\partial \phi^{(1)}}{\partial x_1} + u_1^{(1)}\right)\right] d\Sigma$$

$$D_i = \iint_\Sigma -\frac{\partial w_1^{(1)}}{\partial x_i}\, d\Sigma = \iint_\Sigma \delta(x_1)\delta(x_2)d\Sigma = 1$$

3.8.5 Continuity equation and Vanishing divergence

$$\frac{\partial u_j^{(1)}}{\partial x_j} = \frac{\partial u_1^{(1)}}{\partial x_1} + \frac{\partial u_2^{(1)}}{\partial x_2} = 0$$

$$\text{where } u_j^{(1)} = \frac{1}{2\pi} \frac{\partial}{\partial x_j} (\ln r) - H(x_1)\delta(x_2)\delta_{j1}$$

$$\frac{\partial u_j^{(1)}}{\partial x_j} = \frac{1}{2\pi} \frac{\partial}{\partial x_j}\frac{\partial}{\partial x_j} (\ln r) - \frac{\partial}{\partial x_j} H(x_1)\delta(x_2)\delta_{j1}$$

$$\frac{\partial u_j^{(1)}}{\partial x_j} = \frac{1}{2\pi} \frac{\partial}{\partial x_j}\frac{\partial}{\partial x_j} (\ln r) - \delta_{j1}\frac{\partial}{\partial x_j} H(x_1)\delta(x_2)$$

$$\frac{\partial u_j^{(1)}}{\partial x_j} = \frac{1}{2\pi} \frac{\partial}{\partial x_j}\frac{\partial}{\partial x_j} (\ln r) - \delta_{11}\frac{\partial}{\partial x_1} H(x_1)\delta(x_2) - \delta_{21}\frac{\partial}{\partial x_2} H(x_1)\delta(x_2)$$

$$\frac{\partial u_j^{(1)}}{\partial x_j} = \frac{1}{2\pi} \frac{\partial}{\partial x_j}\frac{\partial}{\partial x_j} (\ln r) - \delta_{11}\frac{\partial}{\partial x_1} H(x_1)\delta(x_2)$$

$$\frac{\partial u_j^{(1)}}{\partial x_j} = \frac{1}{2\pi} \frac{\partial}{\partial x_j}\frac{\partial}{\partial x_j} (\ln r) - \frac{\partial}{\partial x_1} H(x_1)\delta(x_2)$$

$$\frac{\partial u_j^{(1)}}{\partial x_j} = \frac{1}{2\pi} \frac{\partial}{\partial x_j}\frac{\partial}{\partial x_j} (\ln r) - \delta(x_1)\delta(x_2) = 0$$

$$\boxed{\frac{\partial u_j^{(1)}}{\partial x_j} = \frac{1}{2\pi} \frac{\partial}{\partial x_j}\frac{\partial}{\partial x_j} (\ln r) - \delta(x_1, x_2) = 0}$$

3.9 Green's Integral Representation of Eulerlets:

From the Euler equation (12a) and the Eulerlet equation (12b), Consider an area of fluid A in Euler flow, then from the Euler Equation

$$\int_A \left(U\frac{\partial u_i}{\partial y_1} + u_j\frac{\partial u_i}{\partial y_j} + \frac{\partial p}{\partial y_i} + f_i \right) dA = 0$$

where an element of integration is given by $dA = dy_1 * dy_2$ and $\mathbf{y}$ is the vector coordinate of the point in the integration over A. We want a term in the equation that gives the result $u_j(\mathbf{x})$ so, consider the variable $\mathbf{z}=\mathbf{x}-\mathbf{y}$, where $\mathbf{x}$ is a vector coordinate of a point in the fluid. Multiplying the above integral by $u_i(y)$, to obtain point force solutions such that we consider

$f_i^{(j)} = \delta_{ij}\delta(\mathbf{z})$ where, $\delta(\mathbf{z})$ is a Dirac delta function in two-dimensions $\delta(\mathbf{z}) = \delta(z_1) * \delta(z_2)$. Therefore let us consider including further the area integral terms such that

$$\int_A \left(U \frac{\partial u_i^{(k)}}{\partial z_1} + u_j^{(k)} \frac{\partial u_i^{(k)}}{\partial z_j} + \frac{\partial p^{(k)}}{\partial z_i} + \delta\delta_{ik} \right) u_i(\mathbf{y}) dA = 0$$

Hence the last term gives $\int_{v_y} \delta_{ij}\delta(z)u_i(y)dv_y = u_j(x)$ As per required. However, other terms give a volume integral whereas we require a surface integral. So, we are going to use the divergence theorem. Therefore, let us consider including further the volume integral terms such that

$$\int_{v_y} \left[\left(\frac{dp}{dy_i} + U\frac{du_i}{dy_1} + u_j \frac{\partial u_i}{\partial y_j} + f_i \right) u_i^{(m)} - \left(\frac{\partial p^{(m)}}{\partial z_i} + U\frac{\partial u_i^{(m)}}{\partial z_1} + u_j^{(m)} \frac{\partial u_i^{(m)}}{\partial z_j} + f_i^{(m)} \right) u_i \right] dv_y$$
$$= 0$$

Following the boundary integral method for the above variables yielding the adjoint equation satisfied by the Green's functions such that

$$\frac{df(z)}{dx_i} = \frac{dz_j}{dx_i} * \frac{df(z)}{dz_j} = \delta_{ij} \frac{d}{dz_j}f(z) = \frac{d}{dz_j}f(z)$$

$$\frac{df(z)}{dy_i} = \frac{dz_j}{dy_i} * \frac{df(z)}{dz_j} = -\delta_{ij} \frac{d}{dz_j}f(z) = -\frac{d}{dz_j}f(z)$$

$$\therefore \frac{d}{dx_i}f(z) = -\frac{d}{dy_i}f(z)$$

$$\int_{v_y} \left[\left(\frac{dp}{dy_i} + U\frac{du_i}{dy_1} + u_j \frac{\partial u_i}{\partial y_j} + f_i \right) u_i^{(m)} - \left(\frac{-\partial p^{(m)}}{\partial y_i} - U\frac{\partial u_i^{(m)}}{\partial y_1} - u_j^{(m)} \frac{\partial u_i^{(m)}}{\partial y_j} + f_i^{(m)} \right) u_i \right] dv_y$$
$$= 0$$

Let us restrict the theory to problems only where the near-field velocity is such that the vortex field is weak, and so, $\frac{\partial u_i^{(m)}}{\partial y_j} = \frac{\partial u_j^{(m)}}{\partial y_i}$ and $\frac{\partial u_i}{\partial y_j} = \frac{\partial u_j}{\partial y_i}$ and so from the above equation

$$\int_{v_y} \left[\left(\frac{dp}{dy_i} + U\frac{du_i}{dy_1} + u_j \frac{\partial u_j}{\partial y_i} + f_i \right) u_i^{(m)} - \left(\frac{-\partial p^{(m)}}{\partial y_i} - U\frac{\partial u_i^{(m)}}{\partial y_1} - u_j^{(m)} \frac{\partial u_j^{(m)}}{\partial y_i} + f_i^{(m)} \right) u_i \right] dv_y$$
$$= 0$$

$$\int_{v_y} \left[\frac{d(pu_i^{(m)})}{dy_i} + \frac{\partial(p^{(m)}u_i)}{\partial y_i} + U\frac{d(u_i u_i^{(m)})}{dy_1} + \frac{\partial}{\partial y_i}(\frac{1}{2}u_j u_j u_i^{(m)}) + \frac{\partial}{\partial y_i}(\frac{1}{2}u_i u_j^{(m)} u_j^{(m)}) + f_i u_i^{(m)} \right.$$

$$\left. - f_i^{(m)} u_i \right] dv_y = 0$$

Since, $\dfrac{\partial}{\partial y_i}(\dfrac{1}{2}u_j u_j) = u_j \dfrac{\partial u_j}{\partial y_i}$ and $\dfrac{\partial}{\partial y_i}\left(\dfrac{1}{2}u_j^{(m)} u_j^{(m)}\right) = u_j^{(m)} \dfrac{\partial u_j^{(m)}}{\partial y_i}$

Applying the divergence theorem then gives

$$\int_C \left[\frac{d(pu_i^{(m)})}{dy_i} + \frac{\partial(p^{(m)}u_i)}{\partial y_i} + U\frac{d(u_i u_i^{(m)})}{dy_1} + \frac{\partial}{\partial y_i}(\frac{1}{2}u_j u_j u_i^{(m)}) + \frac{\partial}{\partial y_i}(\frac{1}{2}u_i u_j^{(m)} u_j^{(m)}) \right] dl$$

$$= u_i \delta_{ik}$$

$$\int_C \left[\left(p + (\frac{1}{2}u_j u_j) \right) u_i^{(m)} n_i^A + \left(p^{(m)} + \frac{1}{2}u_j^{(m)} u_j^{(m)} \right) u_i n_i^A + U u_i u_i^{(m)} n_i^A \right] dl = u_i \delta_{ik}$$

Where the curve C includes C_B and C_∞ and n_i is outward pointing normal to C_B. There is nobody force in the fluid so $f_i=0$, $\int_A f_i^{(m)} dA = \delta_{im}$. The matching integral is the limit of the far-field Oseen integral which is zero from the above equation, and the outward pointing normal n_i^A is the inward-pointing normal n_i to the body curve C_B. So $n_i = -n_i^A$.

So, $u_E = -\int_{C_B} \left[\left(p + (\frac{1}{2}u_j u_j) \right) u_i^{(m)} n_i + \left(p^{(m)} + \frac{1}{2}u_j^{(m)} u_j^{(m)} \right) u_i n_i + U u_i u_i^{(m)} n_i \right] dl$
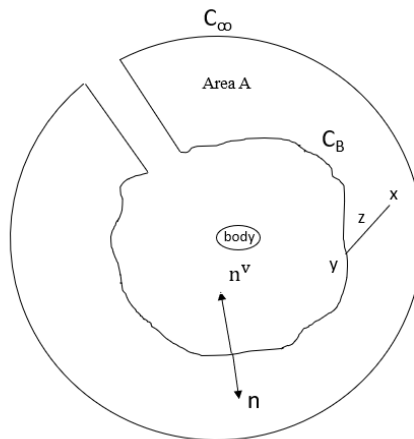
Figure 3.8 Green's Integral representation of Eulerlets.

47

3.10 Flow past a circular cylinder

The novelty in this work is to demonstrate the use of two-dimensional Eulerlets in modelling the bluff body flows. Eulerlets are the Green's function solution to the Euler equations given for two-dimensional as it is explained in the previous section. In this present work, two-dimensional flow past a circular cylinder is considered, and also the far-field is modelled by matching the near-field Eulerlets to the corresponding far-field Oseenlets. The matching far-field and near-field is explained in section 3.10.2 and shown in figure 3.12. The fluid velocity component u_i is represented by two parts, a velocity potential $\phi_{,i}$ and a wake velocity w_i such that $u_i = \phi_{,i} + w_i$. The potential is given in terms of the potential parts of the Eulerlets which can then be represented by a harmonic expansion originating from the origin, which obeys the Laplace equations, such that

$$\phi = \frac{D}{2\pi}\ln r + \sum_{n=1}^{\infty} a_n \frac{\cos n\theta}{r^n} \qquad (15a)$$
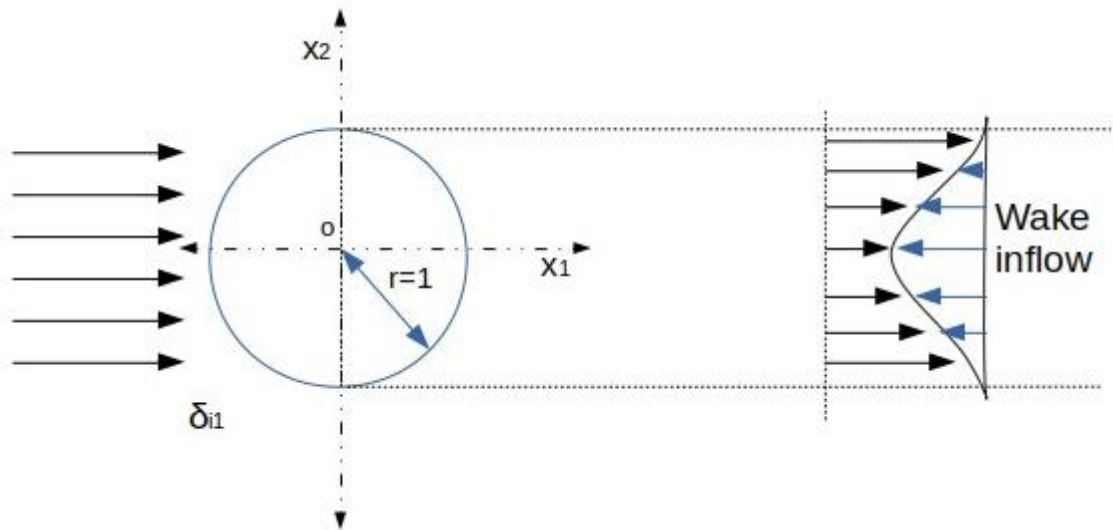
Figure 3.9 Flow past a circular cylinder with wake representation

In equation (15a), cannot have $\sin n\theta$ contribution in the expansion since $D(x_2')$ is symmetric in x_2. For coefficient D related to the drag, and for some unknown coefficients a_n is defined by using Taylor series expansion. Express the wakefield as an integral distribution of drag Eulerlets distributed along the line $x_1 = 0$, $-1 \le x_2 \le 1$ such that,

$$w_i = \int_{-1}^{1} D(x_2') w_i^{(1)}(x - x') \, dx_2' \text{ where } D(x_2') \text{ is drag per unit length.}$$

$$w_i^{(1)}(x_1, x_2) = -H(x_1)\delta(x_2 - x_2')\delta_{j1}$$

48

$$w_i = - \int_{-1}^{1} D(x_2')H(x_1)\delta(x_2 - x_2')\delta_{i1})\,dx_2' \text{ and the drag is}$$

$$D = \int_{-1}^{1} D(x_2)dx_2$$
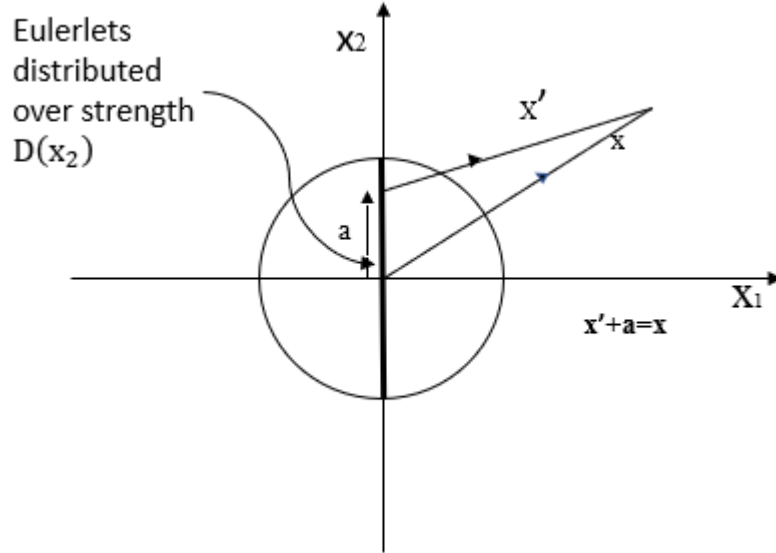
Figure 3.10 Eulerlet distribution

Now we need to check whether outflow and inflow match are not. Here, the outflow is a combination of point source and multipole expansion. Source and multipole expansion are illustrated in figure 3.11. Let $\partial\Sigma_0$ the circumference of a circle of radius "r" and for a point source $\phi \sim \dfrac{D}{2\pi}\ln r$.

$$\textbf{Outflow from point source} = \oint_{\partial\Sigma_0} u_i n_i\,dl = \oint_{\partial\Sigma_0} \frac{\partial\phi}{\partial x_i} n_i\,dl$$

$$\text{As we know, } \frac{\partial\phi}{\partial x_i} = \frac{\partial}{\partial x_i}\frac{D}{2\pi}\ln r = \frac{D}{2\pi r}\frac{\partial r}{\partial x_i}$$

$$\frac{\partial r}{\partial x_1} = \frac{x_1}{r} \Rightarrow \frac{\partial r}{\partial x_j} = \frac{x_j}{r}$$

$$\frac{\partial\phi}{\partial x_i} = \frac{D}{2\pi r}\frac{x_i}{r}$$

$$x_i.\,n_i = (\hat{e}_1.\,r\,\cos\theta + \hat{e}_2 r\,\sin\theta).(\hat{e}_1\,\cos\theta + \hat{e}_2\,\sin\theta)$$

$$\text{Where } \hat{e}_1 = (1,0) \text{ and } \hat{e}_2 = (0,1)$$

$$x_i.\,n_i = r(\cos^2\theta + \sin^2\theta)$$

49
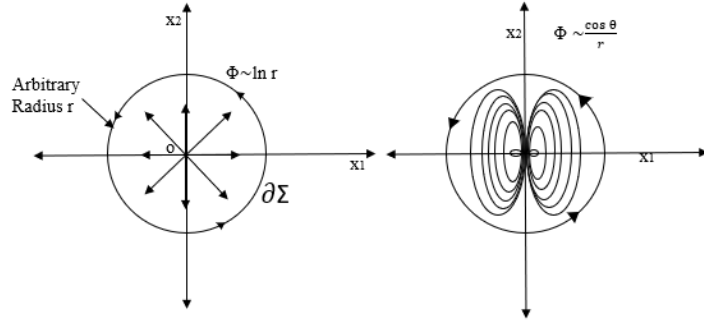
Figure 3.11 Outflow representation for point source and multipole expansion

$$x_i \cdot n_i \text{ on } \partial\Sigma_0, \qquad \text{Outflow from point source} = \oint_{\partial\Sigma_0} \frac{\partial\phi}{\partial x_i} n_i \, dl$$

$$\text{Outflow from point source} = \int_0^{2\Pi} \frac{D}{2\pi r} \frac{r * r}{r} d\theta = D$$

Outflow from point source = D this result is from the **log r** term. Now we must consider the **outflow from the multiple expansion** part of ϕ

$$\phi \sim \sum_{n=1}^{\infty} a_n \frac{\cos n\theta}{r^n} \, dl$$

$$\frac{\partial\phi}{\partial x_i} = \sum_{n=1}^{\infty} a_n \frac{\partial}{\partial x_i} \frac{\cos n\theta}{r^n} \, dl$$

$$\frac{\partial\phi}{\partial x_i} = \sum_{n=1}^{\infty} a_n \left[\cos n\theta \frac{\partial r^{-n}}{\partial x_i} + \frac{1}{r^n} \frac{\partial}{\partial x_i} \cos n\theta \right] dl$$

$$\frac{\partial\phi}{\partial x_i} = \sum_{n=1}^{\infty} a_n \left[-n * r^{-(n+1)} * \cos n\theta \frac{\partial r}{\partial x_i} - \frac{1}{r^n} \sin n\theta \frac{\partial n\theta}{\partial x_i} \right] dl$$

$$\frac{\partial\phi}{\partial x_i} = \sum_{n=1}^{\infty} a_n \left[-n * r^{-(n+1)} * \cos n\theta \frac{\partial r}{\partial x_i} - \frac{n}{r^n} \sin n\theta \frac{\partial\theta}{\partial x_i} \right] dl$$

Now we will find out what is $\dfrac{\partial\theta}{\partial x_i}$, from a circular body with radius 'r' $x_1 = r\cos\theta$; $x_2 = r\sin\theta$; $r = \sqrt{x_1^2 + x_2^2}$ and $\theta = \tan^{-1}\left(\dfrac{x_2}{x_1}\right)$

$$\frac{\partial\phi}{\partial x_1} = \frac{1}{1 + \left(\frac{x_2}{x_1}\right)^2} \frac{\partial}{\partial x_1} \frac{x_2}{x_1} = -\frac{1}{1 + \left(\frac{x_2}{x_1}\right)^2} \frac{x_2}{x_1^2} = -\frac{x_2}{r^2}$$

$$\frac{\partial \phi}{\partial x_2} = \frac{1}{1 + \left(\frac{x_2}{x_1}\right)^2} \frac{1}{x_1} = -\frac{x_1}{r^2}$$

$$\frac{\partial \phi}{\partial x_i} = -\delta_{i1}\frac{x_2}{r^2} + \delta_{i2}\frac{x_1}{r^2}$$

$$\frac{\partial \phi}{\partial x_i} = \frac{1}{r^2}(\delta_{i2}x_1 - \delta_{i1}x_2)$$

$$\frac{\partial \phi}{\partial x_i} = \sum_{n=1}^{\infty} a_n \left[-n * r^{-(n+1)} * \cos n\theta \frac{\partial r}{\partial x_i} - \frac{n}{r^n}\sin n\theta \frac{1}{r^2}(\delta_{i2}x_1 - \delta_{i1}x_2)\right] dl$$

$$\frac{\partial \phi}{\partial x_i} = \sum_{n=1}^{\infty} \frac{-na_n}{r^{(n+2)}} [x_i\cos n\theta + \sin n\theta (\delta_{i2}x_1 - \delta_{i1}x_2)] \, dl$$

$$\frac{\partial \phi}{\partial x_i} n_i = \sum_{n=1}^{\infty} \frac{-na_n}{r^{(n+2)}} [x_i n_i\cos n\theta + \sin n\theta (\delta_{i2}x_1 - \delta_{i1}x_2)n_i] \, dl$$

$$\frac{\partial \phi}{\partial x_i} n_i = \sum_{n=1}^{\infty} \frac{-na_n}{r^{(n+2)}} [x_i n_i\cos n\theta + \sin n\theta (\delta_{i2}x_1 n_i - \delta_{i1}x_2 n_i)] \, dl$$

$$\frac{\partial \phi}{\partial x_i} n_i = \sum_{n=1}^{\infty} \frac{-na_n}{r^{(n+2)}} [x_i n_i\cos n\theta + \sin n\theta (x_1 n_2 - x_2 n_1)] \, dl$$

$$\frac{\partial \phi}{\partial x_i} n_i = \sum_{n=1}^{\infty} \frac{-na_n}{r^{(n+2)}} \int_0^{2\pi} [x_i n_i\cos n\theta + \sin n\theta (\sin\theta \, r\cos\theta - \cos\theta \, r\sin\theta)] \, r d\theta$$

$$\int_0^{2\Pi} \cos n\theta \, d\theta = 0; \quad \frac{\partial \phi}{\partial x_i} n_i = 0 \text{ on } \partial\Sigma_0$$

$$\text{So,} \frac{\partial \phi}{\partial x_i} n_i = 0$$

Outflow from multipole $= \oint_{\partial\Sigma_0} \frac{\partial \phi}{\partial x_i} n_i \, dl = 0$

Outflow from the point source $\oint_{\partial\Sigma_0} \frac{\partial \phi}{\partial x_i} n_i \, dl = D$

Outflow for a potential part = outflow from ln r term + Outflow from multipole

Total outflow for a point source $=D+0=D.$

3.10.1 Outflow from wake

The total wake velocity equation is $\oint_{\partial\Sigma_0} w_i n_i \, dl = \oint_{\partial\Sigma_0} [-H(x_1)D(x_2)\delta_{i1}\ ]n_i \, dl$.

$$\oint_{\partial\Sigma_0} w_i n_i \, dl = - \int_{-1}^{1} D(x_2) \, d x_2 = -D$$

So potential outflow D matches wake inflow-D. The total drag force which is obtained by integrating over the distribution D (x_2). Let us assume the form $D(x_2) = \frac{D}{2}[1 + \cos \pi x_2]$ is the function chosen in the domain of x_2 varies between -1 to +1 and $D(x_2) = 0$ $|x_2|>1$. So,

$$D_1 = \int_{-\infty}^{\infty} D(x_2)dx_2 = -\int_{-1}^{1} \frac{D}{2}[1 + \cos \pi x_2]dx_2 = \frac{D}{2}[x_2 + \frac{1}{\pi}\sin \pi x_2] = D$$

$$D(x_2) = \frac{D}{2}[1 + \cos \pi x_2] = \frac{D}{2}[1 + \cos \pi \sin \theta]$$

$D(-\theta) = \frac{D}{2}[1 + \cos \pi \sin(-\theta)] = \frac{D}{2}[1 + \cos \pi \sin(\theta)] = D(\theta)$ and hence $D(\theta)$ symmetric in θ, Now

$$D_2 = \int_{-\frac{\pi}{2}}^{\frac{\pi}{2}} D(\sin \theta) \sin \theta \ d\theta$$

$D(\sin \theta)$ is symetric; $\sin \theta$ is antisymetric $D(\sin \theta) \sin \theta$ is antisymmetric. All the drag force is in 1 direction which is D_1 is equal to D, however, drag in 2nd direction is zero as expected So, $D_2 = 0$.

3.10.2 Matching far-field and near-field:

Consider an Oseen far-field matched asymptotically to an Euler near field such that the uniform flow field is in the x_1 direction, for the cartesian coordinate system x_1. The Eulerlets are obtained from collapsing the corresponding Oseenlets onto a wake line by suppressing wake diffusion. So, a far-field Oseenlet tends to the equivalent Eulerlet in the near field limit. For example, In the above application, for flow past a circular cylinder, the drag originates from an Euler wake that produces a momentum deficit. Then in the far-field wake diffuses and in the near field diffused wake suppressed because of the viscous diffusion term is negligible in the Navier-stokes equation to give Euler equations, which model the Euler wake. Then in the far-field viscous diffusion term is no longer negligible giving the Oseen equations which model the Oseen wake. On the commonly shared matching boundary,

Oseen field matches the Euler field for high Reynolds number, so $u_i^E = u_i^O$. This means matching also requires $w_{i,1}^E = 0$. So the Euler wake has an unchanging cross-sectional profile in the plane of constant x_1. This then gives the Euler velocity representation in the matching region the same as the Oseen velocity representation which is

$$u_m = \int_{C_B} \left[\frac{d}{dx_1}\left(u_i(y)u_i^{(j)}(z) \right) - \frac{d^2\phi(y)}{dx_1^{(j)}(z)dx_i^{(j)}(z)} u_1^{(j)}(z) + \right.$$

$$\left. \frac{d^2\phi_k^{(j)}(z)}{dx_1^{(j)}(z)dx_i^{(j)}(z)} u_i(y) \right] dl_y \qquad (15b)$$

It is noted that a consequence of the matching is that equation (15b) is linear rather than non-linear. Figure 3.12 gives an understanding of matching near field and far-field.
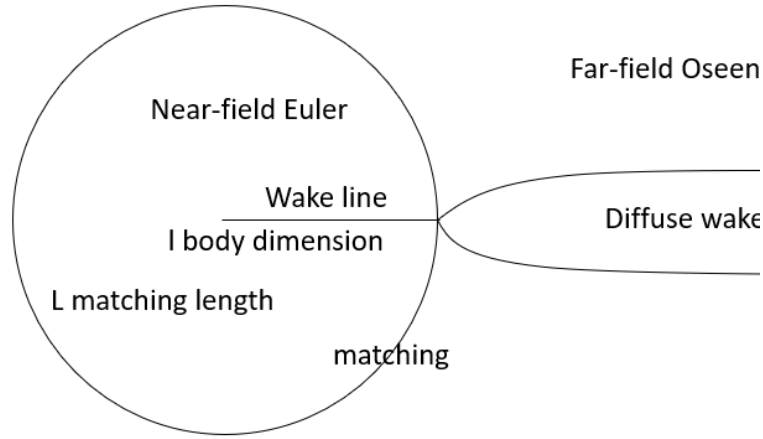
Figure 3.12 Matching between near and far-field

3.10.3 Total velocity field

Now we have to calculate the total velocity and it is illustrated in figure 3.13. The total velocity field is defined as follows.

$$u_i^+ = \delta_{i1} + \frac{\partial \phi}{\partial x_i} + w_i$$

$$u_i^+ = \delta_{i1} + \frac{\partial \phi}{\partial x_i} - H(x_1)D(x_2)\delta_{i1}$$

$$u_i^+ n_i = \delta_{i1}n_i + \frac{\partial \phi}{\partial x_i}n_i - H(x_1)D(x_2)\delta_{i1}n_i$$

$$\therefore \text{ But } \delta_{i1}n_i = \delta_{11}n_1 + \delta_{21}n_2 = n_1$$

$$u_i^+ n_i = n_1 + \frac{\partial \phi}{\partial x_i}n_i - H(x_1)D(x_2)n_1$$

53

The slip boundary condition is $u_i^+ n_i = 0$ on r =1. So, $n_1 + \frac{\partial \phi}{\partial x_i} n_i - H(x_1)D(x_2)n_1 = 0$ here we have to discuss two different cases. One of them is $x_1 < 0$ and $x_1 > 0$.

When $x_1 < 0$, $H(x_1) = 0$

$$n_1 + \frac{\partial \phi}{\partial x_i} n_i = 0 \text{ on } r = 1 \ x_1 < 0 \text{ and } \frac{\pi}{2} < \theta < \frac{3\pi}{2}$$
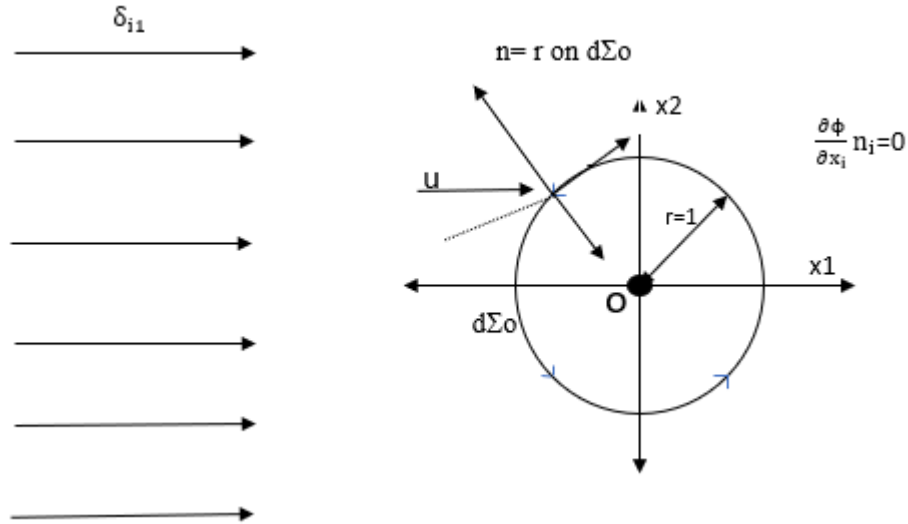
Figure 3.13 Total velocity field

When $x_1 > 0$, $H(x_1) = 1$

$$n_1 + \frac{\partial \phi}{\partial x_i} n_i - D(x_2)n_1 = 0 \text{ on } r = 1 \ x_1 > 0 \text{ and } \frac{3\pi}{2} < \theta < 2\pi$$

To make it simpler we can represent ϕ in polar coordinates and $n_1 = \cos \theta \ n_2 = \sin \theta$.

$$\frac{\partial \phi}{\partial x_i} n_i = \frac{\partial \phi}{\partial x_1} n_1 + \frac{\partial \phi}{\partial x_2} n_2 = n. \nabla \phi \equiv r. \nabla \phi = \frac{\partial \phi}{\partial r}$$

And the velocity equations are

$$\boxed{\begin{aligned} \cos \theta + \frac{\partial \phi}{\partial r} &= 0 \\ \cos \theta + \frac{\partial \phi}{\partial r} - D(x_2) \cos \theta &= 0 \end{aligned}}$$

We know what is ϕ

$$\phi = \frac{D}{2\pi} \ln r + \sum_{n=1}^{\infty} a_n \frac{\cos n\theta}{r^n}$$

54

$$\frac{\partial \phi}{\partial r} = \frac{D}{2\pi r} + \sum_{n=1}^{\infty} a_n \cos n\theta \frac{\partial r^{-n}}{\partial r}$$

$$\frac{\partial \phi}{\partial r} = \frac{D}{2\pi r} + \sum_{n=1}^{\infty} a_n \cos n\theta \, (-n) r^{-(n+1)}$$

$$\frac{\partial \phi}{\partial r} = \frac{D}{2\pi r} - \sum_{n=1}^{\infty} a_n \, n\cos n\theta \, r^{-(n+1)}$$

The boundary of the circle cylinder r=1 and

$$\frac{\partial \phi}{\partial r} = \frac{D}{2\pi} - \sum_{n=1}^{\infty} a_n \, n\cos n\theta$$

And the above equations will be

$$\cos\theta + \frac{D}{2\pi} - \sum_{n=1}^{\infty} a_n \, n\cos n\theta = 0$$

$$\cos\theta + \frac{D}{2\pi} - \sum_{n=1}^{\infty} a_n \, n\cos n\theta - D(x_2)\cos\theta = 0$$

The above two equations are general and we can use for different types of distributions like constant and cosine or the combination of the two. However, we are going to apply Fourier series analysis to the above equations to find out the coefficients a_1 and a_n. To start with multiply both sides with $\cos m\theta \, d\theta$ and the integral limit goes from 0 to π and the equation is

$$\int_0^\pi \cos m\theta \left(\cos\theta + \frac{D}{2\pi} - \sum_{n=1}^{\infty} a_n \, n\cos n\theta \right) d\theta - \int_0^{\frac{\pi}{2}} \cos m\theta D(x_2) \cos\theta \, d\theta = 0$$

Some of the Fourier results we are going to use in this report for below equation are

$$\int_0^\pi \cos n\theta \, \cos m\theta \, d\theta = \frac{1}{2} \int_0^\pi (\cos(m+n)\theta + \cos(m-n)\theta) d\theta$$

If, $m \neq \pm n$	0
$m = \pm n = 0$	π
$m = \pm n \neq 0$	$\dfrac{\pi}{2}$

Now we will discuss about different cases for 'm' as a variable with a radius of the circular cylinder is 1.

$$\int_0^\pi \cos m\theta \left(\cos\theta + \frac{D}{2\pi} - \right) d\theta - \int_0^{\frac{\pi}{2}} \cos m\theta D(x_2) \cos\theta \, d\theta = 0$$

$$\int_0^\pi \cos m\theta \cos\theta d\theta$$

$$+ \int_0^\pi \frac{D}{2\pi} \cos m\theta \, d\theta - \int_0^\pi \sum_{n=1}^\infty a_n \, n\cos n\theta \cos m\theta d\theta - \int_0^{\frac{\pi}{2}} \cos m\theta D(x_2) \cos\theta d\theta = 0.$$

Case :1

The radius of the circular cylinder r=1, m=0

$$\int_0^\pi \cos\theta d\theta + \int_0^\pi \frac{D}{2\pi} d\theta - \int_0^\pi \sum_{n=1}^\infty a_n \, n\cos n\theta \, d\theta - \int_0^{\frac{\pi}{2}} D(x_2) \cos\theta d\theta = 0$$

$$0 + \frac{D}{2} - 0 - \int_0^{\frac{\pi}{2}} D(x_2) \cos\theta d\theta = 0$$

$$\frac{D}{2} = \int_0^{\frac{\pi}{2}} D(x_2) \cos\theta d\theta$$
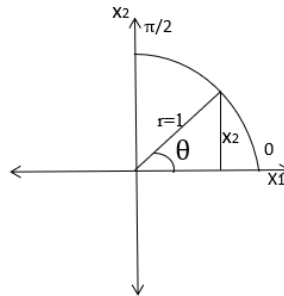
Figure 3.14 Limit change for cosine function from degrees to radians

From the figure $\sin\theta = x_2, \cos\theta \dfrac{d\theta}{dx_2} = 1$

$$\frac{D}{2} = \int_0^1 D(x_2) \, dx_2$$

$$D = \int_{-1}^1 D(x_2) \, dx_2 \tag{16}$$

56

Case :2

m=1, r=1

$$\int_0^\pi \cos m\theta \cos\theta d\theta$$

$$+ \int_0^\pi \frac{D}{2\pi}\cos m\theta \, d\theta - \int_0^\pi \sum_{n=1}^\infty a_n \, n\cos n\theta \cos m\theta d\theta - \int_0^{\frac{\pi}{2}}\cos m\theta D(x_2)\cos\theta d\theta = 0$$

$$\int_0^\pi \cos\theta \cos\theta d\theta$$

$$+ \int_0^\pi \frac{D}{2\pi}\cos\theta \, d\theta - \int_0^\pi \sum_{n=1}^\infty a_n \, n\cos n\theta \cos\theta d\theta - \int_0^{\frac{\pi}{2}}\cos\theta D(x_2)\cos\theta d\theta = 0$$

Use Fourier results and substitute in the above equation. To find the value of a_1 and we will take n=1

$$\frac{\pi}{2} + 0 - a_1\frac{\pi}{2} - \int_0^1 \cos m\theta \, D(x_2)dx_2$$

$$a_1 = 1 - \frac{2}{\pi}\int_0^1 \cos\theta \, D(x_2)dx_2 \tag{17}$$

Case :3

m ≥ 2, r=1

$$\int_0^\pi \cos m\theta \cos\theta d\theta$$

$$+ \int_0^\pi \frac{D}{2\pi}\cos m\theta \, d\theta - \int_0^\pi \sum_{n=1}^\infty a_n \, n\cos n\theta \cos m\theta d\theta - \int_0^{\frac{\pi}{2}}\cos m\theta D(x_2)\cos\theta d\theta = 0$$

$$0 + 0 - ma_m\frac{\pi}{2} - \int_0^1 \cos m\theta D(x_2)dx_2 = 0$$

$$a_m = -\frac{2}{\pi m}\int_0^1 \cos m\theta D(x_2)dx_2 \tag{18}$$

So far, we were discussed about general distribution however, we used constant and cosine distribution in the numerical modelling to match with experimental results. In the above

equations $D(x_2)$ is defined as drag per unit length and it defines the kind of distribution we are looking at as well.

For constant distribution

$$D(x_2) = D/2 \tag{19}$$

For cosine distribution

$$D(x_2) = D/2 + D/2\cos(\pi x_2) \tag{20}$$

The second term in the cosine distribution is represented by an expression of Bessel functions. If we set to zero, we will get constant distribution.

3.10.4 Cosine distribution

As we mentioned, cosine distribution is

$$\begin{cases} D(x_2) = D/2 + D/2\cos(\pi x_2) & |x_2| \leq 1 \\ \qquad\qquad = 0 & \text{Otherwise} \end{cases}$$

Drag

$$D = \oint_{\partial\Sigma} w_i n_1 \, dl$$

$$\text{Drag} = \oint_{\partial\Sigma} [-H(x_1)D(x_2)]n_1 \, dl == \oint_{\partial\Sigma} [-D(x_2)]n_1 \, dl$$

$$\text{Drag} = \oint_{\partial\Sigma} [-D(x_2)] \, d\Sigma = \int_{-1}^{1} D/2(1 + \cos(\pi x_2))dx_2$$

$$\text{Drag} = D$$

From the general equations

$$\cos\theta + \frac{D}{2\pi} - \sum_{n=1}^{\infty} a_n \, n\cos n\theta = 0 \text{ for } x_1 < 0$$

$$\cos\theta + \frac{D}{2\pi} - \sum_{n=1}^{\infty} a_n \, n\cos n\theta - D(x_2)\cos\theta = 0 \text{ for } x_1 > 0$$

But from Abramowitz & Stegun the following evidence used in writing different solutions for the above equations. Abramowitz and Stegun chapter number 9.1.42 and page numbers are 72,361.

$$\cos(\pi \sin \theta) \cos \theta = \sum_{n=0}^{\infty} \frac{2(2n+1)}{\pi} J_{2n+1}(\pi) \cos(2n+1)\theta$$

And the above equation will be

$$\cos \theta + \frac{D}{2\pi} - \sum_{n=1}^{\infty} a_n \, n\cos n\theta - \frac{D}{\pi} \sum_{n=0}^{\infty} (2n+1) J_{2n+1}(\pi) \cos(2n+1)\theta - \frac{D}{2} \cos \theta = 0$$

And the coefficients will be calculated by integrating with multiply both sides with $\cos m\theta \; d\theta$ and the integral limit goes from 0 to π and the equation is

$$\int_0^{\pi} \cos m\theta \left(\cos \theta + \frac{D}{2\pi} - \sum_{n=1}^{\infty} a_n \, n\cos n\theta \right) d\theta$$

$$- \int_0^{\frac{\pi}{2}} \cos m\theta \left(\frac{D}{\pi} \sum_{n=0}^{\infty} (2n+1) J_{2n+1}(\pi) \cos(2n+1)\theta - \frac{D}{2} \cos \theta \right) = 0$$

$$\int_0^{\pi} \cos m\theta \cos \theta \, d\theta + \int_0^{\pi} \frac{D}{2\pi} \cos m\theta \, d\theta - \int_0^{\pi} \sum_{n=1}^{\infty} a_n \, n\cos n\theta \cos m\theta \, d\theta$$

$$- \int_0^{\frac{\pi}{2}} \cos m\theta \left(\frac{D}{\pi} \sum_{n=0}^{\infty} (2n+1) J_{2n+1}(\pi) \cos(2n+1)\theta - \frac{D}{2} \cos \theta \right) d\theta = 0$$

We can use already defined Fourier coefficients for the first three terms in the equation but for the last term we need to write different Fourier solutions again, and the equation is

$$\int_0^{\frac{\pi}{2}} \cos m\theta \cos(2n+1)\theta d\theta = \frac{1}{2} \int_0^{\frac{\pi}{2}} (\cos(2n+1+m)\theta + \cos(2n+1-m)\theta) \, d\theta$$

And the solutions are

m odd, $\quad m \neq \pm(2n+1)$	0
m odd, $\quad m = \pm(2n+1)$	$\dfrac{\pi}{4}$
m even	$\dfrac{(-1)^{\frac{n+m}{2}}(2n+1)}{(2n+1)^2 - m^2}$

Now we can discuss different cases for m and n to find out the coefficients.

Case :1

$$\int_0^\pi \cos m\theta \cos \theta \, d\theta + \int_0^\pi \frac{D}{2\pi} \cos m\theta \, d\theta - \int_0^\pi \sum_{n=1}^\infty a_n \, n\cos n\theta \cos m\theta \, d\theta$$

$$- \int_0^{\frac{\pi}{2}} \cos m\theta \left(\frac{D}{\pi} \sum_{n=0}^\infty (2n+1)J_{2n+1}(\pi) \cos(2n+1)\theta - \frac{D}{2}\cos\theta \right) d\theta = 0$$

When m=0:

$$0 + \frac{D}{2\pi}\pi - 0 - \frac{D}{2} - \frac{D}{\pi}\left(\sum_{n=0}^\infty (-1)^n J_{2n+1}(\pi) \right) = 0$$

Which is true since

$$\sin z \;=\; 2\sum_{n=0}^\infty \left((-1)^n J_{2n+1}(z) \right) \;=\; 2J_1(z) - 2J_3(z) + 2J_5(z) + \ldots\ldots..$$

Evidence is taken from A&S 9.1.48 page 361

$$\text{So,} \frac{D}{\pi}\left(\sum_{n=0}^\infty (-1)^n J_{2n+1}(\pi) \right) = \frac{D}{2\pi}\sin\pi = 0$$

Case :2

$$\int_0^\pi \cos m\theta \cos \theta \, d\theta + \int_0^\pi \frac{D}{2\pi} \cos m\theta \, d\theta - \int_0^\pi \sum_{n=1}^\infty a_n \, n\cos n\theta \cos m\theta \, d\theta$$

$$- \int_0^{\frac{\pi}{2}} \cos m\theta \left(\frac{D}{\pi} \sum_{n=0}^\infty (2n+1)J_{2n+1}(\pi) \cos(2n+1)\theta - \frac{D}{2}\cos\theta \right) d\theta = 0$$

m=1 and n=0(used in wake term only)

$$\frac{\pi}{2} + 0 - \frac{\pi}{2}a_1 - \frac{D}{2}\frac{\pi}{4} - \frac{D}{\pi}\frac{\pi}{4}J_1(\pi) = 0$$

$$\boxed{a_1 = 1 - \frac{D}{4} - \frac{D}{2\pi}J_1(\pi)} \qquad (21)$$

Case :3

$$\int_0^\pi \cos m\theta \cos \theta \, d\theta + \int_0^\pi \frac{D}{2\pi} \cos m\theta \, d\theta - \int_0^\pi \sum_{n=1}^\infty a_n \, n\cos n\theta \cos m\theta \, d\theta$$

$$- \int_0^{\frac{\pi}{2}} \cos m\theta \left(\frac{D}{\pi} \sum_{n=0}^\infty (2n+1)J_{2n+1}(\pi) \cos(2n+1)\theta - \frac{D}{2}\cos\theta \right) d\theta = 0$$

m ≥ 2 even

$$0 + 0 - \frac{\pi}{2}ma_m - \frac{D}{\pi}\sum_{n=0}^{\infty}(2n+1)J_{2n+1}(\pi)\left(\frac{(-1)^n(2n+1)}{(2n+1)^2 - m^2}\right) - \frac{D}{2}*0 = 0$$

$$0 + 0 - \frac{\pi}{2}ma_m - \frac{D}{\pi}\sum_{n=0}^{\infty}(2n+1)J_{2n+1}(\pi)\left(\frac{(-1)^n(2n+1)}{(2n+1)^2 - m^2}\right) - \frac{D}{2}*\frac{(-1)^{\frac{m}{2}}}{1^2 - m^2} = 0$$

$$-\frac{\pi}{2}ma_m = \frac{D}{\pi}\sum_{n=0}^{\infty}J_{2n+1}(\pi)\left(\frac{(-1)^{n+\frac{m}{2}}}{1 - \left(\frac{m}{2n+1}\right)^2}\right) - \frac{D}{2}*\frac{(-1)^{\frac{m}{2}}}{1^2 - m^2}$$

$$a_m = -\frac{2D}{m\pi^2}\sum_{n=0}^{\infty}J_{2n+1}(\pi)\left(\frac{(-1)^{n+\frac{m}{2}}}{1 - \left(\frac{m}{2n+1}\right)^2}\right) - \frac{D}{m\pi}*\frac{(-1)^{\frac{m}{2}}}{1^2 - m^2} \qquad (22)$$

We can use, $\quad J_n(z) = \left(\frac{1}{2}z\right)^n\sum_{k=0}^{\infty}\left(\frac{-z^2}{4}\right)^k\frac{1}{k!\,\Gamma(n+k+1)}$ and $\Gamma(n+k+1)$

$= (n+k)!$ from A&S 6.16.6& 9.1.10

Case :4

$$\int_0^{\pi}\cos m\theta\cos\theta\,d\theta + \int_0^{\pi}\frac{D}{2\pi}\cos m\theta\,d\theta - \int_0^{\pi}\sum_{n=1}^{\infty}a_n\,n\cos n\theta\cos m\theta\,d\theta$$

$$-\int_0^{\frac{\pi}{2}}\cos m\theta\left(\frac{D}{\pi}\sum_{n=0}^{\infty}(2n+1)J_{2n+1}(\pi)\cos(2n+1)\theta - \frac{D}{2}\cos\theta\right)d\theta = 0$$

m ≥ 3 odd

$$0 + 0 - \frac{\pi}{2}ma_m - 0 - \frac{D}{\pi}\frac{\pi}{4}mJ_m(\pi) = 0$$

$$-\frac{\pi}{2}ma_m = \frac{D}{4}mJ_m(\pi)$$

$$a_m = -\frac{D}{2\pi}mJ_m(\pi) \qquad (23)$$

3.10.5 Constant Distribution

From general distribution, we can take a_1 and a_n

$$a_1 = 1 - \frac{2}{\pi}\int_0^1 \cos\theta\, D(x_2)dx_2$$

for constant distribution, $D(x_2) = \frac{D}{2}$ howver, $\int_0^1 f(x)dx_2 = \int_0^{\frac{\pi}{2}} f(x)\cos\theta\, d\theta$

$$a_1 = 1 - \frac{2}{\pi}\int_0^{\frac{\pi}{2}} \cos\theta\cos\theta\, d\theta = 1 - \frac{D}{4}$$

$$a_1 = 1 - \frac{D}{4} \tag{24}$$

$$a_m = -\frac{2}{\pi m}\int_0^1 \cos m\theta\, D(x_2)dx_2$$

$$a_m = -\frac{D}{\pi m}\int_0^{\frac{\pi}{2}} \cos m\theta\cos\theta\, d\theta$$

$$a_m = -\frac{D}{\pi m}\int_0^{\frac{\pi}{2}} \frac{1}{2}(\cos(m+1)\theta + \cos(m-1)\theta)\, d\theta$$

$$a_m = -\frac{D}{2\pi m}\left[\frac{1}{m+1}\cos\left(\frac{m\pi}{2}\right) - \frac{1}{m-1}\cos\left(\frac{m\pi}{2}\right)\right]$$

$$a_m = -\frac{D}{2\pi m}\cos\left(\frac{m\pi}{2}\right)\left(\frac{-2}{m^2-1}\right)$$

$$a_m = -\frac{D}{\pi m(m^2-1)}\cos\left(\frac{m\pi}{2}\right) \tag{25}$$

$$a_m = \begin{cases} 0 & \text{when m is odd} \\ \dfrac{(-1)^{m/2}}{\pi m(m^2-1)} & \text{m is even} \end{cases}$$

4 Numerical modelling and application of Eulerlets

4.1 Overview

This chapter explains about the numerical modelling of the governing equations defined in the previous chapter, boundary conditions, pressure distributions, surface pressure over the circular cylinder, velocity profiles for different Reynolds numbers and comparison with existing results.

4.2 Numerical modelling

As discussed in section 2.9, numerical modelling techniques are helpful to understand the flow characteristics for a variety of models under different flow conditions with reduced cost compared to the experiments in the wind tunnel. Numerical modelling of flow around a circular cylinder still remains a challenging problem in fluid mechanics. It has enriched the physics, and real-life applications have attracted the attention of engineers and scientists for over a century leading to many theoretical and experimental investigations. In this present problem, a uniform steady flow past a fixed body such that in the far-field the Oseen flow approximation holds is considered. The near-field Euler velocity matches to the far-field Oseen velocity asymptotically as the Reynolds number goes to infinity. The matching enforces a near-field with zero vorticity giving the Bernoulli equation for pressure, and a velocity represented by boundary integral distribution of Eulerlets whose strength gives the Euler force over the body boundary. In this representation, a new drag Eulerlet is used that includes a Dirac delta function with zero derivative and describes a wake such that layers of fluid slip past each other. Consequently, D'Alembert's paradox is resolved and the Kutta condition is satisfied. This formulation is tested on uniform flow past a circular cylinder for steady flow up to a Reynolds number 40, mean-steady subcritical laminar flow and turbulent flow. The drag, eddies, far-field wake and pressure drop are all captured and compare favourably with experiment. Fortran programming language is used for the numerical modelling (see Appendix D). Different factors affect the accuracy of the numerical model such as: defining a mathematical model for the behaviour of the physical system, implementing the boundary conditions in the near-field and far-field, matching the different flow regions and rate of convergence for the numerical iterations for high Reynolds numbers (Bengt, 1980). The above factors are discussed in the following sections.

4.3 Separated flow past a circular cylinder

The theoretical results given in section (3) are recapped, and ready for implementation into a numerical method. Consider modelling separated rather than attached flow past a circular cylinder of normalized radius 1 centred at the origin represented by a distribution of Eulerlets producing a wake distribution.

4.3.1 Potential flow

The potential is given in terms of the potential parts in the Eulerlets which can then be represented by a harmonic expansion originating from the origin and, from equation (23)

$$\phi = \frac{D}{2\pi} \ln r + \sum_{n=1}^{\infty} a_n \frac{\cos n\theta}{r^n}$$

for some unknown coefficients a_n, from either use of the Taylor series expansion and D is the drag and outflow strength.

4.3.2 Euler slip wake

Euler slip wake is explained in section (3.8.1). The wake velocity is given in terms of a distribution of the wake velocity of the drag Eulerlets over the cylinder boundary. Each wake Eulerlet singular along the infinite half-line aligned to the x_1-axis. So, this can be represented as originating from a distribution along the line $-1 \leq x_2 \leq 1$, $x_1 = 0$ such that, from equation (24)

$$w_i = - \int_{-1}^{1} d(x_2) H(x_1) \delta(x_1 - x_2) \delta_{i1} dx_2$$

$$= -H(x_1) d(x_2) \delta_{i1} dx_2$$

where $d(x_2)$ is the drag per unit length in the x_2 direction and dx_2 is a differential element of length x_2.

Checks:

$$\text{Outflow} = \int_{d\Sigma_0} \phi_{,i} n_i dd\Sigma = \int_0^{2\pi} \frac{D}{2\pi} (\ln r)_{,i} n_i r \, d\theta = \int_0^{2\pi} \frac{D}{2\pi} \frac{1}{r} \frac{x_i}{r} \frac{x_i}{r} r d\theta = D$$

$$\text{Inflow} = \int_{d\Sigma_0} w_i n_i dd\Sigma = \int_{x_1 > 0} -d(x_2) \delta_{i1} n_i dd\Sigma = \int -d(x_2) dx_2 = -D$$

$$\text{Drag} = -\int_{d\Sigma_0} w_i dd\Sigma = D$$

4.3.3 Euler drag profile

Consider two drag Eulerlet distributions to test against experimental results from equations (27) and (28). These are :

Constant distribution

$$d(x_2) = D/2,$$

and cosine distribution

$$d(x_2) = D/2 + D/2 \cos(\pi x_2)$$

for $|x_2| \geq 1$, and $d(x_2) = 0$ otherwise in both the cases. Then, the Euler drag is

$$\int_{-1}^{1} d(x_2)dx_2 = D.$$

4.3.4 Boundary conditions

Assuming a boundary layer of negligible thickness over the body, then the impermeability condition holds for the Euler velocity

$$u_i^+ n_i = 0 \text{ on } r = 1 \tag{26}$$

$$\left(\delta_{i1} + \frac{\partial\phi}{\partial x_i} - H(x_1)d(x_2)\delta_{i1}\right)n_i = 0 \text{ on } r = 1 \tag{27}$$

$$u_i^+ n_i = n_1 + \frac{\partial\phi}{\partial x_i}n_i - H(x_1)d(x_2)n_1 = 0 \text{ on } r = 1 \tag{28}$$

where u_i^+ is the total Euler velocity, as opposed to u_i which is the perturbed Euler velocity. So, the boundary condition is $n_1 + \frac{\partial\phi}{\partial x_i}n_i - H(x_1)d(x_2)n_1 = 0$ substituting in the potential expression in equation (23)

$$\frac{\partial\phi}{\partial x_i}n_i = \frac{\partial\phi}{\partial x_1}n_1 + \frac{\partial\phi}{\partial x_2}n_2 = \frac{\partial\phi}{\partial x_i}\frac{x_i}{r} = \frac{\partial\phi}{\partial r}$$

$$\phi = \frac{D}{2\pi}\ln r + \sum_{n=1}^{\infty} a_n \frac{\cos n\theta}{r^n}$$

$$\frac{\partial\phi}{\partial r} = \cos\theta + \frac{D}{2\pi} - \sum_{n=1}^{\infty} a_n n \cos n\theta = 0.$$

Consider separately the cases when $x_1 < 0$ and $x_1 > 0$.

When $x_1 < 0$, $H(x_1) = 0$

$$n_1 + \frac{\partial \phi}{\partial x_i} n_i = 0 \text{ on } r = 1 \ x_1 < 0 \text{ and } \frac{\pi}{2} < \theta < \frac{3\pi}{2}$$

$$n_1 + \frac{\partial \phi}{\partial r} = 0 \text{ on } r = 1 \ x_1 < 0 \text{ and } \frac{\pi}{2} < \theta < \frac{3\pi}{2}$$

Substituting in the expression for the potential then we will get

$$\cos \theta + \frac{D}{2\pi} - \sum_{n=1}^{\infty} a_n n \cos n\theta = 0 \text{ on } \ x_1 < 0 \text{ and } \frac{\pi}{2} < \theta < \frac{3\pi}{2}. \tag{29}$$

When $x_1 > 0$, $H(x_1) = 1$

$$n_1 + \frac{\partial \phi}{\partial x_i} n_i - D(x_2)n_1 = 0 \text{ on } r = 1 \ x_1 > 0 \text{ and } \frac{3\pi}{2} < \theta < 2\pi$$

$$n_1 + \frac{\partial \phi}{\partial r} - D(x_2)n_1 = 0 \text{ on } r = 1 \ x_1 > 0 \text{ and } \frac{3\pi}{2} < \theta < 2\pi$$

$$\cos \theta + \frac{D}{2\pi} - \sum_{n=1}^{\infty} a_n n \cos n\theta - D(x_2) \cos \theta = 0 \text{ on } \ x_1 > 0 \text{ and } \frac{3\pi}{2} < \theta < 2\pi. \tag{30}$$

$$\frac{\partial \phi}{\partial x_1} = \phi_{,1} = \frac{D}{2\pi}(\ln r)_{,1} + \sum_{n=1}^{\infty} a_n \left(\frac{\cos n\theta}{r^n} \right)_{,1}$$

$$\frac{\partial \phi}{\partial x_1} = \frac{D}{2\pi r} \cos \theta - \sum_{n=1}^{\infty} a_n \frac{n}{r^{n+1}} \cos(n+1)\theta$$

$$\frac{\partial \phi}{\partial x_2} = \phi_{,2} = \frac{D}{2\pi}(\ln r)_{,2} + \sum_{n=1}^{\infty} a_n \left(\frac{\cos n\theta}{r^n} \right)_{,2}$$

$$\frac{\partial \phi}{\partial x_2} = \frac{D}{2\pi r} \sin \theta - \sum_{n=1}^{\infty} \frac{n}{r^{n+1}} a_n \sin(n+1)\theta.$$

Where a comma denotes a differentiation. $D(x_2)$ is a wake inflow distribution and it can be cosine or constant distribution. The Coefficients a_n are now calculated by applying Fourier analysis integrating over the half-space $\int_0^{\pi} d\theta$. This gives from the section (3):

For Constant distribution	For Cosine distribution
$$a_1 = 1 - \frac{D}{4}$$	$$a_1 = 1 - \frac{D}{4} - \frac{D}{2\pi}J_1(\pi)$$
$$a_m = -\frac{D}{\pi m(m^2 - 1)}\cos\left(\frac{m\pi}{2}\right)$$	$$a_m = -\frac{2D}{m\pi^2}\sum_{n=0}^{\infty}J_{2n+1}(\pi)\left(\frac{(-1)^{n+\frac{m}{2}}}{1-\left(\frac{m}{2n+1}\right)^2}\right)$$ $$-\frac{D}{m\pi} * \frac{(-1)^{\frac{m}{2}}}{1^2 - m^2}$$
$$a_m = \begin{cases} 0 & \text{when m is odd} \\ \dfrac{(-1)^{m/2}}{\pi m(m^2 - 1)} & \text{m is even} \end{cases}$$	$$a_m = -\frac{D}{2\pi}mJ_m(\pi)$$

Table 4-1 Fourier coefficient for constant and cosine distribution.

4.4 Position and merging of near and far-fields

The asymptotic boundary between the near and far-fields is when $x_1 = O(Re)$ from chapter 3, where Re is the Reynolds number. Let L be the far-field length dimension, and l be the near-field length dimension. From the Oseenlets $e^{kx_1}K_0(kr) \approx e^{-\frac{kx_2^2}{2x_1}}$ in the far-field, where $k = \frac{\rho U}{2\mu}$ and K_0 is the modified Bessel function of order zero. So, the wake is exited when $\eta = \frac{kl^2}{2L} = \left(\frac{Re}{4}\right)\left(\frac{l}{L}\right) \to \infty$ which also, therefore, defines the boundary between the near and far-fields. For Reynolds number Re=26, 36 and 40, this occurs even close to the circular cylinder as the Reynolds number is so small the far-field length is not large. However, we must also ensure that in the far-field, the Oseen velocity is a small perturbation of the uniform flow field. So, the choice of b from figure 4.1 must be such that where the Oseen flow approximation holds in the downstream wake, then it is described by Oseen rather than Euler flow. Conversely, where the Oseen flow approximation breaks down in the downstream wake then we move towards an Euler rather than Oseen flow description. This means positioning b at the point just where the Oseen approximation starts to fail. By

inspection of the results in Figures 4.3 and 4.5 we see that this holds at radial distance r=b=4 for Re= 26 and r=b= 6 for Re = 40. We note that the Oseen far-field has the effect of diffusing the wake and consequently closing the eddies downstream: if instead only Euler flow is considered, then the eddies remain open to infinity. We also note that this is different from closed vortex wakes, such as arising from desingularising the Foppl point-vortex system (Elcrat et al., 2000), in that in the former there is a slow-flow eddy with zero circulation at the centre caused by outflow, whereas in the latter there is a singular velocity point-vortex with constant circulation at the centre. We can see from figures 4.3 and 4.5, we have modelling nearly stagnant rotational eddies in the wake that correspond to expected experimental results, as opposed to unrealistic high-rotation constant circulation point vortices in the wake given by the mappings in the Foppl point-vortex system.

The Oseen wake diffusion originates from the modified Bessel function in two-dimensional flow, and the eddy length is a distance of order Re downstream, as expected from experimental observation. To get a smooth transition between Euler and Oseen flow, a merging of the two flow fields is proposed between the radial distances r=a and r=b and represented in the following figure 4.1 and the figure gives an understanding of how the flow merges in the matching region even though it is not an actual representation of the flow domain. To understand the flow domain more clearly and precisely, we would need to calculate what is merging factor and at what distance behind the physical model merging takes place.
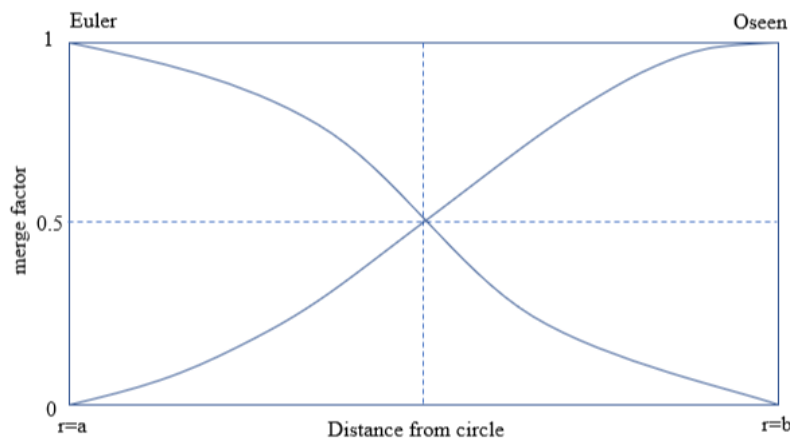
Figure 4.1 Near-field Euler and far-field Oseen flow merging

The discussion about radial distances to smoothen the transition between the two flows does not have an importance when it comes to the actual flow domain but, it is a rough understanding of merging of the near and far-field. As explained, r represents the radial

distance in the flow domain and a & b represents the near & far-field respectively. Merge factor and distances behind the physical model are the other two parameters explained in the thesis. The graph in the lower left-hand corner is reflected about the dotted line of symmetry to get the graphs in the other quadrants, and this graph itself has the quadratic form $y = \propto (r-a)^2$, and so $\propto = \frac{2}{(b-a)^2}$. in this merging region, the velocity is then given as

$$u_i^{merged} = (1-\alpha)u_i^{Euler} + \alpha u_i^{Oseen},$$

Where u_i^{Euler} and u_i^{Oseen} are the Euler and Oseen velocities respectively. We choose a=1 to get the greatest distance and therefore most gradual merging and smooth transition between the two flows. However, it is noted that changing the values of 'a 'does not significantly affect either the size or the position of the eddy in the wake or the wake structure and flow itself. So, the choice for 'a' is not particularly crucial to the outcome of the flow description.

4.5 Results

We consider two Reynolds number for the flow for which there are well-known results, Re=26 with wake distribution strength $\int_{-1}^{1} D(x_2)dx_2$ of 2.0, and Re=40 with wake distribution strength of 1.5. This produces the following flow patterns for Re=26 in figures 4.2 and 4.3. We note a good agreement with the image reproduced in the following figures with VanDyke album of fluid motion (Van Dyke and White, 1982). The separation point is closely matched, and the size and shape of the eddies are reproduced, although the experimental results in figure 4.4 suggest that the wake tail should be curtailed sooner. For these, the matching boundary is very close to the circular cylinder; the Oseen approximation holds immediately to the rear of the circulatory wake eddy. So, the Euler flow is phased out and the Oseen flow phased-in using a simple quadratic merging over the region $1 \leq r \leq 2.0$ for Re=26, and $1 \leq r \leq 5.0$ for Re=40 and this produces the following flow patterns as r is the length of the eddy in the figures 4.2 and 4.3. We note the size and shape of the eddies are reproduced, although the experimental results suggest that the wake tail should be curtailed sooner. Eddy position is too close to the centre line at Reynolds number 26 and wake strength 2.0. Also, this work can be cross verified with both numerical and experimental results, see, for example, Taneda carried out an investigation of the wake behind cylinders at low Reynolds numbers for 28.4 and 41(Taneda, 1956) and recently (Sen, Mittal and Biswas, 2009) investigated flow past a circular cylinder by using the stabilized finite-element method for Re=40.

4.5.1 Streamlines of the flow
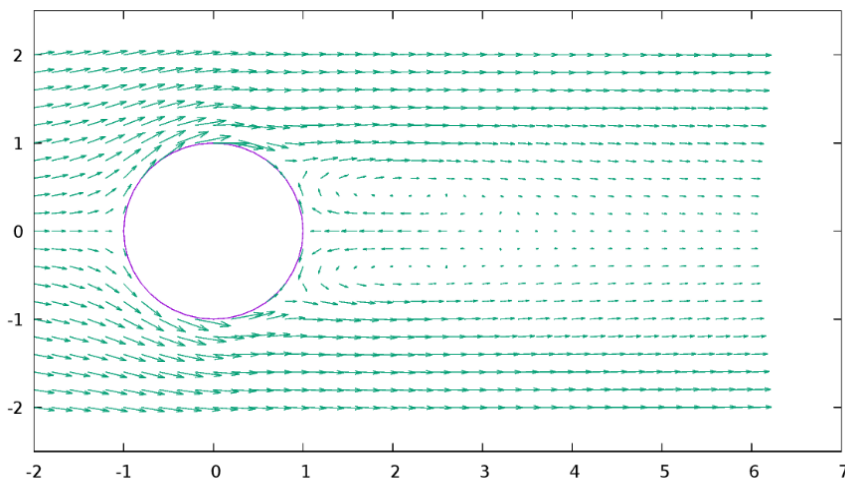
Figure 4.2 Velocity vector representation of Re=26 and wake distribution strength of 2.0
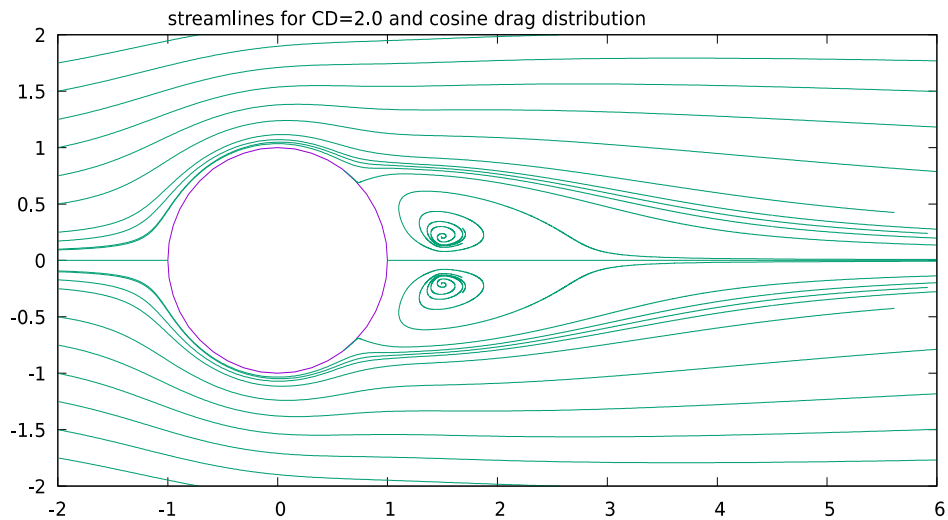
Figure 4.3 Streamlines for Re = 26 and wake distribution strength = 2.0
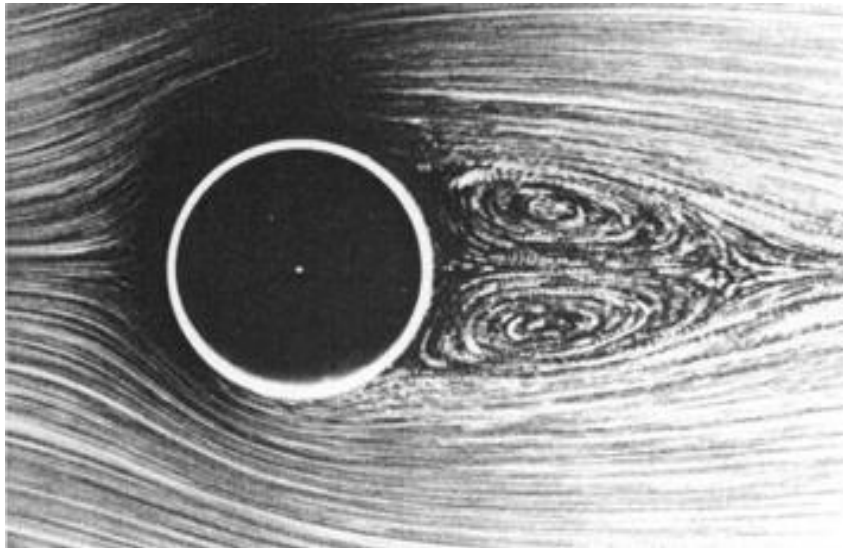
Figure 4.4 Van Dyke Album of flow pattern for Re=26

Similarly, there is a good agreement for Re=40 given in figure 4.6, compared with the image reproduced in figure 4.5 courtesy of Coutanceau Bouard (Coutanceau and Bouard, 1977). The eddy position is similar and the elongation of the eddies with higher Reynolds number is captured. However, the separation point hasn't moved as far upstream as expected and the eddies are more flattened than expected from figure 4.6. Eddy position close but separation point too low down and eddies are elongated. We note that the eddy position is similar and the elongation of the eddies with higher Reynolds number is captured. However, the separation point is lower down and eddies more elongated than expected from the

71

experiment. The following figures show the streamlines and cosine drag distribution graphs are in line with the experimental results as mentioned above.
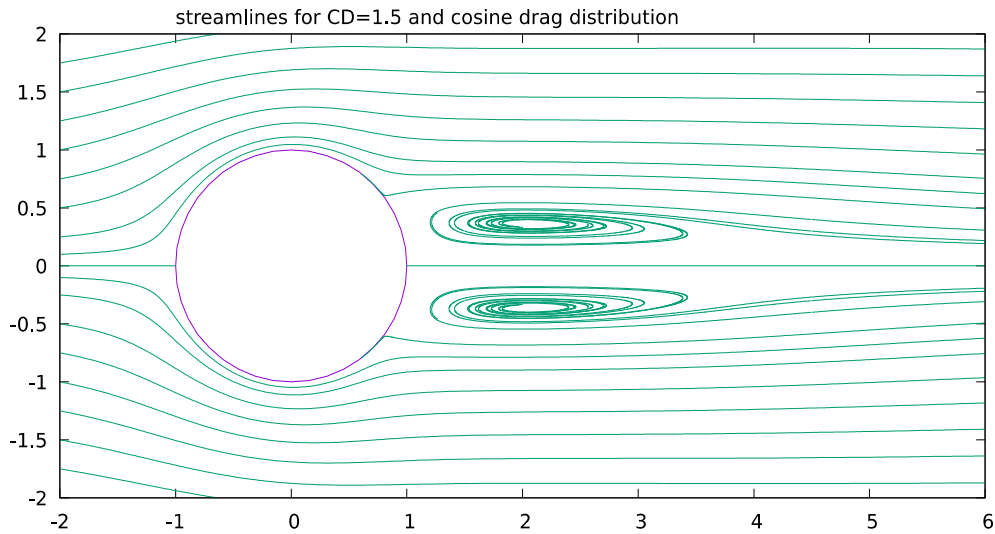
Figure 4.5 Streamlines for Re = 40 and wake distribution strength =1.5
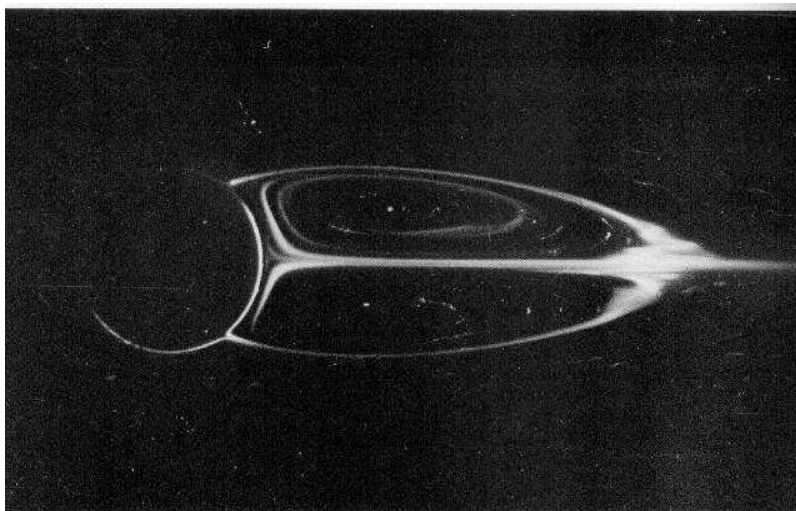
Figure 4.6 Image from Coutanceau Bouard Re=40

4.5.2 Far-field decay of the laminar flow

The below figure 4.7 shows experimental results for the far-field decay at Reynolds number Re= 36 from Kovasnzay (Kovasznay, L.S.G (Department of Aeronautics, 1949) and numerical results were captured at same distances from the back of the cylinder as shown in experiments. We note that the trend in diffusion and the general wake profile is captured. However, the rise at the lip of the wake and momentum deficit is only partially captured, see for example (Tordella and Belan, 2003) for wake profile at distance for x=20d.
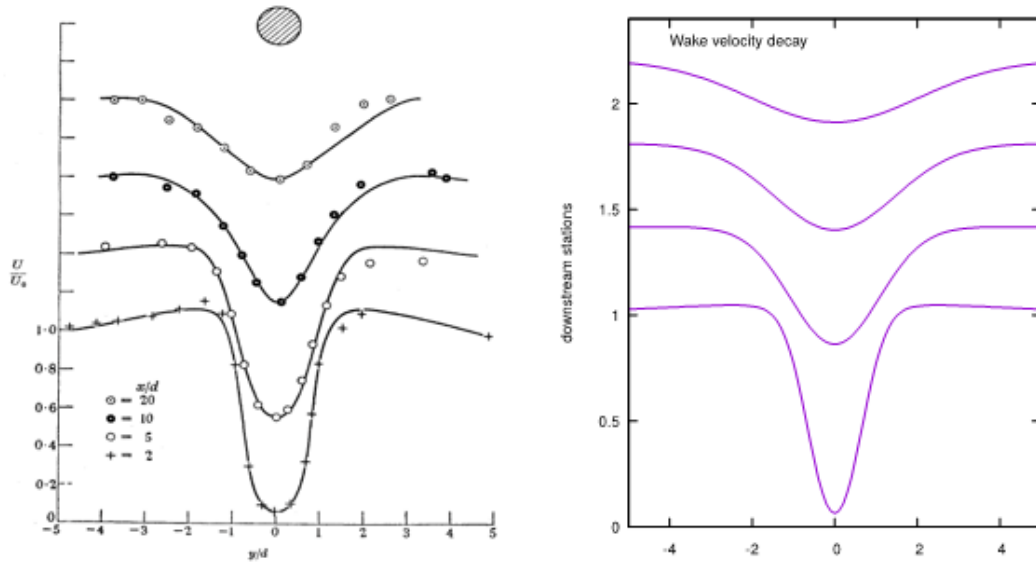
Figure 4.7 Far-field decay from Kovasznay Re=36 and Far-field decay Re=36

4.5.3 Pressure distribution around a circular cylinder

We define the pressure p as an integration over the cylinder starting from the forward stagnation point on the cylinder and then integrate around the circle circumference to the desired point. So, pressure can be defined as follows in terms of coeffect pressure, velocity and density.

$$C_p = \frac{p_{dim}}{\frac{1}{2}\rho u^2}; \ \ p = \frac{p_{dim}}{\rho u^2} \therefore p = \frac{C_p}{2}$$

From figure 4.8

$$x_1 = r\cos\theta, \ \ \ x_2 = r\sin\theta$$

$$r^2 = x^2_1 + x^2_2 = x_i x_j = x_j^2 = x_j x_j$$

$$r=1, \ dl = -rd\theta = -d\theta$$

Integrals are changed from l=0 to $\theta = \pi$ and l=l to $\theta=0$

$$\frac{dr}{dx_i} = \frac{x_j}{r}; \ \ \ \frac{dr}{dx_1} = \frac{x_1}{r} = \cos\theta; \ \ \frac{dr}{dx_2} = \frac{x_2}{r} = \sin\theta$$

Since we considered the radius of the cylinder is 1, $\frac{dx_1}{d\theta} = -\sin\theta \ \ ; \frac{dx_2}{d\theta} = \cos\theta$

p is an Euler pressure, u is Euler velocity, C_p is coefficient of pressure. Finding the pressure around a circular cylinder

$$p = p_o + \int_0^1 \frac{dp}{dl} dl$$

$$\frac{dp}{dl} = \frac{dp}{dx_i} \frac{dx_i}{dl} = \frac{dp}{dx_i} \left(\frac{dx_1}{dl} + \frac{dx_2}{dl} \right)$$

Substituting the $\frac{dp}{dl}$ in the above pressure around a circular cylinder equation
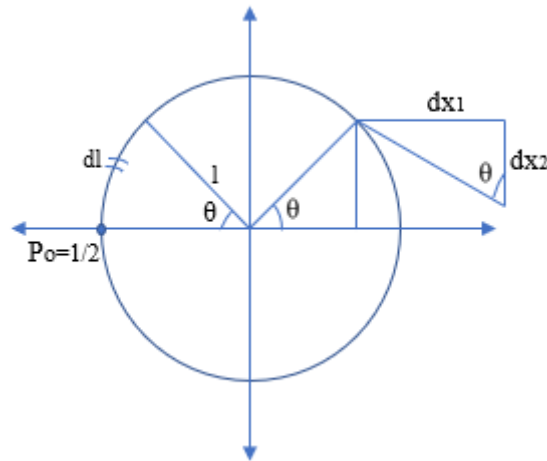
Figure 4.8 Pressure calculation along the circumference of the circular cylinder

$$p = \frac{1}{2} + \int_\pi^\theta \frac{dp}{dx_i} \left(\frac{dx_1}{dl} + \frac{dx_2}{dl} \right) dl$$

$$p = \frac{1}{2} + \int_\pi^\theta \frac{dp}{dx_i} \left(\frac{dx_1}{d\theta} + \frac{dx_2}{d\theta} \right) * -d\theta$$

$$p = \frac{1}{2} - \int_\pi^\theta \left(-\sin\theta \frac{dp}{dx_1} - \cos\theta \frac{dp}{dx_2} \right) * d\theta$$

$$p = \frac{1}{2} - \int_\pi^\theta \left(\sin\theta \frac{dp}{dx_1} - \cos\theta \frac{dp}{dx_2} \right) d\theta$$

$$p = \frac{1}{2} - \int_\pi^\theta \left(t_i \frac{dp}{dx_i} \right) d\theta = \frac{1}{2} - \int_\pi^\theta t_i \left(\frac{dp}{dx_i} \right) d\theta$$

Where t_i, is the clockwise tangent $(t_1, t_2) = (\sin\theta, -\cos\theta)$. Alternatively, the pressure can be determined directly by substituting the velocity $u_j^+ = \delta_{i1} + u_j$ into the Navier Stokes equations

$$u_j^+ u_{i,j}^+ = -p_{,i}^+ + (\frac{1}{Re}) u_{i,jj}^+$$

74

And integrating the pressure around the cylinder circle circumference given by arc length l starting at $\theta = \pi$ such that

$$p^+ = \frac{1}{2} + \int_0^l \frac{dp^+}{dl} dl = \frac{1}{2} - \int_\pi^\theta t_i p^+_{,i} d\theta$$

$$p^+ = \frac{1}{2} + \int_\pi^\theta t_i \left\{ u_j^+ u_{i,j}^+ - \left(\frac{1}{Re}\right) u_{i,jj}^+ \right\} d\theta \qquad (31)$$

Where t_i is the clockwise tangent $(t_1, t_2) = (\sin\theta, -\cos\theta)$. Sharp changes in the wake profile give a large diffusion viscous term of the Navier-Stokes equations. This is supposed to be zero in the Euler approximation. The viscous term in the above equation is negligible for the inviscid Euler flow approximation to hold. However, the Reynolds number of 40 or below is so low that this term is not negligible and so the pressure calculations are not accurate. These inaccuracies are reduced by considering much higher Reynolds number flow. This gives the following distribution of pressure over the cylinder, compared against the experimental results of Grove et al (Grove *et al.*, 1964). The display between the two pressure formulations indicates that the viscous term is not negligible, and so there is a significant limit to the accuracy we may expect, and the difference between the two gives an indication of the expected error in the approximation. It is seen that for the level of approximation indicated by this difference, then the pressure distribution is as close as we can expect to the experimental results at this Reynolds number, which is seen to have a significant error due to the size of the viscous term. However, it is noted that the flow physics, of pressure dropping off at the lee side rear of the cylinder, is captured by the theory.
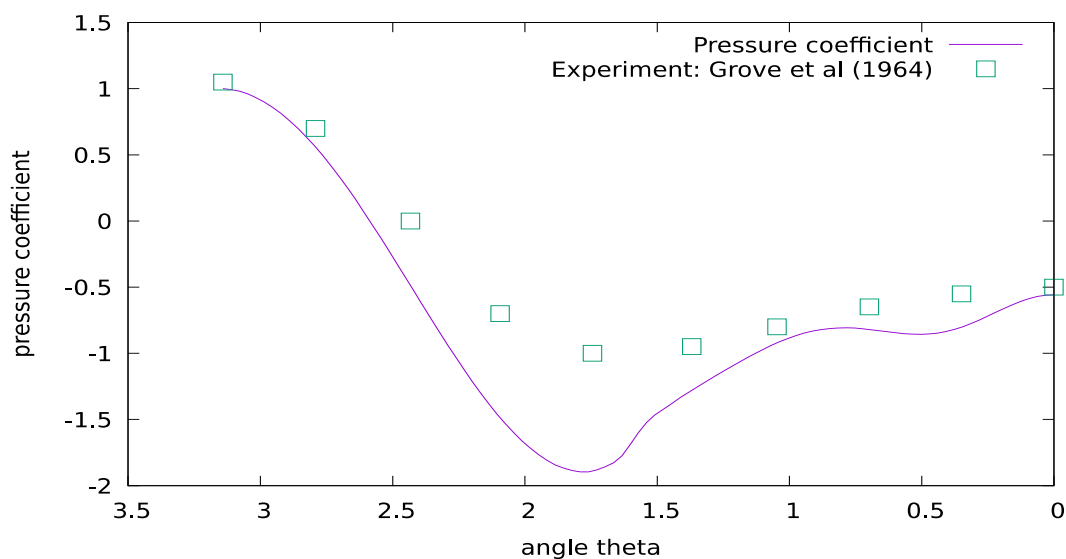
Figure 4.9 Pressure distribution over a circular cylinder at Re=40.

75

4.6 Subcritical laminar flow

Consider sub-critical laminar flow at a Reynolds number of Re=$1.1*10^4$. Although this flow is unsteady, let us further assume that the time-averaged mean flow can still be approximately modelled with the steady flow theory. A constant Eulerlet distribution is chosen, because the pressure in the wake is close to constant. Modelling the flow by a constant distribution of Eulerlets in the wake domain with a wake distribution strength of 2.4 gives a pressure drag coefficient determined from Euler pressure equation (40) as 1.02, and a streamline flow given by figure 4.10. (We note that there is a difference between the wake distribution strength and the pressure drag coefficient, because the pressure drag coefficient is determined from the pressure p^+, whereas the wake distribution is determined from p. It is the calculation from p^+ that gives the pressure drag calculated from the experiment, see the argument given in pressure distribution around a circular cylinder). This compares to the flow visualisation from the experiment for Reynolds number Re=$1.0*10^4$ given by figure 4.11. We see that the model has correctly predicted flow separation on the foreside of the cylinder, and a parabola-like separation streamline. This is in contrast to Gustafsson's Oseen model (Gustafsson and Protas, 2013) which gives flow separation on the lee side and a straight separation streamline.

Using Euler pressure equation (40), the corresponding pressure distribution can be determined and is given in figure 4.10 and compared against the experimental pressure distribution at Reynolds number Re =$1.1*10^4$ reproduced from Batchelor (Batchelor, 2012).
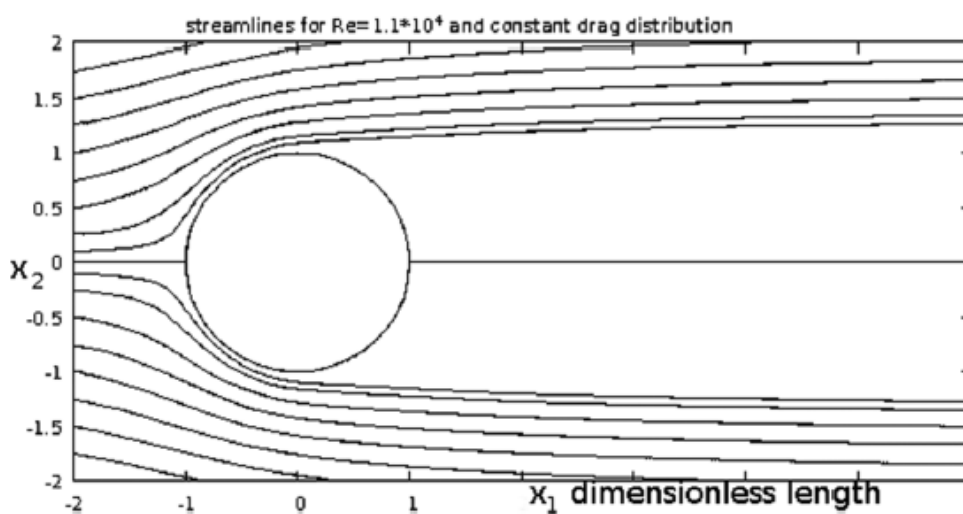
Figure 4.10 Streamlines for subcritical laminar flow
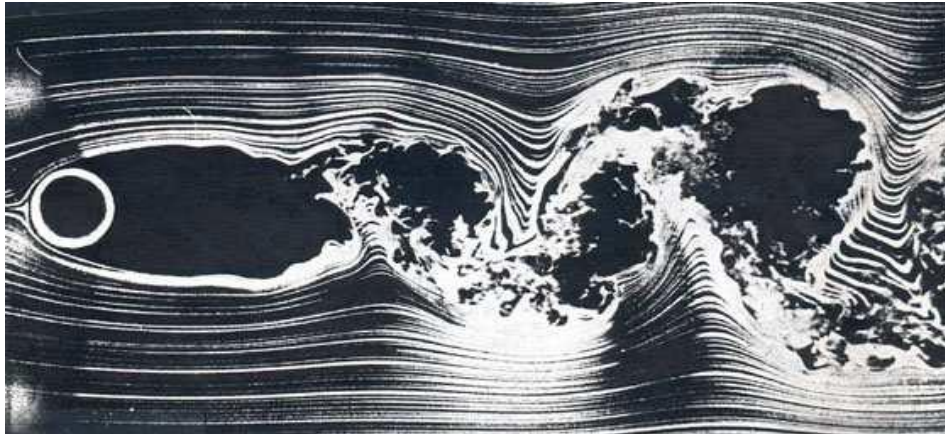
Figure 4.11 Streamlines for Re=1.0∗10^4, [Photograph courtesy Thomas Corke and Hasan Najib

(Illinois Institute of Technology, Chicago)]

It is noted that characteristic features of the physics of the flow are reproduced, such as reversal in the pressure gradient giving flow separation forward of the cylinder at an angle of around 70-80 degrees, and a negative flattened pressure profile in the wake of the cylinder. It is possible to fine-tune the Eulerlet distribution to match more closely the pressure given by the experiment. However, given the variance in the pressure from experiments around this Reynolds number, and also given that steady inviscid flow approximates sub-critical laminar flow, this was deemed not particularly worthwhile because an appropriate closeness between the theory and experiment has been met.
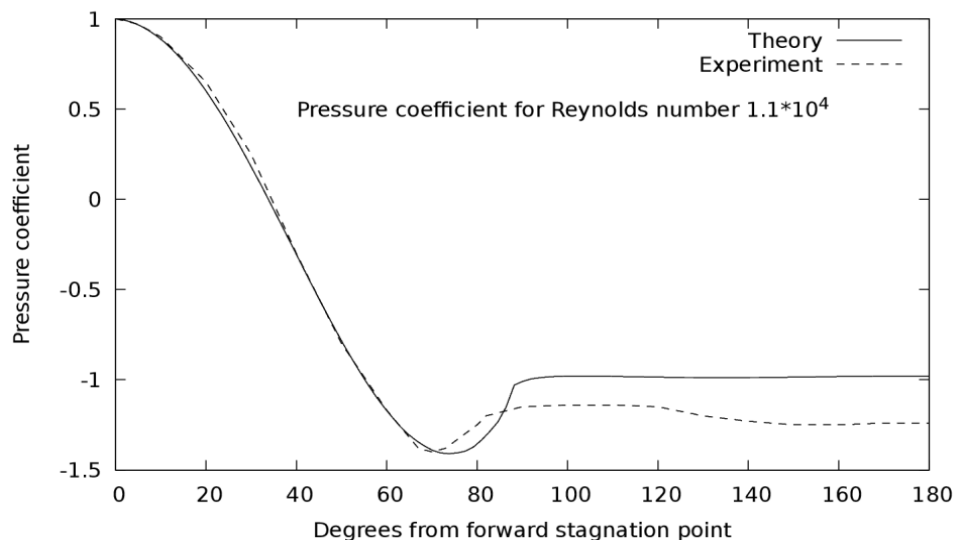
Figure 4.12 Pressure distribution for Re=1.0*10^4

4.7 Turbulent flow

Let us also assume that mean turbulent flow can also be approximately modelled with this steady flow theory. Again, a constant Eulerlet distribution is chosen because of knowledge that the pressure in the wake is close to constant. Modelling the flow by a constant distribution of Eulerlets in the wake domain but this time with the wake distribution strength of 1.5, gives a pressure drag coefficient determined from Euler pressure equation (40) as 0.95, and a streamline flow given by figure 4.13.
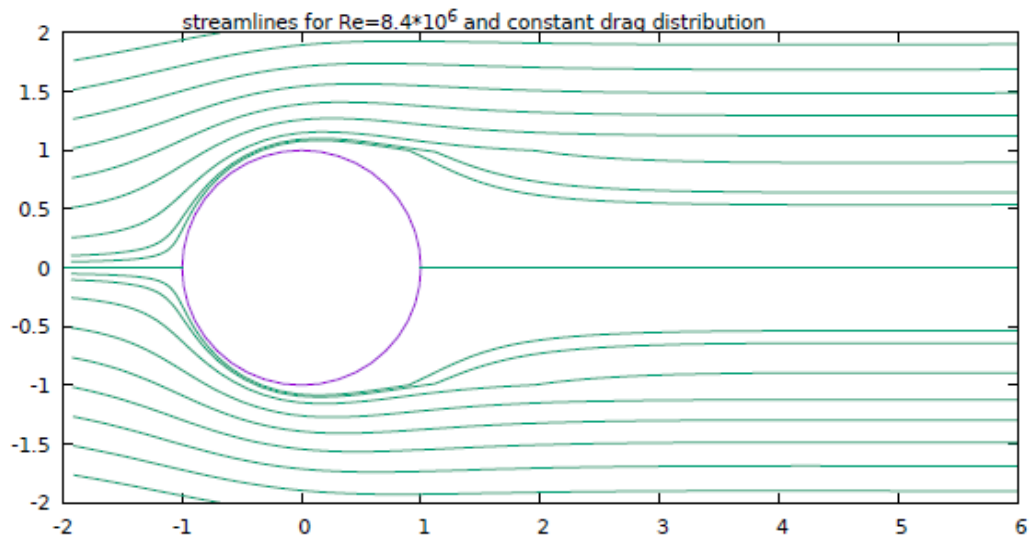
Figure 4.13 Streamlines for turbulent flow of Re=8.4*10^6
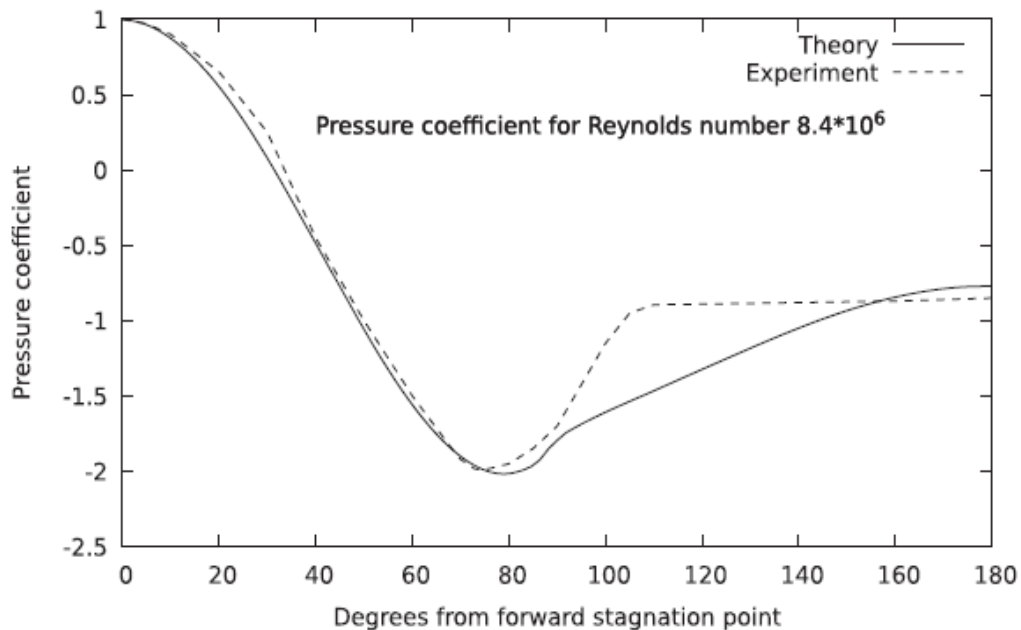
Figure 4.14 Pressure distribution for Re=8.4*10^6

The expected narrowing of the wake in turbulent flow is modelled, see for example Van Dyke's Album of fluid motion for the similar related case of a sphere (Van Dyke and White, 1982). This results in a reduction in the drag coefficient, see for example Batchelor (Batchelor, 2012). Again, it is noted that characteristic features of the physics of the flow are reproduced, such as reversal in the pressure gradient giving separation forward of the cylinder at an angle of around 70-80 degrees, and a negative pressure profile in the wake of the cylinder, see figure 4.14. Again, by fine-tuning the distribution it is possible to get a closer match to experiment but was deemed not worthwhile given the approximations made.

4.8 Discussion

A new Euler flow description is given for the velocity by a boundary integral distribution of Eulerlets whose strength gives the forces distribution over the body boundary, with the drag Eulerlet describing a wake velocity perturbation inflow, but total velocity in the wake moves downstream, see figure 3.9. For potential flows, D'Alembert's paradox exists. However, this description includes an Euler wake and implicitly evaluates drag, and consequently, D'Alembert's paradox does not arise.

The new Euler flow description, therefore, describes a wake velocity as well as a potential flow velocity. The wake velocity regularises the wake in the sense that it removes singularities to enable correct evaluation of the forces from integral evaluations across the wake, and these contributions are captured and represented by Dirac delta functions in the wake velocity representation of the Eulerlets.

Therefore, an Euler flow description for the velocity potential can also be given as an integral distribution of the potential part of the Eulerlets, but this time the integral evaluation across the wake singularity has to be omitted. It is seen that this description represents an overarching description for aerodynamic potential flow representation including thin aerofoil theory, thin wing theory panel and vortex lattice methods, and slender body theory by an appropriate numerical discretisation of the integral; the potential part of the 2-D lift Eulerlet is the clockwise circulation point-vortex, and the potential part of the 3-D lift Eulerlet is the infinitesimal horseshoe vortex.

The wake velocity is also described by an integral distribution of the wake velocity part of the Eulerlets, and so if the non-zero drag is assumed then for a thin aerofoil inclined slightly to the flow direction a wake line will emerge which to a leading approximation is at the trailing edge. This means the Kutta condition is satisfied if the non-zero drag is assumed.

Non-zero drag is expected for a real flow, however negligible the momentum deficit in the boundary layer is, and so we expect the Kutta condition to hold.

The theory was tested against the problem of uniform flow past a circular cylinder for high Reynolds number mean-steady subcritical laminar flow and mean-steady turbulent flow. An analytic formulation is obtained from the Fourier series and compared to experimental results. All the flow physics was captured such as separating streamlines, eddy formation and elongation of the eddy with increasing Reynolds number, far-field wake inflow with the expected decay, and pressure drop in the wake. The pressure distribution, given in Figs. 4.12 and 4.14, streamline separation given in Figs. 4.10 and 4.13, follows the experiment to an acceptable level of accuracy given the approximation of steady Euler flow. The theoretical equivalence to existing attached potential flow theories as well as the close comparison to experimental results for detached flow past a circular cylinder indicates the theory considers have been appropriate.

Chapter 5

5 Experimental overview

In this chapter, the equipment used to conduct the experiments is discussed. Different types of equipment were used are listed below.

- Wind tunnel
- Probe arm
- Traverse mechanism
- Pitot tube
- Hot-wire anemometer
- Flat plate
- Circular cylinder

5.1 Wind tunnels

Wind tunnels help understand the drag, lift stability and controllability or other forces of the aerofoil or bluff body in a flow. It gives us an understanding of the aerodynamics of aircraft, launch vehicles and land vehicles. A wind tunnel consists of an enclosed passage through which air is driven by a motor or any appropriate drive system. A fully supported scale model is fixed in the airstream to duplicate the full-scale aircraft. Anemometers will be used to measure the aerodynamic characteristics. Once we mount the model in the test section, fans will blow air at the required velocity in the desired direction and anemometers records the flow characteristics. Wind tunnels are classified based on speed, mode and test section of operation. Subsonic, transonic and supersonic wind tunnels are few examples for former. Pressure storage, pressure vacuum type are examples for mode based wind tunnels. Open and closed type are examples for the latter. Closed type low-speed wind tunnel is used in the present work. Advancements in the instrumentation and data acquisition technology enable us to measure quickly and accurately.

A closed-circuit wind tunnel has one extra duct in comparison to an open circuit. The air flowing in will recirculate continually with very little or no exchange of air from outside. The high flow quality helps to conduct experiments more efficiently and it consumes less energy compared to the other type of wind tunnels.

The low-speed wind tunnel which is used in this work is closed return wind tunnel with a maximum velocity that can go up to 36m/sec. It is instrumented with six component strain gauge-based balance for measurements of normal force, axial force, pitching moment and pressure distribution as a function of airspeed and angle of attack. We can measure pressure both manually and electronically. The manual will be used to measure individual pressure taps and electronic will be used to measure real-time visualization of the pressure

distribution in the wind tunnel. For the current investigation, we have used additional equipment called a traverse mechanism controlled by a computer connected with a probe arm to hold the different anemometers in the wind tunnel. There are four essential components:
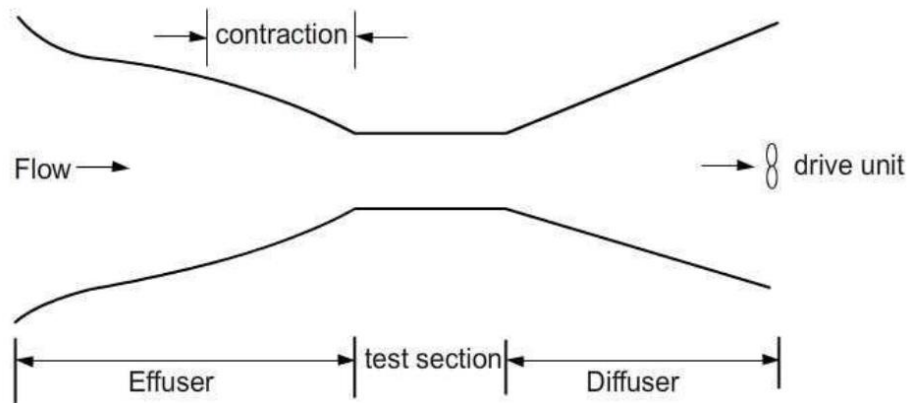
Figure 5.1 Representation of low-speed closed-loop wind tunnel

Inlet Duct or Effuser: After fluid leaves from the settled chamber, enters into inlet duct where the velocity of the fluid increases rapidly. The increase in velocity is due to its aerodynamic shape of the inlet duct. Here, the wind tunnel used in the present work has a contraction ratio of 9:1 and dimensions of 1500mm*1500mm contracted to 600mm*600mm. It helps to send the most effective smooth fluid flow to the test section by using honeycombs and filter screens. The filter screens help to filter the turbulence and obtaining the laminar flow to the test section. As we can remove the air filter mesh to clean when required. The wire mesh is also fixed to smoothen the flow further. This is particularly useful for obtaining laminar flow. The screen is made removable for possible cleaning and the duct is secured to the test section by the flange. The provision is also made for easy removal of the inlet duct and diffuser for possible separation from the test section when required.

Working section or Test section: This is the middle portion of the wind tunnel where objects will be tested under flow conditions. It is placed between the inlet duct and diffuser. It has a cross-section of 1040mm*835mm and 1728mm length dimensions fixed with a transparent window on both sides, which facilitates fixing and viewing of the models. The traverse mechanism is fixed from underneath of the test section. There are many holes drilled on top of the test section to maintain static pressure and ambient pressure the same. There are also a few holes drilled underneath the test section to hold the measuring devices like the hot-wire anemometer.

Diffuser: The diffuser has a very important function as it slows down the velocity of the fluid and makes sure it leaves smoothly. Meanwhile, it efficiently recovers all the kinetic energy of the fluid from the test section. The walls of the diffuser supposed to be smooth otherwise leaving fluid will end up in the turbulence.

Driving unit: Power is supplied continuously to maintain the flow-through section. This is done using a fan or propeller and a motor (Rao and Sahitya, 2015). Wind tunnel experiments can be extended to different models to find the

- Boundary layer investigations
- Influence of aspect ratio on aerofoil performance
- Investigation of buoyancy and blockage effects
- Pressure distribution around a circular cylinder under different flow conditions
- Flow visualization

5.2 Probe arm

The Probe arm is a device to hold the flow anemometer in the wind tunnel. The design of the probe arm is made in different stages. After looking into different ideas, the final design of the probe arm was considered based on the following characteristics.

Design considerations are:

- The probe arm must be able to move more accurately in the wind tunnel
- The probe arm should be easy to install and disassemble
- The aerodynamic shape of the probe arm exposed to the flow part should be smooth and should not affect the flow field
- Minimum flow disturbance
- Small blockage effect in the flow field and should have a minimum weight to traverse in the wind tunnel
- Probe arm should be designed in such a way that it should consider all the safety aspects in the wind tunnel

5.3 Preliminary design

The preliminary probe arm design was to replicate it by a retard stand with some blocks of wood to get the desired elevation. Tape the pitot tube to the vertical rod in the retard stand and manually move the pitot tube.

The next development is to introduce the weights and pulleys with a rotating wheel in the end to move the pitot tube. The angular motion of the wheel will be converted to the linear motion in the pitot tube. There are too many connections in the design associated with some mechanical losses and difficulty of rotating the wheel, in the next design probe arm is going to be fixed on the traverse mechanism.

5.4 Final design

The final approach is to fix the probe arm to a traverse mechanism. The pitot tube should be moving vertically and be able to cover 450mm in the wind tunnel. To satisfy these requirements, a three-piece assembly was required. This assembly consists of a square plate and three different size cylinders for securing the pitot tube and hot-wire anemometers. The first piece has a vertical rod coming out from the underneath of the wind tunnel and which goes on to a cylindrical object with 20mm diameter. They both are separated at 120 degrees.
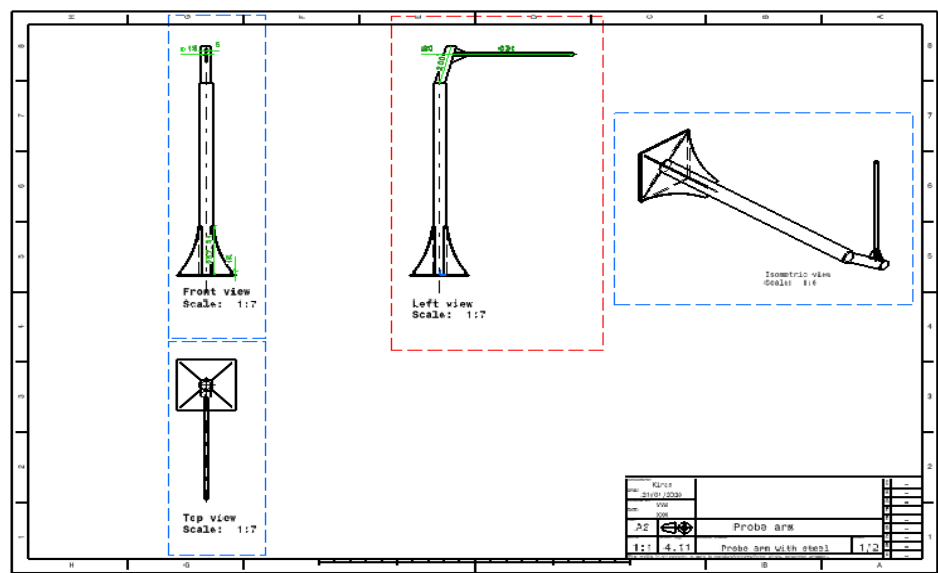
Figure 5.2 Probe arm final design

The second piece consists of a square plate and cylinder fixed like a cantilever beam. These two parts are glued together. The design is quite simple yet effective for the present work. It needs to be tested for different loads to understand deformation and failure analysis.

Deflection and failure will have a serious impact on the results. The third piece, a bolt connection is used to fasten the probe arm to the probe manipulator. Figure 5.2 below provides a good illustration of this assembly.

5.5 Traverse mechanism

There are many different techniques to determine the flow field around an object in a wind tunnel. To obtain accurate pressure field data, the probe's location relative to the test object must be known with a large degree of accuracy. Traversing systems are one of the more efficient systems being used to study the airflow behind an object by using different anemometers like pitot tube and hot-wire. Mainly we look for position accuracy and sweep area over in the test section. The traverse used in this work is from DANTEC Dynamics 2d traversing mechanism. Here are some of the specifications given in the manual. X and Z denote horizontal and vertical direction and their range is 1010mm. It can be used in integration with laser doppler anemometer or particle image velocimetry or constant temperature anemometer.
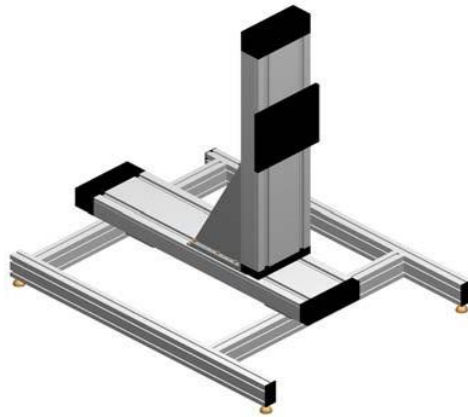
Figure 5.3 2-Dimensional traverse mechanism.

Some of its features are as follows:

- Construction is very rigid with high precision.
- Capacity for the load is quite high.
- Once it reached the limit electromagnetic brake helps to stop automatically.

The below table 5-1 explains about the specifications of the 2-D traverse mechanism.

Specifications		2D Traversing mechanism
Range	X	110 - 2710 mm
	Z	110 - 1510 mm
Speed		Up to 25 mm /sec
Resolution		6.25µm
Dimensions	W	650 mm
	L	X + 540 mm
	H	Z + 620 mm
Maximum dynamic moment		
	Mx	175 Nm
	My	150 Nm
	Mz	340 Nm
Lift capacity		60 kg
Included		• Electromagnetic brake built-in the vertical traverse unit • Mounting plate for Dantec dynamic bench profile or probe support. • Adjustable feet

Table 5-1 2D Traverse mechanism specification

5.6 Controller

The controller sends an electrical signal to traverse mechanism through detachable standard mains cable at a voltage of 100-250VAC and frequency of 50-60HZ. The controller has different options related to traversing and tells whether there is a correct connection through light signals. If traverse is not programmed properly, a hard stop of the traverse is possible by using the emergency knob.

Once all the connections are given, load the traverse stream ware basic software and install. Stream ware basic software's offers a basic interface for controlling the mini constant temperature anemometer (CTA) boxes for acquiring, processing and presenting the data. It helps to understand how to set up the hardware and different types of calibrations. The structure of the stream ware basic has four different databases.

- The project database contains all the projects information.

- Probe library with configuration setup parameters for all Dantec probes.

- Device driver databases like A/D device and traverse system.

- Analysis library for data reduction.

Figure 5.4 2D Controller

This will be explained more detail later in the hot-wire anemometer section 5.10. Specifications of the controller are tabled as follows.

Number of motor power modules	2 or 3
Line Voltage	100-250V AC 50-60Hz
Mains supply	Detachable Standard mains cable
Interface	RS232 and USB
Dimensions WHD	475 * 188 * 410mm
Included	• Motor cable – 5meter • Null modem Cable 3 meter • Emergency stop including cable-5 meter

Table 5-2 Specifications of 2D controller

5.7 Flow measurements

Study of airflow is crucial to understanding the pressure and velocity distributions. Solving Navier-Stokes equations governs detailed behaviour of fluid flow however, a general analytical solution has yet to be given. Direct numerical methods (DNS) can be used to understand the unsteady and turbulent flows, but due to the limitations in the computing methods to model the turbulence, we still rely largely on wind tunnel experiments. Different

types of anemometers are used to understand the flow characteristics in the wind tunnel. In general, we have two different ways to measure velocity, which are pointwise measuring and global wise measuring techniques. In the former, velocity information is calculated at one point in the flow by using pitot tube, hot-wire anemometer and thermal anemometer. In the latter, a whole flow field can be measured by using laser doppler velocimetry, particle image velocimetry, particle tracking velocimetry on (Sun and Zhang, 2007). In the present work pitot tube and hot-wire anemometer are used. Pitot tube works on the Bernoulli principle and a brief explanation of the principle is given in the following section.

5.8 Bernoulli principle

The Bernoulli equation is important in fluid mechanics and its applications to solve the force and energy which is often involved in engineering practice. The Bernoulli equation is a simplified equation of the Euler equations, which assumes of inviscid and incompressible flow along a streamline. Ignoring the friction losses in steady flow energy equations, one can obtain the precise relation of pressure, velocity and elevation called the Bernoulli equation. This equation is widely used, but with restrictions. In general, all fluids are viscous, and flows are associated with a certain component of friction. To use the Bernoulli equation correctly, one must confine the regions of flow which are nearly frictionless assumption holds. The Bernoulli equation is

$$P + \frac{1}{2}\rho v^2 = \text{Constant}$$

P is the static pressure of the fluid.   ρ is the density of the fluid.

V is the velocity of the fluid.

Assumptions for fluid:

- The fluid assumed to be incompressible in the total length of the fluid column, though pressure varies the density of the fluid is constant.
- Assumed to be inviscid, the dissipation of energy through viscous forces is negligible and there should not be any introduction of energy allowed as well.
- This equation is true only on a single streamline and the total energy along the streamline is constant.

- The flow should be irrotational and that should conserve the angular momentum (Qin and Duan, 2017).
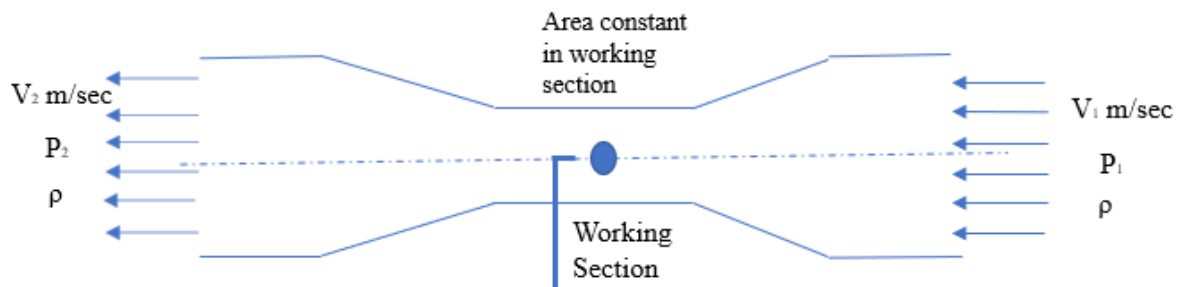
Figure 5.5 Bernoulli representation

For example, when the ideal fluid flows within a pipe, the area of the pipe is small, and the velocity is small, then the pressure is strong.

$$\frac{P_1}{\rho g} + \frac{V_1{}^2}{2g} + z_1 = \frac{P_2}{\rho g} + \frac{V_2{}^2}{2g} + z_2$$

P_1 and P_2 are pressure at inlet and outlet respectively.

V_1 and V_2 are velocity at inlet and outlet respectively.

g is a gravitational acceleration

z_1 and z_2 is the height of the flow at different heights in the flow.

If there is no change in temperature in the fluid flow of the same system, fluid viscosity neglected, and density of the fluid is constant. In this isotropic system, the internal energy is constant, and we use the Bernoulli equation to find the mechanical energy balance in the system. The principle of the Bernoulli equation in the same system works as follows. If the pressure is high velocity is small, that means there is strong pressure for small flow rate. There are so many applications for Bernoulli principle, such as measuring static pressure in the aircraft, water pump and wind tunnel experiments.

5.9 Pitot tube

A Pitot tube is a pressure measurement instrument used to measure fluid flow velocity. It has a wide range of applications in different industries and one important application is finding aircraft velocity relative to the wind speed. In the present work, which

is inviscid incompressible flow, the basic pitot tube consists of a tube pointing directly into the fluid flow and the total pressure in the flow is defined as the pressure attained at the point in the tube brought to rest without any viscous effects. The total pressure is also called as stagnation pressure. A small hole in the side of the pitot tube head allows the pressure in the outer tube to equal to the pressure in the free stream and is called the static pressure. The velocity can be determined from Bernoulli's equation and it can only apply when viscous and inertia forces are incomparable, such that the fluid is inviscid, or has high velocity where viscous forces are negligible (MacMillan, 1957).
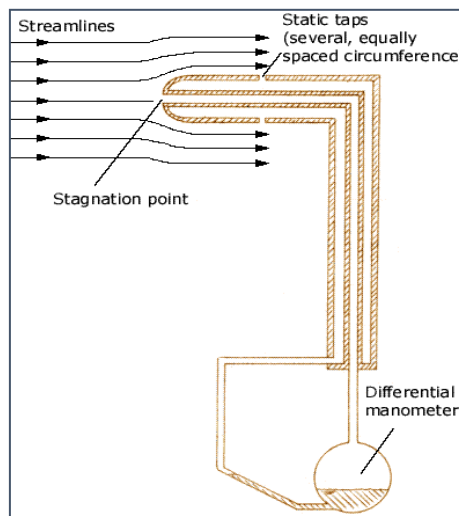
Figure 5.6 Pitot static tube representation for pressure measurement (Ghosh, Muste and Stern, 2010)

We have three different types of pitot tubes available and they are simple pitot tube, static tube and pitot static tube. Simple tube measures the total pressure, Static tube measures the static pressure and pitot-static tube measures the difference between total and static pressure, which gives dynamic pressure (Beck, Payne and Heitman, 2010). So, we measure velocity not pressure with the pitot static tube. It is economical to install and the disturbance in the flow is minimal. Pitot tubes are suited for a variety of environmental conditions including extremely high temperatures and a wide range of pressures (Lester, 1960). Though it got advantages on the other hand it has many limitations as well. Here are some of the limitations.

- It can only work in a clean fluid and they have limited applications in industry as they have low sensitivity, low rangeability and poor accuracy
- If the velocity is low, the difference in pressures is very small and hard to accurately measure with the transducer.

- Easily clogged with foreign materials and sensitivity can be disturbed by the flow direction

- Change in velocity profile develops a very low differential pressure which is difficult to measure (Robinson *et al.*, 2004).

Pitot static tube is used to understand the wind speed of the wind tunnel. So, it is important to understand the possible sources of the measurement error and it could be caused by:

- Incorrect tube construction and installation.

- Measuring below a critical Reynolds number.

- The compressibility of air (Subbarao, 2001).

5.10 Hot-wire anemometer

Hot-wire anemometer (HWA) is a device used to measure the velocity of the fluid in the wind tunnel for laminar, transitional and turbulent boundary layer flows for many different fluids. A hot-wire is placed in the flow and that is heated at a constant temperature. Flow is cooling the temperature and heat energy is dissipated. A constant temperature anemometer uses a wheat stone bridge to maintain the constant voltage in the circuit as the fluid passes. The faster fluid the higher the voltage. Thus, the anemometer measures the speed of the fluid in terms of voltage. It works on the fact that the probe's resistance is proportional to the temperature of the hot- wire (Stainback and Nagabushana, 1993).
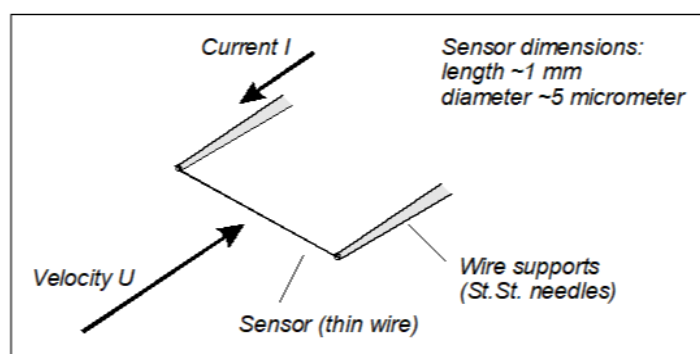
Figure 5.7 Hot-wire anemometer

Configuration of the experiment:

The physical setup of the hot-wire anemometer and its interconnections of transducers, modulus and devices consists of the following:

- A/D device
- Traverse system
- Probes
- CTA bridges
- Cables and mounting probes

The transducer is a device which converts a one form signal to the other form. In this case, it is from speed to voltage (Jensen, 2004).
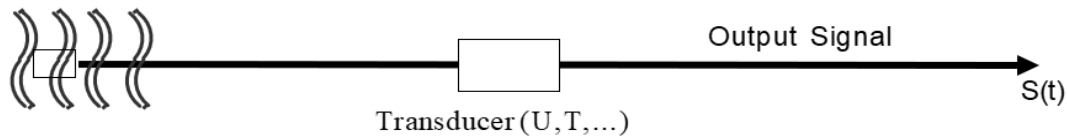
Figure 5.8 Transducer

HWA consists of two probes with a wire placed perpendicular to the flow and the material used is tungsten, platinum or platinum-iridium. Diameter and length of the wire are varying as from 1- 5µm and 1-3mm respectively. King's law gives a relation for heating wire and velocity of the fluid (Comte-bellot, 1976).

$$U^{\frac{1}{2}} = AV^2 + B$$

The hot-wire anemometer works in two ways. One is constant temperature and the other is constant current. In the constant current model, a high current can damage the wire if the cooling fluid is not too low or if the flow is too high wire will not heat up properly. The probe is connected to the Wheatstone bridge and heated by an electric current. An amplifier controls the current to the sensor so that the resistance keeps the temperature constant independent of the cooling of the fluid. Bridge voltage represents the heat transfer and it measures the voltage (Dynamics, 2017). see figure 5.9. Initially, the experiment circuit is in balance. As the resistances R1 and R2 are fixed, R3 is a variable and Rw is a wire resistance which is a function of temperature. The ratio of R1/R2 should balance R3/Rw. As soon as the experiment is started, the circuit is unbalanced and R3 is can be used to adjust to bring the circuit in balance. The process of unbalance and balancing will result in the change in voltage and which results in amplification. So, the feedback current will be adjusted to keep the wire temperature and resistance constant. These changes in current enable us to measure the flow velocity. The final output in the circuit is in analog form, which needs to be changed to digital. The analog to digital converter board acquires the signal and converts into the data-series which is saved in the computer. A/D device is selected based on the number of channels required, sampling rate and sampling mode (Comte-bellot, 1976).
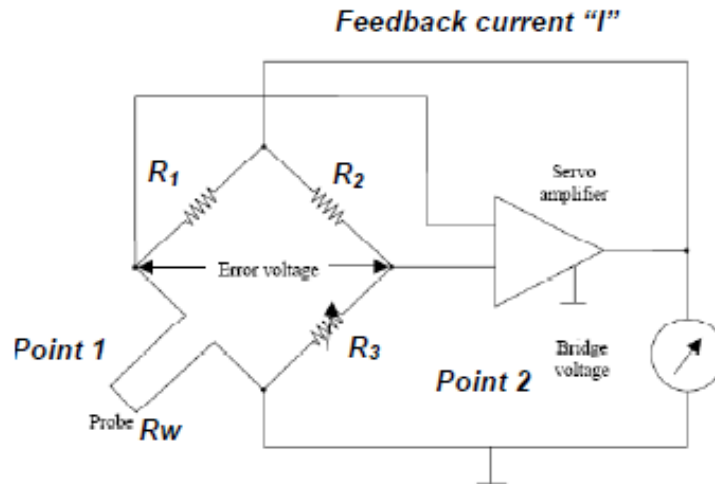
Figure 5.9 Wheatstone bridge

Advantages of Hot-wire anemometer:

- It can respond to the high frequencies up to several MegaHertz (MHZ).
- Accuracy is up to 0.1-0.2% and very low signal to noise ratio.
- Its s very easy to operate and low in cost.

Limitations:

- It should have angle reference and accurate velocity calibration.
- HWA requires a traverse mechanism to use as it is a point measuring equipment.
- Intrusive, access into the flow field with traversing.
- Some error sources, such as temperature change, density change in the fluid, wire properties and contamination.
- It cannot identify the flow direction.
- It is very sensitive to any solid particles.

5.11 Experimental models

The idea of the present work is to test the new Euler theory. So, I have considered basic experimental models to understand the results. The models are flat rectangle plate and circular cylinder with different diameters of 90mm and 63mm. Aluminium is the material used in both the models and they both are machined on a lathe with a required smoothness on the surface. The accuracy of the dimensions of the models is accurate to 0.25% over the length of the model. It is a two-dimensional problem considered on infinite length in the

space. The width of the wind tunnel is 1040mm and the length of the body facing the flow is 900mm. The gap between the cylinder end and the wind tunnel wall is 70mm on each side. The boundary layer thickness is less than 50mm thick at the given Reynolds numbers. The blockage effect which is well within the range and there is minimal effect on the results.
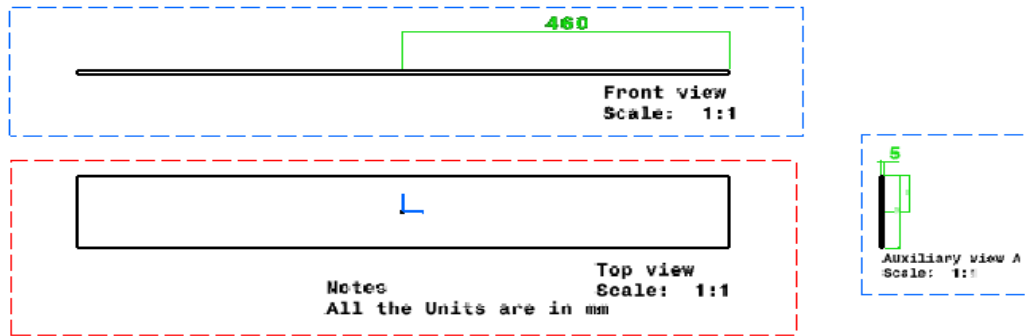
Figure 5.10 Flat plate used in the experiment
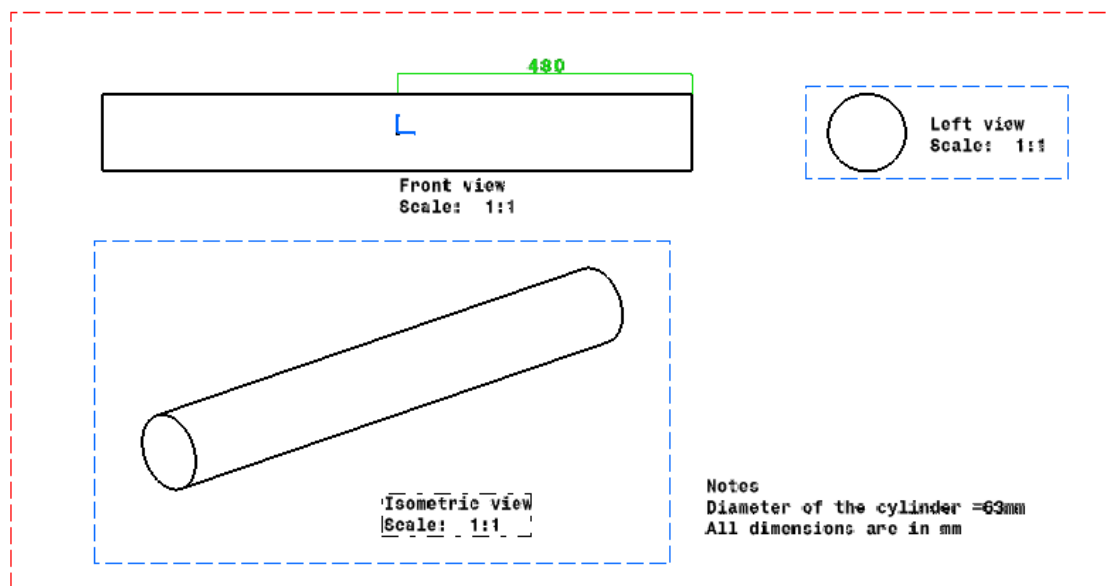
Figure 5.11 Circular cylinders used in the experiment

5.12 Data acquisition system

For pitot tube, measured readings are noted along with the experiment. All data from hot-wire is recorded in the computer using a computer-controlled analog to the digital data collection system. The stream ware software is application software used with multichannel Constant temperature anemometer box. A 6 channel 6 velocity and one temperature channel box are used in the present work. Automatic temperature correction is used to measure the

more accurate velocity readings with temperature effects in the flow. Ambient temperature value should be input to use the temperature probe. The output voltage from the anemometers and temperature corrections are connected to the analog to digital (A/D) input. The stream ware basic software can handle up to 16 A/D channels in total. The multichannel CTA system is an analog instrument controlled by a PC. The analog signals from the CTA anemometer are acquired via an A/D device in the PC. Sampling frequency and the number of samples affect the results. In the present work, 10,000 is used as a sampling frequency and 1024 samples considered. The probe with a wire in between two flanges measures the voltage and converts that into the velocity readings. Each probe will have different resistance and a different combination of on and off switches. In the default setup, the acquired data will be stored as a file and noted as raw data in the project manager (Jorgensen, 2002).

5.13 Experimental setup

The following diagram explains the experimental setup used in this work.
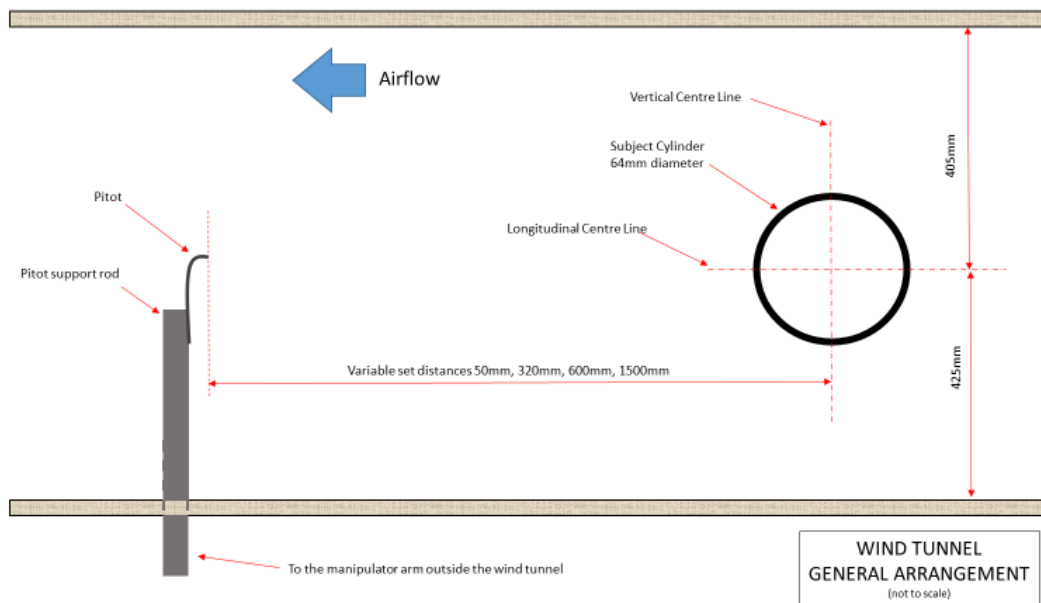
Figure 5.12 Experimental setup in the wind tunnel for a circular cylinder.

6 Experiments and calibration

6.1 Overview

In this chapter, we will discuss the calibration of the wind tunnel, velocity variation in the test section, effect of struts in the wind tunnel, blockage effects, buoyance effects, pitot tube and probe arm calibration, default setup of traverse mechanism, post-processing, and experimental models.

6.2 Calibration of wind tunnel

Wind tunnel calibration is a process of doing the number of tests to find the average value of the flow parameter at one point or a defined volume of a test section for a given tunnel configuration. We cannot operate the wind tunnel without calibrated data and the same data will be used to find the actual operating conditions. The wind tunnel used in the present work has a test section area growing bigger further downstream which helps to adjust with increasing the boundary layer. The six-component strain gauge-based balance is not used for measurements in the present work. The type of calibration is defined by the type of experiments conducted in the wind tunnel. The list of calibration for the wind tunnel is long and time-consuming. So, we would like to concentrate only on that required. The actual parameters are pressure (Dynamic, Static, and Total), velocity and temperature. In the present work, the temperature is not considered as incompressible fluid considered and as well it is 2-dimensional problem so, blockage effects are not considered (Swanson and Clarence, 1944).

6.3 Velocity variation in the test section

Accurate velocity readings at different planes in the test section are very important for finding the aerodynamic characteristics. To measure actual velocity, the determination of reference velocity or dynamic pressure is very important to calculate all dimensionless quantities. Reference velocity is the average flow velocity over the empty wind tunnel with a pitot tube or hot-wire and cannot be calculated once the object is placed in the test section. This is conducted for both pitot tube and hot-wire anemometer (Pope, 1961). For the first experiment, a pitot-static tube is used to calculate the reference dynamic pressure in the empty wind tunnel. It is placed in the test section and where the test object is going to be placed and the dynamic pressure readings are recorded for five different time intervals. All the values are averaged over space to calculate the actual velocity settings for the wind

tunnel. This is repeated at different planes in the test section to understand the velocity change in the wind tunnel.
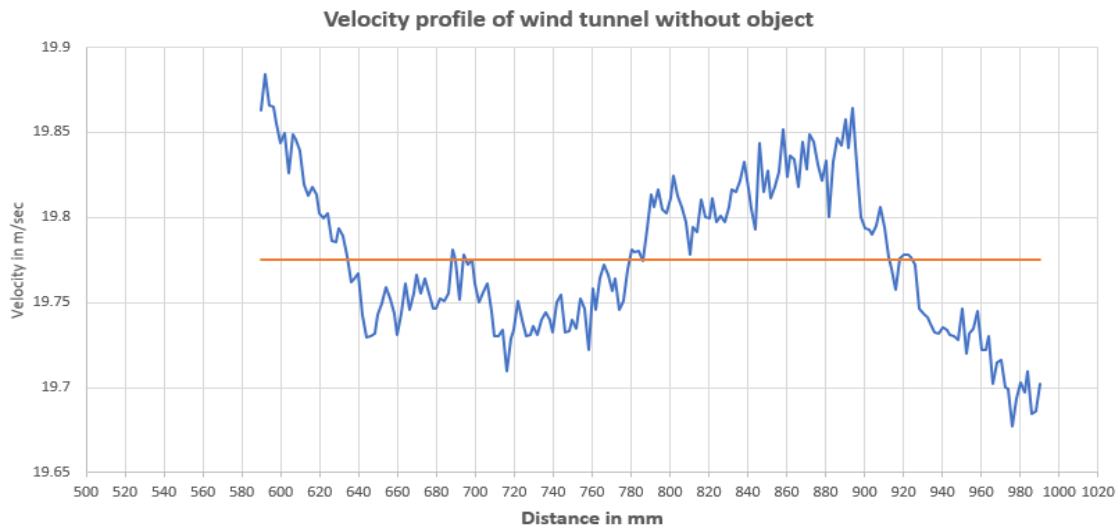
Figure 6.1 Empty tunnel velocity profile with hot-wire anemometer

Velocity is calculated by using the Bernoulli equation; the difference of total pressure and static pressure in the pitot static tube gives the dynamic pressure (Fischer, 2018). For the rest of the experiments, hot-wire anemometer is used to calculate the reference velocity. The pressure transducer is used to calibrate the hot-wire equipment and all the calculations and adjustments are done in pre-programmed hot-wire anemometer software provided by Dantec. The velocity variation in the wind tunnel is captured and it is illustrated in figure 6.1 and the orange line represents the mean velocity line. The percentage of error for a given test is less than 1 per cent (exactly 0.8%) as velocity varies from 19.86m/sec to 19.7m/sec for a given distance in the wind tunnel.

6.4 Effect of struts in the wind tunnel

In the present work, the main intention is to take readings in the vertical axis in three different planes along the test section. As mentioned earlier, the experiments were conducted using a flat plate and circular cylinder. Both of them are fixed differently in the wind tunnel for corresponding experiments. The flat plate is suspended from the top, and the circular cylinder is bolted to the wind tunnel top and bottom internal surface. The experiment is set up in such a way, that the pitot tube is placed in the middle of the test section, supporting rods for circular cylinder and struts for the flat plate are placed far away from the centre and close to the walls of the test section. Struts and supporting rods are placed separately in the wind

97

tunnel without any model and readings are taken with hot-wire and pitot tube. Five different readings are taken at different time intervals at the same point and the procedure is repeated for different points in space. After careful consideration of looking into the readings, the effect of struts in the middle of the test section on dynamic pressure is negligible. Figure 6.2 gives an understanding of the velocity readings for a probe arm with struts in the wind tunnel for different time periods at the same place. As velocity drops from 19.39m/sec to 19.33m.sec and the percentage of error is 0.3 per cent.
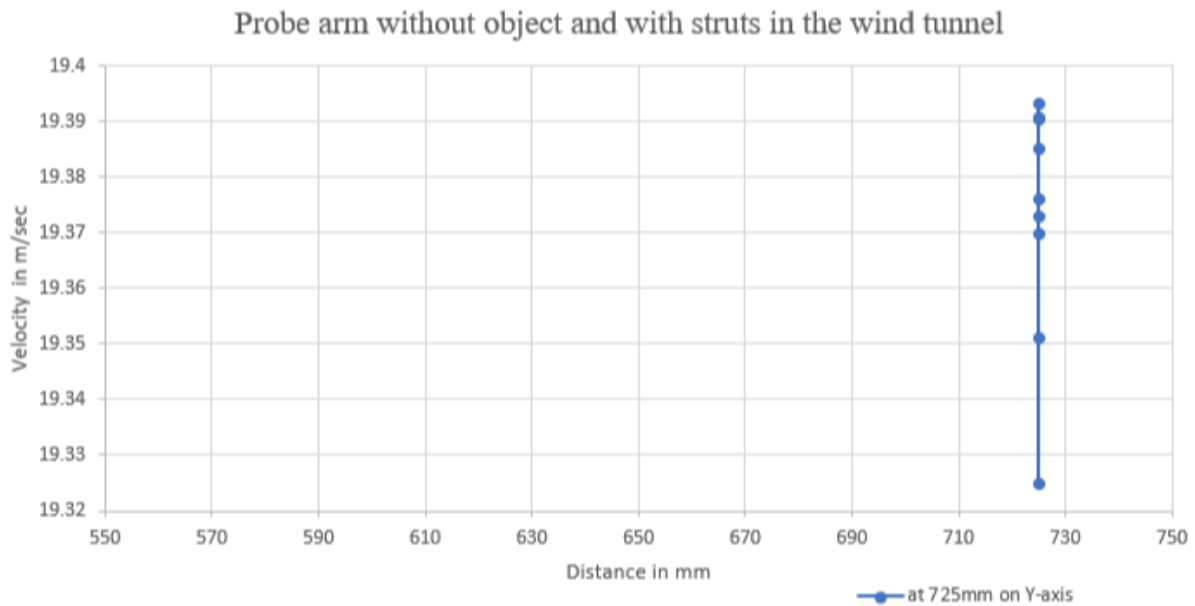
Figure 6.2 Probe arm without the object and with struts in the wind tunnel

6.5 Effect of the probe arm

The probe arm helps to hold the pitot tube or hot-wire in the wind tunnel to take the dynamic pressure readings with pitot tube or velocity readings with hot-wire anemometer at a suggested point. To see whether the probe arm has any impact on the flow, repeat the same experiment as in section 6.4 to understand the impact. The ensuing results suggest no impact unless it is in very close proximity to the probe arm. The pitot tube is 3.5cm out from the probe arm into the flow direction. The probe arm is fixed on the traverse mechanism and comes from underneath of the wind tunnel to hold the pitot tube or hot-wire anemometer. The force acting on the probe arm is calculated using the formula for given conditions of velocity, the density of the fluid and area of the object. Using the same force in the ANSYS finite element package the probe arm deformation and stress are calculated and they are negligible. The data has been tabulated, deformation and stress diagrams are added in Appendix A.

6.5.1 Other factors can affect the flow conditions

- Making sure flow conditioning screens are cleaned for good results.
- Observing the temperature change in the tunnel throughout the day and its impact on the results.

6.6 Blockage effect

The flow past a bluff body in the closed-loop wind tunnel with rigid walls is subject to the blockage effect. However, the model is restricted to a certain scale due to the blockage effect of the wind tunnel. Allowable blockage ratio, which is 5%-10%, is introduced to reduce the effects on the flow characteristics. The ratio is defined as the projected area on the test model on a plane normal to the test section axis over the sectional size of the wind tunnel (Choi and Kwon, 1998). During wind tunnel testing, the local flow field around an object accelerates due to wall restrictions and is called the solid blockage, also defined as the increase in the flow acceleration due to the volume distribution of the body itself. The change in acceleration may result in asymmetric pressure gradient and an increase in the measured drag. It also affects the boundary layer around the bluff body and its thickness. Also increase in the acceleration due to the wind tunnel cross-section restricts the viscous wake behind the bluff body and is called the wake blockage which is also defined as the increase in the flow acceleration which causes the displacement effect of the actual wake. These errors need to be corrected by using standard methods. Wake blockage results in asymmetric pressure gradient and a corresponding drag increment (Hyvärinen and Hyvärinen, 2015)(E. C. Maskell, 1963). The circular cylinder is 900mm long and 90mm diameter. Wind tunnel cross-sectional area is 1040mm*835mm. From the formula, the blockage ratio in the present work is about 9.32%. So, the blockage effect is negligible. The results are mainly concentrating on the centre of the test section and wall blockage is far away from the centre and its impact on the results are also negligible.

6.7 Buoyancy effect

The flow acceleration due to the blockage effect generates skin friction on all the surfaces like wind tunnel walls and surface of the body in contact with the fluid. This, in turn, generates growth of the boundary layer from the start of the test section to downstream, effectively changing the cross-section area of both the body and duct. This results in the drop in static pressure from the start of the boundary layer to the arbitrary point in the downstream. This net change in static pressure in the horizontal direction is called as horizontal buoyancy

(Lauchle, 1978). The wind tunnel used in this present work is constructed with a slightly increasing cross-sectional area to compensate for horizontal buoyancy. So, this effect is negligible (Hyvärinen and Hyvärinen, 2015). The wall divergence for University of Salford wind tunnel is 0.2º along the test section length.

6.8 Pitot tube calibration

For measuring fluid velocity, the pitot-static tube should be able to identify the small changes of pressure, over a few millimetres of change in position, because for our experiments precision in this measurement is very important. In the present work, the pitot tube is calibrated by using Betz manometer. The wind tunnel is set by Betz manometer at a certain velocity and the pitot-static tube is arranged in the flow to measure the actual velocity of the air. Pitot static tube measured the difference between total pressure and static pressure. The density of the air is calculated by using the following formula

$$\rho = 1.2256 * \frac{p}{760} * \frac{288}{T}$$

P is the laboratory atmospheric pressure and T is the tunnel temperature and from Bernoulli's equation

$$P_1 + \frac{1}{2} \rho V_1^2 = P_s + \frac{1}{2} \rho V_s^2$$

P_1 is the pressure in the fluid P_s is the stagnation pressure

V_1 is the velocity of the fluid V_s is the velocity at stagnation point which is zero.

So, the formula will be manipulated as follows

$$V_s^2 = 2 * (P_s - P_1)/ \rho$$

By using the above formula velocity of the fluid in the wind tunnel can be calculated. Betz manometer values are recorded initially and now compare them with pitot tube measured velocity readings. The difference between both is recorded and the experiment repeated five times before the correction factor is determined. The correction factor value is added in the results.

6.9 Hotwire Anemometer calibration

For probe (HWA) calibration, the Dantec calibration unit is used. The stream ware basic software supports the calibrator both manually and automatically fully controlled by software. Calibration establishes a relation between the hot wire anemometer (HWA) output and the flow velocity. A probe is exposed to the known values and the voltage recorded. A curve fit through the points of voltage and velocity will be used as conversion data. Calibration can be done in the wind tunnel in reference to the other anemometers or dedicated probe calibrating equipment like free jet given by Dantec and the same unit is used for calibrating the probe. The stream ware basic software supports the calibrator both manually and automatically fully controlled by software. In the present work, manual two-point hot-wire calibrator is used. Hotwire anemometer results are taken by the average of all the samples for a given frequency and time interval. For example: In this work, the number of samples is taken as 512 with a sampling frequency of 1000 kHz and time interval of 0.512. The uncertainty of a velocity sample acquired at the calibration is 1.5%. When the uncertainty of the calibrator itself is included it increases to 3%. Pitot tube anemometer is used to calibrate the Hotwire anemometer results and the error is less than 3%.
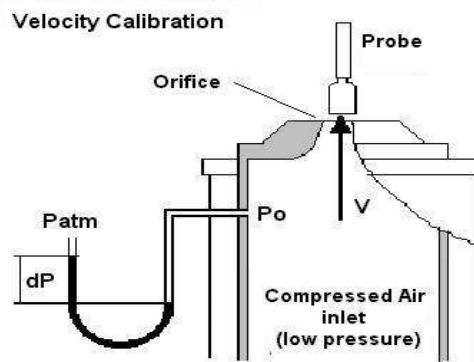
Figure 6.3 Velocity calibration

6.10 Temperature correction considerations

An experiment conducted in the present work used a constant temperature anemometer, that takes around one to one and half-hours to finish. This affects the wind tunnel temperature, which can result in not accurate velocity measurements. The corrections should be added to the output before considering further to avoid the systematic errors from small fluid temperature variations. For every 1° change in temperature gives approximately 2% error in velocity. A temperature sensor is connected to the system along with the probe

before we start the wind tunnel and recorded on the multi-channel CTA. A StreamWare program is written in such a way that change temperature is automatically corrected. The corrected measured data will be saved on the computer.

The 6 multi-channel CTA frame along with the 90P10 (is a series number for temperature probe) temperature probe is used in this work as a reference temperature source for temperature correction. The sensor is calibrated at ambient temperature fluctuations with good sampling rate to understand the temperature data acquired to optimize the temperature correction. It is very important to keep both hot-wire and temperature probe very close to each other in the flow, so they both are exposed to the same temperature. If calibration is not done, the software will pick one of the configuration default values from the probe library and it will be used. This data will be saved as an event and used as a default for the rest of the experiment.

6.10.1 Precautions

- Calibration should be done after 10 minutes of starting the calibrator.
- Enough air pressure should be maintained while doing the calibration.
- There should not be any dust particles as it can damage the calibrator and probe together.

6.11 Procedure

The Hotwire calibrator is easy to operate air calibrator for Hot-wire probes. It provides a free jet for easy access with probes. The calibrator can be operated in two modes: two-point calibration and continues mode. The first one is a stand-alone application and it's not required any extra equipment to work unlike later. In this work, two-point calibration is used and it is placed upright and consequently, it is placed in front of a probe. Two-point calibration can help to find the drift, contamination or damages of the probe. Turn the handlebar marked with low and high to a low position and connect the probe support to an anemometer. Fill all the necessary data like Overheat values and turn the anemometer on. Mount the probe in the calibrating rig, and leave the probe supporting cables unchanged after calibration until the experiment finishes. Ambient pressure and temperature should be noted. Before starting, temperature correction should be added and overheat correction as any unbalance in the circuit should be corrected. Connected a voltmeter to the output if the anemometer and raise the probe slightly above the nozzle and move it sideways. The probe voltage drops to the lower values now, input values into the software about the minimum and

maximum calibration velocity, several calibration points and type of velocity distribution should be chosen with respect to the experiment. Move the probe back to the original position and turn the handle back to the vertical position (high position with velocity 50 m/sec in this case). In between low and high positions, we need to allow the system to be stabilized for a few minutes. The velocity in terms of probe voltage and Bridge voltage at corresponding positions will be recorded in a spreadsheet. The streamware basic software creates a transfer functions in the form of a fifth-order polynomial fit, power law. Curve fitting of calibration data looks as follows.

	U	E1	T(C)	P(kPa)	E1corr	U1calc
1	0.381	1.476	21.900	101.300	1.476	0.382
2	0.889	1.561	21.900	101.300	1.561	0.882
3	1.601	1.640	21.900	101.300	1.640	1.597
4	2.607	1.720	21.900	101.300	1.720	2.617
5	3.930	1.798	21.900	101.300	1.798	3.948
6	5.646	1.875	21.900	101.300	1.875	5.646
7	7.949	1.957	21.900	101.300	1.957	7.939
8	10.878	2.039	21.900	101.300	2.039	10.866
9	14.447	2.121	21.900	101.300	2.121	14.430
10	19.121	2.207	21.900	101.300	2.207	19.108
11	24.946	2.296	21.900	101.300	2.296	24.952
12	31.838	2.383	21.900	101.300	2.383	31.831
13	40.390	2.474	21.900	101.300	2.474	40.440
14	50.651	2.565	21.900	101.300	2.565	50.702
15	61.490	2.646	21.900	101.300	2.646	61.421

Figure 6.4 Example of two-point calibration data
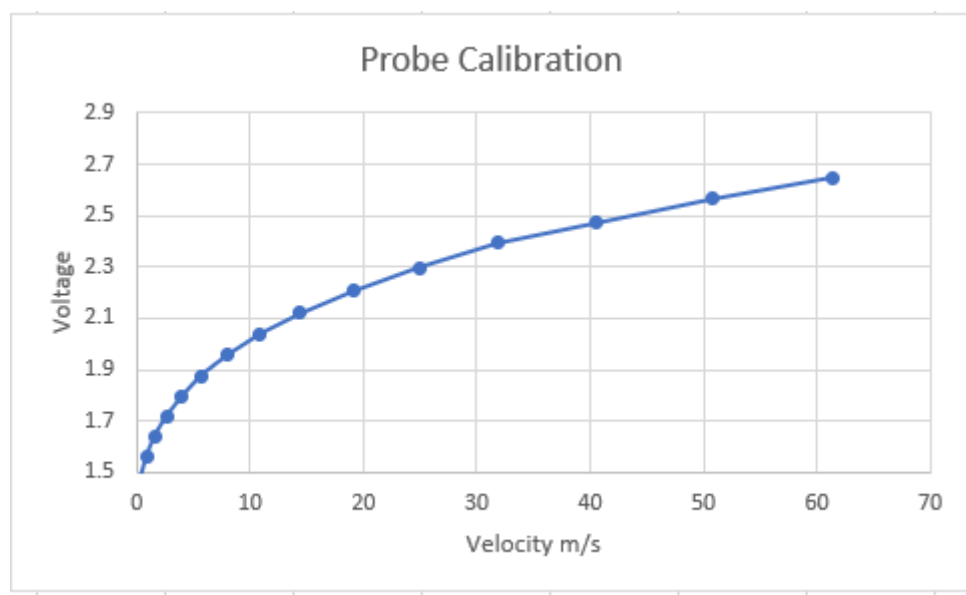
Figure 6.5 Probe calibration graph
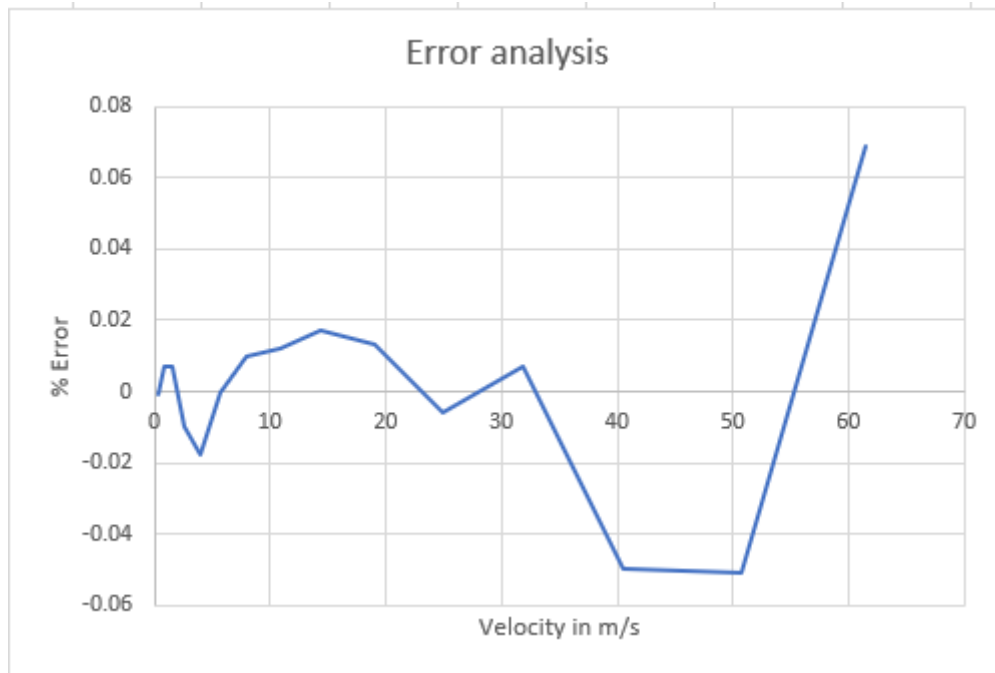
Figure 6.6 Error analysis

The percentage of error from the probe calibration is within the range of 0.07 to -0.05 which is acceptable. The calibration is done and the file needs to be saved to the database and make the readings of the file as a default, otherwise, the latest calibration file will be considered as a default.

6.12 Setup of traverse and hot-wire anemometer

This section demonstrates how to measure the velocity profile in a free wake with a single sensor wire probe. When we run the program, the probe is traversed across the wake, data are acquired in each position and saved in a file. The data is later converted based on the probe calibration and reduced to the mean velocity and root mean square velocity. The physical configuration of the system covers the interconnections of the PC, multi-channel CTA unit and probe. It consists of the following steps.

- Connect the analog output on the multi-channel CTA unit to the Analog/Digital (A/D) device input channel on the connector box for the A/D device with 50 Ohms Bayonet Neill–Concelman (BNC) cable.
- Connect probe and support with a 4m cable to the Probe BNC connector on the multi-channel CTA unit.
- Place the probe in front of the fan.

- Switch power on to both systems.
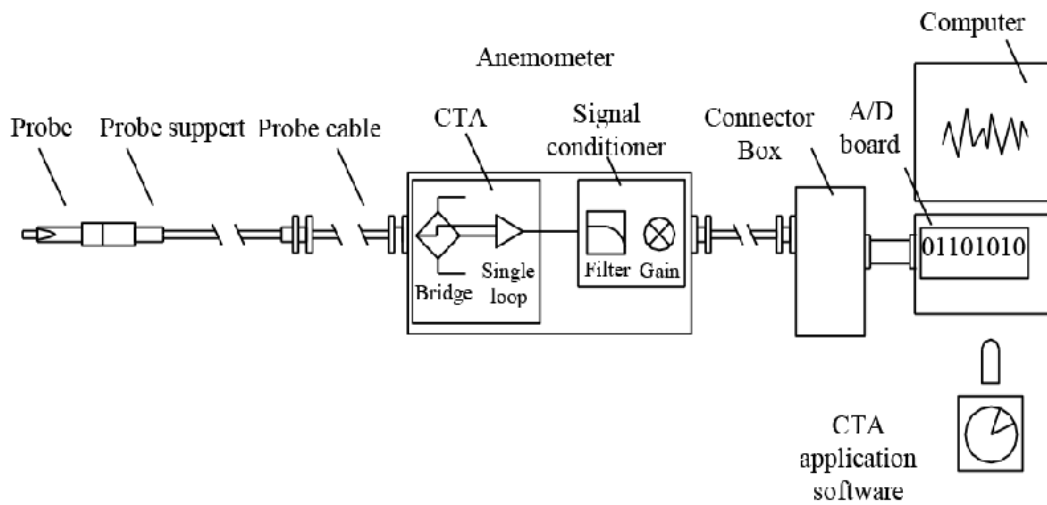
Figure 6.7 Default setup of traverse and hot-wire anemometer

Once the physical setup finished, open the StreamWare basic software in the program manager and create a new database. The structure of the system is as follows.

- Create a database
- Configure device
- System configuration
- Hardware configuration
- Calibration
- Run and acquire and
- Process data.

The whole process of using StreamWare basic software clearly explained in Appendix B. Please refer to the Appendix for further understanding. Once the setup is finished, the wind tunnel needs to be run with the circular cylinder and the velocity profile recorded at each station.

6.13 Post-processing

All the velocity data collected was non-dimensionalised by the free stream velocity, and the distances between the stations and cylinder centre are expressed in multiples of the radius of the cylinder

6.14 Experimental models

All experiments conducted in this dissertation were performed in the closed-circuit low-speed wind tunnel. Different types of models can be used to understand the wake in the near-field, however, flat plate and circular cylinder are used to validate the new theory. The flat plate is used as a benchmark for using hot-wire, probe arm and traverse mechanism to

produce the wake profiles in the near wake. The circular cylinder is used as the standard model in the project, which will be described as the Reynolds range of 10^6, although much of the general description is applicable to other Reynolds numbers. All the experiments conducted in this project are well within the range of Reynolds number given above.

6.15 Flat plate

The flat plate is made of aluminium machined on a lathe and then the surface polished with sandpaper. The dimensions of the flat plate are 1040mm facing into the flow direction and 400mm along the length of the wind tunnel. The flat plate was welded with struts on both sides from the centre at 470mm distance to bolt with the struts suspended from the gauge. The gap between the wall and the end of the flat plate was 50mm.

6.16 Circular cylinder

The cylinders were constructed of heavy aluminium tube machined on a lathe and then polished on the surface with sandpaper. The cylinders used were 90mm and 109mm diameters and spanned the test section. The cylinders diameters were accurate within 0.3% over the span. Unlike using steel struts to mount the model, steel rods of 0.5mm diameter and bolts were used on both sides to hold the cylinder to conduct an experiment. Figure 5.11 is a diagram of a typical cylinder. The gap between the cylinder and wall of the wind tunnel was 70mm. The blockage is well within the range, 9.32% of the total cross-sectional area.

Chapter 7

7 Experimental results

7.1 Summary

This chapter describes all the different type of experiments conducted, and the process to obtain the results.

7.2 Experiments

The experiments are conducted in different phases in the wind tunnel to understand the parameters like right velocity to conduct the experiment, type of model to be used, and at what distance we have to capture the velocity profiles. The flat plate and circular cylinder are used to conduct the experiments. The flat plate experiments are conducted in two stages and circular cylinder experiments are conducted in four stages and they are explained in the following sections.

All the different models used in the experiment are listed below and they are

- Flat plate 900 mm*400 mm*5 mm
- Circular cylinder 64mm &109mm diameter
- Circular cylinder 90mm diameter.

The shape of the model	Width of the flat plate or diameter of the cylinder in mm	Velocity in m/sec	Distance from the back of the model to the cross-section in mm	Equipment used to measure the velocity
Sideview	400	30	• 289 • 382 • 563	Pitot tube
	400	20	• 17.5 • 286 • 566	Pitot tube
	109	20	• 17.5	Pitot tube
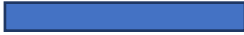
			• 286	
			• 566	
⬤	64	20	• 17.5 • 286 • 566 • 1470	Pitot tube
⬤	109	20	• 2 • 54.5 • 109 • 218 • 327 • 436	Hot-wire anemometer
⬤	90	20	• 2 • 45 • 90	Hot-wire anemometer

Table 7-1 Tabular form of different types of models and their details used in the experiment

7.3 Phase one – The flat plate

This phase was undertaken to determine the wake profile for a flat plate in the wind tunnel at different speeds. The velocities used in this phase are 30ms^{-1} and 20 ms^{-1}. The velocity profiles at different cross-section are captured and they are detailed in the following section. The results are used to understand whether the wake is diffusing and the impact of this work in the second phase is also discussed.

7.3.1 Experimental details

This section will complete the experimental method outlined in chapter 5, detailing the test components and wind tunnel measurements.

7.3.1.1 Test components

The flat plate used in this phase has dimensions 400mm width and 900mm length into the wind tunnel and 5mm thickness. The length of the plate is chosen in such a way to neglect the blockage effect. The following figure:7.1 shows a side view of the test component.

7.3.1.2 Wind tunnel

All the experiments in this work were carried out in the closed wind tunnel with velocity varied between 29.55 ms^{-1} to 30.15 ms^{-1} with an average 30 ms^{-1}, as well as between 19.64 ms^{-1} to 20.23 ms^{-1} with an average 20 ms^{-1}. The Reynolds numbers are 8.0467*10^5 and 5.226*10^5 respectively for the velocities calculated based on the velocity and the area of the model. The air temperature and velocity of the wind tunnel are monitored to be within 5% throughout the run.

7.3.1.3 Measurement planes

Three measurement planes are chosen, located at 289mm, 382mm and 563mm from the back of the flat plate and contain 80 equispaced points distributed to each side of the centre of the flat plate. All these dynamic pressure measurements were done using the pitot tube and traverse mechanism with sample time set up for 15 seconds. The measured dynamic pressure was converted into velocity using the Bernoulli equation for incompressible flow. Figure7.1 gives an understanding of the experiment setup.

Figure 7.1 Experimental setup for flow past a flat plate.

7.3.2 Results and Analysis

Details the results along with any analysis.

7.3.3 Mean velocity contours

As we already discussed in chapter 5, the flat plate is suspended in the test section and the pitot tube controlled by the traverse mechanism which moves from bottom to the top of the wind tunnel at each cross-section. The distance the pitot tube covers at each station or cross-section behind the flat plate for velocity profile was 160m. That means it moves 80mm on both sides from the centre of the model. Betz manometer was used to set the velocity of the wind tunnel to 30 ms^{-1} and 20 ms^{-1} respectively for different experiments in phase one. The pitot tube position in the wind tunnel is different for both the experiments. In stage one pitot tube position for velocity 30 ms^{-1} is nearly behind the thick struts come from the gauge of the wind tunnel. In stage two pitot tube position is changed to the centre of the test section. Wake velocity data at each station is collected by pitot tube and at each point in the cross-section as pitot tube measures the low and high dynamic pressure readings. The recorded low and high dynamic pressure readings will average to find the actual dynamic pressure at each point in the cross-section. The collected data is in dynamic pressure form and it can be converted to velocity by using the Bernoulli equation, the total pressure is equal to the sum of the static pressure and dynamic pressure. The static pressure at the test section is being constant throughout the experiments due to it being exposed to the atmospheric pressure as there are some holes on top of the wind tunnel test section. So, the collected data of dynamic pressure is used to draw a pressure graph to cross-check with the theory and profiles that are displayed in figure 7.2.

As we can see the results from figure 7.2, all the dynamic pressure profiles at each station are moved towards right in the graph. As flat plate has a smooth surface on both sides and the dynamic pressure profile supposed to be symmetric, but from the graph, we can see it is not symmetric. It is not only asymmetric but also the readings are moved away from the centre of the plate. At each station, the experimental data had recovered to the free stream on the bottom side and not on the top side of the profile. It is clear from the result that, there are more viscous forces exist on the top side of the flat plate as a result of thick struts existence in the same lateral axis of the pitot tube.
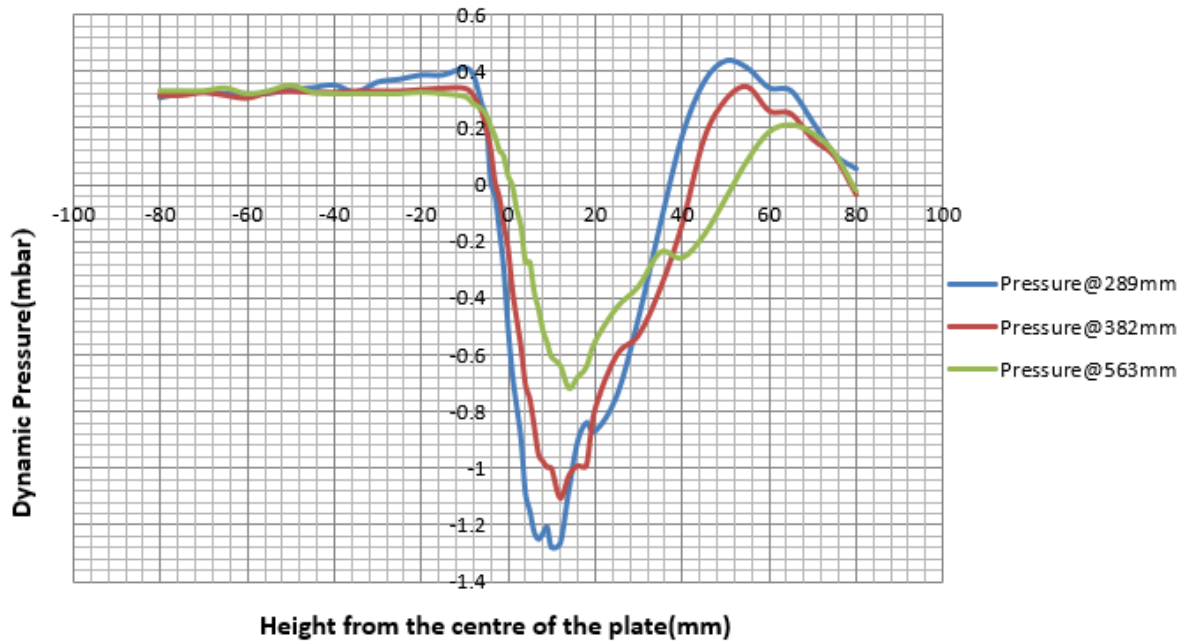
Figure 7.2 Dynamic pressure at different distances from the back of the flat plate at velocity 30m/s
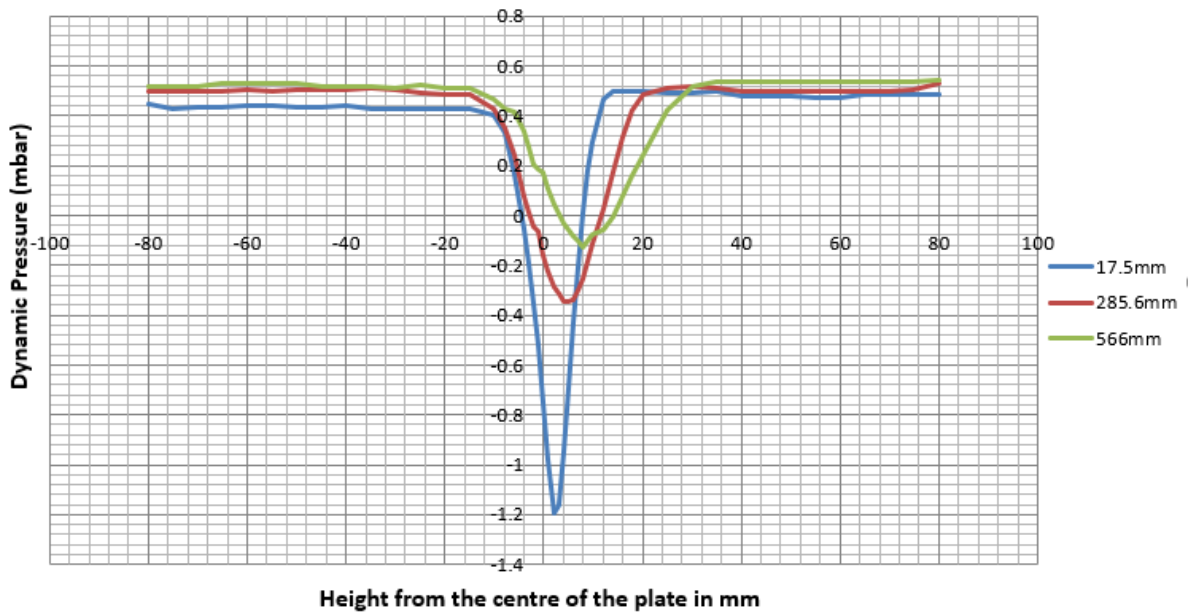
Figure 7.3 Dynamic pressure at different distances from the back of the flat plate at velocity 20m/s

Above, figure 7.3 shows the dynamic pressure profiles for flow past a flat plate at an average wind tunnel velocity of 20 ms^{-1}. The graphs are moved away from the centre of the flat plate however, they are closer to the centre compared to figure 7.1. In this case, dynamic pressure is recovered on both sides and being constant outside the wake profile or in free

stream. As we can see there is no kink on either side of the graph as it reflects the position of the pitot tube in the wind tunnel compared to the previous experiment.

7.3.4 Effect of struts, probe arm and shield on the results

Three struts are used to hold the flat plate and they are placed as shown in figure 7.4. The pitot tube is used to measure the flow characteristics and it is placed right behind the thick strut in stage one. The position of pitot tube affected the results and it reflects in the graphs. As we can see from figure 7.2, the wake is moved away from the centre and there is a kink in the topside of the model graph. The flow is not affected by anything else in the bottom half, however, but the top half of the flat plate is affected by all three struts. The thick struts make a difference to the results and cause viscous flow at the measuring points. So, there is an effect of struts on the results of velocity 30 ms^{-1}. When it comes to the velocity 20 ms^{-1} the struts were not anywhere close to the pitot tube and there is no effect on the results.

As mentioned in the previous chapters, the probe arm is a device to hold the pitot tube and be able to move small distances with the traverse mechanism with minimum disturbances and errors in the flow. The projection of the probe arm to hold the pitot tube into the wind tunnel has very minimal effect on the results. as we can observe from the figure 6.1 and the velocity error is within 1%.

Figure 7.4 Struts to hold the flat plate in the wind tunnel

The shield is a device to make sure flow around the probe arm moves smoothly, obeys the aerodynamics properties and have minimum effect on the flow characteristics. This is manufactured using the 3D printer and polylactic acid (PLA) is the material used. While

conducting the experiment it is screwed to the wind tunnel surface. The length of the pitot tube into the flow direction is long enough to avoid any disturbances caused by the shield, however, the pitot tube is obstructed by the shield and the amount of distance it can move at each station. So, it is taken off from the phase two experiments.

7.3.5 Discussion

It is clear from the graphs; the experimental and theoretical results do not match.

- Because of the experimental setup, and so the following changes are required for the probe arm design.
- The length of the probe arm should be long enough to reach the experimental positions in the wind tunnel.
- The probe arm should be able to cover the required vertical distance at each station to capture the velocity data.

The graphs are clearly stating that wake is diffusing, and the wake profiles are so small to compare to the theoretical results.

7.3.6 Conclusion

I have considered all the issues from phase one to implement in phase two. First, I would like to move from flat plate to circular cylinder to get a decent size of the wake profile. Second, find the right position in the wind tunnel to measure the velocity information and reduce the interference of any other objects like struts and shields. Third, should be able to measure the complete wake profile on both sides of the bluff body.

7.4 Phase two – Circular cylinder

It is established from phase one that changes in the model to identify a constant wake profile. Phase two of the current work extends phase one and aims to reproduce the literature on flow in the wake. The main aim of this phase is to identify the right model, velocity and experimental setup to capture the wake profile. The following sections will complete those outlines with details of the components and conditions used in the experimental stage of this phase.

7.4.1 Experimental details

This section will detail the test components, velocity, measurement planes used in this phase, results, discussion and conclusions.

7.4.2 Test components

Two different types of circular cylinders were used to conduct the experiment and their dimensions are given in table 7.2. Unlike the flat plate, each cylinder was bolted to the top and bottom of the wind tunnel surface. All of them are made of aluminium and machined on the lathe is smoothed by using sandpaper. The length of the cylinder is good enough to neglect the blockage effect. Figure 7.5 shows the side view of the test component.

Number	Diameter in mm	Length of the cylinder in mm	Thickness in mm
1	109	900	5
2	64	900	5

Table 7-2 Phase-two experimental model dimensions

7.4.3 Wind tunnel

All the experiments in this work were carried out in the closed-circuit wind tunnel with velocity varied between 19.64 ms^{-1} to 20.23 ms^{-1} and on an average 20 ms^{-1}. The Reynolds number is $1.45*10^6$, $1.36*10^6$ and $1.1612*10^6$ correspondingly for the diameters 109mm, 64mm and calculated based on the velocity, density and the area of the model. The velocity at each test section is calculated by considering the Betz manometer readings and applied in the following formula.

$$q = \frac{1}{2} * \rho * u^2 = K_1 * z$$

q is the volume of the flow   u is the velocity of the fluid

ρ is the density of the fluid K_1 is the Betz constant and

z is the Betz manometer reading.

The air temperature and velocity of the wind tunnel are being monitored to be within 5% throughout the run.

7.4.4 Measurement planes

The measurements taken in this phase are chosen to determine the right distance to capture the Euler wake and so they all are different from one experiment to the other. Table 7.3 gives a clear understanding of Phase three experiments and it explains about the traverse stations in the wind tunnel with respect to the back of the model. The model was placed in the centre of the wind tunnel with less than 5% tolerance. An inclinometer is used to keep the model parallel to the surface of the wind tunnel. In each experiment, the traverse covered the distance of 400mm together on both sides from the centre of the model at 2mm distance separated from one measuring point to the next measuring point. All the velocity readings are done using pitot tube and hot-wire anemometer and the maximum sample time was 15 seconds using the traverse mechanism.

Number	The diameter of the circular cylinder in mm	Type of Anemometer	Distance from the back of the cylinder to the cross-section in mm
1	109	Pitot tube	• 17.5 • 286 • 566
2	64	Pitot tube	• 50 • 320 • 600 • 1500
3	109	Hot-wire	• 2 • 54.5 • 109 • 218 • 327 • 436

Table 7-3 Measurement planes, anemometers and dimensions of the model used in the phase-two experiment

7.5 Results & Analysis

7.5.1 Mean velocity contours

As can be seen from figure 7.8, the circular cylinder is bolted to the top and bottom of the wind tunnel surface. Pitot tube and hot-wire anemometer were fixed at the width of the centre of the test section. However, the anemometer positions were changed along the length of the test section with respect to the experiments. Once the wind tunnel is ready, Betz manometer was used to set the velocity of the wind tunnel for each experiment. The average dynamic pressure reading at each point in the cross-section is noted. But, in the case of the hot-wire anemometer, the velocity readings are recorded in the computer by using Dantec software. The process of the setup of the software is explained in Appendix B. The circular cylinder with 109mm diameter model experiments was conducted both with pitot tube and hot-wire anemometer. The dynamic pressure graphs were drawn and displayed in the following figure 7.6.

In phase one, it was concluded 20m/sec is the better velocity to conduct the experiments. As each experiment was taking more than an hour time and wind tunnel was going through temperature change, this affected the results. So, velocity is fixed to 20m/sec. The distances traversed in the wind tunnel are the same as flat plate experiments which are 17.5mm, 286mm, and 566mm.
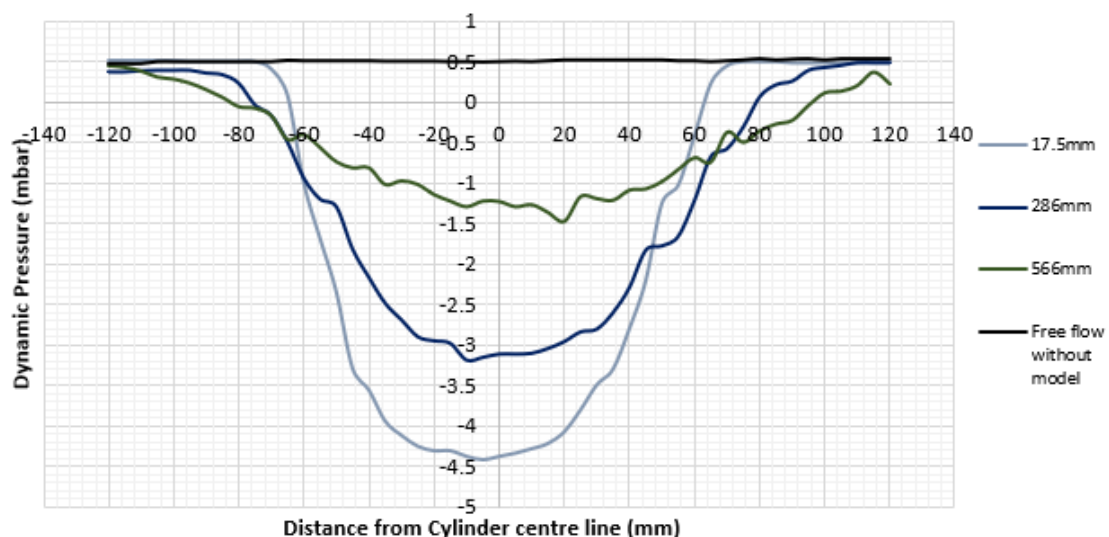
Figure 7.5 Average dynamic pressure behind a circular cylinder longitudinal centre line measured at various set distances behind the cylinder (Cylinder diameter is 109mm, Velocity of air is 20m/s)

From figure 7.5, we can see the dynamic pressure in the free flow experiment is constant across the traverse range without any model in the wind tunnel. The wake profile is captured, and it joins the free stream on both sides of the cylinder in the first two cases of the experiment. However, in the third case from the back of the cylinder, the pitot tube is not able to capture all the velocity profile as with the given set up we can only measure 400mm on both sides of the centre of the cylinder. Hence, I have to reduce the size of the cylinder from 109mm to 64mm to capture all the wake profiles and the new diameter is chosen from experimental understanding.

The next set of experiments were conducted with a change in the size of the cylinder to 64mm the rest of the experimental setup kept the same. The wake velocity measurements at different stations are noted and illustrated in figure 7.6. Once, I have collected the data at stations 17.5mm, 286mm and 566mm and plotted to see the trend, I observe the wake is diffusing. As we can see one extra experiment was conducted compared to the previous experiments. The reason was to identify the way wake diffusion increases from the back of the cylinder. So, a station almost 24 diameters away from the back of the cylinder is chosen. The full wake profile cannot then be traversed at 1500mm, because the width of the downstream wake of a cylinder grows diffusively through viscous and turbulent mixing effects.
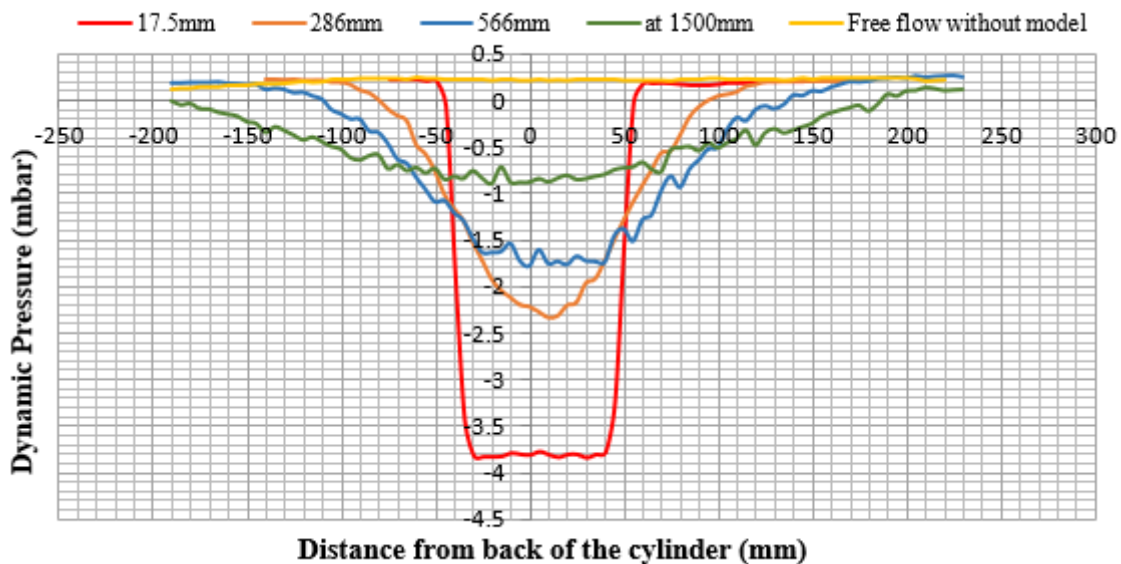
Figure 7.6 Average dynamic pressure behind a circular cylinder longitudinal centre line measured at various set distances behind the cylinder (Cylinder=64mm diameter, measurements made at 20m/s airspeed)

The wake profile in the near region at 17.5mm is not diffused like the other stations in the same graph. The first consideration for the next experiment is to collect the data in the near-field where the wake is not diffused yet. The second consideration is changing the anemometer from the pitot tube to hot-wire. The Reynolds number of every experiment in this work is over 10^6 and the flow is in transitional or nearly turbulent. Hot-wire anemometer is a very good option for such flows and the small size of the sensor which permits minimal flow disturbance of the flow characteristics.

The above two changes are considered for the next experiment with 109mm diameter of a cylinder with hot-wire anemometer. The near-field for this experiment is defined in terms of diameter of the circular cylinder from the back of the cylinder and the distances are 0D,0.5D,1D,2D,3D and 4D. Hot-wire set up is explained in Appendix B. Once the experiment is set up, all the measurements are recorded using hot-wire anemometer software provided by the Dantec. The recorded measurements are plotted in the graphs and they are illustrated in the figure:7.7.
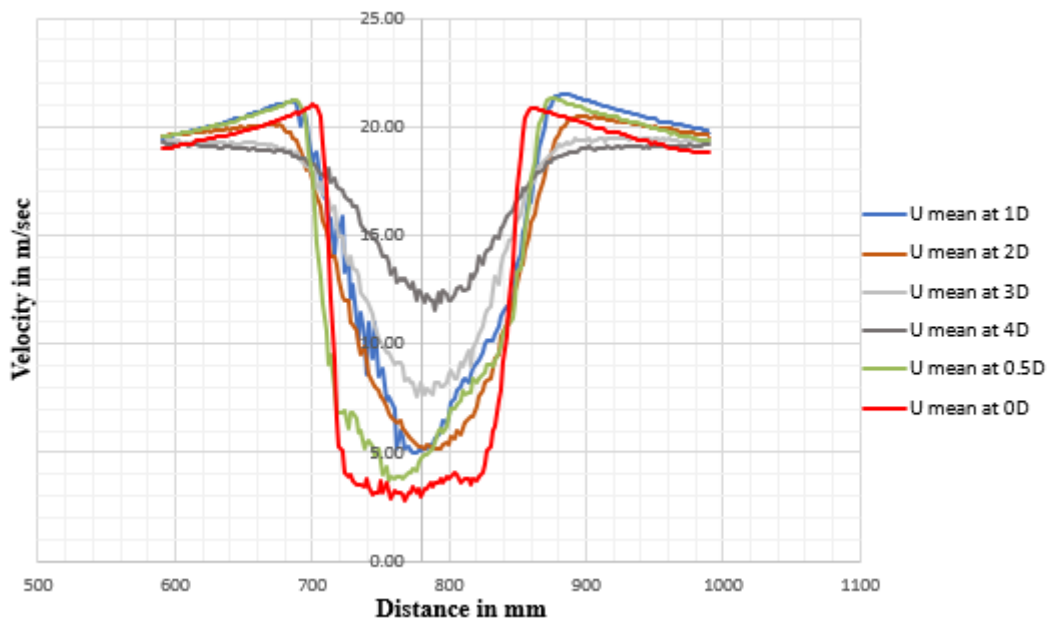
Figure 7.7 Velocity profiles distribution behind a circular cylinder either side of the longitudinal centre line measured at various set distances behind the cylinder vertical centre line (Cylinder =109mm diameter, the velocity of the air=20m/s)

118

7.6 Phase three – Circular cylinder

In phase three, I am interested in conducting the final experiment required to measure the Euler slip wake in the near-field. The following sections will complete those outlines with details of the components and conditions used in the experimental stage of this phase.

7.6.1 Experimental details

Chapter 5 outlined the experimental method used throughout the work of this research and I will be detailing the test components, wind tunnel, measurement planes used in this phase, results, discussion and conclusions in this section.

7.6.2 Test components

I finally conclude the size of the circular cylinder to conduct the final experiment and the details of the model illustrated in the table7-4. The model is screwed to the wind tunnel surface, an aluminium cylinder with 5mm thickness and 900mm length. The surface of the model is smoothed by using sandpaper to the finest accuracy. The length of the cylinder is good enough to neglect the blockage effect.

Number	Diameter in mm	Length of the cylinder in mm	Thickness in mm
1	90	900	5

Table 7-4 Model dimensions used in phase three experiment

7.6.2.1 Wind tunnel

As mentioned in earlier phases, the wind tunnel is a closed-circuit wind tunnel with velocity varied between 20.10 m/s to 20.3 m/s and on an average 20.2m/s is considered in this phase. The Reynolds number for the corresponding velocity, density and the diameter of the model varies between $1.17*10^5$ to $1.23*10^5$. The velocity at each test section is calculated by considering the Betz manometer readings. The air temperature and velocity of the wind tunnel are monitored to be within 5% throughout the run.

7.6.2.2 Measurement planes

The traversing stations for this phase are listed in table 7.5 and they are been consider based on a smoke test which shows in the figure7.8. The model was placed in the centre of the wind tunnel with less than 5% tolerance. An inclinometer is used to keep the model parallel to the surface of the wind tunnel. In each experiment, the traverse covered the distance of 400mm

together on both sides from the centre of the model at 2mm distance separated from one measuring point to the next measuring point. All the velocity readings from a hot-wire anemometer and the maximum sample time were 15 seconds using the traverse mechanism.

Number	The diameter of the circular cylinder in mm	Type of anemometer	Distance from the back of the cylinder to the cross-section in mm
1	90	Hot-wire anemometer	• 0D • 0.5D • 1D

Table 7-5 Measurement planes, anemometers and dimensions of the model used in the phase-two experiment

Figure 7.8 Smoke test for flow past a circular cylinder.

The flow in the wake description is oscillating similar to Karman vortex shedding. But more like a wave motion due to the turbulence in the flow. However, we assume the mean steady motion. From experimental results frequency of the Oscillation for vortices in the wake is about 1HZ.

7.6.3 Results & Analysis

7.6.3.1 Mean velocity Contours

The hot-wire anemometer is used to measure the mean velocity at each traverse station in the wind tunnel. The traverse stations are 0D, 0.5D, and 1D from the back of the cylinder. The data is used to draw a graph and it is illustrated in the following figure 7.9. As we can see the wake profiles are much more aligned compared to the previous experiment with 109mm diameter. The graph suggests that wake profile is not dominated by viscous forces at the traverse stations considered and the contours look as if the constant Euler slip wake has been maintained. Now, if we look at the whole picture, we have the results for uniform flow past a circular cylinder of diameter 90mm in the low-speed wind tunnel operating at a mean velocity of 20.2 m/s. This gives the Reynolds number for the flow around 10^5 so it is in the mean steady laminar flow region, rather than in the transition or turbulent flow. The results from each station are given in the following figure 7.9 without blockage effects.

Even though blockage corrections are negligible, the correction factor is included for each station and the velocity profile illustrated in figure 7.10. The underlying goal of this correction is to improve the accuracy of wind tunnel testing. The total blockage is equal to the sum of the velocity increment caused by solid blockage and wake blockage. The presence of the tunnel walls confining the flow around a model in the test section reduces the area through which the air must flow as compared to free-air conditions and hence, by continuity and Bernoulli's equation, increase the velocity of the air as it flows in the vicinity of the model. This increase of the velocity, which is approximated as constant over the model for customary model sizes is called solid blockage. The following formula gives the solid blockage correction for two-dimensional tunnels is

$$\varepsilon^{sb} = \frac{K_1 * (\text{model volume})}{(c)^{3/2}}$$

Where K_1 equals 0.74 for this model, C is the tunnel cross-section area and ε^{sb} is a solid blockage. An incremental velocity evaluated that is added to the tunnel results to allow for wake blockage.

Wake blockage is $\varepsilon^{wb} = ¼ [(d/h)] C_D$

where, $C_D = D / ((1/2) \rho U^2 A)$
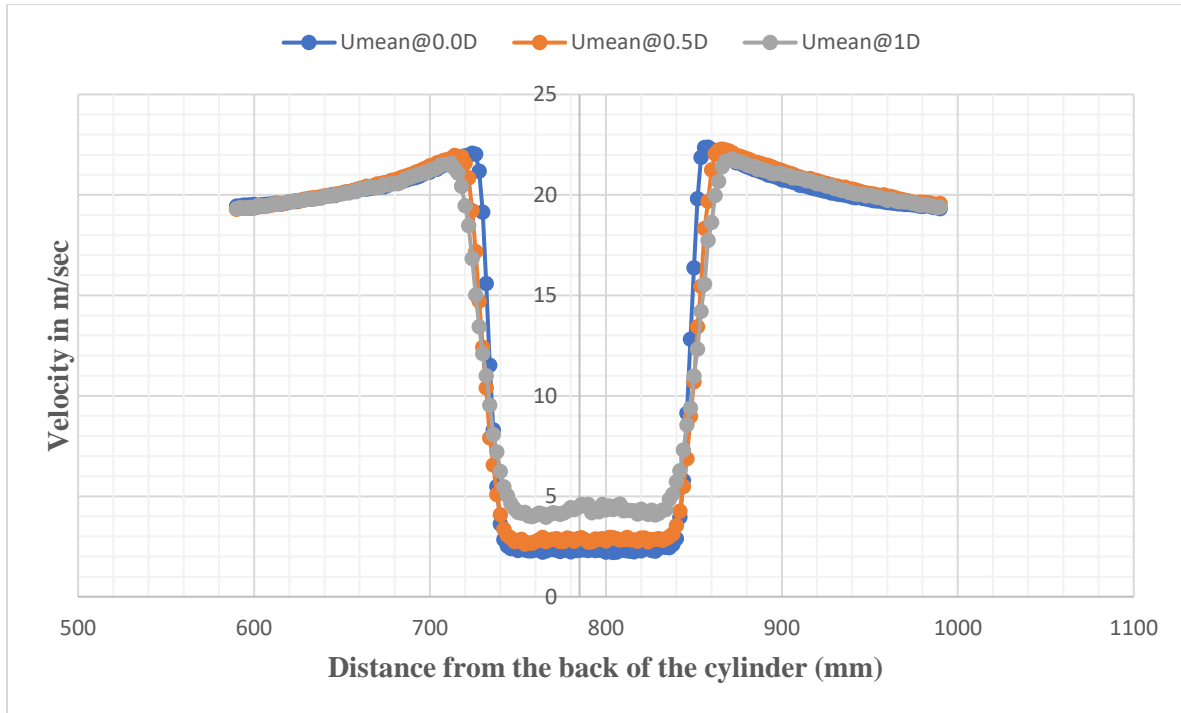
Figure 7.9 Velocity profiles distribution behind a circular cylinder either side of the longitudinal centre line measured at various set distances behind the cylinder vertical centre line (Cylinder =90mm diameter, the velocity of the air=20m/s)

Where d is the model cross-section area, C_D is the uncorrected drag coefficient, h is the height of the wind tunnel, D is an uncorrected drag, ρ is the density of the air in the wind tunnel, A is the cross-sectional area of the model, U is the velocity of the fluid and ε^{wb} is wake blockage.

$$\text{Velocity correction is } V_\infty = V_B * (1 + \varepsilon^{sb} + \varepsilon^{wb})$$

V_B is the uncorrected measured velocity and V_∞ is the corrected measured velocity. The above formulas are used to measure the corrected velocity for all the cases and the velocity profile are illustrated in figure 7.10 (Barlow, H. Rae and Pope, 1999).

From theory, we can recollect the total velocity is the sum of potential and wake velocity. Total velocity, potential velocity, and wake velocity are represented by **u, $\nabla\phi$** and **ω** respectively. Total velocity is measured from wind tunnel tests, potential velocity is calculated by interpolating the measured velocity from the experiments just outside the wake range by using Fortran programming, and the wake velocity is the difference between the above two velocities. The equation for finding wake velocity is

$$\omega = u - \nabla\phi$$

122
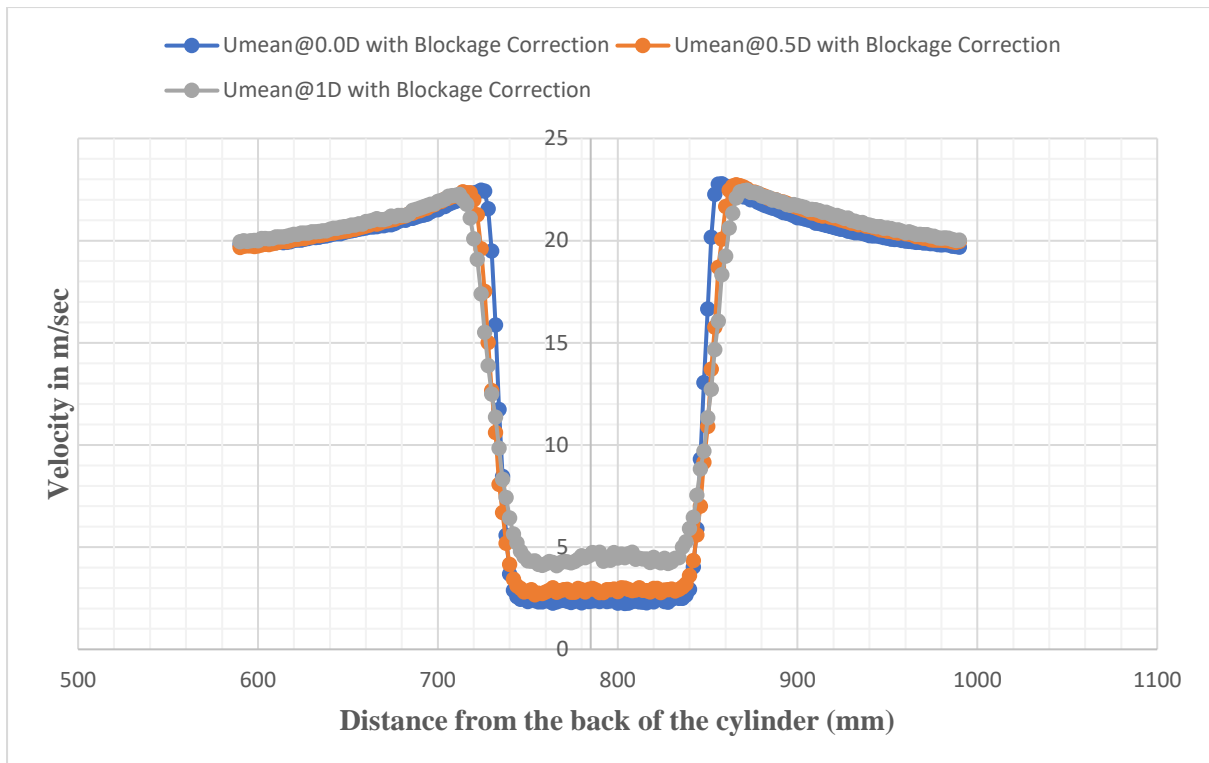
Figure 7.10 Velocity profiles with blockage corrections distribution behind a circular cylinder either side of the longitudinal centre line measured at various set distances behind the cylinder vertical centre line (Cylinder =90mm diameter, the velocity of the air=20m/s)

This reveals the wake velocity at each station. A numerical program simulating flow past a circular cylinder has been written in the Fortran programming language. This program compares theoretical and experimental results of the streamwise velocity at downstream wake cross-sections. It then attempts to match the theory and experiment through an optimisation procedure. If a match is found, then it provides experimental verification of the theory. In particular, it demonstrates that a wake velocity (additional to the standard inviscid flow velocity potential) exists that has the same cross-sectional profile at every downstream wake cross-section. This is an outcome of the new theoretical approach for the wake velocity that, if shown to be present, provides strong experimental evidence for the theory.

The program takes in the raw experimental velocity data from the hot-wire anemometer and then normalizes it with the free-stream value. The cross-sectional position is also obtained by the probe arm controlled by the traverse mechanism, and these distances are also normalised to the radius of the circular cylinder. The velocity readings are also smoothed by averaging, noting that they must be symmetric about the streamwise axis that goes through the centre of the circular cylinder. The percentage change from this smoothing is of order 0.34%. The optimisation procedure calculates the error between the theoretical and

123

experimental velocity values at the different stations and then attempts to minimise it by choosing a different axial distribution of Eulerlets. The error is calculated by summing the absolute difference in theoretical and experimental velocity at 200 positions along each of the three wake cross-sections. The error is then minimised by selecting the particular Eulerlet distribution that gives the least value.

The Eulerlet distribution is given by a polynomial profile symmetric about the streamwise axis, so only even polynomial powers need to be considered. In this case, each coefficient in front of the power is considered a parameter and varied within a range sufficient to capture the minimum error. The following table 7.6 gives an idea of variables and total error and a total number of iterations considered for different steps. Three constants were considered in this particular simulation.

Polynomial profile considered for $d(x_2)$ is an approximated by a fourth-order polynomial and $d(x_2) = a_0 + a_2 x_2^2 + a_4 x_2^4$, where a_0, a_2 and a_4 are coefficients. A polynomial profile symmetric to the streamwise axis with even powers were considered. Three coefficients in the polynomial equation were considered. The equation is only considered with even powers and for every iteration, all coefficients were determined by best fit to the curve to define the exact wake distribution to match with the experimental results.

Number of iterations	2	5	10	20	30	40	50
a_0	0.66	0.60	0.3000	0.300	0.300	0.300	0.30
a_2	0.66	0.65	0.7200	0.6900	0.7000	0.7050	0.696
a_4	-0.66	-0.50	-0.2600	-0.215	-0.2300	-0.2375	-0.224
Total Error	2.5631	2.5427	2.50920	2.4966	2.493781	2.4951	2.4945

Table 7-6 Polynomial coefficients and total error values for different iterations.

After an eight order polynomial equation, the error was not reduced any further and the distribution is almost the same for different order polynomial equations with varied iterations as illustrated in figure 7.11.
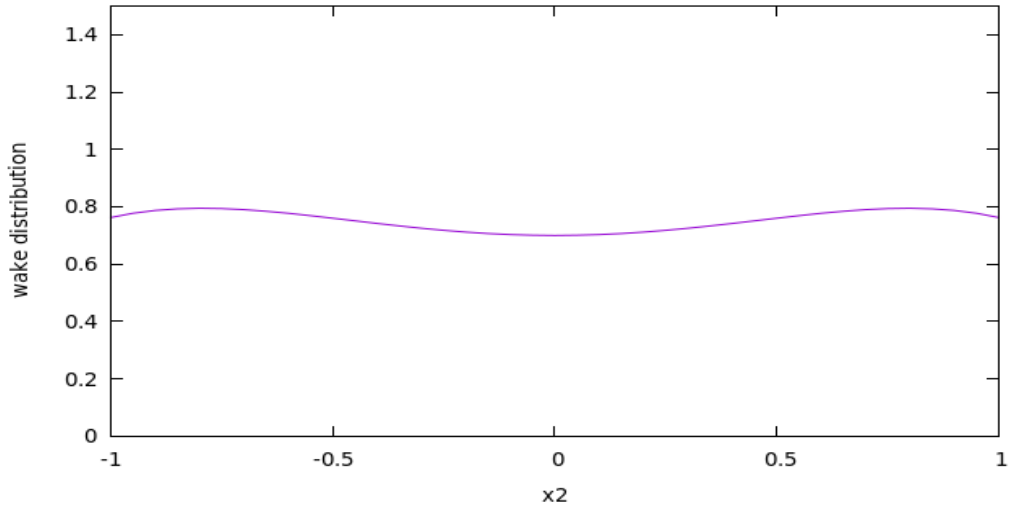
Figure 7.11 Wake distribution result from the numerical program using experimental data.
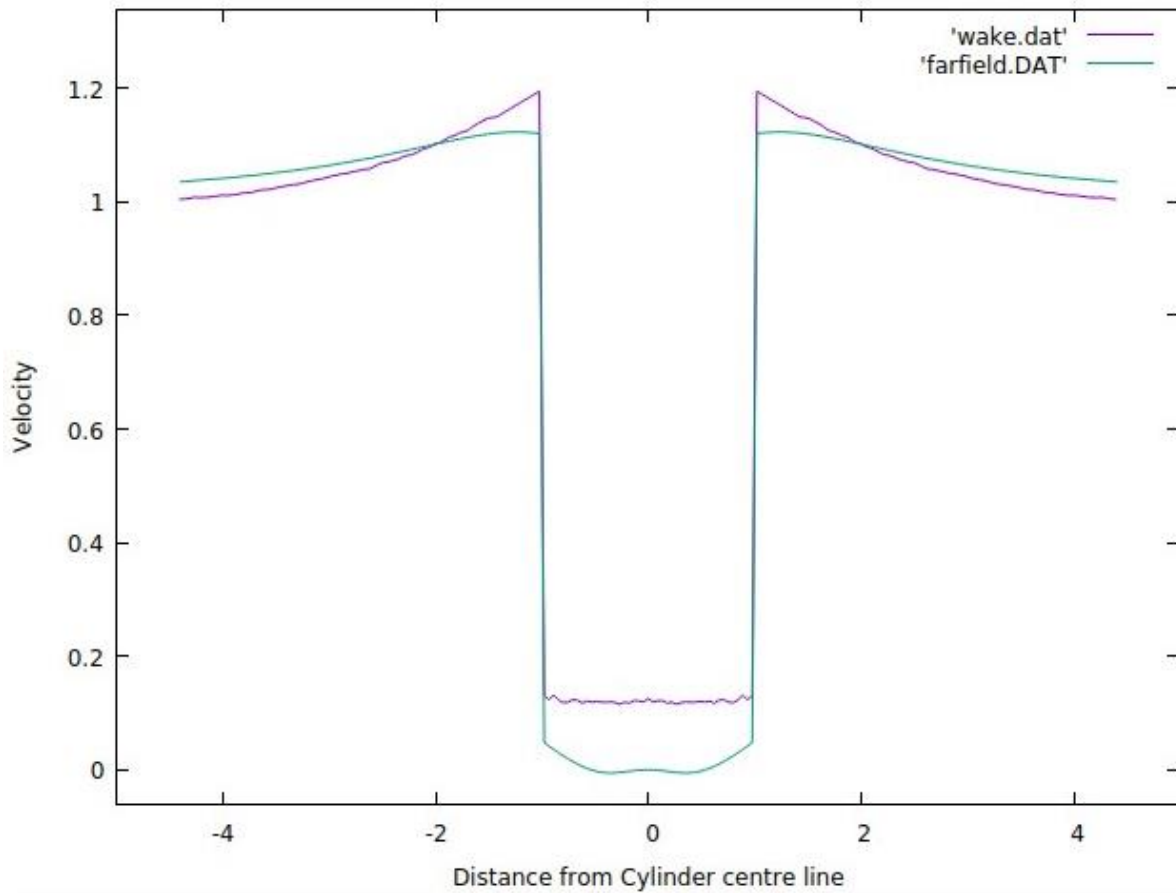
Figure 7.12 Comparison between theoretical and experimental results.

Figure 7.12 illustrates mean velocity result for zero diameter distance from the back of the cylinder for both experimental (violet colour line) and numerical modelling (green line). The main difference between theoretical and experimental results was the rise of the lip in the

125

free stream before mean velocity drops into the wake velocity. Not only that, but the wake velocity in the experiments were also almost flat (constant in the wake).
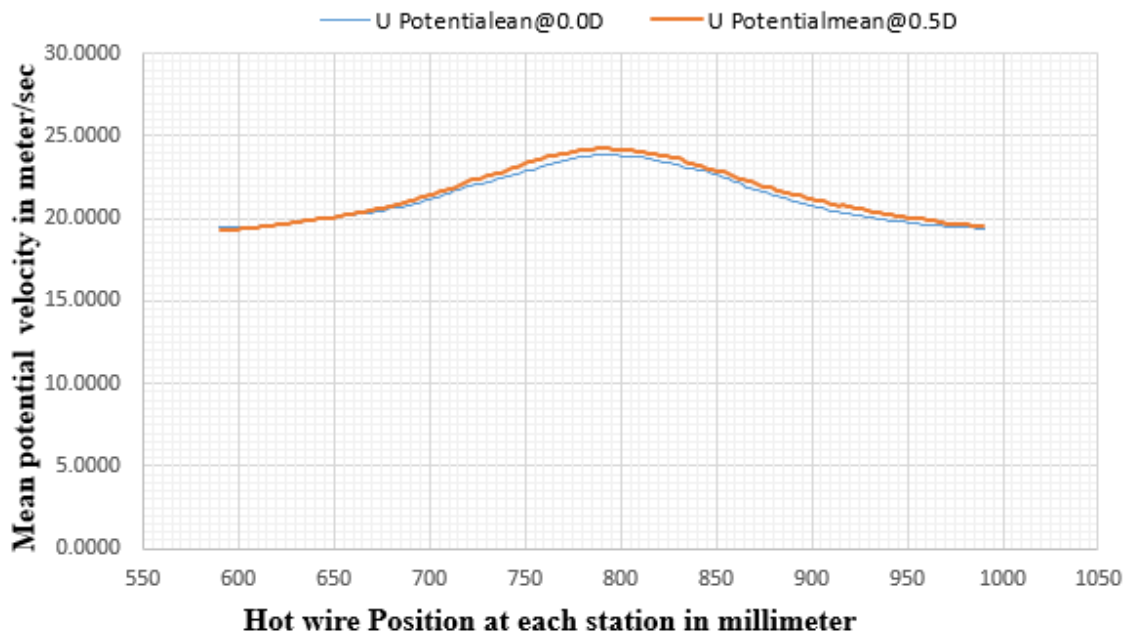
Figure 7.13 Potential velocity distribution for the circular cylinder at different stations from the back of the cylinder at 0D and 0.5D
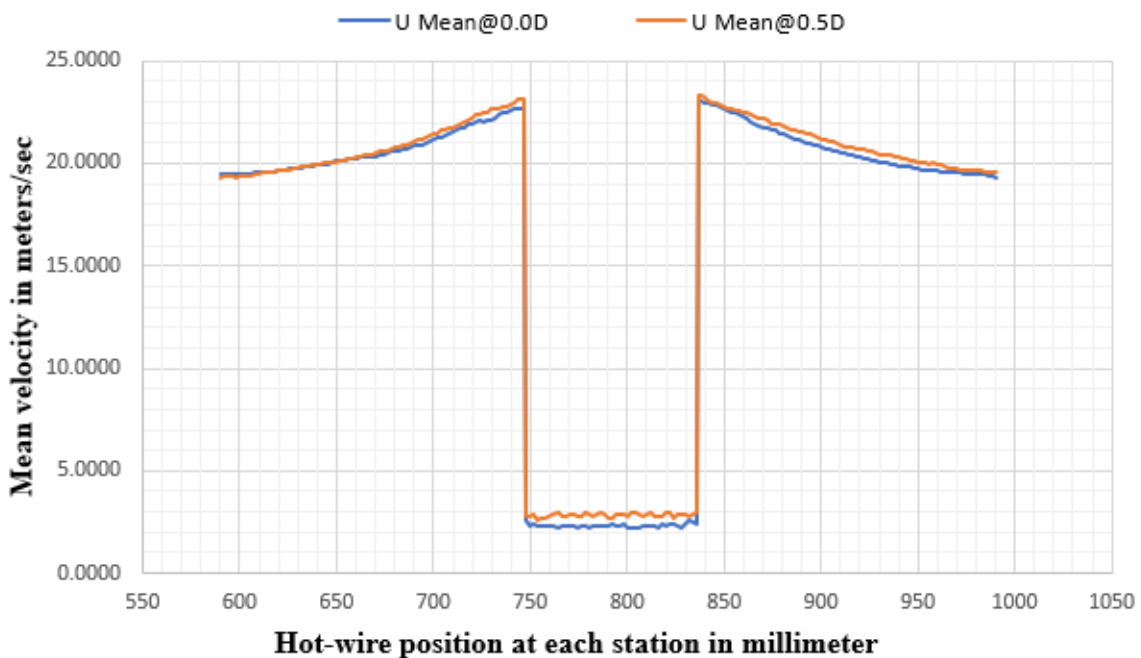
Figure 7.14 Mean velocity distribution for the circular cylinder at different stations from the back of the cylinder at 0D and 0.5D with potential velocity raise before velocity drops into the wake.

From figure 7.13 and 7.14, the rate of loss of potential velocity is the same as the rate of loss of total mean velocity for 0D and 0.5D. That means from 0D to 0.5D the difference of total and potential velocity are the same. Polynomial interpolation now gives an accurate solution and to captures the Euler slip wake for stations 0D and 0.5D and is given in figure 7.15.
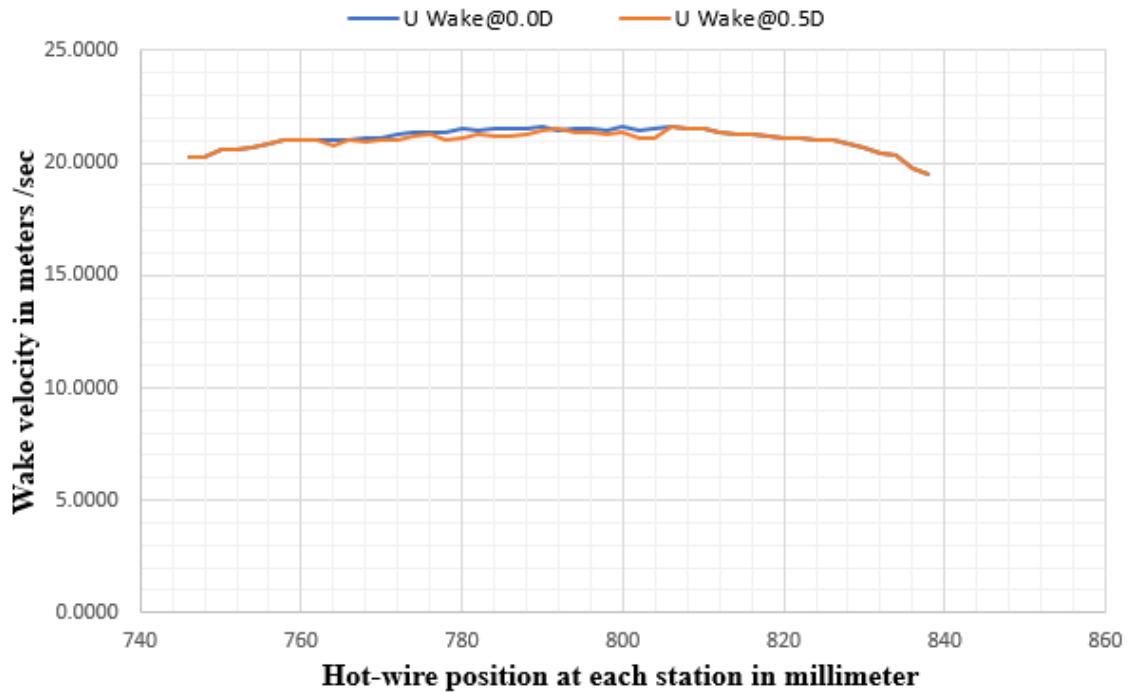
Figure 7.15 Wake velocity at different stations in the wind tunnel from the back of the cylinder at different stations 0D and 0.5D and it shows constant.

Chapter 8

8 Conclusions and future work

8.1 Conclusions

The dissertation has covered theoretical, numerical and experimental aspects of a recently developed Eulelet theory, support was given in the theoretical development with Chadwick and Christian, by application to a circular cylinder using Fourier analysis (Chadwick, Christian and Chalasani, 2018). A Fortran numerical code was developed, based on the Eulerlet theory to predict the flow characteristics past a circular cylinder. In this model, it is seen that an Euler wake velocity exists with constant downstream wake cross-section.

The main thrust of this thesis is to experimentally test the new theory for flow past a circular cylinder in a low-speed wind tunnel by evidencing the existence of the Euler wake velocity. This entailed the use of a hot-wire anemometer attached to a novel design traverse mechanism. The results demonstrate that at zero and half a diameter in the downstream wake, the wake velocity has the same profile, giving credence to the existence of the Euler wake velocity and therefore experimental verification of the Eulerlet theory.

However, at one diameter length in the downstream wake, the wake velocity does not display the profile expected from the Eulerlet theory. An explanation for this is given from smoke tests. In these smoke tests, it is seen that turbulence in the flow causes smoke particles to enter into the wake at one diameter downstream, whereas as half a diameter downstream this does not occur. Presence of the smoke particles means energy is entering into the wake well because of the turbulence. This appears to be demonstrated by the increased velocity in the wake well.

8.2 Future work

Future work will be to evidence the existence of the Euler wake for other flows. In particular, bluff bodies with various elliptical cross-section can be considered. The increased slenderness should mean that turbulence contamination in the wake is delayed, thereby providing a more convincing experimental test for the Eulerlet theory. The flow field is generally quite sensitive to disturbances for a given Reynolds number. Because of the problems faced in this work, it will be a good idea to work on particle tracking in the flow domain by using non-intrusive optical methods like Particle Image Velocimetry (PIV). The

thin flat image gives a clear picture of how the fluid particles are distributed at different stations downstream. It helps to understand at what stations we can capture the data for a given experimental setup.

The Eulerlet theory can be used to calculate the lift force for both 2-dimensional and 3-dimensional problems. Another problem with Euler flow is the plethora of models available, from potential flow slender -body theories, thin-aerofoil theory, panel methods and vortex lattice methods, all seemingly unconnected and disparate. Eulerlets can be extended to provide an overarching general framework that encompasses all these methods and that can then be extended for the next generation time-independent and time-oscillatory manoeuvring problems required in the development of novel swimming/flapping Unmanned Aerial Vehicles (UAVs) and Unmanned Submersible Vehicles (USVs).

9 References

Abramowitz, M. and Stegun, I. N. (1972) *Handbook of Mathematical Functions*. 10th editions. Washington, D.C., United States.

Barlow, J. B., H. Rae, W. and Pope, A. (1999) *Low-Speed Wind Tunnel Testing, 3rd Edition*. 3rd edn. NewYork: John Willey & Sons. Available at: http://eu.wiley.com/WileyCDA/WileyTitle/productCd-0471557749.html.

Batchelor, G. K. (2012) 'An Introduction to the Fluid Dynamics.', *Cambridge University Press*. Available at: https://doi.org/10.1017/CBO9780511800955.

Beck, B. T., Payne, G. and Heitman, T. (2010) 'The aerodynamics of the pitot-static tube and its current role in non-ideal engineering applications', *ASEE Annual Conference and Exposition, Conference Proceedings*, 15.1204(1), pp. 1–16.

Bengt, F. (1980) 'A numerical study of steady viscous flow past a circular cylinder', *Journal of Fluid Mechanics*, 98(4), pp. 819–855. doi: 10.1017/S0022112080000419.

Bertin, J. J. and Smith, Michael, L. (2002) *Aerodynamics for Engineers*. 4th edition. Prentice-Hall. Available at: https://www.pearson.com/us/higher-education/program/Bertin-Aerodynamics-for-Engineers-6th-Edition/PGM152588.html.

Borker, N. S. and Koch, D. L. (2018) 'Slender body theory for particles with non-circular cross-sections', *Journal of Fluid Mechanics*, 877, pp. 1098–1133. doi: 10.1017/jfm.2019.625.

Burr, K. P. (2003) *Marine Hydrodynamics*, *MIT-Department of Ocean Engineering*. Available at: http://web.mit.edu/fluids-modules/www/potential_flows/LecturesHTML/lec02/lecture2.html.

Chadwick, E. (1998) 'The far-field Oseen velocity expansion', *Proceedings of the Royal Society A: Mathematical, Physical and Engineering Sciences*, 454(1976), pp. 2059–2082. doi: 10.1098/rspa.1998.0249.

Chadwick, E. (2002) 'A slender-body theory in Oseen flow', *Proceedings of the Royal Society A: Mathematical, Physical and Engineering Sciences*, 458(2024), pp. 2007–2016. doi: 10.1098/rspa.2002.0996.

Chadwick, E. (2005) 'A slender-wing theory in potential flow', *Proceedings of the Royal Society A: Mathematical, Physical and Engineering Sciences*, 461(2054), pp. 415–432.

Chadwick, E. (2006) 'The vortex line in steady, incompressible Oseen flow', *Proceedings of the Royal Society A: Mathematical, Physical and Engineering Sciences*, 462(2066), pp. 391–401. doi: 10.1098/rspa.2005.1593.

Chadwick, E. *et al.* (2010) 'Experimental verification of an Oseen flow slender body theory', *Journal of Fluid Mechanics*, 654, pp. 271–279. doi: 10.1017/S0022112010001333.

Chadwick, E. A. (2013) 'The far-Field green's integral in stokes flow from the boundary integral formulation', *CMES - Computer Modeling in Engineering and Sciences*, 96(3), pp. 177–184. doi: 10.3970/cmes.2013.096.177.

Chadwick, E., Christian, J. and Chalasani, K. (2018) 'Using eulerlets to model steady uniform flow past a circular cylinder', *European Journal of Computational Mechanics*. Taylor & Francis, 27(5–6), pp. 469–478. doi: 10.1080/17797179.2018.1550960.

Chadwick, E., Christian, J. and Chalasani, K. (2019) 'A theoretical description of Euler flow using Eulerlets for a body in a uniform flow field', *Physics of Fluids*, 31, p. 047106. doi:

10.1063/1.5088132.

Chadwick, E. and Hatam, A. (2007) 'The physical interpretation of the lift discrepancy in Lanchester-Prandtl lifting wing theory for Euler flow, leading to the proposal of an alternative model in Oseen flow', *Proceedings of the Royal Society A: Mathematical, Physical and Engineering Sciences*, 463(2085), pp. 2257–2275. doi: 10.1098/rspa.2007.1870.

Chadwick, E. and Kapoulas, A. (2014) 'Using Eulerlets to give a boundary integral formulation in Euler flow and discussion on applications', *CMES - Computer Modeling in Engineering and Sciences*, 102(4), pp. 331–343.

Choi, C. K. and Kwon, D. K. (1998) 'Wind tunnel blockage effects on aerodynamic behaviour of bluff body', *Wind and Structures, An International Journal*, 1(4), pp. 351–364. doi: 10.12989/was.1998.1.4.351.

Comte-bellot, G. (1976) 'Hot-wire anemometry', *Fluid Mech*, 8(1), pp. 209–231. Available at: https://doi.org/10.1146/annurev.fl.08.010176.001233.

Coutanceau, M. and Bouard, R. (1977) 'Experimental determination of the main features of the viscous flow in the wake of a circular cylinder in uniform translation. Part 1. Steady flow', *Journal of Fluid Mechanics*, 79(2), pp. 231–256. doi: 10.1017/S0022112077000135.

Craft, T. . (2010) *Inviscid Flows*, *The University of Manchester*. DOI: http://cfd.mace.manchester.ac.uk/twiki/pub/Main/TimCraftNotes_All_Access/fl3-inviscid.pdf.

Darrigol, O. and Frisch, U. (2007) *From Newton'sMechanics to Euler Equations*, *Physics S in press*. Available at: https://homepages.warwick.ac.uk/~masbu/turb_symp/sept07_presentations/euler-warwick2007.pdf.

Day, M. A. (1990) 'The no-slip condition of fluid dynamics', *Erkenntnis*, 33(3), pp. 285–296. doi: 10.1007/BF00717588.

Dennis, S C R and Shimshoni, M. (1965) 'The Steady Flow of a Viscous Fluid past a Circular Cylinder', *Aeronautical Research Council*, (797). Available at: http://naca.central.cranfield.ac.uk/reports/arc/cp/0797.pdf.

Dennis, S. C. R. and Gau-Zu, C. (1970) 'Numerical solutions for steady flow past a circular cylinder at Reynolds numbers up to 100', *Journal of Fluid Mechanics*, 42(1970), pp. 471–489. Available at: https://doi.org/10.1017/S0022112070001428.

Dennis, S. and Kochbiyik, S. (1990) 'The solution of two-dimensional oseen flow problems using integral conditions', *IMA Journal of Applied Mathematics (Institute of Mathematics and Its Applications)*, 45(1), pp. 1–31. doi: 10.1093/imamat/45.1.1.

Van Dyke, M. and White, F. M. (1982) *An Album of Fluid Motion*, *Journal of Fluids Engineering*. California, United States: The Parabolic press.

Dynamics, D. (2017) 'Constant Temperature Anemometer'. Denmark. Available at: https://www.dantecdynamics.com/solutions-applications/solutions/fluid-mechanics/constant-temperature-anemometry-cta/#:~:text=Constant Temperature Anemometry (CTA)%2C, probes inserted into the flow.

E. C. Maskell (1963) 'A Theory of the Blockage Effects on, Bluff Bodies and Stalled Wings in a Closed Wind Tunnel', *Aeronautical Research Council Reports and Memoranda*, (3400).

Elcrat, A. *et al.* (2000) 'Some steady vortex flows past a circular cylinder', *Journal of Fluid Mechanics*, 409, pp. 13–27. Available at: https://www.cambridge.org/core/journals/journal-

of-fluid-mechanics/article/some-steady-vortex-flows-past-a-circular-cylinder/6EFA98118B85F1D19AE13523914786EB.

Favier, D. (2010) 'The Role of Wind Tunnel Experiments in CFD Validation', *Encyclopedia of Aerospace Engineering*. doi: 10.1002/9780470686652.eae034.

Fehrm, B. (2017) 'Aircraft drag reduction', *Leeham News and Analysis*. Available at: https://leehamnews.com/2017/12/22/bjorns-corner-aircraft-drag-reduction-part-10/.

Filon, L. N. G. (1926) 'The Forces on a Solid Body in a Stream of Viscous Fluid', *Philosophical Transactions of the Royal Society A: Mathematical, Physical and Engineering Sciences*, 236(759), pp. 25–75. doi: 10.1098/rsta.1936.0010.

Filon, L. N. G. (1927) 'On the Second Approximation to the "Oseen" Solution for the Motion of a Viscous Fluid', *Philosophical Transactions of the Royal Society A: Mathematical, Physical and Engineering Sciences*, 227(647–658), pp. 93–135. doi: 10.1098/rsta.1928.0004.

Fischer, O. (2018) *Investigation of Correction Methods for Interference Effects in Open-Jet Wind Tunnels*, *Investigation of Correction Methods for Interference Effects in Open-Jet Wind Tunnels*. doi: 10.1007/978-3-658-21379-4.

Fishwick, N and Chadwick, E. (2006) 'The evaluation of the far-field integral in the Green's function representation for steady Oseen flow', *Phys. Fluids*, 18(113101-1-113101–5). Available at: http://dx.doi.org/10.1063/1.2388248.

Ghosh, S., Muste, M. and Stern, F. (2010) *Experimental Fluid Dynamics and Uncertainty Assessment Methodology*. Available at: Experimental Fluid Dynamics and Uncertainty Assessment Methodology.

Grove, A. S. *et al.* (1964) 'An Experimental investigation of the steady separated flow past a circular cylinder', *Journal of Fluid Mechanics*, 19(1), pp. 60–80. doi: 10.1017/S0022112064000544.

Gustafsson, J. and Protas, B. (2013) 'On oseen flow for large Reynolds numbers', *Theoretical and Computational Fluid Dynamics*, 27(5), pp. 665–680. doi: 10.1007/s00162-011-0256-4.

Hyvärinen, A. and Hyvärinen, H. (2015) 'Investigation of blockage correction methods for full-scale wind tunnel testing of trucks', *KTH, Royal Institute of Technology*. Available at: https://www.semanticscholar.org/paper/Investigation-of-blockage-correction-methods-wind-Hyvärinen/3bab2be08ea029384917ce250d5b39e872124e99.

Imai, I. (1951) 'On the asymptotic behaviour of viscous fluid flow at a great distance from a cylindrical body, with special reference to Filon's paradox', *Proceedings of the Royal Society of London. Series A. Mathematical and Physical Sciences*, 208(1095), pp. 487–516. doi: 10.1098/rspa.1951.0176.

Jensen, K. . (2004) 'Flow Measurement Techniques', *ENCIT (Belgium)*, 15(2 (APRIL, 1974)), pp. 96–106. doi: 10.1016/b978-0-7506-1305-7.50011-8.

Johnson, C. and Hoffman, J. (2010) *D'Alembert's Paradox: new resolution*, *The world as Computation*. Available at: https://claesjohnsonmathscience.wordpress.com/article/d-alembert-s-paradox-yvfu3xg7d7wt-2/.

Jones, R.T, N. R. (1979) 'Classical Aerodynamic Theory', *NASA Reference Publication*, (December). Available at: http://web.stanford.edu/~cantwell/AA200_Course_Material/AA200_References/Jones_Classical_Aerodynamic_Theory.pdf.

Jorgensen, F. E. (2002) *How to measure turbulence with hot-wire anemometers - a practical*

guide. Edited by D. Dynamics. Skovlunde, Denmark. Available at: https://www.dantecdynamics.com/components/hot-wire-and-hot-film-probes/.

Kaplun (1957) 'Low Reynolds Number Flow Past a Circular Cylinder', *Journal of Mathematics and Mechanics*, 6(5), pp. 595–603. doi: 10.1093/oseo/instance.00225923.

Kartha, S. A. (2017) *Fluid mechanics Notes*. Available at: http://www.iitg.ac.in/kartha/CE203FM/Lectures/Week6/Lecture_17 The Material Derivative.pdf.

Kiya, M. and Arie, M. (1977) 'An Inviscid Bluff-Body Wake Model with the Far-Wake Displacement Effect', *Transactions of the Japan Society of Mechanical Engineers*, 43(369), pp. 1755–1764. doi: 10.1299/kikai1938.43.1755.

Kovasznay, L.S.G (Department of Aeronautics, T. J. H. U. (1949) 'Hot-wire investigation of the wake behind cylinders at low Reynolds numbers', *Proceedings of the Royal Society of London. Series A. Mathematical and Physical Sciences*, 198(1053), pp. 174–190. doi: 10.1098/rspa.1949.0093.

Lamb, F. R. S. (1911) 'On the Uniform Motion of a Sphere through a Viscous Fluid', *Rayleigh, Phil.*, 21(29), p. 121.

László, S. and Wiedemann, E. (2012) 'Incompressible Fluid Flows', *Arch.Rational Mech. Anal.*, 206, pp. 333–366. doi: 10.1007/s00205-012-0540-5 Young.

Lauchle, G. C. (1978) 'Horizontal Buoyancy Effects on the Pressure Distribution of an Axisymmetric body operating in a Cylinder Duct', *Naval Sea Systems Command*.

Lester, W. G. S. (1960) 'The Flow past a Pitot Tube at Low Reynolds Numbers', *Report and Memoranda Aeronautical ...*, (3240). Available at: http://aerade.cranfield.ac.uk/ara/arc/rm/3240.pdf.

Lighthill, M. J. (1960) 'Note on the swimming of slender fish', *Journal of Fluid Mechanics*, 9(2), pp. 305–317. doi: 10.1017/S0022112060001110.

Lighthill, M. J. (1971) '5. Large-Amplitude Elongated-Body Theory of Fish Locomotion', *Mathematical Biofluiddynamics*, pp. 103–116. doi: 10.1137/1.9781611970517.ch5.

Lindgren, E. R. (1999) 'The Motion of a Sphere in an Incompressible Viscous Fluid at Reynolds Numbers Considerably Less Than One', *Physica Scripta*, 60(2), pp. 97–110. doi: 10.1238/physica.regular.060a00097.

MacMillan, F. a. (1957) 'Experiments on Pitot-Tubes in Shear Flow', *Aeronautical Research Council Reports and Memoranda*, p. 14. Available at: https://www.researchgate.net/deref/http%3A%2F%2Fstacks.iop.org%2FMST%2F14%2F1449.

Martin, P. A. and Rizzo, F. J. (1995) 'Partitioning, boundary integral equations, and exact Green's functions', *International Journal for Numerical Methods in Engineering*, 38(20), pp. 3483–3495. doi: 10.1002/nme.1620382007.

Newman, J. N. (1970) 'Applications of Slender-Body Theory in Ship Hydrodynamics', *Annual Review of Fluid Mechanics*, 2(1), pp. 67–94. doi: 10.1146/annurev.fl.02.010170.000435.

Pope, A. (1961) 'Wind Tunnel calibration Techniques', *North Atlantic Treaty Organization Advisory Group for Aeronautical Research and Development*, 294167(54), p. 13. Available at: https://arc.aiaa.org/doi/abs/10.2514/4.476624.

Prabhakara, S. and Deshpande, M. D. (2004) 'The no-slip boundary condition in fluid mechanics', *Resonance*, 9(5), pp. 61–71. doi: 10.1007/bf02834016.

Proudman, I. and Pearson, J. R. A. (1957) 'Expansions at small Reynolds numbers for the flow past a sphere and a circular cylinder', *Journal of Fluid Mechanics*, 2(3), pp. 237–262. doi: 10.1017/S0022112057000105.

Qin, R. and Duan, C. (2017) 'The principle and applications of Bernoulli equation', *Journal of Physics: Conference Series*, 916(1). doi: 10.1088/1742-6596/916/1/012038.

Rao, B. R. and Sahitya, R. (2015) 'Numerical And Experimental Investigation of The Flow Field Around NACA 0012 Aerofoil', *IRD India*, (4), pp. 18–26. Available at: https://www.semanticscholar.org/paper/Numerical-And-Experimental-Investigation-of-The-Rao-Sahitya/608b0a5d092f4bec9d3b49529f19a4a4f62502e0.

Robinson, R. A. *et al.* (2004) 'Problems with Pitots - Issues With Flow Measurement in Stacks', *Iet*, (May/June), pp. 1–3. Available at: https://www.semanticscholar.org/paper/Problems-with-Pitots.-Issues-with-flow-measurement-Robinson-Butterfield/0dde5c3826e11848387d04ed96fcc5119bdffbf4.

Sen, S., Mittal, S. and Biswas, G. (2009) 'Steady separated flow past a circular cylinder at low Reynolds numbers', *Journal of Fluid Mechanics*, 620(2009), pp. 89–119. doi: 10.1017/S0022112008004904.

Smith, R. (2008) *Wind Tunnels and CFD*, *Symscape, Computational Fluid Dynamics software for all*. Available at: https://www.symscape.com/blog/wind-tunnels-and-cfd.

Stainback, P. C. and Nagabushana, K. A. (1993) 'Review of hot-wire anemometry techniques and the range of their applicability', *American Society of Mechanical Engineers, Fluids Engineering Division (Publication) FED*, 167, pp. 93–133.

Subbarao, P. M. V. (2001) *Practical Aspects of using Pitot tube*. India. Available at: http://web.iitd.ac.in/~pmvs/course_mel705.php.

Sun, Y. and Zhang, Y. (2007) 'An overview of room air motion measurement: Technology and application', *HVAC and R Research*, 13(6), pp. 929–950. doi: 10.1080/10789669.2007.10391463.

Swanson, R. S. and Clarence, L. G. (1944) 'Wind-Tunnel Calibration and Correction Procedures for Three-Dimensional Models', *NATIONAL ADVISORy COMMITTEE FOR AERONAUTICS*, (I). Available at: https://digital.library.unt.edu/ark:/67531/metadc65430/.

Taneda, S. (1956) 'Experimental Investigation of the Wakes behind Cylinders and Plates at Low Reynolds Numbers.', *Journal of the Physical Society of Japan*, 11(3), pp. 302–307.

Tobias, S. . (2005) *Applied Mathematics and fluid mechanics*. Available at: http://www1.maths.leeds.ac.uk/~smt/TEACHING/MATH3454/chapter2_new.pdf.

Tordella, D. and Belan, M. (2003) 'A New matched asymptotic expansion for the intermediate and far flow behind a finite body', *Physics of Fluids*, 15(7), pp. 1897–1906. doi: 10.1063/1.1580482.

Tuckerman, L. . (1976) 'Notes on Aerodynamic Forces of Airship Hulls', *National Advisory Committee for Aeronautics*, Technical(129), pp. 1–35. Available at: https://digital.library.unt.edu/ark:/67531/metadc53814/.

Yu, Z. and Eloy, C. (2018) 'Extension of Lighthill's slender-body theory to moderate aspect ratios', *Journal of Fluids and Structures*, 76, pp. 84–94. doi: 10.1016/j.jfluidstructs.2017.09.010.

Appendix A

9.1 Summary

Here in this Appendix explained about the design, meshing of the probe arm and static structural analysis for the given load with pictures taken from CATIA and ANSYS tools are illustrated in figures.

9.2 Design and Analysis of a probe arm

CATIA delivers the unique ability not only to model any product but to do so in the context of its real-life behaviour. It enables design engineers to simulate the designs early into the design process where it is more cost-effective to identify and fix problems and enhance productivity. The below probe arm is sketched by using simple CATIA tools and extruded in workbench.
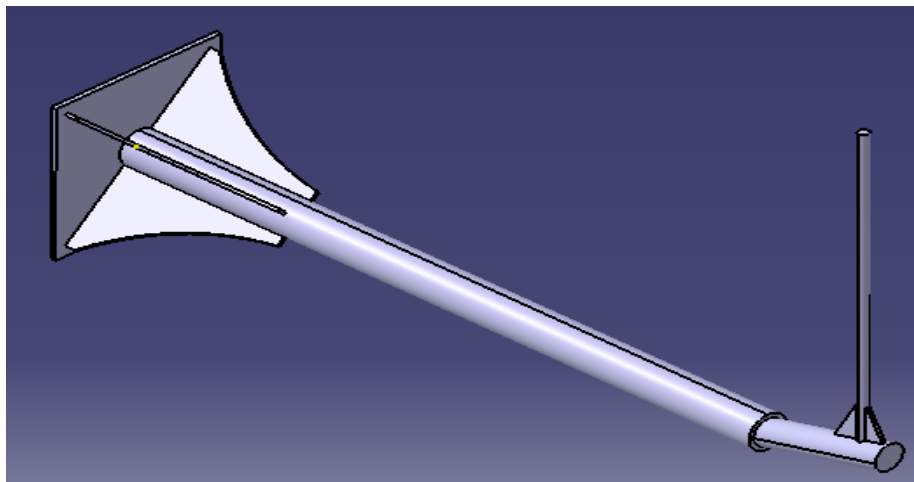
Figure 9.1 Probe arm design

Once design finished the .stp file exported to the ANSYS to analyze by applying boundary conditions. The square plate is fixed to traverse mechanism and shield will be fixed to the wind tunnel test section surface. Pitot tube will be tied to the vertical cylindrical rod. Approximately 1N force is applying on the windshield, which is calculated from the coefficient of drag with order 1.

$$C_d = O(1) = \frac{F}{\frac{1}{2}\rho U^2 A}$$

C_d is the coefficient of drag ρ is the density of air

F force acting in the wind tunnel   A is an area of the object

135

9.3 Meshing

After the geometry has been generated, the 3D model is then meshed by using tetrahedrons. vertical cylinder is the main part projected in the flow. So, we mainly concentrated on the cylindrical object and meshing is done until it converged. The results are plotted in the following figure 9.3.
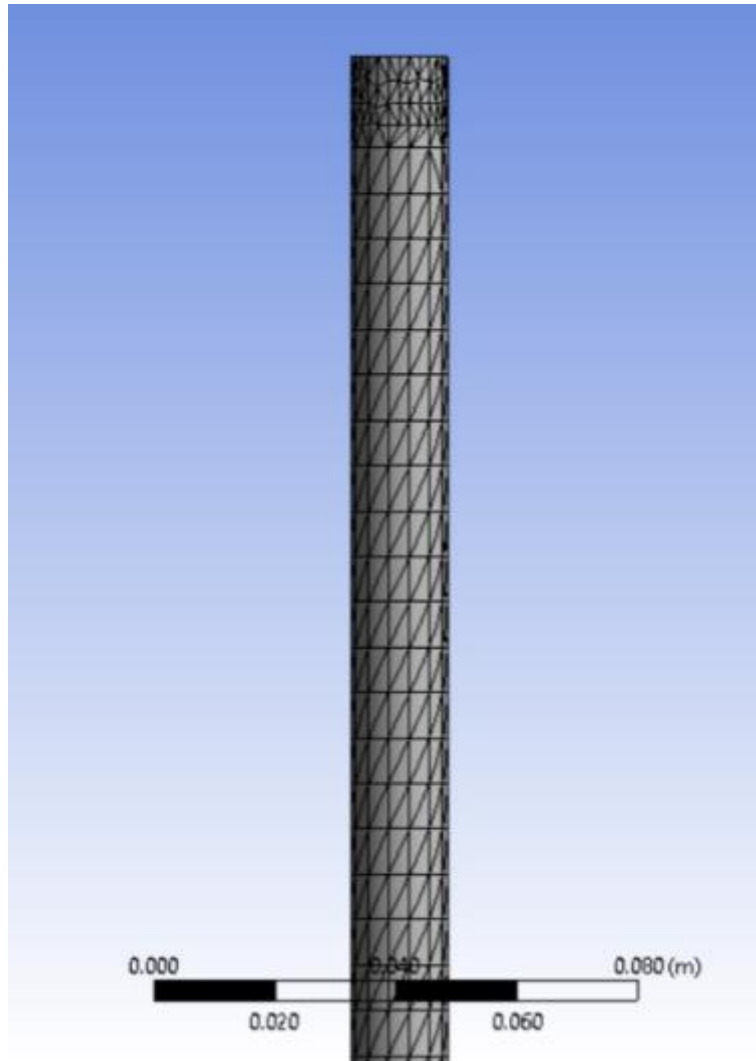
Figure 9.2 Probe arm meshing

Number of Elements	1470	2577	33835	4305	5319	6708
Maximum equivalent stress	1.15E+07	1.12E+07	1.11E+07	1.10E+07	1.11E+07	1.09E+07

Table 9-1 Grid Independence data.

As a number of meshing elements are increased maximum equivalent stress increase until it reached to 3835 elements and then it converged. This helps to find the appropriate grid size to use to proceed to achieve the most accurate result with a minimum number of elements.
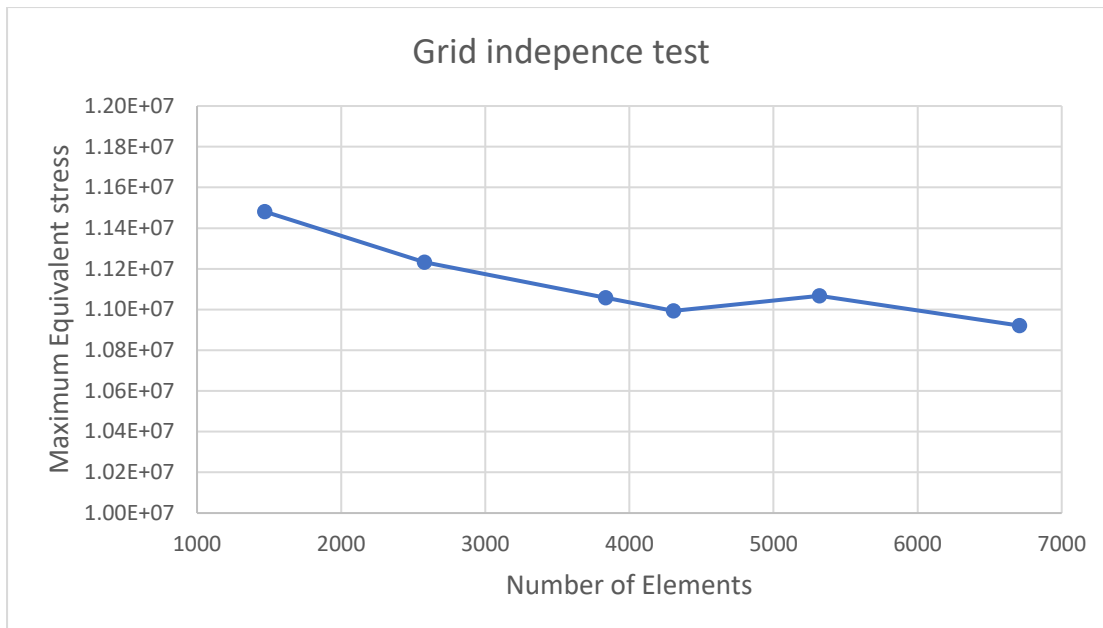
Figure 9.3 Grid independence test

9.4 Loads and constraints

After meshing, loads and constraints are applied. The probe arm plate is fixed as it is bolted on the traverse mechanism. A static load 25N on X-axis, Y&Z- components are ramped to 0N on vertical road and shield. The red coloured parts are fixed objects and load is acting on them.
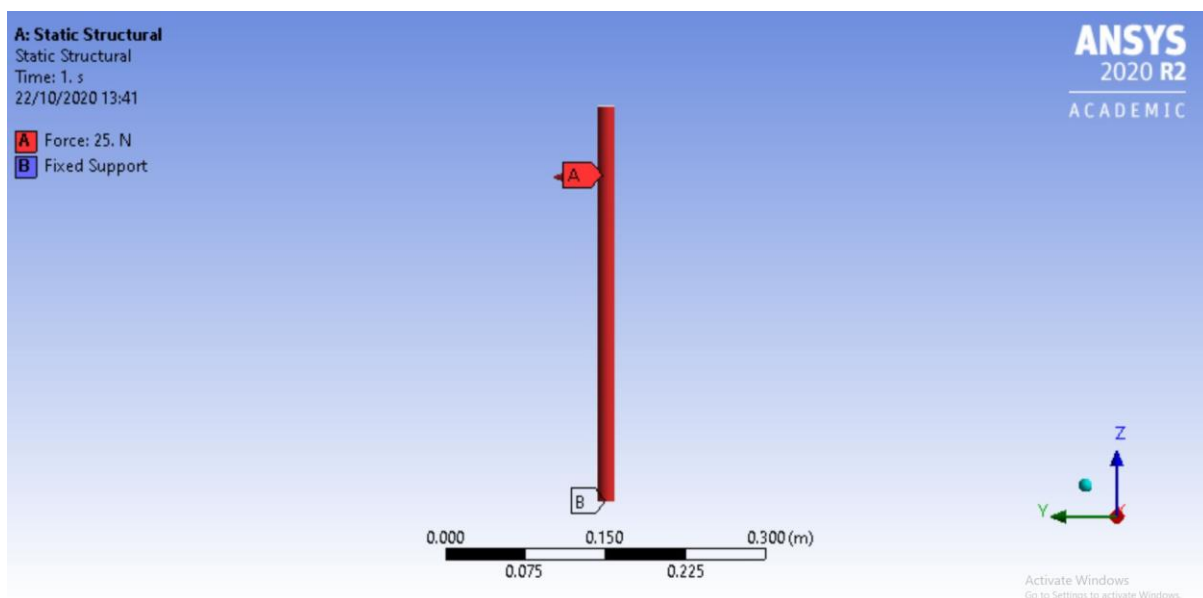
Figure 9.4 Probe arm meshing with different colours

After applying load and boundary conditions, the following results are obtained for total deformation and equivalent stress.

9.5 Total deformation
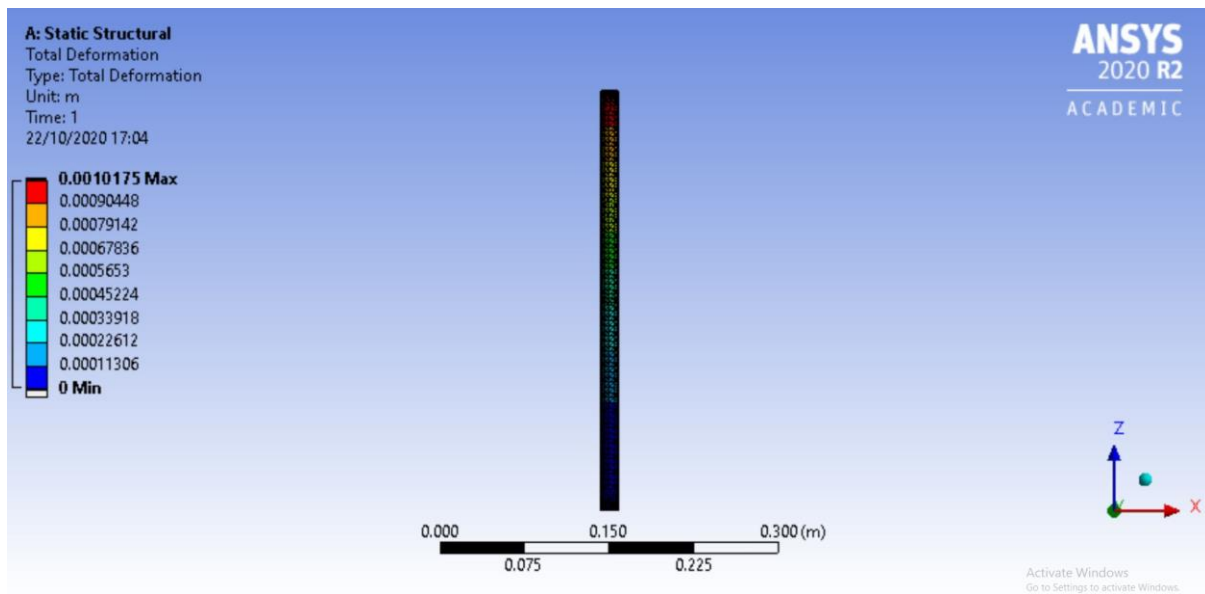
Figure 9.5 Distribution of deformation of the probe arm

9.6 Equivalent stress
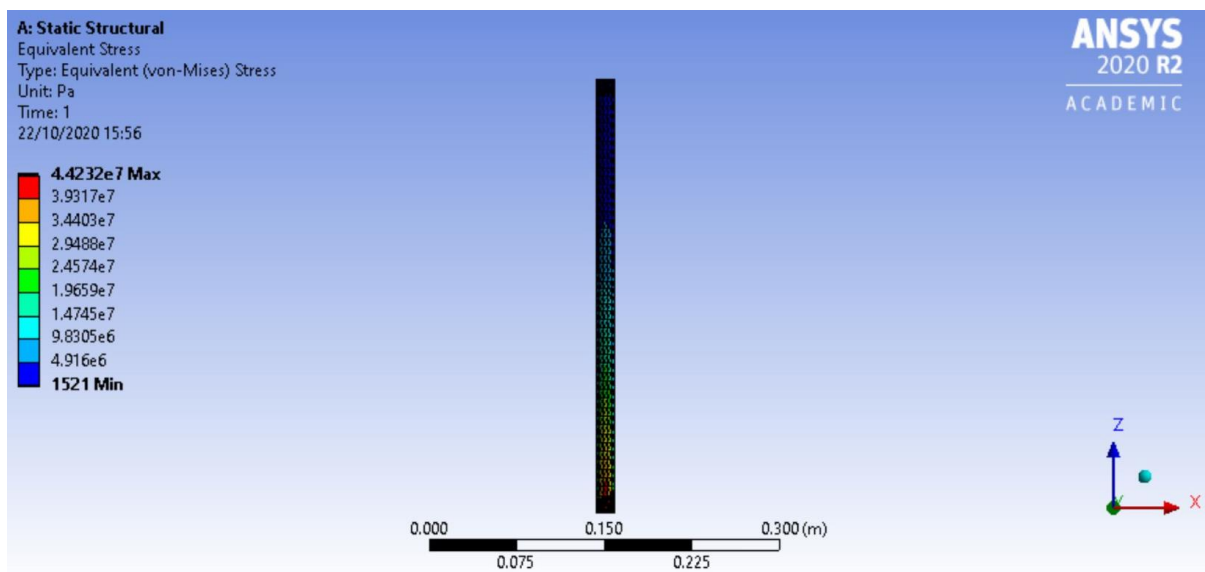
Figure 9.6 Distribution of equivalent stress on the probe arm

The distribution of stress and deformation through the probe arm is shown in above figure9.5 & 9.6. From the results, we can clearly say that for a given static load and boundary conditions, the probe arm will be safer and it deforms 1mm.

Initially, the model is considered to manufactures using 3d printer with materials of polylactic acid (PLA) and acrylonitrile butadiene styrene (ABS). In the Ansys simulation, PLA shows a lot of promising results and ABS is expensive compared to the PLA. So, for the final product, PLA is considered and tested in the wind tunnel. Though the Ansys results are promising, The probe arm deflection in the wind tunnel is more than expected and it is affecting the results as well. After conducting a few experiments, it is changed to structural steel with better stiffness and less deformation.

The probe is made of PLA, ABS and structural steel, mechanical properties are given below.

Name of the Material	Tensile Strength (Mpa)	Yield Strength (Mpa)	Young's Modulus (Gpa)	Poison's ratio	Elongation (%)	Density(kg/m3)
PLA	46	36	3.5	0.36	10	1250
ABS	40	40	2.2	0.35	23-25	1070
Structural Steel	400	220	200	0.27	25	7850

Table 9-2 Mechanical properties of the different material used for machining probe arm.

10 Appendix B

10.1 Dantec software configuration for traverse mechanism with hot-wire anemometer

In this section, a step by step traverse mechanism setup is explained in detail. It starts with how to create a database, project, device, traverse setup and traverse grid. Also explained about hardware configuration for traverse mechanism and hot-wire anemometer, how to choose the right traverse mechanism, scheduling time and data acquisition.

10.1.1.1 Procedure

Create a database by choosing the new database from the file menu. A new dialogue box will open and type the name of the database and choose okay.

We will set the traverse mechanism first and then move on to the hot-wire anemometer. Three different steps to be done in traverse and they are as follows.

- Traverse setup
- Defining the traverse grid
- Load the traverse grid into the default setup.
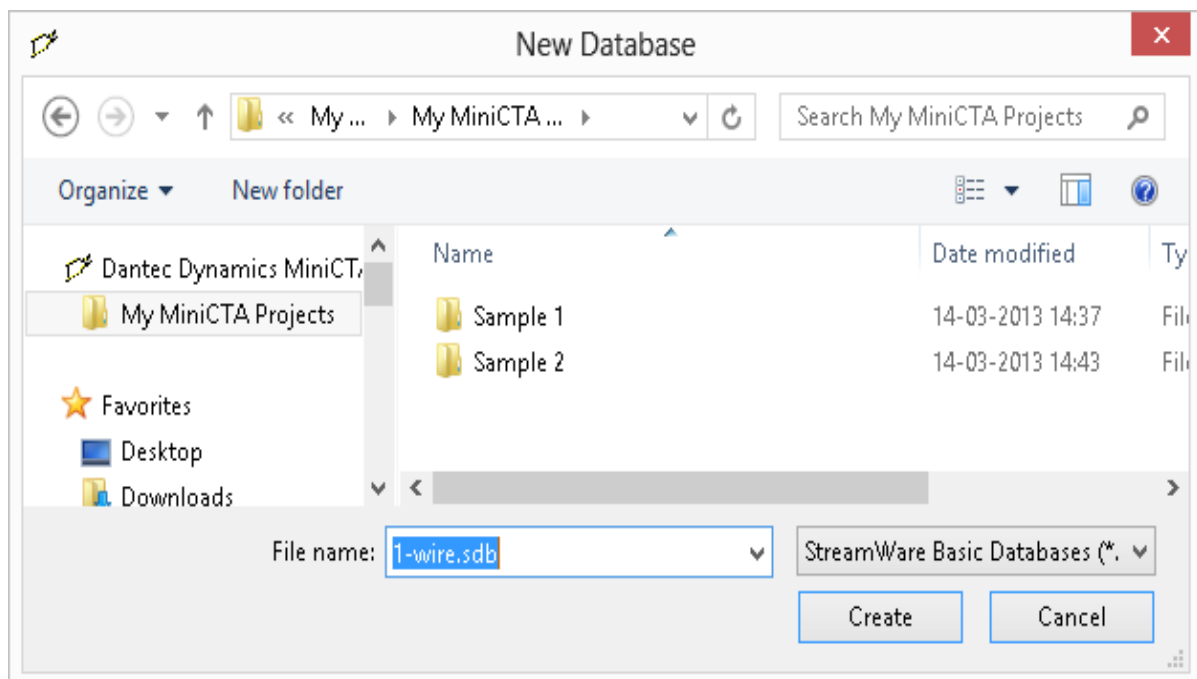
Figure 10.1 Creating the new database for saving all the experimental data.

Create a Project A new window will open as follows. Enter the name of the project and add comments about the project.
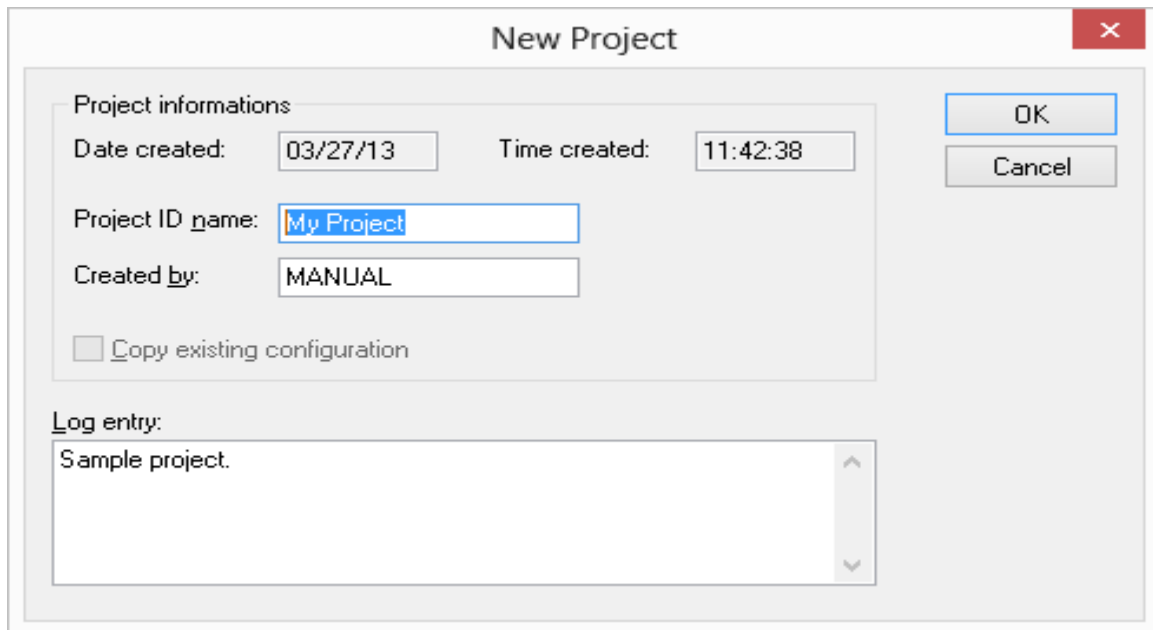
Figure 10.2 Creating a project ID for the experiment.

Configure Devices Choose the A/D driver which is NI DAQmx supported devices and click okay. A path is defined from the project to the translation driver.
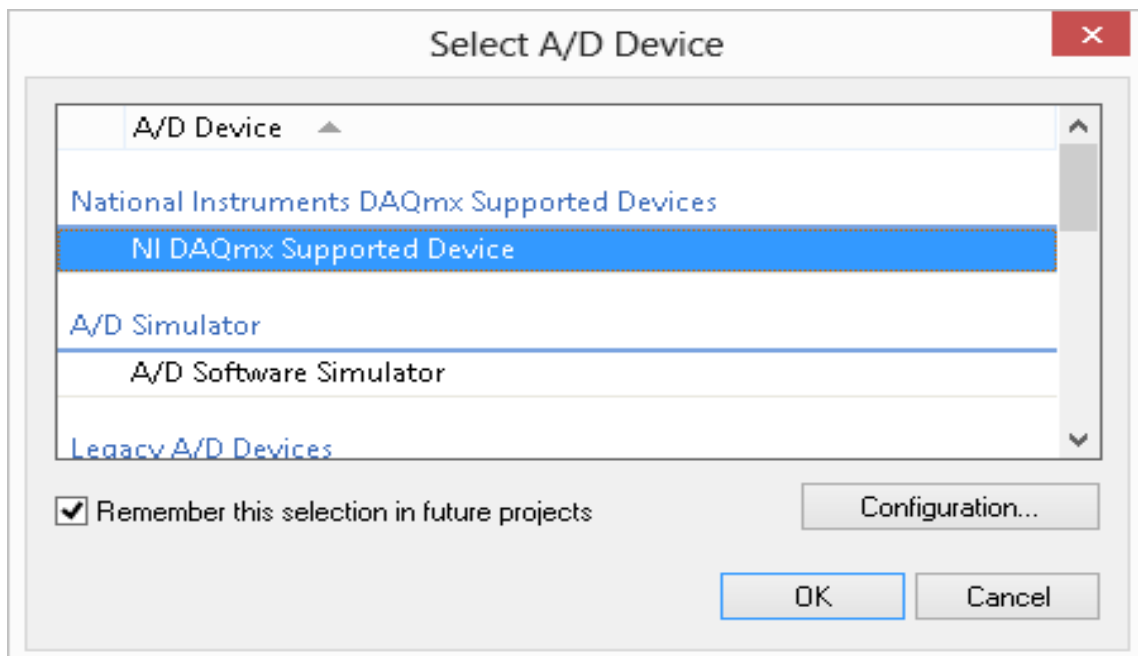
Figure 10.3 Choosing the analog to the digital device

141

10.1.1.2 Traverse setup

Choose a traverse option from the menu and the following dialogue box will open as shown in figure 11.4. We have five different tabs available in the traverse configuration. First, choose general and pick up the options move to the home position and reset reference then choose the speed as per the requirement of the experiment and I choose 5mm/s. Accuracy will be compromised if we choose to go faster than 5mm/sec as we are moving in a small distance at each step. Limits and reference will give us a chance to restrict the traverse in a range as I did not restrict. Axis assignment is chosen for both as it is a two-dimensional traverse and it is illustrated in figure 11.4.
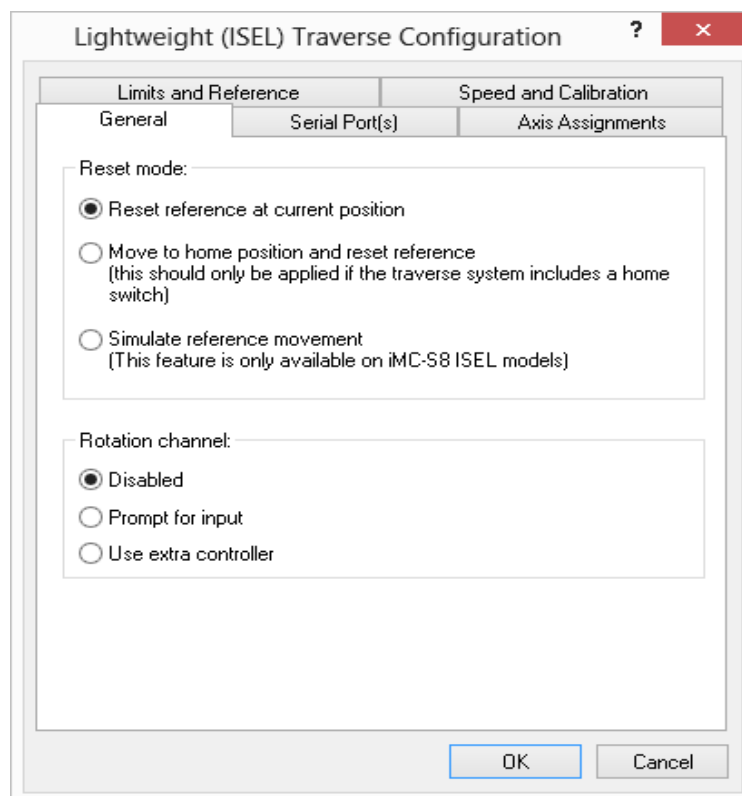
Figure 10.4 Configuration set up for lightweight traverse mechanism.

10.1.1.3 Defining traverse grid

Choose a traverse grid from the setup menu, the grid dialogue box opens as follows. In two-dimensional traverse system we can choose a start position, increment and number of positions for X and Y-axis. An event can be saved by double click on the menu box with the appropriate name and it will appear in the project manager list.
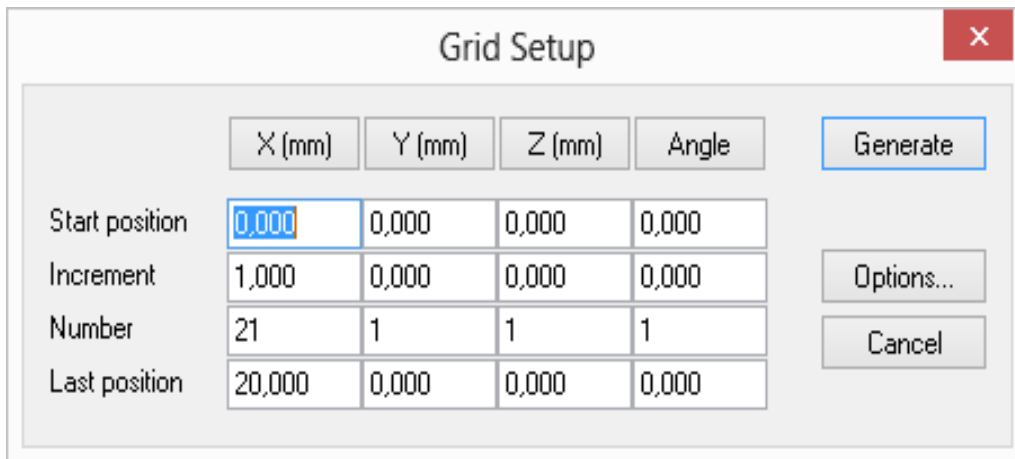
Figure 10.5 Traverse grid setup for the experiment.

Load the traverse grid into the default setup: This need to be done after we did with the probe setup. But in this work, we will be discussing here for continuing the topic. So, to move the probe, we need to use the traverse grid.
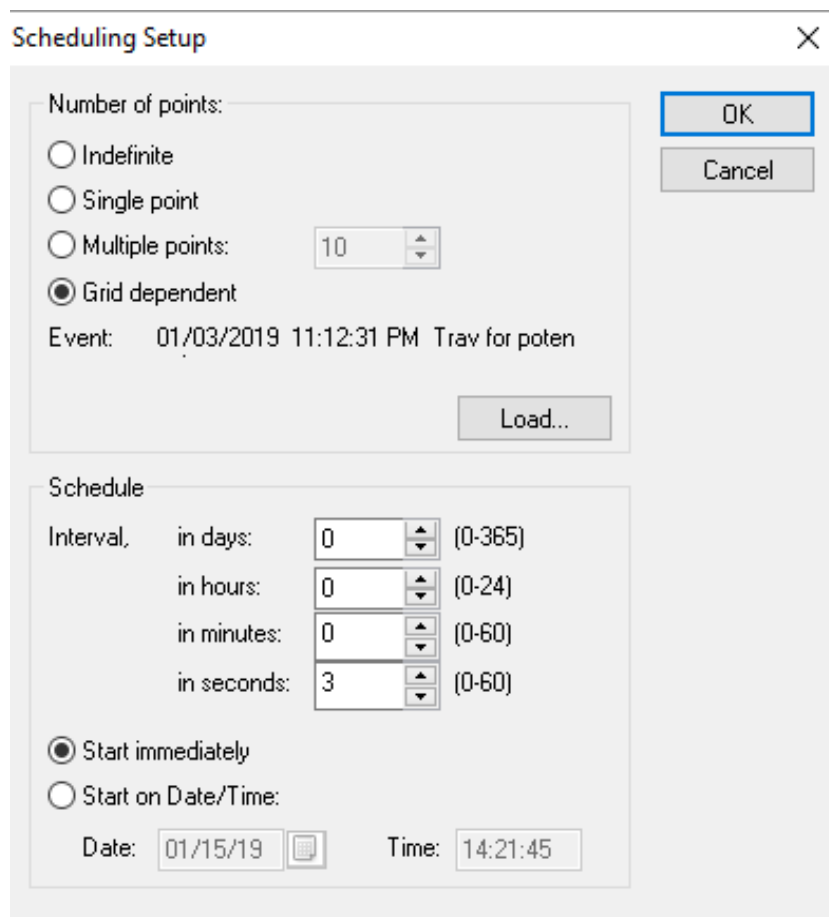
Figure 10.6 Scheduling setup for experiment.

To do that we need to follow the following steps. Choose a default setup box from the project menu, which looks like ⬚. Then choose a group schedule icon and select the grid-dependent radio button and click on the load button. Select the traverse event and choose okay. Click on the position input icon ⬚ and choose move traverse directly to the position specified in grid option and click okay.

System configuration Now we can configure the system by choosing the probe, cable, probe support and A/D input channel.

- Choose the single wire sensor probe icon, and select the 55P11 wire, 55H20 support and a 4m BNC cable then click okay. The probe, support and cable are now added to the map. It is default connected to the A/D input channel. The CTA configuration is finished.

- Similarly, temperature probe 90P10 need to be added to the system. A new dialogue window with two probes will be listed and we need to choose the temperature probe and click okay. This will setup the temperature probe for corrections.
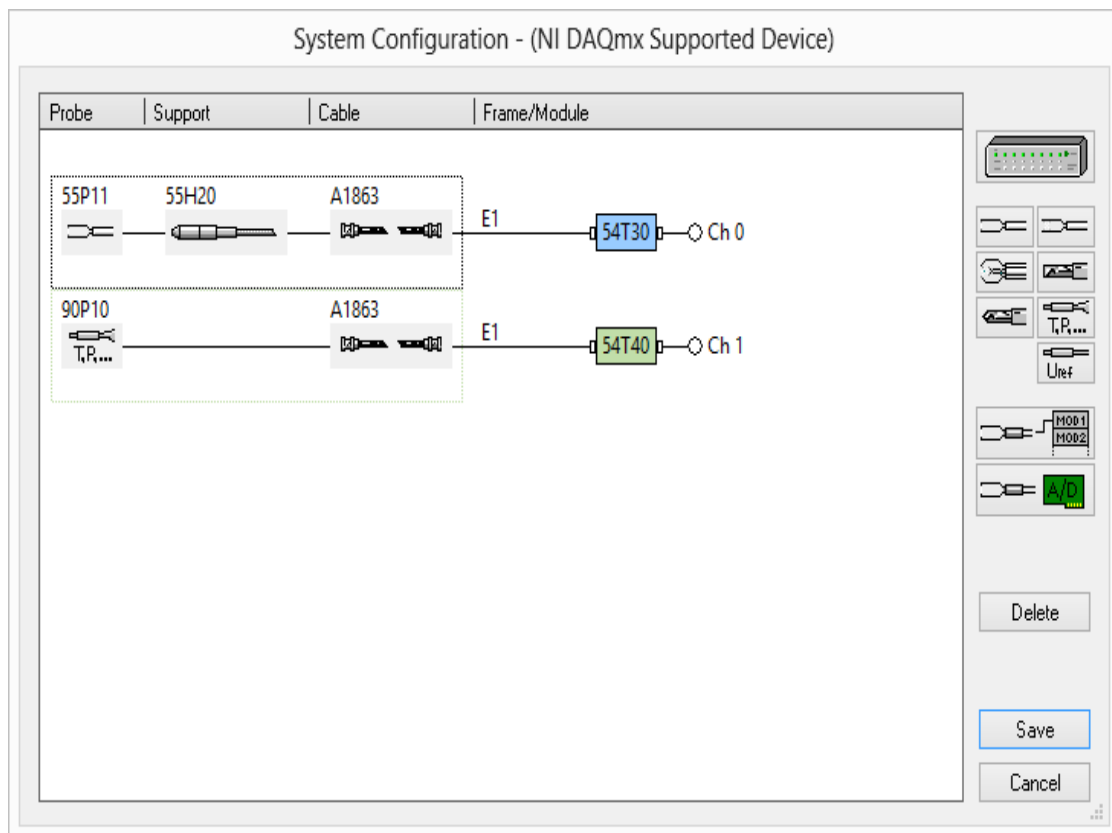
Figure 10.7 Final system configuration of the hot-wire anemometer probe and temperature probe.

10.1.1.4 Hardware configuration

- The Reference temperature should be noted as it is defined as the temperature at which cold resistance of the probe is measured. The resistance and overheat ratio values can copy from the probe container.

- Select the MiniCTA type and probe number. Input the reference temperature and cold resistance in the field from the label on the probe container.

- Update the probe operating data and the corresponding dip switch settings in the MiniCTA unit are displayed.

- This setting is updated manually by the user via the settings of dip switches inside the MiniCTA unit. Wrong settings can damage the probe.
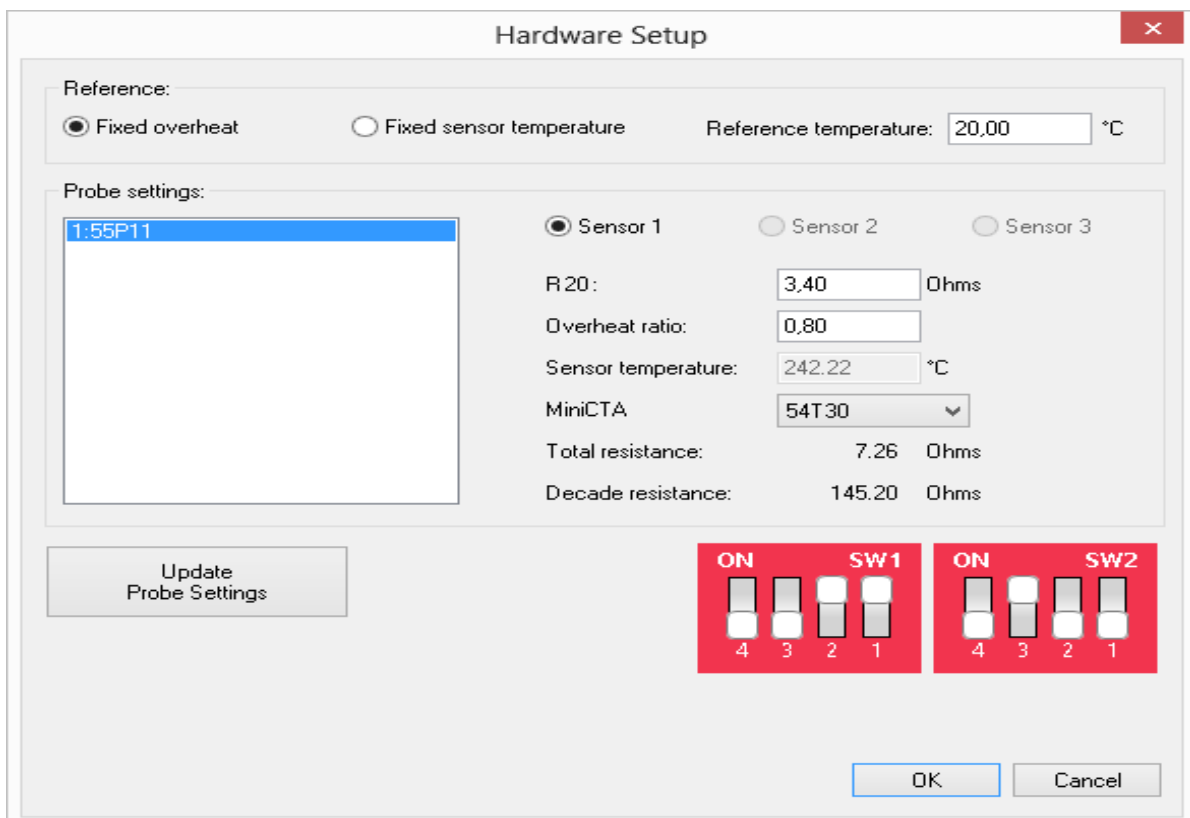
Figure 10.8 Hardware setup for Experiment.

Run and acquire to have two systems.

- Run online
- Run measurement

Run online helps to understand the velocity immediately and data displays but it does not save. We can choose velocity or voltage from calibration in the output.
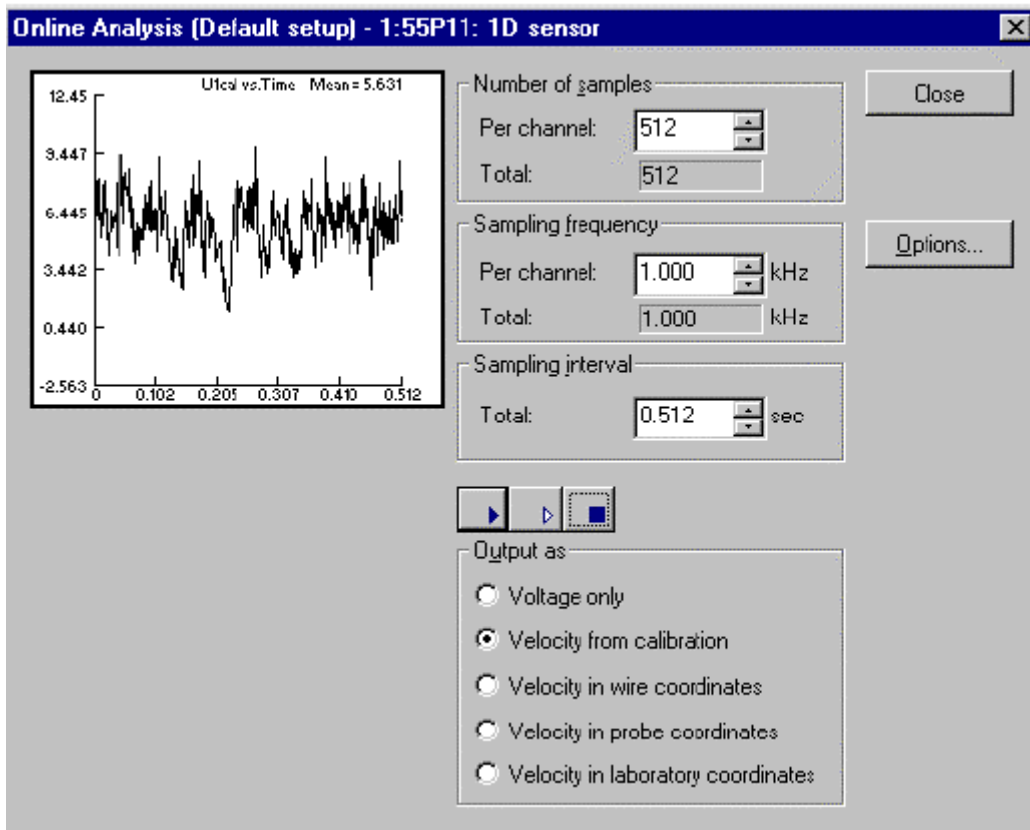
Figure 10.9 Default setup of online analysis for the given setup of Experiment.

Let's discuss the default setup of **run measurement** and it will help us to carry out the measurements followed by data reductions. The default setup contains five fixed processes. They are:

- Hardware setup
- Traverse
- Data acquisition
- Scheduling setup
- Data reduction.

Choose the run measurement button in the main toolbar and the following dialogue box opens. It consists of buttons for hardware setup, position input setup, A/D conversion setup, scheduling setup and data reduction.

Hardware setup and traverse systems are already defined. So, we will move on to A/D device. Initially, we have chosen a device configuration. Here we need to define the sampling frequency and the number of samples. In the present work different size of samples are considered to understand the effect in the output. However, the sampling frequency of 10,000 is resulting almost same as 15000 and 20000.
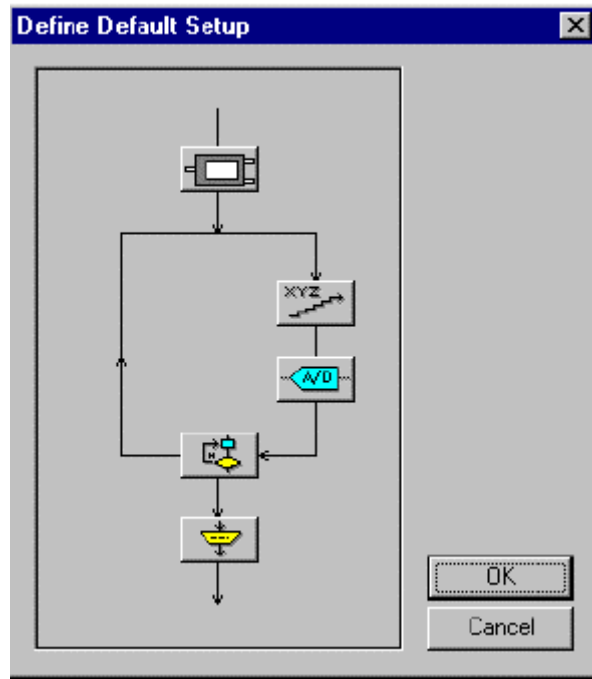
Figure 10.10 Sampling frequency setup for the experiment.

The longer we work on wind tunnel the more internal temperature will rise and it affects the results. Since increasing the Sampling frequency is not affecting the results, I have chosen 10000 sampling frequency.
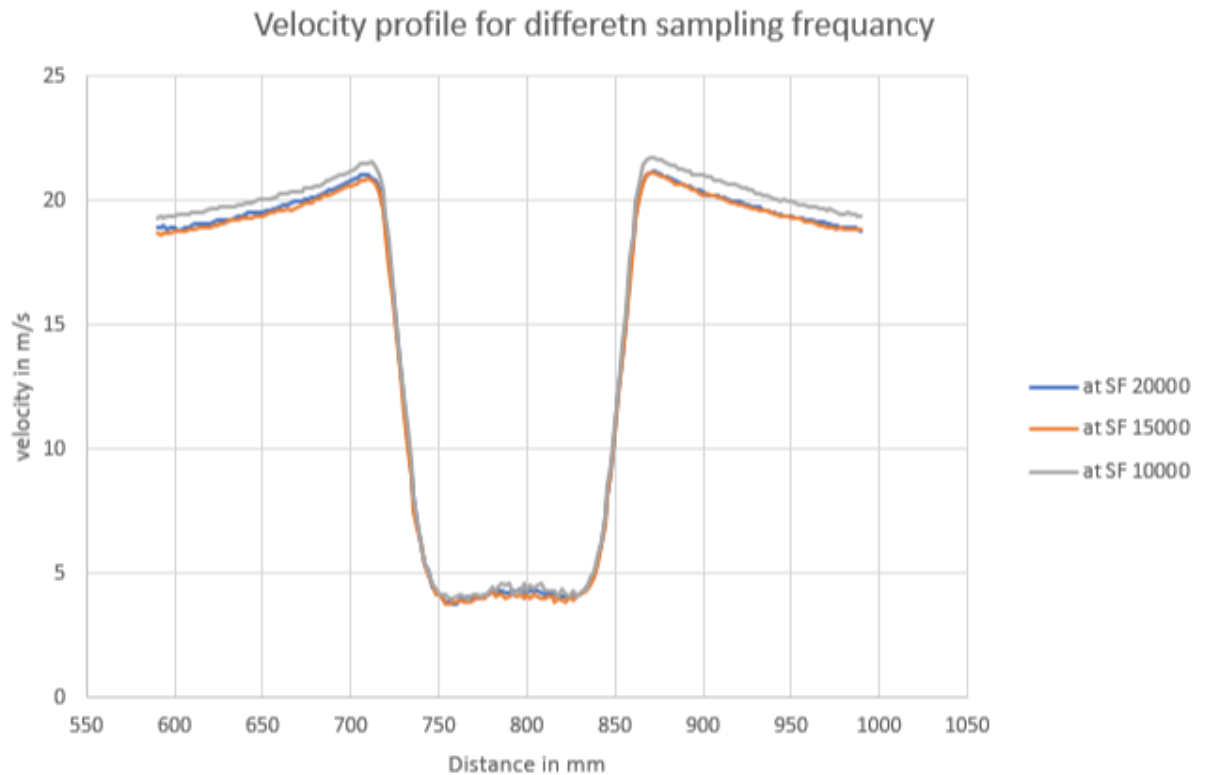
Figure 10.11 Velocity profiles for different sampling frequency for velocity 20m/sec.

The next step in the process is the **scheduling setup.** In this option, we can choose whether we want grid-dependent or manual traverse moving and how long the delay between the measuring points in the wind tunnel. We can control the start date and time as well. Once we have done with all the options, we are ready to take some velocity calibrations. **Data reduction** The data reduction is the process of reducing the raw data to statistical quantities.

11 Appendix C

11.1 Summary

This section explains about Fourier coefficients and the results used in the present work.

11.2 Fourier coefficients

$$\int_0^\pi \cos n\theta \, \cos m\theta \, d\theta = \frac{1}{2} \int_0^\pi (\cos(m+n)\theta + \cos(m-n)\theta) d\theta$$

Case :1

If $m \neq \pm n$

$$\int_0^\pi \cos n\theta \, \cos m\theta \, d\theta = \frac{1}{2} \int_0^\pi (\cos(m+n)\theta + \cos(m-n)\theta) d\theta$$

$$= \frac{1}{2} \left[\frac{1}{m+n} \sin(m+n)\theta + \frac{1}{m-n} \sin(m+n)\theta \right] \text{ and the integral goes from } 0 \to \pi$$

$$\int_0^\pi \cos n\theta \, \cos m\theta \, d\theta = \frac{1}{2} \int_0^\pi (\cos(m+n)\theta + \cos(m-n)\theta) d\theta = 0$$

Case :2

If $m = \pm n$, m=0

$$\int_0^\pi \cos n\theta \, \cos m\theta \, d\theta = \frac{1}{2} \int_0^\pi (\cos(m+n)\theta + \cos(m-n)\theta) d\theta$$

$$\int_0^\pi \cos n\theta \, \cos m\theta \, d\theta = \frac{1}{2} \int_0^\pi (\cos(2m)\theta + \cos(m-m)\theta) d\theta$$

$$\int_0^\pi \cos n\theta \, \cos m\theta \, d\theta = \frac{1}{2} \int_0^\pi (2) d\theta$$

$$\boxed{\int_0^\pi \cos n\theta \, \cos m\theta \, d\theta = \pi}$$

Case :3

$m = \pm n$, m$\neq$0

$$\int_0^\pi \cos n\theta \, \cos m\theta \, d\theta = \frac{1}{2} \int_0^\pi (\cos(m+n)\theta + \cos(m-n)\theta) d\theta$$

$$\int_0^\pi \cos n\theta \, \cos m\theta \, d\theta = \frac{1}{2}\int_0^\pi (\cos(2m)\theta + \cos(m-m)\theta)d\theta$$

$$\int_0^\pi \cos n\theta \, \cos m\theta \, d\theta = \frac{1}{2}\int_0^\pi (\cos(2m)\theta + 1)d\theta$$

$$\int_0^\pi \cos n\theta \, \cos m\theta \, d\theta = \frac{1}{2}[(\sin 2\pi - \sin 0) + (\pi - 0)] = \frac{\pi}{2}$$

$m \neq \pm n$	0
$m = \pm n = 0$	π
$m = \pm n \neq 0$	$\dfrac{\pi}{2}$

Cosine distribution, Abramowitz & Stegan statement proof from page 27

$$\cos(\pi \sin\theta)\cos\theta = \left[J_0(\Pi) + 2\sum_{n=1}^{\infty} J_{2n}(\Pi)\cos(2n\theta)\right]\cos\theta$$

$$= J_0(\Pi)\cos(\theta) + \sum_{n=1}^{\infty} J_{2n}(\Pi)[\cos(2n-1)\theta + \cos(2n+1)\theta]$$

$$= \sum_{n=0}^{\infty} J_{2n}(\Pi)\cos(2n+1)\theta + \sum_{m=1}^{\infty} J_{2m}(\Pi)\cos(2m-1)\theta$$

Where m=n+1

$$= \sum_{n=0}^{\infty} [J_{2n}(\Pi) + J_{2n+2}(\Pi)]\cos(2n+1)\theta$$

$$\boxed{\cos(\Pi \sin\theta)\cos\theta = \sum_{n=0}^{\infty} \frac{2(2n+1)}{\Pi} J_{2n+1}(\Pi)\cos(2n+1)\theta}$$

$$\frac{\partial\phi}{\partial x_1} = \phi_{,1} = \frac{D}{2\pi}(\ln r)_{,1} + \sum_{n=1}^{\infty} a_n \left(\frac{\cos n\theta}{r^n}\right)_{,1}$$

$$\frac{\partial\phi}{\partial x_1} = \frac{D}{2\pi r}\cos\theta + \sum_{n=1}^{\infty} a_n \left(\cos n\theta\left(\frac{-n}{r^{n+1}}\cos\theta\right) + \frac{(-n\sin n\theta)}{r^n}\left(\frac{-\sin\theta}{r}\right)\right)$$

$$\frac{\partial\phi}{\partial x_1} = \frac{D}{2\pi r}\cos\theta + \sum_{n=1}^{\infty} a_n \frac{n}{r^{n+1}}(-\cos n\theta\cos\theta + \sin n\theta\sin\theta)$$

$$\frac{\partial\phi}{\partial x_1} = \frac{D}{2\pi r}\cos\theta + \sum_{n=1}^{\infty} a_n \frac{n}{r^{n+1}}(-\cos n\theta\cos\theta + \sin n\theta\sin\theta)$$

$$\boxed{\frac{\partial\phi}{\partial x_1} = \frac{D}{2\pi r}\cos\theta - \sum_{n=1}^{\infty} a_n \frac{n}{r^{n+1}}\cos(n+1)\theta}$$

$$\frac{\partial\phi}{\partial x_2} = \phi_{,2} = \frac{D}{2\pi}(\ln r)_{,2} + \sum_{n=1}^{\infty} a_n \left(\frac{\cos n\theta}{r^n}\right)_{,2}$$

$$\frac{\partial\phi}{\partial x_2} = \frac{D}{2\pi r}\sin\theta + \sum_{n=1}^{\infty} a_n \left(\cos n\theta\left(\frac{-n}{r^{n+1}}\sin\theta\right) + \left(\frac{-n\sin n\theta}{r^n}\right)\frac{(-\cos\theta)}{r}\right)$$

$$\frac{\partial\phi}{\partial x_2} = \frac{D}{2\pi r}\sin\theta - \sum_{n=1}^{\infty}\frac{n}{r^{n+1}}a_n(\cos n\theta\sin\theta + \sin n\theta\cos\theta)$$

$$\boxed{\frac{\partial\phi}{\partial x_2} = \frac{D}{2\pi r}\sin\theta - \sum_{n=1}^{\infty}\frac{n}{r^{n+1}}a_n\sin(n+1)\theta}$$

12 Appendix D

12.1 Fortran programming

Fortran program written for this work.

```fortran
program circle

  double precision :: pi, A(50),CD,D,cdcheck

  double precision :: epsilon,getepsilon,eta

  double precision :: getRe,getcd,getd,getk,getA,getdist

  double precision :: x1,x2,dx2,theta,dt

  double precision :: u2,u1array(0:40,0:20),u2array(0:40,0:20)

  double precision :: w1,w2,u1calc,u2calc,umax

  double precision :: u1pert,u1pertcalc,dphidx1,dphidx1calc,dphidx2,dphidx2calc

  double precision :: p,cp,r,k,Re,pzero

  double precision :: y1,y2

  double precision :: w1euler, w2euler, w1oseen, w2oseen

  double precision :: alpha,alphafn,b,c,w1eulercalc

  double precision :: w1oseencalc,w2oseencalc

  double precision :: dist(-20:20)

  double precision :: du1dx1,du1dx2,du2dx1,du2dx2

  double precision :: d2phidx11,d2phidx12,dw1dx2,dw1dx22,d2phidx11calc,d2phidx12calc

  double precision :: integrand,dtheta,errortot

  double precision :: CDopt,epsilonopt,etaopt

  integer i,j,n,m,timesteps

  integer ii,jj,nn,mm,kk,pp


  pi=4.0d0*datan(1.0d0)
```

```fortran
! parameter values Re, CD and epsilon (parameters.f95)

! Reynolds number Re

Re=getRe()

k=getk(Re)

nn=50

mm=50

pp=50


open(unit=25, file="erroropt.dat")

open(unit=30, file="minerror.dat")

errortotrun=1000.0d0

do jj=0,mm

  do kk=0,pp

    do ii=0,nn

      ! Drag coefficient CD

      ! CD=getcd()

      CD=dble(ii)*0.6d0/dble(nn)+0.3

      D=getd(CD)

      ! epsilon, wake velocity distribution

      ! 0 is constant, 1 is cosine, fraction is between two

      ! epsilon=getepsilon()

      epsilon=dble(jj)*0.6d0/dble(mm)+0.3

!       epsilon=dble(jj)*1.0d0/dble(mm)

      ! eta is constant

!       eta= dble(kk)*1.0d0/dble(pp)

      eta=dble(kk)*0.9d0/dble(pp)-0.8
```

```fortran
!          write(*,*) 'Reynolds number= ',Re, 'cd= ',cd,'epsilon= ',epsilon,'eta= ',eta
!          end parameter values Re, CD, epsilon and eta


!          calculate far field plot
!          write to file farfield.DAT
         call farfieldopt(epsilon,CD,errortot,eta)
         if (ii.eq.(nn/2)) write(25,*) epsilon,eta,errortot
!          end calculate far field plot
         if (errortot.lt.errortotrun) then
           errortotrun=errortot
           cdopt=cd
           epsilonopt=epsilon
           etaopt=eta
         end if
         write(30,*) 'CD,epsilon,eta,errortot = ',CD,epsilon,eta,errortot
        end do
       end do
       write(25,*)
       write(*,*) 'jj= ',jj
      end do
     close(25)
     close(30)


! run for minimum values that have been found
epsilon = epsilonopt
CD = cdopt
```

```fortran
  eta =etaopt

  errortot = errortotrun

!  epsilon = 0.75d0

!  CD = 1.0d0

!  eta = -1.0d0


  write(*,*) "optimal values are: "

  write(*,*) "epsilon = ",epsilon

  write(*,*) "CD = ",CD

  write(*,*) "eta = ",eta

  write(*,*) "errortot = ",errortot


  ! calculate far field plot

  ! write to file farfield.DAT and wake.dat

  call farfieldopt(epsilon,CD,errortot,eta)

  ! end calculation for minimum values

  write(*,*) "errortot = ",errortot


  ! plot wake velocity distribution

  ! write to dist.DAT for wake velocity distribution

  open(unit=14, file="dist.DAT")

  dx2=0.05d0

  n=20

  do i=-n,n

    x2=dx2*dble(i)

    dist(i)=getdist(x2,epsilon,CD,eta)
```

```fortran
    write(14,*) x2,dist(i)

  end do

  close(14)

  ! end plot wake veloctity distribution

end program circle
```

!Bessel functions

```fortran
double precision function JN(z,n)

  double precision z, fact

  integer n,k

  JN = ((0.5*z)**n)/fact(n)

  do k=1,20

  JN = JN+((0.5*z)**n)*((-0.25*z**2)**k)/(fact(k)*fact(n+k))

end do

  ! setting JN=0.0 effectively gives constant distribution

!  JN=0.0d0

  return

end function JN


! Modified Bessel function

double precision function I0(x)

  double precision x, t, xhalfeminxI0

t=x/3.75

  if (x < 0.0d0) then

  else if (x < 3.75) then
```

```
   I0 = 1.0d0+3.5156229*t**2+3.0899424*t**4+1.2067492*t**6 &
   +0.2659732*t**8+0.0360768*t**10+0.0045813*t**12
 else if (x >= 3.75) then
   xhalfeminxI0 = 0.39894228+0.01328592/t**1 &
   +0.00225319/t**2-0.00157565/t**3 &
   +0.00916281/t**4-0.02057706/t**5 &
   +0.02635537/t**6-0.01647633/t**7 &
   +0.00392377/t**8
   I0=xhalfeminxI0*dexp(x)/dsqrt(x)
 end if
 return
end function I0


double precision function K0(x)
 double precision x, t, xhalfexK0, I0
 t=x/2.0d0
 if (x < 0.0d0) then
 else if (x < 2.0d0) then
   K0 = -dlog(t)*I0(x)-0.57721566 &
     +0.42278420*t**2+0.23069756*t**4 &
     +0.03488590*t**6+0.00262698*t**8 &
     +0.00010750*t**10+0.00000740*t**12
 else if (x >= 2.0d0) then
   xhalfexK0 = 1.25331414-0.07832358/t &
     +0.02189568/t**2-0.01062446/t**3 &
     +0.00587872/t**4-0.00251540/t**5 &
```

```
          +0.00053208/t**6

     K0=xhalfexK0*dexp(-x)/dsqrt(x)

   end if

   return

end function K0


double precision function I1(x)

  double precision x, t, xminoneI1,xhalfeminxI1

  t=x/3.75


  if (x < 0.0d0) then

  else if (x < 3.75) then

     xminoneI1 = 0.5d0+0.87890594*t**2+0.51498869*t**4 &

        +0.15084934*t**6+0.02658733*t**8 &

        +0.00301532*t**10+0.00032411*t**12

    I1=x*xminoneI1

  else if (x >= 3.75) then

     xhalfeminxI1 = 0.39894228-0.03988024/t**1 &

     -0.00362018/t**2+0.00163801/t**3 &

     -0.1031555/t**4+0.02282967/t**5 &

     -0.02895312/t**6+0.01787654/t**7 &

     -0.00420059/t**8

    I1=xhalfeminxI1*dexp(x)/dsqrt(x)

   end if

   return

end function I1
```

```fortran
double precision function K1(x)

  double precision x, t, xK1, xhalfeminxK1, I1

  t=x/2.0d0


  if (x < 0.0d0) then
  else if (x < 2.0d0) then

    xK1 = x*dlog(t)*I1(x)+1.0d0+0.15443144*t**2 &

      -0.67278579*t**4-0.18156897*t**6 &

      -0.01919402*t**8-0.00110404*t**10 &

      -0.00004686*t**12

    K1 = xK1/x

  else if (x >= 2.0d0) then

    xhalfexK1 = 1.25331414+0.23498619/t &

      -0.03655620/t**2+0.01504268/t**3 &

      -0.00780353/t**4+0.00325614/t**5 &

      -0.00068245/t**6

    K1=xhalfexK1*dexp(-x)/dsqrt(x)

  end if

  return

end function K1


!Functions used

double precision function getA(m,epsilon,eta)

  integer :: m

  double precision :: epsilon,eta
```

```fortran
    double precision :: pi

    double precision :: dx2,x2

    integer :: i,n

    double precision :: getdist,dist(100000)

    double precision :: JN,AEVEN

    double precision :: D,CD,getcd,getd


    pi=4.0d0*datan(1.0d0)

    !CD=getcd()

    D=getd(CD)


    ! get Fourier coefficients

    !general

! integration dx2, steps n

    dx2=0.00001d0

    n=100000

! integral of dist from 0 to 1

    do i=1,n

       x2=dx2*dble(i)

       dist(i)=getdist(x2,epsilon,CD,eta)

    end do


    getA=0.0d0

    do i=1,n

       x2=dx2*dble(i)

       getA=getA-dist(i)*dcos(dble(m)*dasin(x2))
```

160

```fortran
      end do

    getA=getA*2.0d0*dx2/(dble(m)*pi)

    if (m.eq.1) getA=getA+1.0d0


    ! Cosine

    ! note: gnu extension JN double: getA=1.0-D/4.0-D*DBESJN(1,pi)/(2.0*pi)

     ! check if even or odd

  ! if ((m/2+m/2).eq.m) then

  !    getA=AEVEN(m,D)

  ! else

  !    getA=-D*JN(pi,m)/(2.0*pi)

  ! end if

  ! if (m.eq.1) getA=1.0-D/4.0-D*JN(pi,1)/(2.0*pi)


    ! Constant

  ! if ((m/2+m/2).eq.m) then

  !    getA=(2.0*D/(2.0*pi*m))*((-1.0)**(m/2))/(dble(m)**2-1.0)

  ! else

  !    getA=0.0d0

  ! end if

  ! if (m.eq.1)  getA=1.0-D/4.0

    ! end get Fourier coefficients

    return

  end function getA
```

```fortran
double precision function getAopt(m,epsilon,CD,eta)

  integer :: m

  double precision :: epsilon,eta

  double precision :: pi

  double precision :: dx2,x2

  integer :: i,n

  double precision :: getdist,dist(100000)

  double precision :: JN,AEVEN

  double precision :: D,CD,getcd,getd


  pi=4.0d0*datan(1.0d0)
! CD=getcd()

  D=getd(CD)


  ! get Fourier coefficients

  !general
! integration dx2, steps n

  dx2=0.00001d0

  n=100000
! integral of dist from 0 to 1

  do i=1,n

    x2=dx2*dble(i)

    dist(i)=getdist(x2,epsilon,CD,eta)
!    write(*,*) 'disti is',dist(i)

  end do
```

```fortran
    getAopt=0.0d0
  do i=1,n
    x2=dx2*dble(i)
    getAopt=getAopt-dist(i)*dcos(dble(m)*dasin(x2))
  end do
  getAopt=getAopt*2.0d0*dx2/(dble(m)*pi)
  if (m.eq.1) getAopt=getAopt+1.0d0


  return
end function getAopt


double precision function getdist(x2,epsilon,CD,eta)
  double precision :: x2,epsilon,epsilontmp,eta
  double precision :: pi
  double precision :: getdistcos,getdistconst
  double precision :: CD,getcd,D,getd
  double precision :: lamda
  integer i,n


  pi=4.0d0*datan(1.0d0)
! CD=getcd()
  D=getd(CD)


  getdist = epsilon + CD*x2**2 + eta*x2**4
  ! general merged beside
! if (dabs(x2).le.(dabs(1.0d0-epsilon))) then
```

```
!    getdist=D/(2.0d0-epsilon)

! else

!    getdist=(D/(4.0d0-2.0d0*epsilon))*(1.0d0-dcos((pi/epsilon)*(dabs(x2)-1.0d0)))

! end if


! write(*,*) 'getdist is ', getdist


 ! general merged epsilon and lamda

 ! lamda = 0.4d0

! lamda = 0.0d0

! if (dabs(x2).le.(dabs(1.0d0-epsilon-lamda))) then

!    getdist=D/(2.0d0-2.0d0*lamda-epsilon)

! else if (dabs(x2).le.(dabs(1.0d0-lamda))) then

!        getdist=(D/(4.0d0-4.0d0*lamda-2.0d0*epsilon))*(1.0d0-dcos((pi/epsilon)*(dabs(x2)-
1.0d0+lamda)))

! else

!    getdist=0.0d0

! end if


 ! cosine inside

! if (dabs(x2).le.(dabs(epsilon))) then

!    getdist=(D/(2.0d0*epsilon))*(1.0d0+dcos((pi/epsilon)*dabs(x2)))

! else

!    getdist=0.0d0

! end if
```

```
! cosine

! getdist=(D/2.0d0)*(1.0d0+dcos(pi*x2))

! epsilontmp=1.0d0

!          getdistcos=(D/(4.0d0-2.0d0*epsilontmp))*(1.0d0-dcos((pi/epsilontmp)*(dabs(x2)-
1.0d0)))


! constant

! if (dabs(x2).le.(dabs(epsilon))) then

!    getdist=D/(2.0d0*epsilon)

! else

!    getdist=0.0d0

! end if


! getdist=D/2.0d0

! epsilontmp=0.0d0

! getdistconst=D/(2.0d0-epsilontmp)


! general averaged

! getdist=epsilon*getdistcos+(1.0d0-epsilon)*getdistconst


! try cos(pi*x2/2)

! getdist=(pi*D/4.0d0)*dcos(pi*x2/2.0d0)


! try 1-cos(pi*x2/2)

! getdist=(pi*D/4.0d0)*(1.0d0-dcos(pi*x2/2.0d0))

! getdist=(pi*D/4.0d0)*(1.0d0-dcos(pi*(dabs(x2)-1.0d0)/2.0d0))
```

```fortran
    !double hump cos(2*pi*x2)

!  getdist=(D/2.0d0)*(1.0d0+dcos(2.0d0*pi*x2))


  return

end function getdist


double precision function alphafn(b,c,r)

  double precision b,c,r,bcmid

  ! MERGED

  ! provides smoothing function in range b to c

  ! when r <= b then alphafn is 1.0 Euler

  ! when r >= c then alphafn is 0.0 Oseen

  ! quadratic smoothing in between reflected about mid-point


  bcmid=(b+c)/2.0d0

  if (r .le. bcmid) then

    alphafn = (2.0d0*((c-b)/2.0d0)**2-(r-b)**2)/(2.0d0*((c-b)/2.0d0)**2)

  else if (r.gt.bcmid.and.r.le.c) then

    alphafn = ((r-c)**2)/(2.0d0*((c-b)/2.0d0)**2)

  else

    alphafn = 0.0d0

  end if

  ! END MERGED

  ! EULER

  ! use this for Euler
```

```fortran
!  alphafn = 1.0d0

! END EULER


  return
end function alphafn


double precision function getd(CD)
  double precision CD
  getd=CD
  return
end function getd


double precision function getk(Re)
  double precision Re
  getk=Re/4.0d0
  return
end function getk


double precision function AEVEN(m,D)
  integer n,m
  double precision D,pi,JN


  pi=4.0*atan(1.0)


  AEVEN=0.0d0
  do n=0,20
```

```fortran
AEVEN=AEVEN+((2.0*D)/(m*(pi**2)))*((1.0)**(n+m/2)*JN(pi,2*n+1)/((dble(m)/(2*dble(
n)+1.0))**2-1.0))

end do

AEVEN=(2.0*D/(2.0*pi*m))*((-1.0)**(m/2))/(dble(m)**2-1.0)+AEVEN

return

end function AEVEN


double precision function u1calc(x1,x2,D,w1,A)

double precision :: x1,x2,D,w1,A(50)

double precision :: pi

double precision :: r,theta

integer n


pi=4.0d0*datan(1.0d0)

r=dsqrt(x1**2+x2**2)

theta = sign(dacos(x1/r),x2)


u1calc = 0.0d0

do n=1,50

   u1calc=u1calc-n*A(n)*(dcos((dble(n)+1)*theta)/(r**(n+1)))

end do

u1calc=u1calc+D*(dcos(theta))/(2.0*pi*r)+1.0+w1

return

end function u1calc


double precision function u2calc(x1,x2,D,w2,A)
```

```fortran
      double precision x1,x2,D,w2,A(50),r,theta,pi

      integer n


      pi=4.0d0*datan(1.0d0)

      r=dsqrt(x1**2+x2**2)

      theta = sign(dacos(x1/r),x2)

      u2calc=0.0d0

      do n=1,50

         u2calc=u2calc-n*A(n)*(dsin((dble(n)+1)*theta)/(r**(n+1)))

      end do

      u2calc=u2calc+D*dsin(theta)/(2.0*pi*r)+w2

      return

      end function u2calc


      double precision function d2phidx11calc(x1,x2,D,A)

       double precision :: x1,x2,D,A(50)

       double precision :: pi

       double precision :: r,theta

       integer n


       pi=4.0d0*datan(1.0d0)

       r=dsqrt(x1**2+x2**2)

       theta = sign(dacos(x1/r),x2)


       d2phidx11calc = 0.0d0

       do n=1,50
```

```fortran
      d2phidx11calc=d2phidx11calc+n*(n+1)*A(n)*(dcos((dble(n)+2)*theta)/(r**(n+2)))
    end do
    d2phidx11calc=d2phidx11calc-D*(dcos(2.0d0*theta))/(2.0*pi*(r**2))
    return
  end function d2phidx11calc


double precision function d2phidx12calc(x1,x2,D,A)
  double precision :: x1,x2,D,A(50)
  double precision :: pi
  double precision :: r,theta
  integer n


  pi=4.0d0*datan(1.0d0)
  r=dsqrt(x1**2+x2**2)
  theta = sign(dacos(x1/r),x2)


  d2phidx12calc = 0.0d0
  do n=1,50
    d2phidx12calc=d2phidx12calc+n*(n+1)*A(n)*(dsin((dble(n)+2)*theta)/(r**(n+2)))
  end do
  d2phidx12calc=d2phidx12calc-D*(dsin(2.0d0*theta))/(2.0*pi*(r**2))
  return
end function d2phidx12calc


double precision function u1pertcalc(x1,x2,D,w1,A)
  double precision x1,x2,D,A(50),r,theta,pi,w1
```

170

```fortran
      integer n

      pi=4.0d0*datan(1.0d0)
      r=dsqrt(x1**2+x2**2)
      theta = sign(dacos(x1/r),x2)

      u1pertcalc = 0.0d0
      do n=1,50
        u1pertcalc=u1pertcalc-n*A(n)*(dcos((dble(n)+1)*theta)/(r**(n+1)))
      end do
      u1pertcalc=u1pertcalc+D*(dcos(theta))/(2.0*pi*r)+w1
      return
      end function u1pertcalc


      double precision function dphidx1calc(x1,x2,D,A)
      double precision x1,x2,D,A(50),r,theta,pi
      integer n

      pi=4.0d0*datan(1.0d0)
      r=dsqrt(x1**2+x2**2)
      theta = sign(dacos(x1/r),x2)

      dphidx1calc = 0.0d0
      do n=1,50
        dphidx1calc=dphidx1calc-n*A(n)*(dcos((dble(n)+1)*theta)/(r**(n+1)))
      end do
```

```fortran
      dphidx1calc=dphidx1calc+D*(dcos(theta))/(2.0*pi*r)
     return
    end function dphidx1calc


    double precision function dphidx2calc(x1,x2,D,A)
     double precision x1,x2,D,w2,A(50),r,theta,pi
     integer n


     pi=4.0d0*datan(1.0d0)
     r=dsqrt(x1**2+x2**2)
     theta = sign(dacos(x1/r),x2)
     dphidx2calc=0.0d0
     do n=1,50
       dphidx2calc=dphidx2calc-n*A(n)*(dsin((dble(n)+1)*theta)/(r**(n+1)))
     end do
     dphidx2calc=dphidx2calc+D*dsin(theta)/(2.0*pi*r)
     return
    end function dphidx2calc


    double precision function w1eulercalc(x1,x2,epsilon,CD,eta)
     double precision x1,x2,epsilon,getdist,CD,eta


     if ((x1.gt.0.0).and.(dabs(x2).le.1.0)) then
       w1eulercalc=-getdist(x2,epsilon,CD,eta)
      else
       w1eulercalc=0.0d0
```

```fortran
      end if

    return

  end function w1eulercalc


  double precision function w1oseencalc(x1,x2,epsilon,CD,eta)

    double precision x1,x2,epsilon,Re,getRe,k,getk,CD,getcd,D,getd,pi,eta

    double precision K0,K1,getdist

    double precision w1oseenlet,range,dy,y1,y2,rxy

    integer l


    pi=4.0d0*datan(1.0d0)


    ! get Reynolds number Re, this is where to change Re

    Re=getRe()

    k=getk(Re)


    ! Drag coefficient CD, this is where to change CD

    !CD=getcd()

    D=getd(CD)

    ! end parameter values Re and CD


    w1oseencalc=0.0d0

    range=2.0d0

    do l=1,20

      dy=range/20

      y1=0.0d0
```

```
    y2=-1.0d0+dy/2.0d0+(l-1)*dy

    rxy=dsqrt((x1-y1)**2+(x2-y2)**2)


    w1oseenlet=-(1.0d0/(2.0d0*pi))*k*dexp(k*x1)*(K1(k*rxy)*x1/rxy+1.0d0*K0(k*rxy))

    ! general

    w1oseencalc=w1oseencalc+getdist(y2,epsilon,CD,eta)*w1oseenlet*dy

    ! cosine

    ! w1oseencalc=w1oseencalc+(D/2.0)*(dcos(pi*y2)+1)*w1oseenlet*dy

    ! constant

    !w1oseencalc=w1oseencalc+(D/2.0)*w1oseenlet*dy

  end do

  return

end function w1oseencalc


double precision function w2oseencalc(x1,x2,epsilon,CD,eta)

  double precision x1,x2,Re,k,CD,D,pi,epsilon,getdist,eta

  double precision getRe,getk,getcd,getd

  double precision K1

  double precision w2oseenlet,range,dy,y1,y2,rxy

  integer l


  pi=4.0d0*datan(1.0d0)

  ! get Reynolds number Re, this is where to change Re

  Re=getRe()

  k=getk(Re)

  ! Drag coefficient CD, this is where to change CD
```

```fortran
    !CD=getcd()

    D=getd(CD)

    ! end parameter values Re and CD


    w2oseencalc=0.0d0

    range=2.0d0

    do l=1,20

       dy=range/20

       y1=0.0d0

       y2=-1.0d0+dy/2.0d0+(l-1)*dy

       rxy=dsqrt((x1-y1)**2+(x2-y2)**2)

       w2oseenlet=-(1.0d0/(2.0d0*pi))*k*dexp(k*x1)*K1(k*rxy)*x2/rxy

       ! general

       w2oseencalc=w2oseencalc+getdist(y2,epsilon,CD,eta)*w2oseenlet*dy

       ! cosine

       ! w2oseencalc=w2oseencalc+(D/2.0)*(dcos(pi*y2)+1)*w2oseenlet*dy

       ! constant

       ! w2oseencalc=w2oseencalc+(D/2.0)*w2oseenlet*dy

    end do

    return

end function w2oseencalc


double precision function fact(n)

    integer n

    fact =1.0d0

    do k=1,n
```

```fortran
    fact = fact*dble(k)

  end do

  return

end function fact
```

!Subroutinies used

```fortran
subroutine streamline(x1,x2,dt,timesteps,epsilon)

  double precision :: x1,x2,dt,epsilon,eta

  integer :: timesteps


  double precision :: pi,Re,getRe,k,getk,CD,getcd,D,getd,A(50),getA

  double precision :: AEVEN,JN


  double precision :: y1,y2,r,theta

  double precision :: u1,u2,w1,w2,u1calc,u2calc,umax

  double precision :: u1pert,u1pertcalc,dphidx1,dphidx1calc

  double precision :: w1euler,w2euler,w1eulercalc

  double precision :: w1oseen,w2oseen,w1oseencalc,w2oseencalc


  double precision :: alpha,alphafn,b,c

  integer :: i,j,n,m


  pi=4.0d0*datan(1.0d0)


  ! parameter values Re and CD

  ! get Reynolds number Re
```

```fortran
Re=getRe()

k=getk(Re)


! Drag coefficient CD

CD=getcd()

D=getd(CD)

! end parameter values Re and CD


! calculating A(m) Fourier coefficients

! general

do m=1,50

   A(m)=getA(m,epsilon)

end do


!timestep along streamline

do j=0,timesteps

   r=dsqrt(x1**2+x2**2)

   ! w Euler

   w1=w1eulercalc(x1,x2,epsilon,CD,eta)

   w2=0.0d0


   u1=u1calc(x1,x2,D,w1,A)

   u2=u2calc(x1,x2,D,w2,A)


   x1=x1+u1*dt

   x2=x2+u2*dt
```

```fortran
      write(11,*) x1,x2

    end do

    write(11,*)

  end subroutine streamline


  subroutine streamlineback(x1,x2,dt,timesteps,epsilon)

    double precision x1,x2,dt,epsilon,eta

    double precision :: pi, A(50),CD,D,AEVEN

    double precision :: JN,getRe,getcd,getd,getk,getA

      double precision :: theta

    double precision :: u1,u2,w1,w2,u1calc,u2calc,umax

    double precision :: u1pert,u1pertcalc,dphidx1,dphidx1calc

    double precision :: p,cp,r,k,Re

    double precision :: y1,y2

    double precision :: w1euler, w2euler, w1oseen, w2oseen

    double precision :: alpha,alphafn,b,c,abmid,w1eulercalc

    double precision :: w1oseencalc,w2oseencalc

    integer i,j,n,m,timesteps


    pi=4.0d0*datan(1.0d0)


    ! parameter values Re and CD

    ! get Reynolds number Re

    Re=getRe()

    k=getk(Re)
```

```fortran
! Drag coefficient CD

CD=getcd()

D=getd(CD)

! end parameter values Re and CD


! calculating A(m) Fourier coefficients

! general

do m=1,50

  A(m)=getA(m,epsilon)

end do


! backwards time step along streamline

do j=0,timesteps

  r=dsqrt(x1**2+x2**2)

  ! w Euler

  w1=w1eulercalc(x1,x2,epsilon,CD,eta)

  w2=0.0d0

  u1=u1calc(x1,x2,D,w1,A)

  u2=u2calc(x1,x2,D,w2,A)

  x1=x1-u1*dt

  x2=x2-u2*dt

  write(11,*) x1,x2

end do

write(11,*)

end subroutine streamlineback
```

```fortran
subroutine farfield(epsilon)

 double precision x1,x2,dt,epsilon,eta

 double precision :: pi, A(50),CD,D,AEVEN

 double precision :: JN,getRe,getcd,getd,getk,getA

 double precision :: theta

 double precision :: u1,u2,w1,w2,u1calc,u2calc,umax

 double precision :: u1pert,u1pertcalc,dphidx1,dphidx1calc

 double precision :: p,cp,r,k,Re

 double precision :: y1,y2

 double precision :: w1euler, w2euler, w1oseen, w2oseen

 double precision :: alpha,alphafn,b,c,abmid,w1eulercalc

 double precision :: w1oseencalc,w2oseencalc

 double precision :: x21(200),x22(200),x23(200)

 double precision :: u21exp(200),u22exp(200),u23exp(200)

 double precision :: u21theory(200),u22theory(200),u23theory(200)

 double precision :: u21symmexp(200),u22symmexp(200),u23symmexp(200)

 double precision :: error(199),errortot

 double precision :: deltax


 integer i,j,n,m,timesteps

 pi=4.0d0*datan(1.0d0)

 ! parameter values Re and CD

 ! get Reynolds number Re

 Re=getRe()

 k=getk(Re)
```

```fortran
! Drag coefficient CD

CD=getcd()

D=getd(CD)

! end parameter values Re and CD


! calculating A(m) Fourier coefficients

! general

do m=1,50

  A(m)=getA(m,epsilon)

end do


! calculate velocity from theory

! do j=-50,50

do j=-99,99

  x1=1.067d0

  !   x2=0.1d0*dble(j)

  x2=(2.0d0*dble(j))/45.0d0

  r=dsqrt(x1**2+x2**2)

  w1=w1eulercalc(x1,x2,epsilon,CD,eta)

  u1=u1calc(x1,x2,D,w1,A)

  u21theory(j+100)=u1

  write(12,*) x2,u1

end do

write(12,*)


! do j=-50,50
```

```fortran
      do j=-99,99

        x1=2.0d0

        !    x2=0.1d0*dble(j)

        x2=(2.0d0*dble(j))/45.0d0

        r=dsqrt(x1**2+x2**2)

        w1=w1eulercalc(x1,x2,epsilon,CD,eta)

        u1=u1calc(x1,x2,D,w1,A)

        u22theory(j+100)=u1

        write(12,*) x2,u1+0.5d0

      end do

      write(12,*)


!  do j=-50,50

      do j=-99,99

        x1=3.0d0

        !    x2=0.1d0*dble(j)

        x2=(2.0d0*dble(j))/45.0d0

        r=dsqrt(x1**2+x2**2)

        w1=w1eulercalc(x1,x2,epsilon,CD,eta)

        u1=u1calc(x1,x2,D,w1,A)

        u23theory(j+100)=u1

        write(12,*) x2,u1+1.0d0

      end do

      write(12,*)

      ! end calculate velocity from theory
```

```fortran
! give velocity from experimental data

! read raw data from file velocity@0.txt

open(unit=10, file="velocity@1.txt")


do i=1,200

  read(10,*) x21(i),u21exp(i)

end do

read(10,*)

do i=1,200

  read(10,*) x22(i),u22exp(i)

end do

read(10,*)

do i=1,200

  read(10,*) x23(i),u23exp(i)

end do


! normalise experimental data

do i=1,200

  ! centre data

  x21(i) = x21(i)-792

  x22(i) = x22(i)-792

  x23(i) = x23(i)-792


  ! normalise distance

  x21(i) = x21(i)/45.0

  x22(i) = x22(i)/45.0
```

```fortran
  x23(i) = x23(i)/45.0

end do


!normalise the velocity

do i=1,200

  u21exp(i) = u21exp(i)/19.323

  u22exp(i) = u22exp(i)/19.569

  u23exp(i) = u23exp(i)/19.394

end do


! symmetrize velocity

do i=1,99

  u21symmexp(100-i)=(u21exp(100+i)+u21exp(100-i))/2.0d0

  u21symmexp(100+i)=u21symmexp(100-i)

end do

u21symmexp(100)=u21exp(100)

u21symmexp(200)=u21exp(200)


do i=1,99

  u22symmexp(100-i)=(u22exp(100+i)+u22exp(100-i))/2.0d0

  u22symmexp(100+i)=u22symmexp(100-i)

end do

u22symmexp(100)=u22exp(100)

u22symmexp(200)=u22exp(200)


do i=1,99
```

```fortran
      u23symmexp(100-i)=(u23exp(100+i)+u23exp(100-i))/2.0d0

      u23symmexp(100+i)=u23symmexp(100-i)

   end do

   u23symmexp(100)=u23exp(100)

   u23symmexp(200)=u23exp(200)

! end symmetrize velocity


! write normalised data to file gnuplotwake.dat

   open(unit=22, file="wake.dat")


   do i=1,200

      write(22,*) x21(i),u21symmexp(i)

   end do

   write(22,*)


   do i=1,200

      write(22,*) x22(i),0.5d0+u22symmexp(i)

   end do

   write(22,*)


   do i=1,200

      write(22,*) x23(i),1.0d0+u23symmexp(i)

   end do


   close (10)

   close (22)
```

185

```fortran
! write error between theory and experiment

deltax=x21(2)-x21(1)

errortot=0.0d0

do i=1,199

  error(i) = u21symmexp(i)-u21theory(i)

  errortot = errortot +error(i)

end do


do i=1,199

  error(i) = u22symmexp(i)-u22theory(i)

  errortot = errortot +error(i)

end do


do i=1,199

  error(i) = u23symmexp(i)-u23theory(i)

  errortot = errortot +error(i)

end do

errortot=errortot*deltax

write(*,*) 'errortot is ',errortot

! end write error
end subroutine farfield


subroutine farfieldopt(epsilon,CD,errortot,eta)

  double precision x1,x2,dt,epsilon,eta

  double precision :: pi, A(50),CD,D,AEVEN
```

```fortran
      double precision :: JN,getRe,getcd,getd,getk,getA,getAopt

      double precision :: theta

      double precision :: u1,u2,w1,w2,u1calc,u2calc,umax

      double precision :: u1pert,u1pertcalc,dphidx1,dphidx1calc

      double precision :: p,cp,r,k,Re

      double precision :: y1,y2

      double precision :: w1euler, w2euler, w1oseen, w2oseen

      double precision :: alpha,alphafn,b,c,abmid,w1eulercalc

      double precision :: w1oseencalc,w2oseencalc

      double precision :: x21(200),x22(200),x23(200)

      double precision :: u21exp(200),u22exp(200),u23exp(200)

      double precision :: u21theory(200),u22theory(200),u23theory(200)

      double precision :: u21symmexp(200),u22symmexp(200),u23symmexp(200)

      double precision :: error(199),errortot

      double precision :: deltax


      integer i,j,n,m,timesteps


      pi=4.0d0*datan(1.0d0)


! parameter values Re and CD
! get Reynolds number Re
      Re=getRe()
      k=getk(Re)


! Drag coefficient CD
```

```fortran
! CD=getcd()

 D=getd(CD)


 ! end parameter values Re and CD


 ! calculating A(m) Fourier coefficients

 ! general

 do m=1,50

   A(m)=getAopt(m,epsilon,CD)

 end do


 ! calculate velocity from theory

 open(unit=12, file="farfield.DAT")

! do j=-50,50

 do j=-99,99

   x1=1.00635d0

   !    x2=0.1d0*dble(j)

   x2=(2.0d0*dble(j))/45.0d0

   r=dsqrt(x1**2+x2**2)

   w1=w1eulercalc(x1,x2,epsilon,CD,eta)

   u1=u1calc(x1,x2,D,w1,A)

   u21theory(j+100)=u1

   write(12,*) x2,u1

 end do

 write(12,*)
```

```fortran
!  do j=-50,50
  do j=-99,99
    x1=2.0d0
    !   x2=0.1d0*dble(j)
    x2=(2.0d0*dble(j))/45.0d0
    r=dsqrt(x1**2+x2**2)
    w1=w1eulercalc(x1,x2,epsilon,CD,eta)
    u1=u1calc(x1,x2,D,w1,A)
    u22theory(j+100)=u1
    write(12,*) x2,u1+0.5d0
  end do
  write(12,*)


!  do j=-50,50
  do j=-99,99
    x1=3.0d0
    !   x2=0.1d0*dble(j)
    x2=(2.0d0*dble(j))/45.0d0
    r=dsqrt(x1**2+x2**2)
    w1=w1eulercalc(x1,x2,epsilon,CD,eta)
    u1=u1calc(x1,x2,D,w1,A)
    u23theory(j+100)=u1
    write(12,*) x2,u1+1.0d0
  end do
  write(12,*)
  close(12)
```

```fortran
! end calculate velocity from theory


! give velocity from experimental data
! read raw data from file velocity@0.txt
open(unit=10, file="velocity@1.txt")
do i=1,200
  read(10,*) x21(i),u21exp(i)
end do
read(10,*)
do i=1,200
  read(10,*) x22(i),u22exp(i)
end do
read(10,*)
do i=1,200
  read(10,*) x23(i),u23exp(i)
end do
close (10)


! normalise experimental data
do i=1,200
  ! centre data
  x21(i) = x21(i)-792
  x22(i) = x22(i)-792
  x23(i) = x23(i)-792


  ! normalise distance
```

```fortran
  x21(i) = x21(i)/45.0

  x22(i) = x22(i)/45.0

  x23(i) = x23(i)/45.0

end do


!normalise the velocity

do i=1,200

  u21exp(i) = u21exp(i)/19.323

  u22exp(i) = u22exp(i)/19.569

  u23exp(i) = u23exp(i)/19.394

end do


! symmetrize velocity

do i=1,99

  u21symmexp(100-i)=(u21exp(100+i)+u21exp(100-i))/2.0d0

  u21symmexp(100+i)=u21symmexp(100-i)

end do

u21symmexp(100)=u21exp(100)

u21symmexp(200)=u21exp(200)


do i=1,99

  u22symmexp(100-i)=(u22exp(100+i)+u22exp(100-i))/2.0d0

  u22symmexp(100+i)=u22symmexp(100-i)

end do

u22symmexp(100)=u22exp(100)

u22symmexp(200)=u22exp(200)
```

```fortran
do i=1,99

  u23symmexp(100-i)=(u23exp(100+i)+u23exp(100-i))/2.0d0

  u23symmexp(100+i)=u23symmexp(100-i)

end do

u23symmexp(100)=u23exp(100)

u23symmexp(200)=u23exp(200)
! end symmetrize velocity


! write normalised data to file gnuplotwake.dat
open(unit=22, file="wake.dat")
do i=1,200

  write(22,*) x21(i),u21symmexp(i)

end do
write(22,*)


do i=1,200

  write(22,*) x22(i),0.5d0+u22symmexp(i)

end do

  write(22,*)


  do i=1,200

  write(22,*) x23(i),1.0d0+u23symmexp(i)

  end do
close (22)
```

```fortran
! write error between theory and experiment

deltax=abs(x21(2)-x21(1))

errortot=0.0d0

do i=1,199

   error(i) = abs(u21symmexp(i)-u21theory(i))

   errortot = errortot +error(i)

end do


do i=1,199

   error(i) = abs(u22symmexp(i)-u22theory(i))

   errortot = errortot +error(i)

end do


do i=1,199

   error(i) = abs(u23symmexp(i)-u23theory(i))

   errortot = errortot +error(i)

end do

errortot=errortot*deltax

! end write error

end subroutine farfieldopt


subroutine slineplot(epsilon)

 double precision dt,x1,x2,epsilon

 integer timesteps, i


! start calculating streamlinelines
```

```fortran
! from position x1, x2, calculate new position at
! time step dt to number of timesteps
dt=0.01
timesteps= 1500
do i=0,6
  ! streamlines above
  x1=-2.0
  x2=0.25+0.25*dble(i)
  call streamline(x1,x2,dt,timesteps,epsilon)
  ! streamlines below
  x1=-2.0
  x2=-0.25-0.25*dble(i)
  call streamline(x1,x2,dt,timesteps,epsilon)
end do


! streamline starting at (-2,0.175)
timesteps= 2000
! streamlines above
x1=-2.0
x2=0.175
call streamline(x1,x2,dt,timesteps,epsilon)
! streamlines below
x1=-2.0
x2=-0.175
call streamline(x1,x2,dt,timesteps,epsilon)
```

```fortran
! streamline starting at (-2,0.35)

timesteps= 2000

! streamlines above

x1=-2.0

x2=0.35

call streamline(x1,x2,dt,timesteps,epsilon)

! streamlines below

x1=-2.0

x2=-0.35

call streamline(x1,x2,dt,timesteps,epsilon)


! streamline starting at (6.0,0.55)

timesteps= 4000

! streamlines above

x1=6.0

x2=0.55

call streamlineback(x1,x2,dt,timesteps,epsilon)

! streamlines below

x1=6.0

x2=-0.55

call streamlineback(x1,x2,dt,timesteps,epsilon)


! streamline starting at (6.0,0.6)

timesteps= 4000

! streamlines above

x1=6.0
```

```
x2=0.6

call streamlineback(x1,x2,dt,timesteps,epsilon)

! streamlines below

x1=6.0

x2=-0.6

call streamlineback(x1,x2,dt,timesteps,epsilon)


! streamline starting at (6.0,0.65)

timesteps= 4000

! streamlines above

x1=6.0

x2=0.65

call streamlineback(x1,x2,dt,timesteps,epsilon)

! streamlines below

x1=6.0

x2=-0.65

call streamlineback(x1,x2,dt,timesteps,epsilon)


! an eddy

!  timesteps= 1315

timesteps= 3000

x1= 1.1

x2=  0.5

call streamline(x1,x2,dt,timesteps,epsilon)

x1= 1.1

x2=  0.5
```

```
call streamlineback(x1,x2,dt,timesteps,epsilon)

! its reflection

x1= 1.1

x2= -0.5

call streamline(x1,x2,dt,timesteps,epsilon)

x1= 1.1

x2= -0.5

call streamlineback(x1,x2,dt,timesteps,epsilon)


! a smaller eddy

!  timesteps= 1000

 timesteps= 3000

x1= 1.5

x2= 0.3

call streamline(x1,x2,dt,timesteps,epsilon)

x1= 1.5

x2= 0.3

call streamlineback(x1,x2,dt,timesteps,epsilon)

! its reflection

x1= 1.5

x2= -0.3

call streamline(x1,x2,dt,timesteps,epsilon)

x1= 1.5

x2= -0.3

call streamlineback(x1,x2,dt,timesteps,epsilon)
```

```
! start free streamline from body

! first part from body

!  timesteps=325

timesteps=3000

x1=0.6

x2=0.8

call streamline(x1,x2,dt,timesteps,epsilon)

! reflection

x1=0.6

x2=-0.8

call streamline(x1,x2,dt,timesteps,epsilon)

! second part from wake

timesteps=4150

x1=1.5

x2=0.81575

call streamline(x1,x2,dt,timesteps,epsilon)

x1=1.5

x2=0.81575

call streamlineback(x1,x2,dt,timesteps,epsilon)

! reflection

x1=1.5

x2=-0.81575

call streamline(x1,x2,dt,timesteps,epsilon)

x1=1.5

x2=-0.81575

call streamlineback(x1,x2,dt,timesteps,epsilon)
```

```
! end free streamline


! centreline to left

write(11,*) -2.0,0.0

write(11,*) -1.0,0.0

write(11,*)

! centreline to right

write(11,*) 1.0,0.0

write(11,*) 6.0,0.0

write(11,*)


! end calculating streamline lines
end subroutine slineplot


subroutine slineploteuler(epsilon)

  double precision dt,x1,x2,epsilon

  integer timesteps, i


  ! start calculating streamlinelines

  ! from position x1, x2, calculate new position at

  ! time step dt to number of timesteps

  dt=0.01

  timesteps= 1500

  do i=0,6

    ! streamlines above

    x1=-2.0
```

```fortran
  x2=0.25+0.25*dble(i)

  call streamline(x1,x2,dt,timesteps,epsilon)

  ! streamlines below

  x1=-2.0

  x2=-0.25-0.25*dble(i)

  call streamline(x1,x2,dt,timesteps,epsilon)

end do


! streamline starting at (-2,0.175)

timesteps= 2000

! streamlines above

x1=-2.0

x2=0.175

call streamline(x1,x2,dt,timesteps,epsilon)

! streamlines below

x1=-2.0

x2=-0.175

call streamline(x1,x2,dt,timesteps,epsilon)


! streamline starting at (-2,0.35)

timesteps= 2000

! streamlines above

x1=-2.0

x2=0.35

call streamline(x1,x2,dt,timesteps,epsilon)

! streamlines below
```

```fortran
x1=-2.0

x2=-0.35

call streamline(x1,x2,dt,timesteps,epsilon)


! streamline starting at (6.0,0.55)

timesteps= 4000

! streamlines above

x1=6.0

x2=0.55

call streamlineback(x1,x2,dt,timesteps,epsilon)

! streamlines below

x1=6.0

x2=-0.55

call streamlineback(x1,x2,dt,timesteps,epsilon)


! streamline starting at (6.0,0.6)

timesteps= 4000

! streamlines above

x1=6.0

x2=0.6

call streamlineback(x1,x2,dt,timesteps,epsilon)

! streamlines below

x1=6.0

x2=-0.6

call streamlineback(x1,x2,dt,timesteps,epsilon)
```

```
! streamline starting at (6.0,0.65)

timesteps= 4000

! streamlines above

x1=6.0

x2=0.65

call streamlineback(x1,x2,dt,timesteps,epsilon)

! streamlines below

x1=6.0

x2=-0.65

call streamlineback(x1,x2,dt,timesteps,epsilon)


! an eddy

!  timesteps= 1315

timesteps= 3000

x1= 1.1

x2=  0.5

call streamline(x1,x2,dt,timesteps,epsilon)

x1= 1.1

x2=  0.5

call streamlineback(x1,x2,dt,timesteps,epsilon)

! its reflection

x1= 1.1

x2= -0.5

call streamline(x1,x2,dt,timesteps,epsilon)

x1= 1.1

x2= -0.5
```

```
     call streamlineback(x1,x2,dt,timesteps,epsilon)


     ! a smaller eddy
!  timesteps= 1000
  timesteps= 3000
  x1= 1.5
  x2= 0.3
  call streamline(x1,x2,dt,timesteps,epsilon)
  x1= 1.5
  x2= 0.3
  call streamlineback(x1,x2,dt,timesteps,epsilon)
  ! its reflection
  x1= 1.5
  x2= -0.3
  call streamline(x1,x2,dt,timesteps,epsilon)
  x1= 1.5
  x2= -0.3
  call streamlineback(x1,x2,dt,timesteps,epsilon)


  ! start free streamline from body
  ! first part from body
!  timesteps=325
  timesteps=3000
  x1=0.6
  x2=0.8
  call streamline(x1,x2,dt,timesteps,epsilon)
```

```
! reflection

x1=0.6

x2=-0.8

call streamline(x1,x2,dt,timesteps,epsilon)

! second part from wake

timesteps=4150

x1=1.5

x2=0.81575

call streamline(x1,x2,dt,timesteps,epsilon)

x1=1.5

x2=0.81575

call streamlineback(x1,x2,dt,timesteps,epsilon)

! reflection

x1=1.5

x2=-0.81575

call streamline(x1,x2,dt,timesteps,epsilon)

x1=1.5

x2=-0.81575

call streamlineback(x1,x2,dt,timesteps,epsilon)

! end free streamline


! centreline to left

write(11,*) -2.0,0.0

write(11,*) -1.0,0.0

write(11,*)

! centreline to right
```

```
  write(11,*) 1.0,0.0

  write(11,*) 6.0,0.0

  write(11,*)


  ! end calculating streamline lines
end subroutine slineploteuler


subroutine slineplotRe40CD2(epsilon)

  double precision dt,x1,x2,epsilon

  integer timesteps, i


  ! start calculating streamlinelines

  ! from position x1, x2, calculate new position at

  ! time step dt to number of timesteps

  dt=0.01

  timesteps= 1500

  do i=0,6

    ! streamlines above

    x1=-2.0

    x2=0.25+0.25*dble(i)

    call streamline(x1,x2,dt,timesteps,epsilon)

    ! streamlines below

    x1=-2.0

    x2=-0.25-0.25*dble(i)

    call streamline(x1,x2,dt,timesteps,epsilon)

  end do
```

! streamline starting at (-2,0.35)

timesteps= 2000

! streamlines above

x1=-2.0

x2=0.35

call streamline(x1,x2,dt,timesteps,epsilon)

! streamlines below

x1=-2.0

x2=-0.35

call streamline(x1,x2,dt,timesteps,epsilon)

! streamline starting at (6.0,0.25)

timesteps= 4000

! streamlines above

x1=6.0

x2=0.25

call streamlineback(x1,x2,dt,timesteps,epsilon)

! streamlines below

x1=6.0

x2=-0.25

call streamlineback(x1,x2,dt,timesteps,epsilon)

! streamline starting at (6.0,0.125)

timesteps= 4000

! streamlines above

```
x1=6.0

x2=0.125

call streamlineback(x1,x2,dt,timesteps,epsilon)

! streamlines below

x1=6.0

x2=-0.125

call streamlineback(x1,x2,dt,timesteps,epsilon)


! an eddy

timesteps= 1315

x1= 1.1

x2=  0.5

call streamline(x1,x2,dt,timesteps,epsilon)

x1= 1.1

x2=  0.5

call streamlineback(x1,x2,dt,timesteps,epsilon)

! its reflection

x1= 1.1

x2= -0.5

call streamline(x1,x2,dt,timesteps,epsilon)

x1= 1.1

x2= -0.5

call streamlineback(x1,x2,dt,timesteps,epsilon)


! a smaller eddy

timesteps= 1000
```

```fortran
x1= 1.5

x2= 0.3

call streamline(x1,x2,dt,timesteps,epsilon)

x1= 1.5

x2= 0.3

call streamlineback(x1,x2,dt,timesteps,epsilon)

! its reflection

x1= 1.5

x2= -0.3

call streamline(x1,x2,dt,timesteps,epsilon)

x1= 1.5

x2= -0.3

call streamlineback(x1,x2,dt,timesteps,epsilon)


! start free streamline from body

! first part from body

!  timesteps=325

timesteps= 3000

x1=0.6

x2=0.8

call streamline(x1,x2,dt,timesteps,epsilon)

! reflection

x1=0.6

x2=-0.8

call streamline(x1,x2,dt,timesteps,epsilon)

! second part from wake
```

```
    timesteps=4150

    x1=1.5

    x2=0.81575

    call streamline(x1,x2,dt,timesteps,epsilon)

    x1=1.5

    x2=0.81575

    call streamlineback(x1,x2,dt,timesteps,epsilon)

    ! reflection

    x1=1.5

    x2=-0.81575

    call streamline(x1,x2,dt,timesteps,epsilon)

    x1=1.5

    x2=-0.81575

    call streamlineback(x1,x2,dt,timesteps,epsilon)

    ! end free streamline


    ! centreline to left

    write(11,*) -2.0,0.0

    write(11,*) -1.0,0.0

    write(11,*)

    ! centreline to right

    write(11,*) 1.0,0.0

    write(11,*) 6.0,0.0

    write(11,*)

    ! end calculating streamlinelines

end subroutine slineplotRe40CD2
```

```fortran
subroutine slineplotRe40CD1pt1(epsilon)

 double precision dt,x1,x2,epsilon

 integer timesteps, i


 ! start calculating streamlinelines

 ! from position x1, x2, calculate new position at

 ! time step dt to number of timesteps

 dt=0.01

 timesteps= 1500

 do i=0,6

   ! streamlines above

   x1=-2.0

   x2=0.25+0.25*dble(i)

   call streamline(x1,x2,dt,timesteps,epsilon)

   ! streamlines below

   x1=-2.0

   x2=-0.25-0.25*dble(i)

   call streamline(x1,x2,dt,timesteps,epsilon)

 end do

 timesteps= 2000

 x1=-2.0

 x2=0.1

 call streamline(x1,x2,dt,timesteps,epsilon)

 ! streamlines below

 x1=-2.0
```

```
x2=-0.1

call streamline(x1,x2,dt,timesteps,epsilon)


timesteps= 4000

! streamlines above

x1= 1.5

x2=  0.3

call streamline(x1,x2,dt,timesteps,epsilon)

x1= 1.5

x2=  0.3

call streamlineback(x1,x2,dt,timesteps,epsilon)

x1= 2.5

x2=  0.3

call streamline(x1,x2,dt,timesteps,epsilon)

x1= 2.5

x2=  0.3

call streamlineback(x1,x2,dt,timesteps,epsilon)

timesteps= 10000

x1= 4.5

x2=  0.3

call streamline(x1,x2,dt,timesteps,epsilon)

x1= 4.5

x2=  0.3

call streamlineback(x1,x2,dt,timesteps,epsilon)

x1= 4.5

x2=  0.4
```

```
call streamline(x1,x2,dt,timesteps,epsilon)

x1= 4.5

x2=  0.4

call streamlineback(x1,x2,dt,timesteps,epsilon)


timesteps= 4000

! streamlines reflection

x1= 1.5

x2= -0.3

call streamline(x1,x2,dt,timesteps,epsilon)

x1= 1.5

x2= -0.3

call streamlineback(x1,x2,dt,timesteps,epsilon)

x1= 2.5

x2= -0.3

call streamline(x1,x2,dt,timesteps,epsilon)

x1= 2.5

x2= -0.3

call streamlineback(x1,x2,dt,timesteps,epsilon)



timesteps= 10000

x1= 4.5

x2= -0.3

call streamline(x1,x2,dt,timesteps,epsilon)

x1= 4.5
```

```fortran
x2=  -0.3

call streamlineback(x1,x2,dt,timesteps,epsilon)

x1= 4.5

x2=  -0.4

call streamline(x1,x2,dt,timesteps,epsilon)

x1= 4.5

x2=  -0.4

call streamlineback(x1,x2,dt,timesteps,epsilon)

timesteps= 4000

! start free streamline from body

! first part from body

timesteps= 3000

x1=0.6

x2=0.8

call streamline(x1,x2,dt,timesteps,epsilon)

! reflection

x1=0.6

x2=-0.8

call streamline(x1,x2,dt,timesteps,epsilon)

! end free streamline


! centreline to left

write(11,*) -2.0,0.0

write(11,*) -1.0,0.0

write(11,*)

! centreline to right
```

```fortran
  write(11,*) 1.0,0.0

  write(11,*) 6.0,0.0

  write(11,*)

  ! end calculating streamlinelines
end subroutine slineplotRe40CD1pt1
```

!Experimental data files

```fortran
program normalvelocity

  implicit none

  double precision :: x21(200),x22(200),x23(200),u21(200),u22(200),u23(200)

  double precision :: u21symm(200),u22symm(200),u23symm(200)

  double precision :: blank

  integer ::i

! read raw data from file velocity@0.txt

  open(unit=10, file="velocity@1.txt")

      ! read(unit=10,fmt=1001) x

        do i=1,200

          read(10,*) x21(i),u21(i)

        end do

        read(10,*) blank

        do i=1,200

          read(10,*) x22(i),u22(i)

        end do

        read(10,*) blank

        do i=1,200

          read(10,*) x23(i),u23(i)
```

```fortran
      end do

! normalise data

  do i=1,200

    ! centre data

    x21(i) = x21(i)-792

    x22(i) = x22(i)-792

    x23(i) = x23(i)-792

        ! normalise distance

    x21(i) = x21(i)/45.0

    x22(i) = x22(i)/45.0

    x23(i) = x23(i)/45.0

  end do


!normalise the velocity

  do i=1,200

    u21(i) = u21(i)/19.323

    u22(i) = u22(i)/19.569

    u23(i) = u23(i)/19.394

   end do

  do i=1,99

    u21symm(100-i)=(u21(100+i)+u21(100-i))/2.0d0

    u21symm(100+i)=u21symm(100-i)

  end do

  u21symm(100)=u21(100)

  u21symm(200)=u21(200)

  do i=1,99
```

```fortran
        u22symm(100-i)=(u22(100+i)+u22(100-i))/2.0d0

          u22symm(100+i)=u22symm(100-i)

        end do

        u22symm(100)=u22(100)

        u22symm(200)=u22(200)

        do i=1,99

          u23symm(100-i)=(u23(100+i)+u23(100-i))/2.0d0

          u23symm(100+i)=u23symm(100-i)

        end do

        u23symm(100)=u23(100)

        u23symm(200)=u23(200)
! write normalised data to file gnuplotwake.dat

 open(unit=12, file="wake.dat")


   do i=1,200

     write(12,*) x21(i),u21symm(i)

   end do

   write(12,*)

   do i=1,200

     write(12,*) x22(i),0.5d0+u22symm(i)

   end do

   write(12,*)

   do i=1,200

   write(12,*) x23(i),1.0d0+u23symm(i)

   end do

 close (10)
```

```fortran
  close (12)

end program normalvelocity



!Error calculation area under the curve

Program Area


 real :: h,a,b

 double precision  :: Intgl21,Intgl22,Intgl23,Inttot,deltax

 Integer :: i,N

 double precision :: x21(200),x22(200),x23(200)

 double precision :: u21symmexp(200),u22symmexp(200),u23symmexp(200)

 double precision :: blank


 open(unit=25, file="error.dat")

 ! read in error data

 do i=1,199

   read(25,*) x21(i),u21symmexp(i)

 end do

 read(25,*)


 do i=1,199

   read(25,*) x22(i),u22symmexp(i)

 end do

 read(25,*)


 do i=1,199
```

```fortran
      read(25,*) x23(i),u23symmexp(i)

end do

close (25)

! end read in error data


! evaluate integral

open(unit=26,file="Intgl.dat")

deltax=x21(2)-x21(1)

Intgl21=0.0d0

do i=1,199

   Intgl21 = Intgl21+u21symmexp(i)

end do

Intgl21=Intgl21*deltax

write(26,*) 'error integral at first station is ', Intgl21


Intgl22=0.0d0

do i=1,199

   Intgl22 = Intgl22+u22symmexp(i)

end do

Intgl22=Intgl22*deltax

write(26,*) 'error integral at second station is ', Intgl22


Intgl23=0.0d0

do i=1,199

   Intgl23 =  Intgl23+u23symmexp(i)

end do
```

```fortran
Intgl23=Intgl23*deltax

write(26,*) 'error integral at third station is ', Intgl23


Inttot=Intgl21+Intgl22+Intgl23

write(26,*) 'total error is ', Inttot

close (26)

! end evaluate integral
end Program Area
```